Two-fluid Simulations of Magnetic Reconnection with a Kinetic Closure for the Electron Pressure Anisotropy

by

Obioma Ogonna Chinyerem Ohia

B.S., Iowa State University (2007)

Submitted to the Department of Physics
in partial fulfillment of the requirements for the degree of

Doctor of Philosophy in Physics

at the

MASSACHUSETTS INSTITUTE OF TECHNOLOGY

September 2014

Signature redacted

Author .....
Department of Physics
August 15, 2014

Signature redacted

Certified by..... .....
Jan Egedal
Associate Professor
Signature redacted Thesis Supervisor

Accepted by..... .....
Krishna Rajagopal
Professor, Associate Department Head for Education

Two-fluid Simulations of Magnetic Reconnection with a Kinetic Closure for the Electron Pressure Anisotropy

by

Obioma Ogonna Chinyerem Ohia

Submitted to the Department of Physics
on August 15, 2014, in partial fulfillment of the
requirements for the degree of
Doctor of Philosophy in Physics

Abstract

Magnetic reconnection is a rapid rearrangement of magnetic line topology in a plasma that can allow magnetic energy to heat, drive macroscopic flows, or accelerate particles in space and laboratory plasmas. Though reconnection affects global plasma dynamics, it depends intimately on small-scale electron physics. In weakly-collisional plasmas, electron pressure anisotropy resulting from the electric and magnetic trapping of electrons strongly affects the structure surrounding the electron diffusion region and the electron current layer. Previous fluid models and simulations fail to account for this anisotropy. In this thesis, new equations of state that accurately describe the electron pressure anisotropy in cases of sufficiently strong guide magnetic field are implemented in fluid simulations and are compared to previous fluid models and kinetic simulations. Elongated current layers in the reconnection region, driven, in part, by this pressure anisotropy, appear as part of a self-regulating mechanism of electron pressure anisotropy. The structure depends on plasma parameters, with low guide fields yielding longer layers.

Thesis Supervisor: Jan Egedal
Title: Associate Professor

Acknowledgments

There is an African adage, whose exact origins are unknown by the author, that says "If you want to go quickly, go alone. If you want to go far, go together". For me to complete this long journey, I have to give thanks to the many people who have touched my life. I'm very grateful to my advisor, Prof. Jan Egedal for taking me into his group, providing guidance, support, mentorship, and allowing me to grow as a scientist. I'd like to thank Prof. Miklos Porkolab and Prof. John Belcher for serving on my committee and for their valuable feedback. I'd also like to thank the VTF group, in particular Dr. Ari Le and Dr. Arturs Vrublevskis for their physics discussions and collaborations. I would like to thank external collaborator Dr. Vyacheslav "Slava" Lukin for the HiFi framework and Dr. William Daughton for kinetic simulation data.

Additionally I'd like to thank Dean Blanche Staton, Monica Orta, and Dr. Christopher M. Jones of the MIT community that gave me the guidance that I needed to persevere. I can't give enough thanks to my family, friends and my Academy of Courage Minority Engineers family, who provided the support, encouragement, friendship and community that made this journey a little easier, in particular Dr. Legena Henry who is a role model for many. I'd like to thank my sister Okwuoma Aniagu, my brother Nkemkweruka Ohia, and my other-brothers Jimmy Chan and Hassan Masoom for pushing me to become the person I am today.

I'd like to thank my parents Dr. Uche Ohia and Prof. Chinyerem Ohia for my mind and my heart, and for everything they've done for me. Finally, I'd like to thank The Creator, for making all things possible.

Contents

List of Figures

Chapter 1

Introduction

Magnetic Reconnection is a process in plasmas which converts magnetic field energy into particle energy through an often rapid change in magnetic field line topology and is seen as a driver of explosive events such as solar flares, coronal mass ejections, and magnetic substorms in the Earth's magnetotail [1–4]. Though reconnection affects global plasma properties and dynamics, it depends intimately on local violations of the ideal plasma limit through small scale electron physics [1]. In collisionless plasmas, electron pressure anisotropy has been shown to develop near the reconnection region due to electric and magnetic trapping of electrons [5]. Recently, new Equations of State that accurately relate magnetic field aligned pressure anisotropy to the local density and magnetic fields have been derived, applicable to guide-field reconnection where the electron magnetic moment is conserved [6]. In this dissertation, these new equations of state are implemented in a fluid simulation and compared to traditional fluid simulations and accurate kinetic simulations. In addition, predictions of the structure of the reconnection region are tested, and the global implications of this new electron physics are studied.

1.1 Magnetic Reconnection

In many magnetized plasma systems, such as the solar atmosphere, or "corona", and the Earth's magnetosphere, the large amount of energy released in explosive events

must come from magnetic fields [3], as other energy reservoirs, such as the systems thermal or gravitational content, are insufficient. The conversion of magnetic energy must be due to reconnection as conversion due to the diffusion or biharmonic mixing (hyper-diffusion) of magnetic field lines would take much to long to explain dynamic events. For systems of interest, the diffusion time, τ_D, or the biharmonic mixing time, τ_H, are many orders of magnitude longer than the timescales of these events, which are near the order of the Alfvén time of the propagation of magnetic perturbations τ_A. The slow Sweet-Parker model of reconnection is of order $\sqrt{\tau_A \tau_D}$ [7] which is significantly shorter than diffusion or biharmonic mixing alone. Faster reconnection models typically have time scales of τ_A/R where R is the reconnection rate and is of order 10^{-1}.

On typical dynamic time scales, sufficiently hot, extended plasmas, which characterizes many relevant plasmas, are approximately ideal; the magnetic field is "frozen" to the plasma motion and field line connectivity is conserved, that is, if two plasma elements are connected by a magnetic field line at one time, they will remain connected at later times as shown in Figure 1-1a. Plasma motion can twist and distort field lines leading to high stresses along magnetic field lines. Under ideal plasma conditions, the magnetic fields would be unable to relax into a simpler geometry and release large amounts of their energy. However, in localized regions with small spatial scales, nonideal processes in plasma can become important, breaking the ideal plasma constraint. This local nonideality has a global effect, allowing magnetic fields to "break and reconnect", releasing energy through a rearrangement of magnetic geometry and also allows plasma from different regions to mix, shown in Figure 1-1b [1].

A simple reconnection scenario is that with a strong current sheet forming in the boundary of two magnetic fields with oppositely directed in-plane components (the magnetic fields may also have a guide-field component normal to the plane) depicted in Figure 1-2. Far from the boundary region, the plasma is approximately ideal while in the boundary region, termed the diffusion region, nonideal effects such as resistivity or nongyrotropic (off-diagonal) electron pressure, allow the plasma to break and reconnect at an "X-point" or an "X-line". The subsequent relaxation or

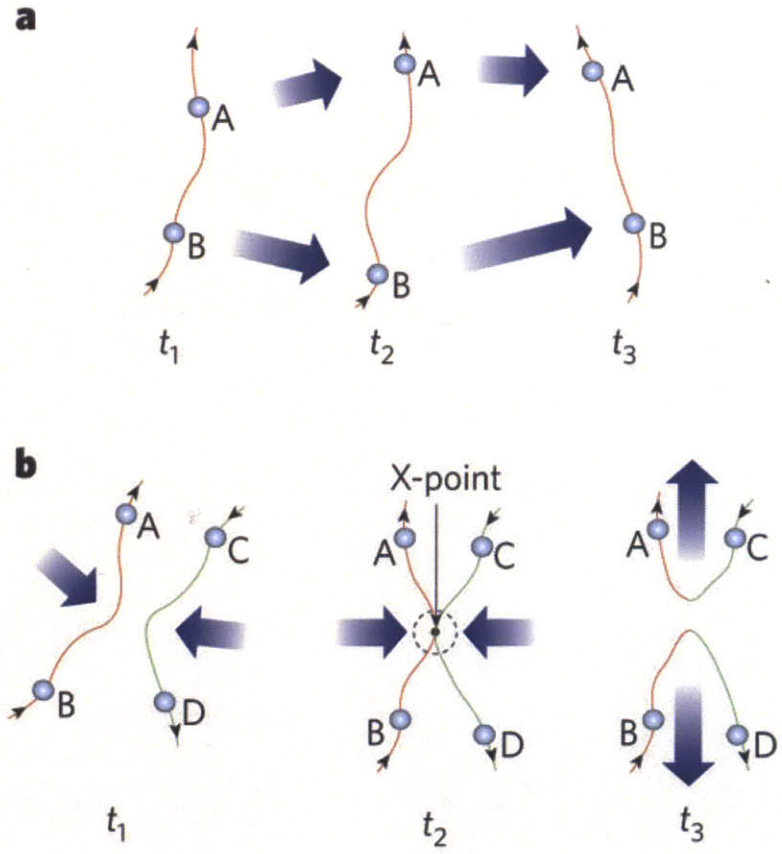

Figure 1-1: (a) Magnetic field lines frozen to plasma flows (blue arrows) such that two plasma elements initially connected by the a field line at time t_1 remain connected for all later times. (b) Two oppositely directed field lines with plasma elements A, B, C, and D move towards one another at t_1. At t_2 they meet and reconnect at an X-point such that A, C and B, D are connected at t_3. The tension along the bent field lines then drives the newly connected lines away from one another. (Ref [8]).

straightening of the newly reconnected field lines drives plasma away from the X-line, lowering the plasma pressure near the X-line. Additional plasma and frozen-in field flow into the diffusion region due to the low pressure, allowing more field lines to reconnect, continuing in a self-sustaining process until the global system has evolved into a relaxed state.

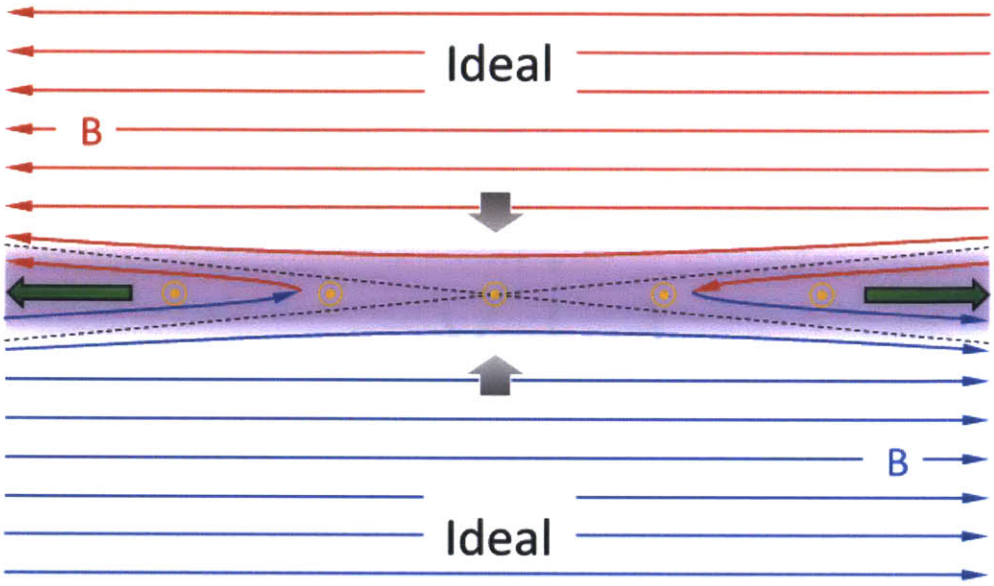

Figure 1-2: Regions of oppositely directed magnetic field lines (red and blue lines) with an corresponding out of plane current (yellow circles) between them. Plasma inflow (vertical grey arrows) carry magnetic field lines into the non-ideal region (purple) where they can reconnect (multi-colored lines) and are subsequently ejected (horizontal green arrows).

1.2 Astrophysical Reconnection

As mentioned above, magnetic reconnection is an important process in many astrophysical systems. One of the earliest motivations of the study of reconnection was to understand the various dynamics of the solar corona, especially solar flares. Flares are tremendous bursts of radiation emanating from the solar corona, and are often accompanied by a large ejection of coronal mass, termed a coronal mass ejection. Large flares release up to 10^{25} joules (about 100,000 times the energy consumption of the world each year [9] or 10 times the energy that the Earth receives from the sun

each year) in a span of 2 to 20 minutes [3]. Magnetic reconnection was first developed to explain the link between magnetic nulls, such as X-lines, and solar flares [1,10–12]. Although oversimplified, early solar flare models involved the reconnection of magnetic fields of current regions in the corona [7,13]. A cartoon of Sweet's model of two pairs of sunspots approaching one another is shown in Figure 1-3, with reconnection occurring at the point N in Figure 1-3. Currently a complete model for solar flares has yet to be developed, however, there is ample evidence linking magnetic reconnection to solar flare occurrence [14–18] and particle acceleration [19–21].

In addition to solar phenomena, reconnection is also important to the Earth's magnetosphere. The dipole field of the Earth shields it from most of the charged particles in the solar wind, but reconnection allows solar wind to couple to the magnetosphere by allowing the interplanetary magnetic field (IMF) lines in the solar wind to connect to the magnetic field lines of the magnetosphere. This process, first suggested by Dungey [22], is depicted in Figure 1-4. Due to the solar wind, the dayside of the magnetosphere is compressed while the nightside is stretched into a magnetotail. In Figure 1-4, southward IMF and the Earth's northward magnetic field depicted by lines 1' and 1, meet and reconnect at the magnetopause, the boundary between the Earth's magnetic field and local plasma from the solar wind. The reconnected field lines are dragged to the nightside of the Earth, depicted through lines 1-5 in Figure 1-4. The tail configuration could be unstable [23] and another reconnection event would occur for field line 6, releasing energy and closing the Earth's field lines at the lobes [24]. The new dipole field lines move toward and around the Earth, depicted by lines 6-9 in Figure 1-4. This motion of geomagnetic fields produce polar cap flow patterns, also depicted in Figure 1-4. This process, which happens intermittently and driven by magnetic reconnection, not only allows solar wind plasma and energy to enter the magnetosphere, but also allows them to be released during a magnetic substorms in the magnetotail [4,25].

Many observations supporting the role of magnetic reconnection in the dynamics of the Earth's magnetosphere, have been obtained by in-situ magnetic and plasma measurements taken by spacecraft orbiting the Earth. Earliest observations of plasma

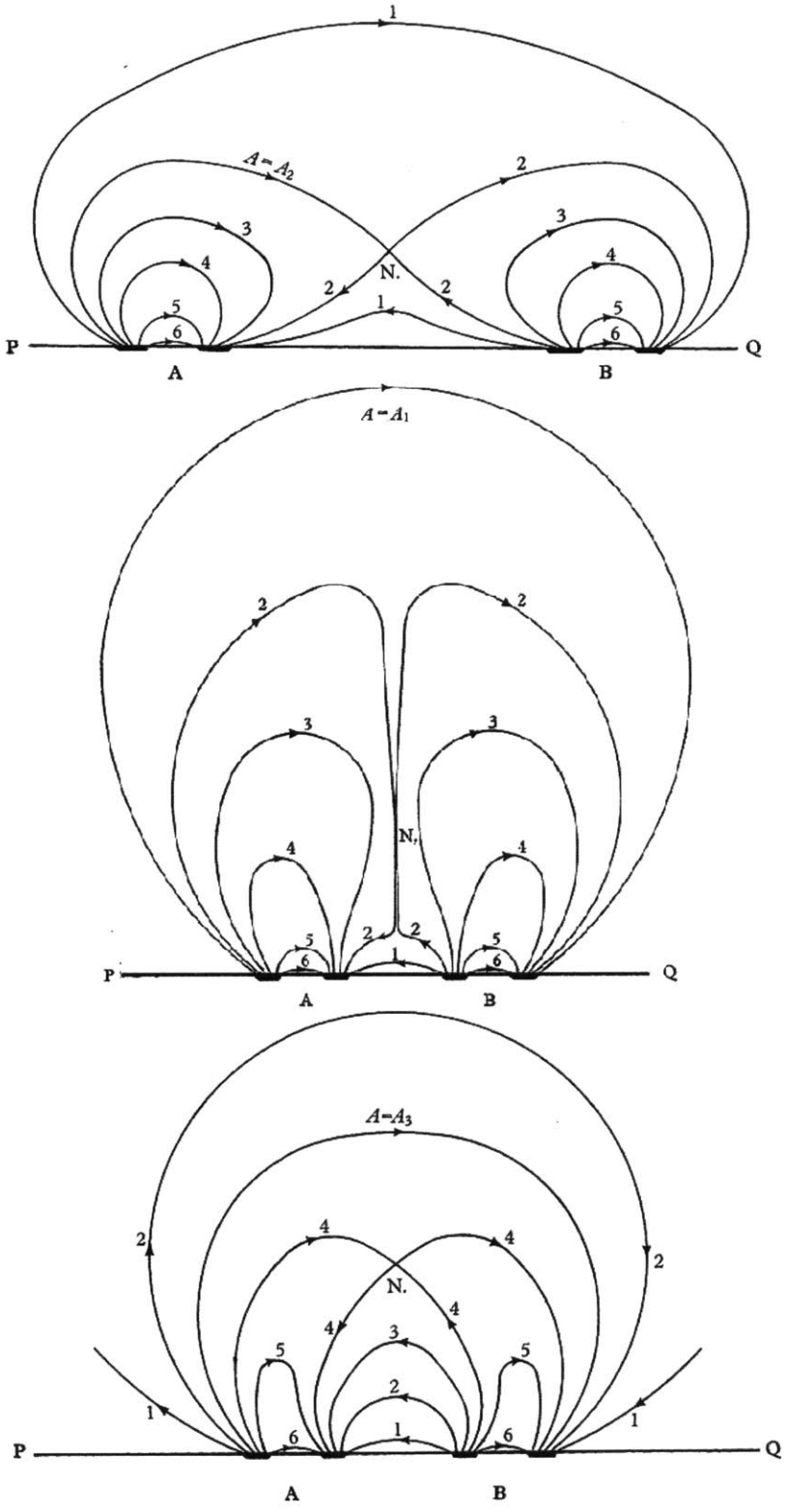

Figure 1-3: Evolution of magnetic field line topology as two pairs of sunspots approach one another, as depicted by Sweet. The reconnection site is marked by point N while numbers trace magnetic field lines. (Ref [13]).

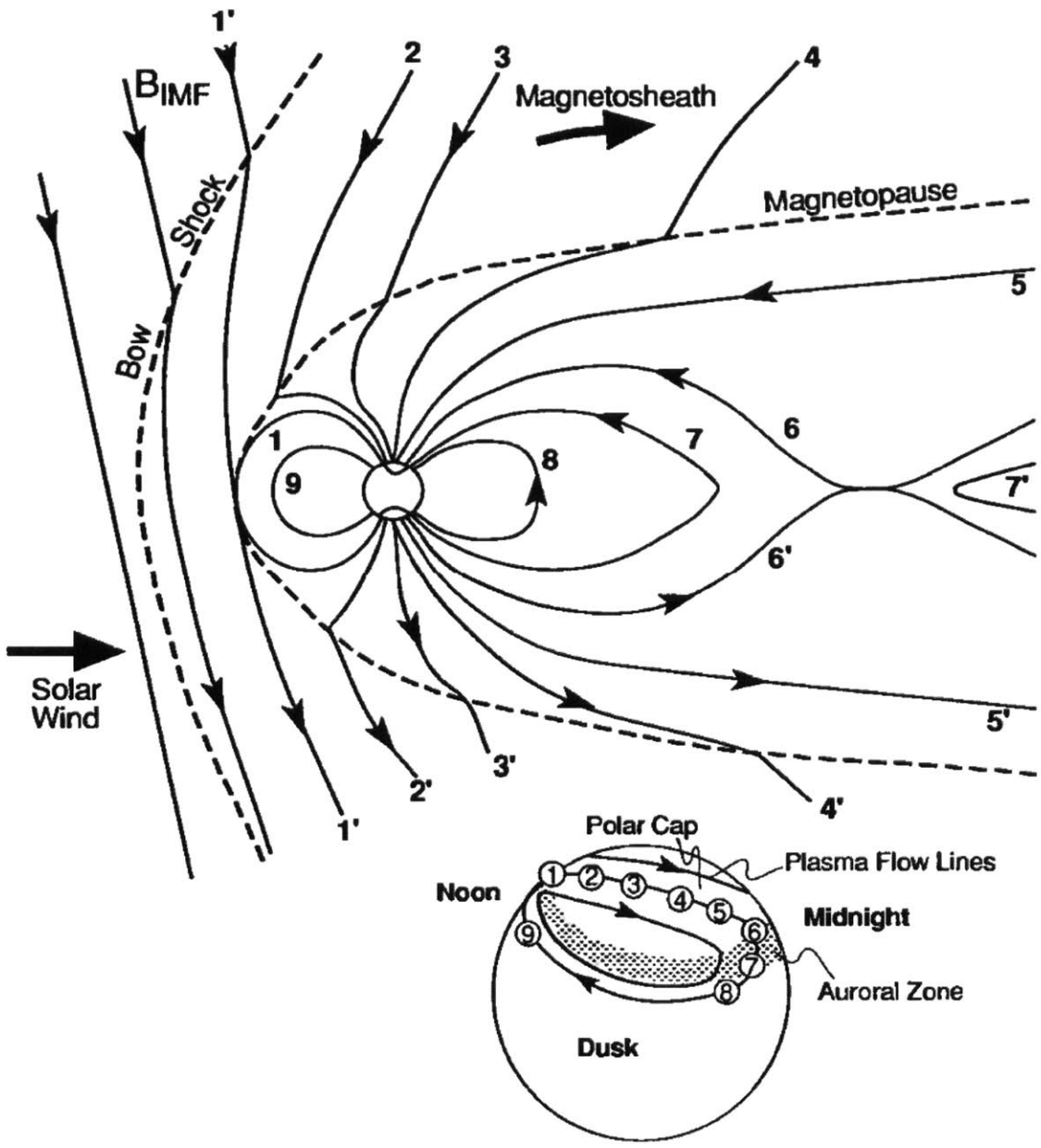

Figure 1-4: Dungey's model of plasma flows in the magnetosphere. The interplanetary magnetic field depicted by line 1' reconnects with the Earth's magnetic field depicted by line 1. The newly connected lines are dragged across the Earth by the solar wind shown by numbers 1-5. Reconnection occurs for field lines 6 and 6' and the newly reconnected lines relax toward and around the Earth. This flow pattern is traced onto the polar caps below. (Ref [25]).

jet signatures of reconnection in the magnetopause were made by the International-Sun-Earth-Explorer (ISEE) satellites [26,27]. A cartoon and data of the first reported event are shown in Figure 1-5. A plethora of supporting observations of reconnection signatures in the magnetopause have been made since [28,29], including simultaneous observations of oppositely directed plasma jets from an X-line [30]. In addition, measurements also suggest spacecrafts have passed through reconnection diffusion regions [31–34].

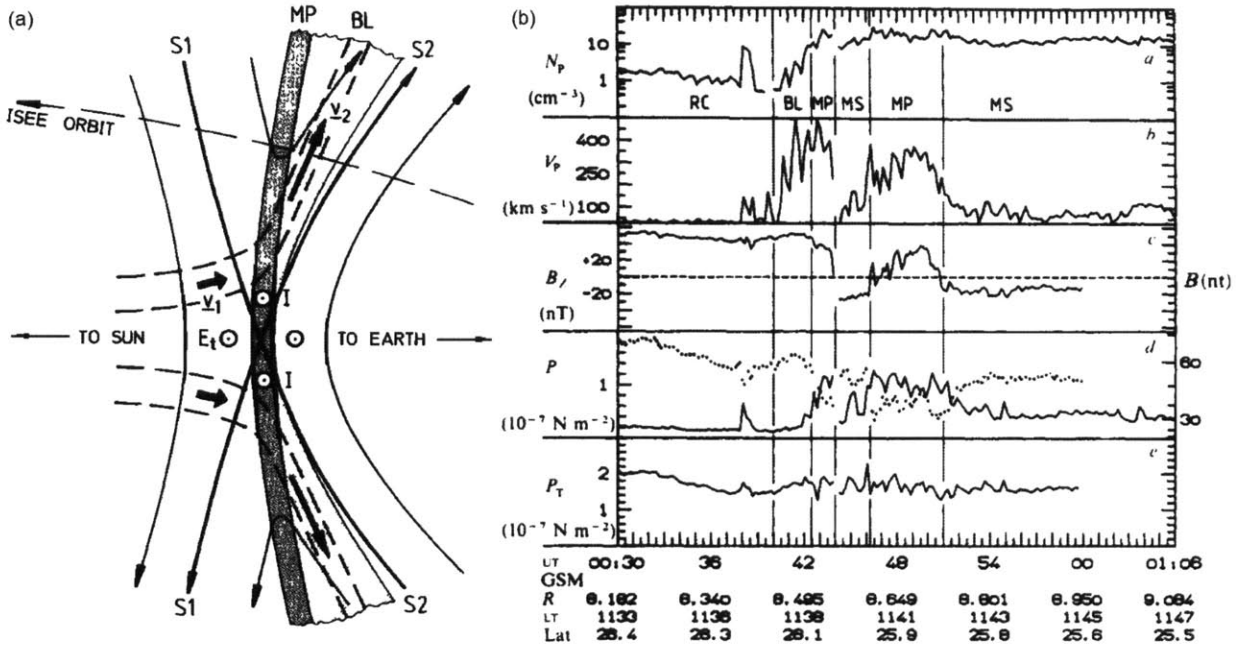

Figure 1-5: (a) Cartoon of path of ISEE 1 satellite. From right to left, ISEE went through the ring current (RC) region, boundary layer (BL), magnetopause (MP) and the magnetosheath (MS). (Ref [26]). (b) Plasma and magnetic field data from the ISEE satellite. Due to boundary motion, there are multiple magnetopause crossings. (Ref [27]).

Early in-situ measurements of the magnetotail also observed signatures of magnetic reconnection [35]. However, these observations were not uniquely predicted by reconnection models [36]. Magnetic reconnection in the magnetotail has since been vigorously measured and verified by the GEOTAIL, WIND, Cluster, and THEMIS (Time History of Events and Macroscale Interactions during Substorms) spacecrafts [37–43] as well as the structure of the reconnection region [44–46], particle acceleration [47], and the link between reconnection and magnetic substorms [24, 48]. Fur-

thermore, the Magnetospheric Multiscale (MMS) mission is scheduled to be launched soon, allowing even higher resolution measurements to study the microphysics of magnetic reconnection [49–51].

Reconnection signatures have also been observed in the Earth's magnetosheath [52, 53], the magnetospheres of Mercury [54, 55] and Mars [56, 57] and even in the magnetotail of Venus [58], whose magnetotail is due solely to the IMF as Venus has a negligible intrinsic field. Evidence of reconnection has been seen in Jupiter [59, 60] Saturn [61, 62] and Uranus [63, 64]. Finally, there is ample evidence of reconnection in the solar wind [65–69].

1.3 Reconnection in Laboratory Plasma

Magnetic reconnection has been observed in many laboratory plasma experiments, including torodial magnetic confinement devices ("tokamaks") designed for the study of controlled nuclear fusion [70]. Sawtooth oscillations, an oscillation of the core temperature of the plasma characterized by a gradual increase followed by a rapid decrease in temperature, were first reported in the Symmetric Tokamak [71]. A schematic of the measurement setup and a trace that corresponds to the electron temperature of the core are shown in Figure 1-6a. The sawtooth oscillation was first explained using magnetic reconnection by Kadomtsev. In the model, as the core is heated, reconnection allows a cold island to form and eventually replace the heated core, the latter being ejected by an internal kink mode [72] as depicted in Figure 1-6b. The model was initially successful in explaining observations, but later proved insufficient [73]. Despite this, the sawtooth oscillations are understood to be due to reconnection [4,74,75] and will strongly impact the operation of ITER [70,76], the first experimental fusion reactor in the world. More violent disruptive instabilities that can rapidly deposit stored tokamak energy onto chamber walls also rely on the magnetic topology changing properties of reconnection [77, 78]. In addition, reconnection is necessary for self-organizing magnetically confined plasmas [79, 80] such as reverse-field pinches (RFPs) [81, 82] and spheromaks [83, 84].

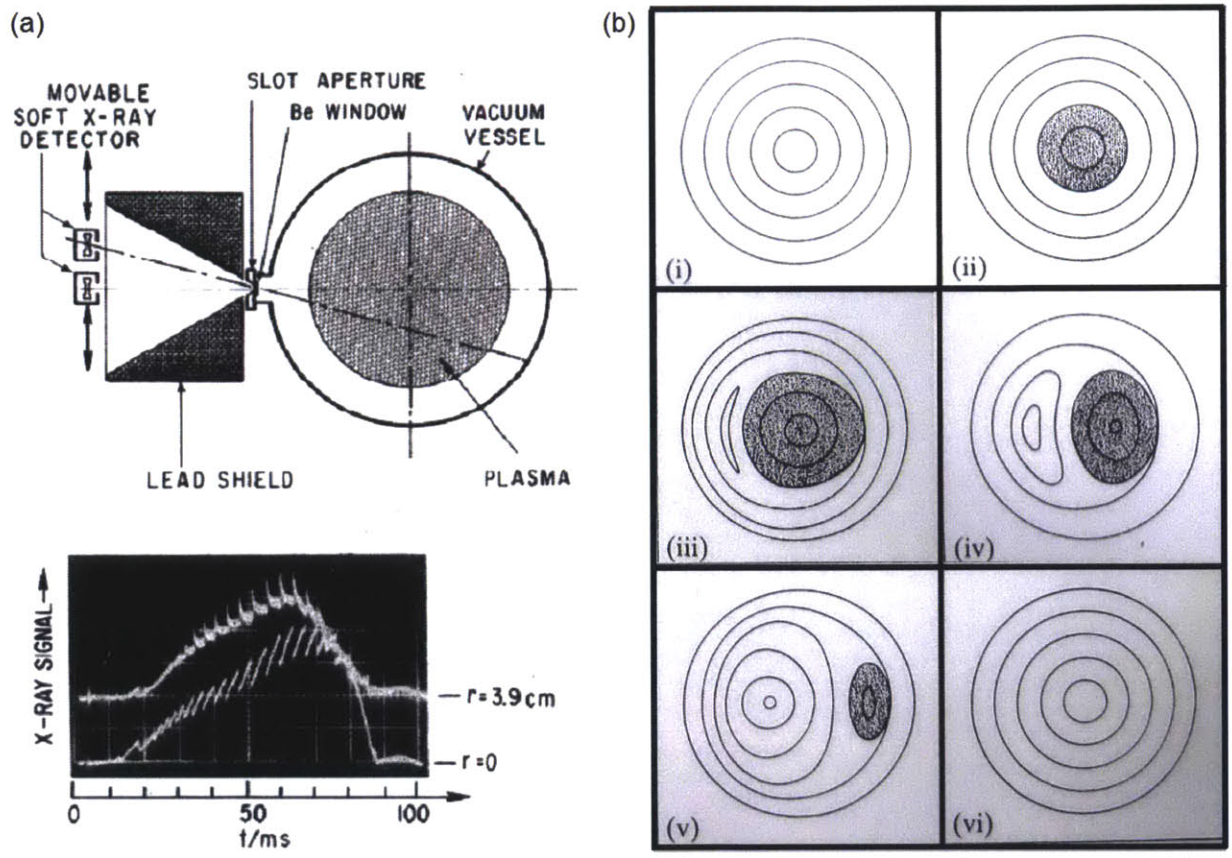

Figure 1-6: (a) Trace of X-Ray signal indicating sawtooth oscillations in the core (r=0) and an "inverted" signal at a distance from the core (r=3.9cm). (Ref [71]). (b) Kadomtsev's model for sawtooth oscillations shown with poloidal flux surfaces, where the core is heated and eventually replaced by a new magnetic island. (Ref [72]).

Basic plasma physics experiments have also reported magnetic reconnection, including several experiments dedicated studying reconnection. Many early laboratory reconnection experiments were conducted on short pulse "pinch" plasmas discharges but had difficulties making detailed measurements on the dynamic, high density plasmas due to the unavailability of diagnostics with sufficient resolution [85–90]. A later linear discharge experiment at UCLA that induced reconnection using interacting current channels was able to study reconnection in more detail, though only the electrons were magnetized in the plasma [91–93]. More recently, reconnection has been studied in more controlled experiments. The Magnetic Reconnection Experiment (MRX) at PPPL has performed driven reconnection experiments without a guide-field [94]. Notably, MRX conducted the first quantitative tests of the classical Sweet Parker model of magnetic reconnection [95, 96] and was able to identify Hall physics signatures [97]. At MIT, the Versatile Toroidal Facility (VTF) has studied the general case of reconnection with a guide-field in the collisionless regime [98]. The experiment not only studied driven [99] reconnection, but also observed spontaneous transition to fast reconnection [100], and demonstrated this could be fully three-dimensional, with nonaxisymmetric onset [101, 102]. Plots of the current density and reconnection rate with spontaneous transition in the two-dimensional configuration are shown in Figure 1-7. VTF also observed microphysics effects in reconnection [103, 104]. To further study magnetic reconnection in regimes that can be considered truly collisionless, a new experiment, the Terrestrial Reconnection Experiment (TREX) is currently being implemented at the University of Wisconsin-Madison. TREX will be the largest dedicated reconnection experiment and will be able to investigate the role electron pressure anisotropy on reconnection dynamics and particle heating (J. Egedal, private communication).

Magnetic reconnection has also been observed in inherently three-dimensional systems. The Swarthmore Spheromak Experiment has studied reconnection through the merging of spheromaks [105] and observed two-fluid effects [106]. At Los Alamos, the Reconnection Scaling Experiment (RSX) has studied undriven reconnection of magnetic flux ropes and has observed onset and cessation of reconnection [107, 108].

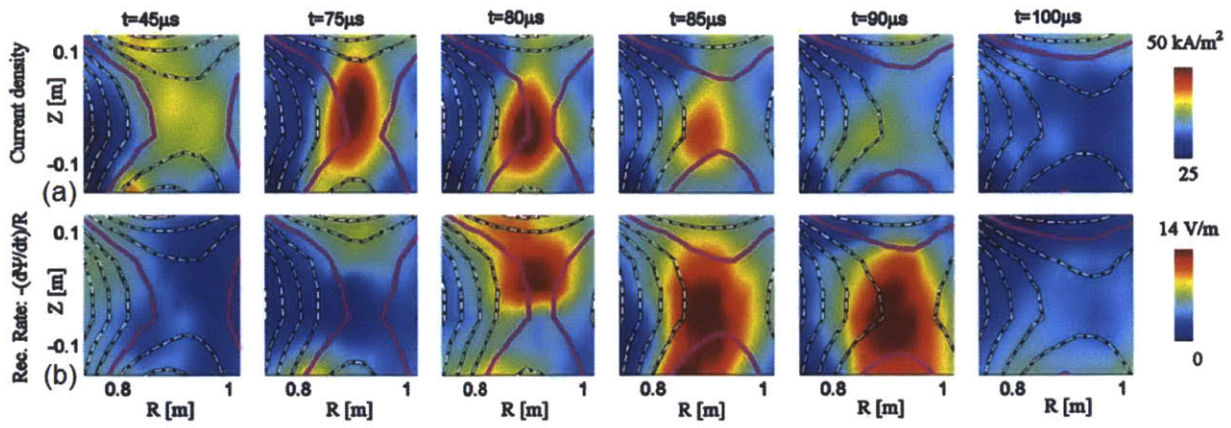

Figure 1-7: Profiles of the (a) current density and (b) reconnection rate along with projections of the poloidal magnetic field measured at the Versatile Toroidal Facility. (Ref [100]).

Finally, magnetic reconnection has been observed in high-energy density plasma bubbles generated by lasers illuminating metal foil [109]. Strong magnetic fields can be generated due to large density and temperature gradients and these fields may exhibit fast driven reconnection [110, 111].

1.4 Computational Simulations of Reconnection

The magnetic reconnection process has also been extensively studied through the use of computer simulations. Most reconnection simulations can be classified as either continuum, particle, or hybrid codes. Many continuum codes are based on fluid models [112], though there have also been some efforts to simulation reconnection in phase (physical and velocity) space [113–115]. Particle codes simulate reconnection by calculating a large number of particle trajectories [116]. Though computationally expensive, this method does not require a closure like in physical fluid models. Hybrid codes are a combination of the two approaches, often treating ions as particles and electrons as a fluid [117]. There has also been recent effort to develop composite codes that embed a kinetic domain that employing particle methods into a region of a domain that employs fluid methods, solving both simultaneously [118, 119].

Early fluid simulations of magnetic reconnection used a single fluid description

of plasma and introduced localized enhancement [120] or current dependent resistivity, [121] or used specific boundary conditions [122] to reproduce fast Petchek reconnection. However, results from general simulations with uniform resistivity on a relatively large domain agreed with Sweet-Parker reconnection using values taken just upstream from the reconnection region [123]. Similar results had been seen in early, course, particle in cell (PIC) simulations as well [124].

Attention shifted toward the treatment of ions and electrons separately since at scales smaller than the ion inertial length, their motion decouples, [125], leading to characteristic out-of-plane quadrupolar magnetic (Hall) fields [126]. Aided by increased computing power, various types of reconnection simulations demonstrated the importance of this ion inertial length physics to the structure and rate of reconnection [127–132]. In particular, results from the Geospace Environmental Modeling (GEM) Magnetic Reconnection Challenge indicate, at least for the case of zero to moderate guide-fields, the reconnection rate is fast and insensitive to the field breaking mechanism when Hall physics is included [133,134]. The GEM challenge employed fluid codes with and without Hall physics (Hall Magnetohydrodynamics [MHD] and Resistive MHD, respectively), hybrid codes, and PIC codes to simulate the same 2.5 dimensional reconnection scenario. A plot of the reconnected flux as a function of time for some of the simulations is shown in Figure 1-8; the reconnection rate is the slope of the reconnected flux.

PIC codes in particular have been used to examine the electron physics of reconnection as this physics determines the structure of the diffusion region and governs the dissipation mechanism and energetics. The nongyrotropic terms of the electron pressure tensor, which are responsible for dissipation and break the frozen-in condition [2, 135–137], have been studied in particle codes and appear to depend on electron scale lengths [138–142]. Simulations in large two-dimensional domains can investigate the structure of the reconnection region and have found the formation of highly elongated electron current layers. An example of layer elongation is depicted in Figure 1-9. These layers, which have also been observed by spacecraft [143], can become unstable and trigger the formation of magnetic islands, which could change

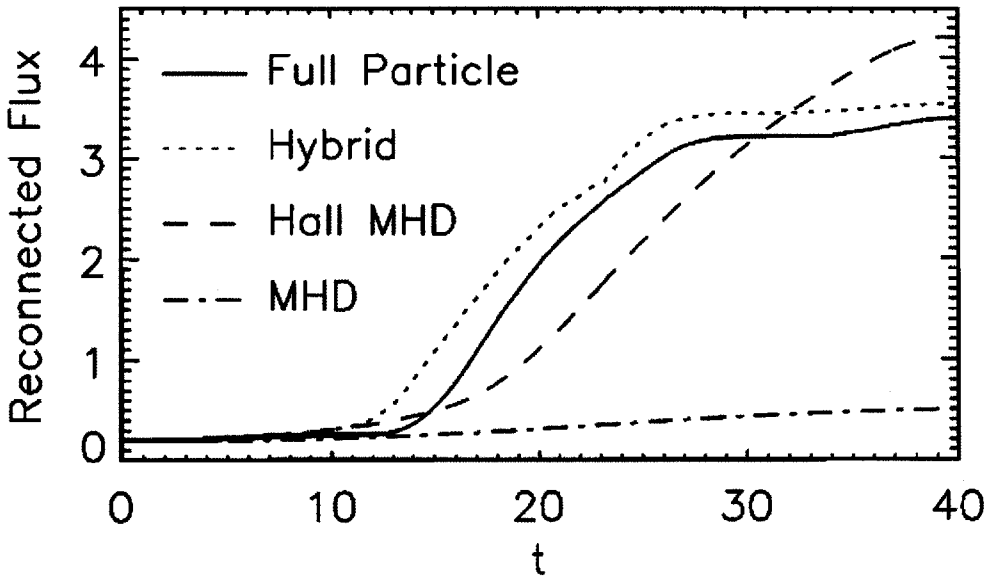

Figure 1-8: Reconnected flux versus time for a variety of codes: full particle (PIC), hybrid, Hall MHD, and Resistive MHD. (Ref [133]).

reconnection dynamics [144–153].

Reconnecting current layers have also been studied in three dimensions with a variety of boundary conditions to examine the role that current driven instabilities, turbulence, waves, and the formation 3D structures have on reconnection dynamics and particle acceleration [155–161]. Some signatures seen in these simulations have been detected in astrophysical and laboratory plasmas [104, 162], even though most particle simulations are performed at lower ion-electron mass ratios to decrease the range of spatial and temporal scales necessary to resolve. Even in 2D, particle simulations with proton-electron mass ratios are very computationally intensive, especially in the presence of a guide-field, which further reduces the gyroradius and increases the gyrofrequency. However, there is evidence that results from particle codes can be strongly affected by mass ratio [148, 153, 163, 164] due to kinetic, mass dependent, processes such as adiabatic particle trapping and pitch angle scattering; simulations at realistic proton electron mass ratios have been conducted to explore this topic [153, 161, 165, 166].

In contrast to particle codes, though spatial and temporal scales in fluid simulations have mass ratio dependence, any included kinetic processes are set by the

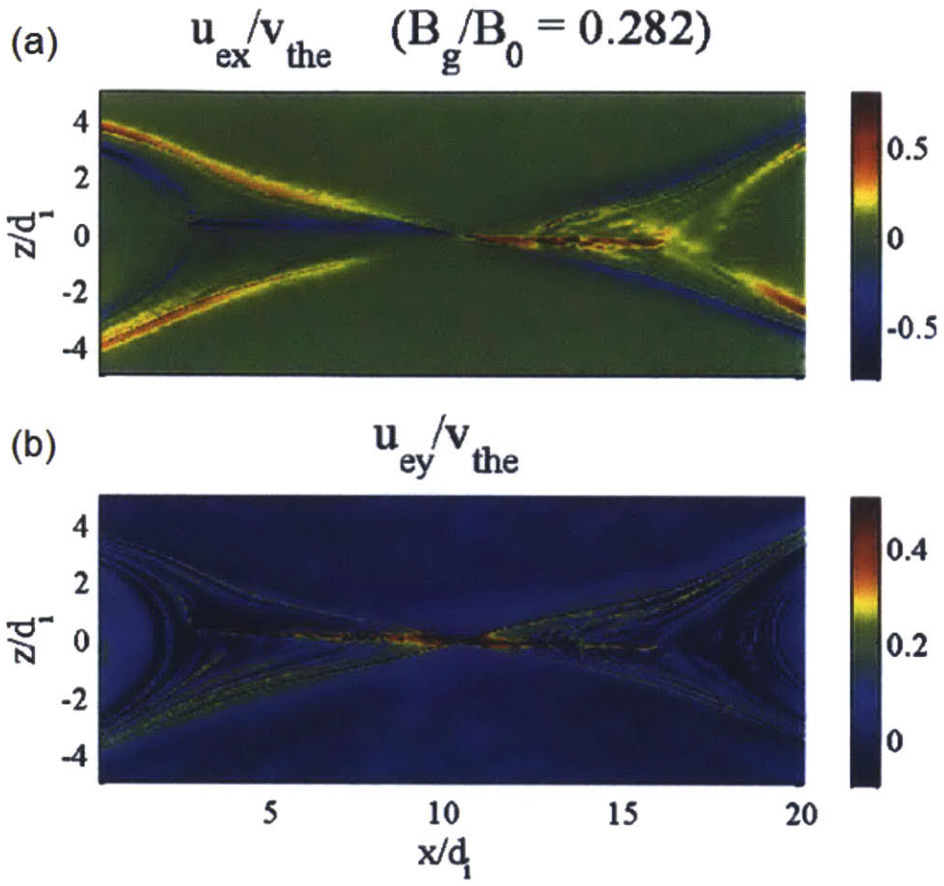

Figure 1-9: The in-plane outflow (a) and out-of-plane (b) electron velocities normalized the electron thermal velocity in a Particle-in-Cell simulation. (Ref [154]).

governing model implemented. This could allow fluid codes capture the essential physics of kinetic effects at physical mass ratios, while simulating at lower ratios. Using PIC simulations as a guide, efforts have been made to analytically model kinetic processes very near the X-line region [142, 167–170]. Some models that have been considered employ methods to model electron heat flux or higher electron moments and include either some averaging method or separate differential equations evolving electron pressure components [167–169]. So far, simulations that implement these methods have found limited agreement with their kinetic counterparts [171,172]. Others have used particle trajectories near X-line geometries to develop electron distribution functions [142,170]. However, the author is not aware of the implementation of these models into fluid codes.

1.5 Summary and Outline

While the above models focused on regions near the X-line of magnetic reconnection where nongyrotropic electron effects can dominate, a new model of anisotropy in the gyrotropic (diagonal) components of electron pressure due to particle trapping has been developed and this is described by new Equations of State (EoS) [6]. This dissertation will focus on the implementation of the new EoS in computational fluid simulations to study magnetic reconnection. Chapter 2 reviews modeling of plasma using two-fluid descriptions and discusses common fluid closures. Chapter 3 reviews magnetic topology conservation, magnetic reconnection, and fluid models of steady reconnection. Chapter 4 introduces the new EoS that describe electron pressure anisotropy. Modifications to the EoS are also introduced to limit electron pressure anisotropy in lieu of isotropization by pitch angle scattering. Chapter 5 describes the development of a fluid code using the HiFi framework that implements the new EoS description of electron pressure in addition to a control code that uses an isotropic electron description. These two codes are compared to kinetic simulation using the VPIC code. Chapter 6 describes a series of anisotropic and isotropic simulations with a range of plasma conditions that explores the structure of the reconnection region.

A predictive model of conditions of the current layer is developed and applied to simulation results. Simulations at two different mass ratios on a larger domain are compared, and these results are also compared to spacecraft data. Chapter 7 is a summary that emphasizes new results obtained in this dissertation.

Chapter 2

Modeling Plasma

Before discussing models of magnetic reconnection, it is necessary to discuss the modeling of weakly-collisional magnetized plasma. The low collisionality makes it difficult to properly model the plasma at small length scales and short time scales. In addition, because the plasma is magnetized, dynamics are greatly affected by changes of magnetic topology due to reconnection.

This chapter reviews methods of describing magnetized plasma, specifically equations that describe ion-electron fluid plasma dynamics. Common schemes of fluid closure by prescribing the pressure evolution of fluid plasma are also reviewed.

2.1 Characterizing Magnetized Plasma

A magnetized plasma is a plasma that has an external magnetic field strong enough to affect particle dynamics. Charged particles in magnetic fields tend move freely along and gyrate around magnetic field lines. The rate of gyration is the species gyro-frequency and is given by

$$\Omega_s = \frac{Z_s e B}{m_s}, \tag{2.1}$$

where e is the magnitude of the electron charge, Z_s is the species charge, and m_s is the species mass. A magnetized plasma can be characterized by the radius of this gyration being much less than the length scale of the plasma. A parameter that is

often used to characterize the dynamics of plasma in a magnetic field is the ratio of species thermal energy density to the magnetic energy density β_s, given by

$$\beta_s = \frac{2\mu_0 p_s}{B^2}. \tag{2.2}$$

A low β_s indicates species dynamics is dominated by the magnetic field. Finally, magnetic field disturbances in a species plasma often propagate at the Alfvén velocity, given by

$$V_{As}^2 = \frac{B^2}{\mu_0 m_s n_s}. \tag{2.3}$$

In electron-ion plasmas, disturbances typically propagate at the ion Alfvén velocity.

2.2 The Distribution Function

In a very fundamental picture, plasma can be modeled as a large collection of charged particles. At any instant, each particle has a position and velocity, specifying its location in phase space. However, instead of tracking the trajectory of individual particles, the plasma can be characterized by the distribution functions $F_s(\boldsymbol{x}, \boldsymbol{v}, t)$ for each species s, which describes the instantaneous density of particles of the species as a function of phase-space location. The number of particles between position $\boldsymbol{x}$ and $\boldsymbol{x} + \mathrm{d}\boldsymbol{x}$ with velocity between $\boldsymbol{v}$ and $\boldsymbol{v} + \mathrm{d}\boldsymbol{v}$ at time t is given by $F_s(\boldsymbol{x}, \boldsymbol{v}, t)\,\mathrm{d}\boldsymbol{x}\,\mathrm{d}\boldsymbol{v}$. The distribution function gives a very detailed description of the plasma.

Bulk plasma properties can be calculated from the distribution function by taking weighted velocity-space averages of the distribution function. The density of particles at position $\boldsymbol{x}$ is found by summing the phase-space density over all velocities with position $\boldsymbol{x}$, thus $\int F_s(\boldsymbol{x}, \boldsymbol{v}, t)\,\mathrm{d}\boldsymbol{v} = n_s(\boldsymbol{x})$ where $n_s(\boldsymbol{x})$ is the species density. This is called the zeroth moment of the distribution function. Similarly, the average velocity or flow velocity is found from the first moment, $\int \boldsymbol{v} F_s(\boldsymbol{x}, \boldsymbol{v}, t)\,\mathrm{d}\boldsymbol{v} = n_s(\boldsymbol{x})\langle \boldsymbol{v} \rangle_s = n_s(\boldsymbol{x})\boldsymbol{V}_s(\boldsymbol{x})$ where $\boldsymbol{V}_s(\boldsymbol{x})$ is the species flow velocity. Therefore, describing the evolution of the phase-space density is sufficient to model plasma.

From Liouville's Theorem, the phase-space density behaves like an incompressible

fluid (that flows in phase-space) and is governed by the conservation equation

$$\frac{\mathrm{d}F_s}{\mathrm{d}t} = \frac{\partial F_s}{\partial t} + \frac{\mathrm{d}\boldsymbol{x}}{\mathrm{d}t}\cdot\frac{\partial F_s}{\partial \boldsymbol{x}} + \frac{\mathrm{d}\boldsymbol{v}}{\mathrm{d}t}\cdot\frac{\partial F_s}{\partial \boldsymbol{v}} = \frac{\partial F_s}{\partial t} + \boldsymbol{v}\cdot\frac{\partial F_s}{\partial \boldsymbol{x}} + \boldsymbol{a}_s\cdot\frac{\partial F_s}{\partial \boldsymbol{v}} = 0. \tag{2.4}$$

Here $\boldsymbol{a}_s$ is the acceleration of particles of the species. For non-relativistic particles with charge $Z_s e$, this acceleration is due to the classical Lorentz force

$$\boldsymbol{a}_s = \frac{Z_s e}{m_s}(\boldsymbol{E} + \boldsymbol{v}\times\boldsymbol{B}). \tag{2.5}$$

This is a deceptively simple formulation. The distribution function and the fields depend sensitively on the phase-space location of individual particles; both have very fine-scale structure. Progress can be made by using the ensemble average of these quantities, which smooths these quantities in phase space. Taking the ensemble average of the conservation equation 2.4 yields

$$\frac{\partial\langle F_s\rangle}{\partial t} + \boldsymbol{v}\cdot\frac{\partial\langle F_s\rangle}{\partial \boldsymbol{x}} + \langle\boldsymbol{a}_s\rangle\cdot\frac{\partial\langle F_s\rangle}{\partial \boldsymbol{v}} + \left\langle\Big(\boldsymbol{a}-\langle\boldsymbol{a}\rangle\Big)\cdot\frac{\partial}{\partial\boldsymbol{v}}\Big(F_s-\langle F_s\rangle\Big)\right\rangle = 0. \tag{2.6}$$

Defining

$$f_s \equiv \langle F_s\rangle \tag{2.7}$$

$$C_s[f] \equiv -\left\langle\Big(\boldsymbol{a}-\langle\boldsymbol{a}\rangle\Big)\cdot\frac{\partial}{\partial\boldsymbol{v}}\Big(F_s-\langle F_s\rangle\Big)\right\rangle, \tag{2.8}$$

then 2.6 can be rewritten as

$$\frac{\partial f_s}{\partial t} + \boldsymbol{v}\cdot\frac{\partial f_s}{\partial \boldsymbol{x}} + \frac{Z_s e}{m_s}(\boldsymbol{E}+\boldsymbol{v}\times\boldsymbol{B})\cdot\frac{\partial f_s}{\partial \boldsymbol{v}} = C_s[f], \tag{2.9}$$

which is referred to as Boltzmann's Equation. Here and from now on, the ensemble average brackets $\langle\ldots\rangle$ have been dropped from the electromagnetic field terms for simplicity. The term on the right hand side of this expression is called the collision operator. It captures the fine-scale structure of the original distribution function and fields. However, many plasmas of interest are effectively collisionless [173]. In planetary magnetospheres, the plasma density is low enough that effectually, particles

don't collide with one another. In the solar corona, for phenomena of interest, such as during a quick release of magnetic energy, the dynamics of that region are also effectively collisionless. When collisions can be ignored, 2.9 becomes

$$\frac{\partial f_s}{\partial t} + \boldsymbol{v} \cdot \frac{\partial f_s}{\partial \boldsymbol{x}} + \frac{Z_s e}{m_s}(\boldsymbol{E} + \boldsymbol{v} \times \boldsymbol{B}) \cdot \frac{\partial f_s}{\partial \boldsymbol{v}} = 0. \tag{2.10}$$

This is known as the Vlasov Equation [174].

2.3 Moments of the Vlasov Equation

Though the Vlasov Equation is a great simplification of the original phase-space density equation, solving the Vlasov Equation is still difficult in many situations. Instead a fluid description of collisionless plasma is formed by calculating moments of the Vlasov Equation and using Maxwell's equations to describe the evolution of the electromagnetic fields. This approach reduces the dimensions of the problem from phase-space to position space, and allows plasma to be modeled using techniques from computational fluid dynamics. The m_{th} moment of the Vlasov Equation is computed from

$$\int \boldsymbol{v}^{\otimes m} \left[\frac{\partial f_s}{\partial t} + \boldsymbol{v} \cdot \frac{\partial f_s}{\partial \boldsymbol{x}} + \frac{Z_s e}{m_s}(\boldsymbol{E} + \boldsymbol{v} \times \boldsymbol{B}) \cdot \frac{\partial f_s}{\partial \boldsymbol{v}} \right] \mathrm{d}\boldsymbol{v} = 0. \tag{2.11}$$

Here $\boldsymbol{v}^{\otimes m}$ is the m_{th} outer product of $\boldsymbol{v}$. The first two terms are straightforward to compute since both differentiation operators commute with velocity-space integration. The third terms can be computed using integration by parts and Gauss's Theorem. Since physical distribution functions have finite norms, any terms evaluated at infinity due to Gauss's Theorem are zero.

The zeroth moment of the Vlasov equation, the continuity equation, is given by

$$\frac{\partial n_S}{\partial t} + \nabla \cdot \left(n_s \langle \boldsymbol{v} \rangle_s \right) = 0. \tag{2.12}$$

The first moment, when multiplied by the species mass, yields the momentum con-

servation equation

$$\frac{\partial}{\partial t}\Big(m_s n_s \langle \boldsymbol{v} \rangle_s\Big) + \nabla \cdot \Big(m_s n_s \langle \boldsymbol{v}\boldsymbol{v} \rangle_s\Big) - Z_s e n_s \Big(\boldsymbol{E} + \langle \boldsymbol{v} \rangle_s \times \boldsymbol{B}\Big) = 0. \tag{2.13}$$

The second moment, again multiplied by the species mass, yields an energy conservation equation

$$\begin{aligned}\frac{\partial}{\partial t}\Big(m_s n_s \langle \boldsymbol{v}\boldsymbol{v} \rangle_s\Big) + \nabla \cdot \Big(m_s n_s \langle \boldsymbol{v}\boldsymbol{v}\boldsymbol{v} \rangle_s\Big) \\ - Z_s e n_s \Big(\langle \boldsymbol{v} \rangle_s \boldsymbol{E} + \boldsymbol{E}\langle \boldsymbol{v} \rangle_s + n_s \langle \boldsymbol{v}\boldsymbol{v} \rangle_s \times \boldsymbol{B} - \boldsymbol{B} \times n_s \langle \boldsymbol{v}\boldsymbol{v} \rangle_s\Big) = 0.\end{aligned} \tag{2.14}$$

Here $n_s \langle \boldsymbol{v}^{\otimes m} \rangle$ denotes the m_{th} moment of the distribution function. One thing to notice about these expressions is that each moment equation depends on a higher moment. This is because the second term in 2.11 couples moment m to moment $(m+1)$ (the third term also couples moment m to moment $(m-1)$). This coupling to higher moments will never lead to a closed set of equations; the systems will always have more unknowns than knowns. The termination of this hierarchy of equation is called closure; here, the second moment will suffice, and the closure of this system will be addressed in subsequent sections.

Moments of the distribution function can be expressed in terms of more physical parameters. Since $\langle \boldsymbol{v} \rangle = \boldsymbol{V}$, let $\boldsymbol{w} \equiv \boldsymbol{v} - \boldsymbol{V}$ be the relative velocity such that $\langle \boldsymbol{w} \rangle = 0$. Then

$$\langle \boldsymbol{v}\boldsymbol{v} \rangle = \boldsymbol{V}\boldsymbol{V} + \langle \boldsymbol{w}\boldsymbol{w} \rangle \tag{2.15}$$

$$\langle \boldsymbol{v}\boldsymbol{v}\boldsymbol{v} \rangle = \boldsymbol{V}\boldsymbol{V}\boldsymbol{V} + \boldsymbol{V}\langle \boldsymbol{w}\boldsymbol{w} \rangle + \langle \boldsymbol{w}\boldsymbol{V}\boldsymbol{w} \rangle + \langle \boldsymbol{w}\boldsymbol{w} \rangle \boldsymbol{V} + \langle \boldsymbol{w}\boldsymbol{w}\boldsymbol{w} \rangle \tag{2.16}$$

and the pressure tensor can be defined as

$$\bar{\mathbf{P}}_s^{tot} \equiv \int m_s \boldsymbol{w}\boldsymbol{w} f_s \, \mathrm{d}\boldsymbol{w}. \tag{2.17}$$

Note that this tensor is symmetric and has 6 independent components. The heat flux

tensor is defined as

$$\bar{\mathbf{Q}}_s \equiv \int m_s \boldsymbol{www} f_s \, \mathrm{d}\boldsymbol{v}. \tag{2.18}$$

This tensor also has symmetries such that only 10 of its 27 components are independent. Using these definitions, equations 2.12, 2.13, and 2.14 become [175]

$$\frac{\partial n_s}{\partial t} + \nabla \cdot \Big(n_s \boldsymbol{V}_s \Big) = 0 \tag{2.19}$$

$$\frac{\partial}{\partial t}\Big(m_s n_s \boldsymbol{V}_s \Big) + \nabla \cdot \Big(m_s n_s \boldsymbol{V}_s \boldsymbol{V}_s + \bar{\mathbf{P}}_s^{tot} \Big) - Z_s e n_s \Big(\boldsymbol{E} + \boldsymbol{V}_s \times \boldsymbol{B} \Big) = 0 \tag{2.20}$$

$$\begin{aligned}
&\frac{\partial}{\partial t}\Big(m_s n_s \boldsymbol{V}_s \boldsymbol{V}_s + \bar{\mathbf{P}}_s^{tot} \Big) \\
&\quad + \nabla \cdot \Big(m_s n_s \boldsymbol{V}_s \boldsymbol{V}_s \boldsymbol{V}_s + \boldsymbol{V}_s \bar{\mathbf{P}}_s^{tot} + \bar{\mathbf{P}}_s^{tot} \boldsymbol{V}_s + \bar{\mathbf{Q}}_s \Big) + \Big[\nabla \cdot (\bar{\mathbf{P}}_s^{tot} \boldsymbol{V}_s) \Big]^{\mathrm{T}} \\
&\quad - Z_s e n_s \left[\boldsymbol{V}_s \boldsymbol{E} + \boldsymbol{E} \boldsymbol{V}_s + \left(n_s \boldsymbol{V}_s \boldsymbol{V}_s + \frac{\bar{\mathbf{P}}_s^{tot}}{m_s} \right) \times \boldsymbol{B} - \boldsymbol{B} \times \left(n_s \boldsymbol{V}_s \boldsymbol{V}_s + \frac{\bar{\mathbf{P}}_s^{tot}}{m_s} \right) \right] \\
&\quad = 0.
\end{aligned} \tag{2.21}$$

Equation 2.20 can be further simplified using 2.19 multiplied by $m_s \boldsymbol{V}_s$. With some rearrangement, this can be written as

$$m_s n_s \frac{\mathrm{d}\boldsymbol{V}_s}{\mathrm{d}t} = Z_s e n_s \Big(\boldsymbol{E} + \boldsymbol{V}_s \times \boldsymbol{B} \Big) - \nabla \cdot \bar{\mathbf{P}}_s^{tot}, \tag{2.22}$$

where

$$\frac{\mathrm{d}}{\mathrm{d}t} \equiv \frac{\partial}{\partial t} + \boldsymbol{V}_s \cdot \nabla \tag{2.23}$$

is the convective derivative, which describes temporal differentiation for an observer moving with the fluid velocity $\boldsymbol{V}_s$. Equation 2.21 can also be simplified by using $m_s \boldsymbol{V}_s \boldsymbol{V}_s$ times 2.19 and using 2.20 multiplied by $\boldsymbol{V}_s$ on the left and again on the right. The resulting equation for the evolution of the pressure tensor is [176]

$$\frac{\mathrm{d}\bar{\mathbf{P}}_s^{tot}}{\mathrm{d}t} + \bar{\mathbf{P}}_s^{tot} \nabla \cdot \boldsymbol{V}_s + \bar{\mathbf{P}}_s^{tot} \cdot \nabla \boldsymbol{V}_s + \Big[\bar{\mathbf{P}}_s^{tot} \cdot \nabla \boldsymbol{V}_s \Big]^{\mathrm{T}} + \nabla \cdot \bar{\mathbf{Q}}_s = \frac{Z_s e}{m_s} \Big(\bar{\mathbf{P}}_s^{tot} \times \boldsymbol{B} - \boldsymbol{B} \times \bar{\mathbf{P}}_s^{tot} \Big). \tag{2.24}$$

Further progress with 2.24 is made by splitting the pressure tensor $\bar{\mathbf{P}}_s^{tot}$ into two components

$$\bar{\mathbf{P}}_s^{tot} = \bar{\mathbf{P}}_s + \bar{\mathbf{\Pi}}_s, \tag{2.25}$$

where $\bar{\mathbf{P}}_s$ is a diagonal tensor representing conventional pressure, and $\bar{\mathbf{\Pi}}_s$ is a generalized viscosity tensor. For magnetized, collisionless, low beta plasma, the generalized viscosity tensor can be discarded for time scales longer than the species gyro-period [177]. To prevent flow singularities in reconnection simulations, it is necessary to retain some form of viscosity, though it is not necessary to capture the exact dynamics of a species on times scales shorter than its gyro-period. Here the generalized viscosity tensor will have a form similar to that of a neutral gas dominated by collisions [178], which is the traceless stress tensor

$$\bar{\mathbf{\Pi}} \simeq -m_s n_s \nu_s \left[\nabla \boldsymbol{V}_s + (\nabla \boldsymbol{V}_s)^{\mathrm{T}} - \frac{2}{3}(\nabla \cdot \boldsymbol{V}_s)\bar{\mathbf{I}} \right], \tag{2.26}$$

where $\bar{\mathbf{I}}$ is the identity matrix and ν_s is the species viscous diffusivity. By specifying the $\bar{\mathbf{\Pi}}$, the off-diagonal terms of the pressure tensor have been closed and therefore only the diagonal terms of 2.24 are needed. Furthermore, since charged particle motion is very different parallel to magnetic field lines versus perpendicular them, sometimes it is useful decompose the diagonal pressure into parallel and perpendicular pressure by letting

$$\bar{\mathbf{P}}_s = p_{s\perp}\left(\bar{\mathbf{I}} - \hat{b}\hat{b}\right) + p_{s\parallel}\hat{b}\hat{b}, \tag{2.27}$$

where $\hat{b}$ is a unit vector in the direction of the magnetic field line. Taking the double dot product of 2.24 with $\hat{b}\hat{b}$ yields

$$\begin{aligned} &\frac{\mathrm{d}p_{s\parallel}}{\mathrm{d}t} - \bar{\mathbf{\Pi}}_s : \frac{\mathrm{d}\hat{b}\hat{b}}{\mathrm{d}t} + p_{s\parallel}\nabla \cdot \boldsymbol{V}_s + \\ &\quad 2p_{s\parallel}\hat{b}\hat{b} : \nabla \boldsymbol{V}_s + 2\hat{b}\hat{b} : \bar{\mathbf{\Pi}}_s \cdot \nabla \boldsymbol{V}_s + \nabla \cdot \left(\bar{\mathbf{Q}}_s : \hat{b}\hat{b}\right) - 2\hat{b} \cdot \bar{\mathbf{Q}}_s : \nabla \hat{b} = 0. \end{aligned} \tag{2.28}$$

Taking the double dot product of 2.24 with $\bar{\mathbf{I}} - \hat{b}\hat{b}$ yields

$$2\frac{\mathrm{d}p_{s\perp}}{\mathrm{d}t} + \bar{\mathbf{\Pi}}_s : \frac{\mathrm{d}\hat{b}\hat{b}}{\mathrm{d}t} + 4p_{s\perp}\nabla\cdot\boldsymbol{V}_s - 2p_{s\perp}\hat{b}\hat{b} : \nabla\boldsymbol{V}_s$$
$$+ 2\left(\bar{\mathbf{I}} - \hat{b}\hat{b}\right) : \bar{\mathbf{\Pi}}_s \cdot \nabla\boldsymbol{V}_s + \nabla\cdot\left[\bar{\mathbf{Q}}_s : \left(\bar{\mathbf{I}} - \hat{b}\hat{b}\right)\right] + 2\hat{b}\cdot\bar{\mathbf{Q}}_s : \nabla\hat{b} = 0. \quad (2.29)$$

Finally, if the plasma pressure is isotropic, then $p_{s\perp} = p_{s\parallel} = p_s$ and combining equations 2.28 and 2.29 yields

$$3\frac{\mathrm{d}p_s}{\mathrm{d}t} + 5p_s\nabla\cdot\boldsymbol{V}_s + 2\bar{\mathbf{\Pi}}_\mathbf{s} : \nabla\boldsymbol{V}_s + \nabla\cdot\left(\bar{\mathbf{Q}}_s : \bar{\mathbf{I}}\right) = 0. \quad (2.30)$$

Equations 2.28 and 2.29 describe the evolution of an anisotropic plasma pressure that is isotropic perpendicular to magnetic field lines and differs along the magnetic field line, while 2.30 describes the evolution of an isotropic plasma pressure. In both cases, off-diagonal components of the pressure tensor have been closed, but both descriptions still depend on the unknown heat flux tensor. Often, an ad-hoc description is prescribed for this tensor. These closure schemes will be detailed later. For now, taking moments of Vlasov's equation to obtain expressions for species continuity, conservation of momentum, and conservation of energy are sufficient.

2.4 Ion-Electron Plasmas - Two Fluid description

Using descriptions from Section 2.3, the density and momentum of a singly charged ion-electron plasma can be described by fluid equations combined with Maxwell's equations

$$\frac{\partial n_i}{\partial t} + \nabla\cdot\left(n_i\boldsymbol{V}_i\right) = 0 \quad (2.31)$$

$$\frac{\partial n_e}{\partial t} + \nabla\cdot\left(n_e\boldsymbol{V}_e\right) = 0 \quad (2.32)$$

$$\frac{\partial}{\partial t}\left(m_i n_i \boldsymbol{V}_i\right) + \nabla\cdot\left(m_i n_i \boldsymbol{V}_i\boldsymbol{V}_i + \bar{\mathbf{P}}_i + \bar{\mathbf{\Pi}}_i\right) - e n_i\left(\boldsymbol{E} + \boldsymbol{V}_i \times \boldsymbol{B}\right) = 0 \quad (2.33)$$

$$\frac{\partial}{\partial t}\left(m_e n_e \boldsymbol{V}_e\right) + \nabla\cdot\left(m_e n_e \boldsymbol{V}_e\boldsymbol{V}_e + \bar{\mathbf{P}}_e + \bar{\mathbf{\Pi}}_e\right) + e n_e\left(\boldsymbol{E} + \boldsymbol{V}_e \times \boldsymbol{B}\right) = 0 \quad (2.34)$$

$$\nabla \cdot \boldsymbol{E} = \frac{e}{\varepsilon_0}\left(n_i - n_e\right) \tag{2.35}$$

$$\nabla \cdot \boldsymbol{B} = 0 \tag{2.36}$$

$$\nabla \times \boldsymbol{E} = -\frac{\partial \boldsymbol{B}}{\partial t} \tag{2.37}$$

$$\nabla \times \boldsymbol{B} = \mu_0 e\left(n_i \boldsymbol{V}_i - n_e \boldsymbol{V}_e\right) + \varepsilon_0 \mu_0 \frac{\partial \boldsymbol{E}}{\partial t}. \tag{2.38}$$

Here, all that is needed to close this system is to describe the diagonal electron and ion pressures $\bar{\mathbf{P}}_e$ and $\bar{\mathbf{P}}_i$, which will be done later. This model often includes more physics than needed, and can be simplified in certain plasma regimes. For nonrelativistic plasma phenomena, the speed of light in vacuum can be taken to be much larger than any other characteristic velocity. The speed of light can tend towards infinity by letting $\varepsilon \to 0$ [179]. In addition, in this limit, following from 2.35, the plasma is quasi-neutral:

$$n_i - n_e \simeq 0 \Rightarrow n_i \simeq n_e \equiv n. \tag{2.39}$$

Using the smallness of the electron-to-ion mass ratio $m_e/m_i = \xi$, it is helpful to introduce the center-of-mass velocity $\boldsymbol{V}$

$$\boldsymbol{V} \equiv \frac{m_i \boldsymbol{V}_i + m_e \boldsymbol{V}_e}{m_i + m_e} \tag{2.40}$$

and current density $\boldsymbol{J}$

$$\boldsymbol{J} \equiv en\left(\boldsymbol{V}_i - \boldsymbol{V}_e\right). \tag{2.41}$$

Then the ion velocity becomes

$$\boldsymbol{V}_i = \boldsymbol{V} + \frac{\xi}{1+\xi}\frac{\boldsymbol{J}}{ne} = \boldsymbol{V} + \mathcal{O}(\xi). \tag{2.42}$$

Similarly, the electron velocity is rewritten

$$\boldsymbol{V}_e = \boldsymbol{V} - \frac{1}{1+\xi}\frac{\boldsymbol{J}}{ne} = \boldsymbol{V} - \frac{\boldsymbol{J}}{ne} + \mathcal{O}(\xi). \tag{2.43}$$

In addition, in the nonrelativistic limit, Ampere's Law 2.38 becomes

$$\nabla \times \boldsymbol{B} = \mu_0 \boldsymbol{J}. \tag{2.44}$$

From this, it follows the current density is divergenceless

$$\nabla \cdot \boldsymbol{J} = 0. \tag{2.45}$$

Finally, the continuity equations lead to

$$\frac{\partial n}{\partial t} + \nabla \cdot (n\boldsymbol{V}) = 0. \tag{2.46}$$

Total momentum conservation can be found by combining the electron and ion momentum equations, eliminating the electric field term

$$mn\left[\frac{\partial \boldsymbol{V}}{\partial t} + \boldsymbol{V} \cdot \nabla \boldsymbol{V} + \chi^2 \xi \frac{\boldsymbol{J}}{ne} \cdot \nabla \frac{\boldsymbol{J}}{ne}\right] = \boldsymbol{J} \times \boldsymbol{B} - \nabla \cdot \left[\bar{\mathbf{P}}_i + \bar{\mathbf{P}}_e + \bar{\mathbf{\Pi}}_{ie}(\boldsymbol{V}, \boldsymbol{J})\right], \tag{2.47}$$

where $m = m_i + m_e \simeq m_i$ and $\bar{\mathbf{\Pi}}_{ie} = \bar{\mathbf{\Pi}}_i + \bar{\mathbf{\Pi}}_e$. This expression can be used to replace the ion momentum equation. The momentum conservation equations can be simplified by examining the dominant terms at different scales. The species gyroperiod is the smallest time scale relevant to species behavior for magnetic reconnection in low beta plasmas while the inertial length $d_s = V_{As}/\Omega_s$ is approximately the smallest length scale at which fluid theory properly describes behavior. The ion Alfvén velocity V_{Ai} can be taken as the characteristic velocity of bulk plasma flow. Then at large scales $L > \xi^{-1/2} d_i$ and long times $T > \tau_i$, the dominant terms in the total momentum equation are

$$mn\boldsymbol{V} \cdot \nabla \boldsymbol{V} = \boldsymbol{J} \times \boldsymbol{B} - \nabla \cdot \left(\bar{\mathbf{P}}_i + \bar{\mathbf{P}}_e\right), \tag{2.48}$$

and for the electron momentum equation,

$$\boldsymbol{E} + \boldsymbol{V} \times \boldsymbol{B} = 0. \tag{2.49}$$

Equation 2.49 is called Ideal Ohm's Law and the fluid plasma model that uses equations 2.48 and 2.49 is called Ideal Magnetohydrodynamics or Ideal MHD. At ion inertial length scales $L \sim d_i$ and times $T \sim \tau_i$, the dominant terms in the total momentum equation are

$$mn\frac{\mathrm{d}\boldsymbol{V}}{\mathrm{d}t} = \boldsymbol{J} \times \boldsymbol{B} - \nabla \cdot \left[\bar{\mathbf{P}}_i + \bar{\mathbf{P}}_e + \bar{\boldsymbol{\Pi}}_{ie}(\boldsymbol{V})\right], \tag{2.50}$$

for the electron momentum equation,

$$\boldsymbol{E} + \boldsymbol{V} \times \boldsymbol{B} = \frac{1}{ne}\boldsymbol{J} \times \boldsymbol{B} - \frac{1}{ne}\nabla \cdot \bar{\mathbf{P}}_e. \tag{2.51}$$

The $\boldsymbol{J} \times \boldsymbol{B}$ term in 2.51 is often referred to as the Hall Term and the fluid plasma model that uses equations 2.50 and 2.51 is fittingly called Hall Magnetohydrodynamics or Hall MHD. At electron inertial scales $L \sim \xi^{1/2} d_i = d_e$ and $T \sim \tau_e$, the dominant terms in the total momentum equation are

$$mn\frac{\partial \boldsymbol{V}}{\partial t} = \bar{\boldsymbol{\Pi}}_i(\boldsymbol{V}), \tag{2.52}$$

for the electron momentum equation,

$$\boldsymbol{E} = \frac{1}{ne}\boldsymbol{J} \times \boldsymbol{B} - \frac{1}{ne}\nabla \cdot \left[\bar{\mathbf{P}}_e + \bar{\boldsymbol{\Pi}}_e(\boldsymbol{J})\right] + \frac{m_e}{e}\frac{\partial}{\partial t}\left(\frac{\boldsymbol{J}}{ne}\right) - \frac{m_e}{e}\frac{\boldsymbol{J}}{ne} \cdot \nabla\frac{\boldsymbol{J}}{ne}. \tag{2.53}$$

Note that at electrons scales, the ion motion here is dominated by viscosity and is diffusive. Plasma dynamics at this scale primarily depends on electron physics. For fluid simulations, length scales below the electron inertial length are also important for stability. At numerical scales $L \sim \xi^{3/4} d_i = \xi^{1/4} d_e$, the dominant terms in the total momentum equation are once again

$$mn\frac{\partial \boldsymbol{V}}{\partial t} = \bar{\boldsymbol{\Pi}}_{ie}(\boldsymbol{V}), \tag{2.54}$$

for the electron momentum equation,

$$\boldsymbol{E} = -\frac{1}{ne}\nabla\cdot\bar{\boldsymbol{\Pi}}_e\left(\boldsymbol{J}\right) + m_e\frac{\partial}{\partial t}\left(\frac{\boldsymbol{J}}{ne}\right) - m_e\frac{\boldsymbol{J}}{ne}\cdot\nabla\frac{\boldsymbol{J}}{ne}. \tag{2.55}$$

At numerical scales, the electron motion here is forced advective diffusion while ion motion remains diffusive. The terms that dominate at any scale can be collected, resulting in the total momentum equation

$$mn\frac{\mathrm{d}\boldsymbol{V}}{\mathrm{d}t} = \boldsymbol{J}\times\boldsymbol{B} - \nabla\cdot\left[\bar{\mathbf{P}}_i + \bar{\mathbf{P}}_e + \bar{\boldsymbol{\Pi}}_{ie}(\boldsymbol{V})\right] \tag{2.56}$$

and the electron momentum equation

$$\boldsymbol{E}+\boldsymbol{V}\times\boldsymbol{B} = \frac{1}{ne}\boldsymbol{J}\times\boldsymbol{B} - \frac{1}{ne}\nabla\cdot\left[\bar{\mathbf{P}}_e + \bar{\boldsymbol{\Pi}}_e\left(\boldsymbol{J}\right)\right] + m_e\frac{\partial}{\partial t}\left(\frac{\boldsymbol{J}}{ne}\right) - m_e\frac{\boldsymbol{J}}{ne}\cdot\nabla\frac{\boldsymbol{J}}{ne}. \tag{2.57}$$

Thus far, continuity, momentum, and Maxwell's equations have been simplified using the large speed of light, small mass ratio, and scaling arguments. To form a closed fluid plasma model, the closure of the energy equations must be addressed.

2.5 Common Energy Closure Schemes

Once again the energy equations for the diagonal of the pressure tensor are

$$3\frac{\mathrm{d}p_s}{\mathrm{d}t} + 5p_s\nabla\cdot\boldsymbol{V}_s + 2\bar{\boldsymbol{\Pi}}_s : \nabla\boldsymbol{V}_s + \nabla\cdot\left(\bar{\mathbf{Q}}_s : \bar{\mathbf{I}}\right) = 0 \tag{2.58}$$

when assuming isotropic pressure and

$$\begin{aligned}\frac{\mathrm{d}p_{s\|}}{\mathrm{d}t} - \bar{\boldsymbol{\Pi}}_s : \frac{\mathrm{d}\hat{b}\hat{b}}{\mathrm{d}t} + p_{s\|}\nabla\cdot\boldsymbol{V}_s \\ + 2p_{s\|}\hat{b}\hat{b} : \nabla\boldsymbol{V}_s + 2\hat{b}\hat{b} : \bar{\boldsymbol{\Pi}}_s\cdot\nabla\boldsymbol{V}_s + \nabla\cdot\left(\bar{\mathbf{Q}}_s : \hat{b}\hat{b}\right) - 2\hat{b}\cdot\bar{\mathbf{Q}}_s : \nabla\hat{b} = 0\end{aligned} \tag{2.59}$$

and

$$2\frac{\mathrm{d}p_{s\perp}}{\mathrm{d}t} + \bar{\boldsymbol{\Pi}}_s : \frac{\mathrm{d}\hat{b}\hat{b}}{\mathrm{d}t} + 4p_{s\perp}\nabla\cdot\boldsymbol{V}_s - 2p_{s\perp}\hat{b}\hat{b} : \nabla\boldsymbol{V}_s$$
$$+ 2\left(\bar{\mathbf{I}} - \hat{b}\hat{b}\right) : \bar{\boldsymbol{\Pi}}_s \cdot \nabla\boldsymbol{V}_s + \nabla\cdot\left[\bar{\mathbf{Q}}_s : \left(\bar{\mathbf{I}} - \hat{b}\hat{b}\right)\right] + 2\hat{b}\cdot\bar{\mathbf{Q}}_s : \nabla\hat{b} = 0 \qquad (2.60)$$

when assuming an anisotropic plasma with a parallel component and a perpendicular component.

There are two basic methods of achieving plasma closure. Asymptotic closure uses small parameters to systematically develop expressions for higher moments. Truncation closure arbitrarily assumes expressions for higher moments. The simplest truncation schemes can be expressed by using heat flux tensors that resemble that of a neutral, collision-dominated gas [178]. There, to lowest order, the heat flux depends linearly on temperature gradients. Using this as a starting point, for isotropic plasma, let

$$\bar{\mathbf{Q}}_s : \bar{\mathbf{I}} = -2n_s\kappa_s\nabla T_s, \qquad (2.61)$$

where κ_s is a coefficient of species heat flux and $T_s = p_s/n_s$ is the species temperature. Often, the flow divergence term can be replaced by rewriting the species continuity equation 2.19 as

$$\frac{1}{n_s}\frac{\mathrm{d}n_s}{\mathrm{d}t} = -\nabla\cdot\boldsymbol{V}_s. \qquad (2.62)$$

Using the above expressions, the isotropic pressure equation 2.58 becomes

$$\frac{3}{2}\frac{\mathrm{d}p_s}{\mathrm{d}t} - \frac{5}{2}\frac{p_s}{n_s}\frac{\mathrm{d}n_s}{\mathrm{d}t} + \bar{\boldsymbol{\Pi}}_s : \nabla\boldsymbol{V}_s = \nabla\cdot\left(n_s\kappa_s\nabla T_s\right), \qquad (2.63)$$

and, after combining the first two terms,

$$\frac{n_s^\Gamma}{\Gamma - 1}\frac{\mathrm{d}}{\mathrm{d}t}\left(\frac{p_s}{n_s^\Gamma}\right) + \bar{\boldsymbol{\Pi}}_s : \nabla\boldsymbol{V}_s = \nabla\cdot\left(n_s\kappa_s\nabla T_s\right). \qquad (2.64)$$

Here, $\Gamma = 5/3$ is the adiabatic index which depends on the degrees of freedom of the system. Two simple isotropic closures can be found in the limiting cases of κ_s. In the

limit of $\kappa_s \to \infty$, the heat flux term is finite if the temperature is uniform and

$$\nabla T_s = 0 \Rightarrow T_s = T_{s0}, \tag{2.65}$$

where T_{s0} is a constant. This is considered the isothermal limit since the plasma species temperature is uniform. Taking the limit $\kappa_s \to 0$ and letting $\bar{\bar{\Pi}}_s \to 0$ results in the expression

$$\frac{\mathrm{d}}{\mathrm{d}t}\left(\frac{p_s}{n_s^\Gamma}\right) = 0. \tag{2.66}$$

This is considered the adiabatic limit since there is no heat flow and the plasma follows an adiabatic equation of state in the frame of the moving plasma.

For anisotropic plasma, making the assumption that heat flux depends linearly on temperature gradients results in the expressions

$$\bar{\mathbf{Q}}_s : \hat{b}\hat{b} = -n_s\kappa_{\perp s}\nabla_\perp T_{\parallel s} - n_s\kappa_{\parallel s}\nabla_\parallel T_{\parallel s} \tag{2.67}$$

$$\bar{\mathbf{Q}}_s : \left[\bar{\mathbf{I}} - \hat{b}\hat{b}\right] = -2n_s\kappa_{\perp s}\nabla_\perp T_{\perp s} - 2n_s\kappa_{\parallel s}\nabla_\parallel T_{\perp s} \tag{2.68}$$

$$\hat{b}\cdot\bar{\mathbf{Q}}_s : \nabla\hat{b} = -n_s\kappa_{\perp s}\hat{b}\cdot\nabla\hat{b}\cdot\nabla_\perp T_{\parallel s} - n_s\kappa_{\parallel s}\hat{b}\cdot\nabla_\parallel T_{\perp s}\nabla\cdot\hat{b}, \tag{2.69}$$

where $\kappa_{\parallel s}$ and $\kappa_{\perp s}$ are the coefficients of species heat flux in the parallel and perpendicular directions, respectively and $T_{\parallel s} \equiv p_{s\parallel}/n_s$ and $T_{\perp s} \equiv p_{s\perp}/n_s$ are the parallel and perpendicular species temperatures, respectively. Also define

$$\nabla_\parallel \equiv \hat{b}\hat{b}\cdot\nabla \tag{2.70}$$

as the parallel gradient and

$$\nabla_\perp \equiv \nabla - \nabla_\parallel \tag{2.71}$$

as the perpendicular gradient. Once again, these expressions allow closure of the fluid equations by eliminating the heat flux tensor. Typically in collisionless plasma, heat flux along magnetic field lines is much greater than across them [177], which can be represented here as $\kappa_{\perp s} \ll \kappa_{\parallel s}$. Then, to lowest order, the parallel pressure equation

2.59 becomes

$$\frac{\mathrm{d}p_{s\parallel}}{\mathrm{d}t} - \bar{\boldsymbol{\Pi}}_s : \frac{\mathrm{d}\hat{b}\hat{b}}{\mathrm{d}t} + p_{s\parallel}\nabla\cdot\boldsymbol{V}_s + 2p_{s\parallel}\hat{b}\hat{b} : \nabla\boldsymbol{V}_s$$
$$+ 2\hat{b}\hat{b} : \bar{\boldsymbol{\Pi}}_s \cdot \nabla\boldsymbol{V}_s + 2n_s\kappa_{\parallel s}\hat{b}\cdot\nabla_\parallel T_{\perp s}\nabla\cdot\hat{b} = \nabla\cdot\left(n_s\kappa_{\parallel s}\nabla_\parallel T_{\parallel s}\right), \tag{2.72}$$

and for the perpendicular pressure equation 2.60

$$2\frac{\mathrm{d}p_{s\perp}}{\mathrm{d}t} + \bar{\boldsymbol{\Pi}}_s : \frac{\mathrm{d}\hat{b}\hat{b}}{\mathrm{d}t} + 4p_{s\perp}\nabla\cdot\boldsymbol{V}_s - 2p_{s\perp}\hat{b}\hat{b} : \nabla\boldsymbol{V}_s$$
$$+ 2\left(\bar{\mathbf{I}} - \hat{b}\hat{b}\right) : \bar{\boldsymbol{\Pi}}_s \cdot \nabla\boldsymbol{V}_s - 2n_s\kappa_{\parallel s}\hat{b}\cdot\nabla_\parallel T_{\perp s}\nabla\cdot\hat{b} = \nabla\cdot\left(2n_s\kappa_{\parallel s}\nabla_\parallel T_{\perp s}\right). \tag{2.73}$$

In this case, a useful limit is when $\kappa_{\parallel s} \to 0$ and $\bar{\boldsymbol{\Pi}} \to 0$. Then 2.62 can be used to obtain

$$\frac{\mathrm{d}p_{s\parallel}}{\mathrm{d}t} - \frac{p_{s\parallel}}{n_s}\frac{\mathrm{d}n_s}{\mathrm{d}t} + 2p_{s\parallel}\hat{b}\hat{b} : \nabla\boldsymbol{V}_s = 0 \tag{2.74}$$

for the parallel pressure and

$$\frac{\mathrm{d}p_{s\perp}}{\mathrm{d}t} - 2\frac{p_{s\perp}}{n_s}\frac{\mathrm{d}n_s}{\mathrm{d}t} - p_{s\perp}\hat{b}\hat{b} : \nabla\boldsymbol{V}_s = 0 \tag{2.75}$$

for the perpendicular pressure. In the ideal MHD regime, the Ideal Ohm's Law equation 2.49 can be combined with Faraday's Law 2.37 yielding

$$\frac{\mathrm{d}\boldsymbol{B}}{\mathrm{d}t} = \boldsymbol{B}\cdot\nabla\boldsymbol{V} - \boldsymbol{B}\nabla\cdot\boldsymbol{V}. \tag{2.76}$$

Taking the dot product of the above expression with $\boldsymbol{B}$ and dividing by B^2 yields

$$\frac{1}{2B^2}\frac{\mathrm{d}B^2}{\mathrm{d}t} = \hat{b}\hat{b} : \nabla\boldsymbol{V} + \frac{1}{n_s}\frac{\mathrm{d}n_s}{\mathrm{d}t}, \tag{2.77}$$

where 2.62 has been used to replace the divergence of the species flow. This expression can be used to replace the $\hat{b}\hat{b} : \nabla\boldsymbol{V}_s$ term in equations 2.74 and 2.75 yielding

$$\frac{\mathrm{d}p_{s\parallel}}{\mathrm{d}t} - 3\frac{p_{s\parallel}}{n_s}\frac{\mathrm{d}n_s}{\mathrm{d}t} + \frac{p_{s\parallel}}{B^2}\frac{\mathrm{d}B^2}{\mathrm{d}t} = \frac{B^2}{n_s^3}\frac{\mathrm{d}}{\mathrm{d}t}\left(\frac{p_{s\parallel}B^2}{n^3}\right) = 0, \tag{2.78}$$

which reduces to

$$\frac{\mathrm{d}}{\mathrm{d}t}\left(\frac{p_{s\parallel}B^2}{n^3}\right) = 0 \tag{2.79}$$

for the parallel pressure and

$$\frac{\mathrm{d}p_{s\perp}}{\mathrm{d}t} - \frac{p_{s\perp}}{n_s}\frac{\mathrm{d}n_s}{\mathrm{d}t} - \frac{p_{s\perp}}{2B^2}\frac{\mathrm{d}B^2}{\mathrm{d}t} = n_s B\frac{\mathrm{d}}{\mathrm{d}t}\left(\frac{p_{s\perp}}{n_s B}\right) = 0, \tag{2.80}$$

which reduces to

$$\frac{\mathrm{d}}{\mathrm{d}t}\left(\frac{p_{s\perp}}{n_s B}\right) = 0 \tag{2.81}$$

for the perpendicular pressure. Equations 2.79 and 2.81 are refered to as the double adiabatic equations or the CGL equations [177]. They describe the anisotropic evolution of species pressure in the limit of no heat flow in the ideal MHD regime.

2.6 Summary

This chapter described methods of modeling magnetized, ion-electron plasma dynamics using a fluid formulation. Vlasov's equation describes the evolution of a species distribution function in the collisionless limit. Tensor moments of Vlasov's equation yields a set of dynamic equations for fluid quantities. However, since each fluid equation depends on a higher moment of the distribution, the set of equations are not closed. A complete fluid description can be obtain by invoking a closure scheme, such as assuming isothermal or adiabatic conditions as shown in this chapter, or through an asymptotic approach where low order solutions for the distribution function are obtained.

Chapter 3

Modeling Reconnection

Magnetic reconnection provides a means of efficient conversion of magnetic energy to kinetic energy through changes to the magnetic topology. It requires a departure from the ideal plasma limit which generally occurs in localized regions in weakly-collisional plasmas. Models of magnetic reconnection have been studied extensively, in particular to understand the rapid rates of reconnection seen in plasmas and the structures that develop in the reconnection region.

This chapter reviews the Frozen-In Law of ideal plasmas and the closely related concept of conservation of magnetic topology. This framework allows the differentiation of non-ideal plasma conditions that preserve topology versus conditions that change topology and "break" magnetic field lines. Finally, steady state models of reconnection are reviewed.

3.1 Frozen-In Law

In Ideal Magnetohydrodynamics, magnetic field lines and plasma flows are intimately coupled, constraining magnetic field line evolution. This can be seen from combining Faraday's law

$$\frac{\partial \boldsymbol{B}}{\partial t} = -\nabla \times \boldsymbol{E} \tag{3.1}$$

and the Ideal Ohm's Law

$$\boldsymbol{E} + \boldsymbol{V} \times \boldsymbol{B} = 0 \tag{3.2}$$

yielding

$$\frac{\partial \boldsymbol{B}}{\partial t} = \nabla \times (\boldsymbol{V} \times \boldsymbol{B}). \tag{3.3}$$

The change in flux through a surface bounded by a closed contour moving with the fluid can be found by integrating 3.3. The left hand side can be evaluated using Leibniz Integral Rule and the fact $\boldsymbol{B}$ is divergence-less to yield

$$\iint_{S(t)} \frac{\partial \boldsymbol{B}}{\partial t} = \frac{\mathrm{d}}{\mathrm{d}t} \iint_{S(t)} \boldsymbol{B} \cdot \mathrm{d}\boldsymbol{A} + \oint_{\partial S(t)} \boldsymbol{V} \times \boldsymbol{B}. \tag{3.4}$$

The right hand side of 3.3 can be evaluated using Stokes Theorem

$$\iint_{S(t)} \nabla \times (\boldsymbol{V} \times \boldsymbol{B}) = \oint_{\partial S(t)} \boldsymbol{V} \times \boldsymbol{B}. \tag{3.5}$$

Equating these to sides, it is clear that

$$\frac{\mathrm{d}}{\mathrm{d}t} \iint_{S(t)} \boldsymbol{B} \cdot \mathrm{d}\boldsymbol{A} = 0. \tag{3.6}$$

Hence, the magnetic flux through a surface, with each point of the surface moving with the local plasma velocity, is conserved. Extending the contour bounding the surface along the magnetic field line creates a tube referred to as a magnetic flux tube. The Ideal Frozen-In Law 3.3 implies that motions of the plasma and magnetic field retain the integrity of flux tubes, that is the flux tubes cannot be "broken" but can be twisted around by the plasma. Taking magnetic field lines to be infinitely thin flux tubes, then 3.3 also implies magnetic field lines maintain their integrity and are therefore "frozen" into the plasma. [173, 180]

The above discussion described conservation of magnetic flux or flux freezing in Ideal MHD. However, in extended collisionless MHD models of plasma, magnetic flux is not necessarily conserved with plasma flow (but may be conserved with other flows). The next section will introduce magnetic topology conservation.

3.2 Conservation of Magnetic Topology

Closely connected to flux-freezing is the more general conservation of magnetic topology, or the connectivity, of the field lines. Following the arguments of Biskamp [180] The condition for topology conservation can be shown by first expressing the magnetic field $\boldsymbol{B}$ in terms of a mapping function $\boldsymbol{F}_B(\boldsymbol{x}, s, t)$ such that

$$\boldsymbol{B} = \frac{\partial F_B(\boldsymbol{x}, s, t)}{\partial s}, \tag{3.7}$$

where

$$\boldsymbol{F}(\boldsymbol{x}, 0, t) = \boldsymbol{x} \tag{3.8}$$

and the field lines are parameterized by s (for example the displacement along a field line). A flow $\boldsymbol{u}$ that transports the magnetic field can also be expressed by a mapping function $\boldsymbol{F}_u(\boldsymbol{x}, t, t_0)$ such that

$$\boldsymbol{u} = \frac{\partial \boldsymbol{F}_u(\boldsymbol{x}, t, t_0)}{\partial t}, \tag{3.9}$$

with

$$\boldsymbol{F}_u(\boldsymbol{x}, t_0, t_0) = \boldsymbol{x}. \tag{3.10}$$

The flow preserves topology if any two points on the same field line at $t = t_0$ remain on the same field line for $t > t_0$. That is for some $\boldsymbol{x} = \boldsymbol{F}_B(\boldsymbol{x}, 0, t_0)$ and $\boldsymbol{y} = \boldsymbol{F}_B(\boldsymbol{x}, s, t_0)$ which are on the same field line at $t = t_0$, then at a later time $t > t_0$, the points, which are transported to $\boldsymbol{x}'$ and $\boldsymbol{y}'$ by the flow $\boldsymbol{u}$, so that $\boldsymbol{x}' \equiv \boldsymbol{F}_u(\boldsymbol{x}, t, t_0)$ and $\boldsymbol{y}' \equiv \boldsymbol{F}_u(\boldsymbol{y}, t, t_0)$ are still on the same field line. Therefore $\boldsymbol{y}$ can be found by transporting $\boldsymbol{x} \rightarrow \boldsymbol{x}'$ and then traversing this corresponding field line by s':

$$\boldsymbol{y}' = \boldsymbol{F}_B[\boldsymbol{x}', s', t] = \boldsymbol{F}_B[\boldsymbol{F}_u(\boldsymbol{x}, t, t_0), s', t], \tag{3.11}$$

where $s' = s'(s,t)$ is an arbitrary function to allow for parallel flows. Additionally, $\boldsymbol{y}$ can be found by transporting $\boldsymbol{y} \rightarrow \boldsymbol{y}'$:

$$\boldsymbol{y}' = \boldsymbol{F}_u\left[\boldsymbol{y}, t, t_0\right] = \boldsymbol{F}_u\left[\boldsymbol{F}_B\left(\boldsymbol{x}, s, t_0\right), t, t_0\right]. \tag{3.12}$$

Expressions 3.11 and 3.12 should be equal for magnetic topology conservation

$$\boldsymbol{F}_B\left[\boldsymbol{F}_u\left(\boldsymbol{x}, t, t_0\right), s', t\right] = \boldsymbol{F}_u\left[\boldsymbol{F}_B\left(\boldsymbol{x}, s, t_0\right), t, t_0\right]. \tag{3.13}$$

Derivatives with respect to s and t should be equal as well:

$$\partial_t \partial_s \boldsymbol{F}_B\left[\boldsymbol{F}_u\left(\boldsymbol{x}, t, t_0\right), s', t\right] = \partial_s \partial_t \boldsymbol{F}_u\left[\boldsymbol{F}_B\left(\boldsymbol{x}, s, t_0\right), t, t_0\right]. \tag{3.14}$$

Then, making use of definitions 3.7 and 3.10,

$$\partial_t\Big\{\boldsymbol{B}\left[\boldsymbol{F}_u\left(\boldsymbol{x}, t, t_0\right), s', t\right] \partial_s s'\Big\} = \partial_s\Big\{\boldsymbol{u}\left[\boldsymbol{F}_B\left(\boldsymbol{x}, s, t_0\right), t, t_0\right]\Big\} \tag{3.15}$$

and differentiating again

$$\frac{\partial \boldsymbol{B}}{\partial t} + \boldsymbol{u} \cdot \nabla \boldsymbol{B} + \boldsymbol{B} \frac{\partial^2 s'}{\partial s \partial t} = \boldsymbol{B} \cdot \nabla \boldsymbol{u}. \tag{3.16}$$

Using the vector identity

$$\boldsymbol{B} \cdot \nabla \boldsymbol{u} - \boldsymbol{u} \cdot \nabla \boldsymbol{B} = \nabla \times (\boldsymbol{u} \times \boldsymbol{B}) - \boldsymbol{u} \nabla \cdot \boldsymbol{B} + \boldsymbol{B} \nabla \cdot \boldsymbol{u}$$

and noting that $\boldsymbol{B}$ is divergenceless yields

$$\frac{\partial \boldsymbol{B}}{\partial t} = \nabla \times (\boldsymbol{u} \times \boldsymbol{B}) + \boldsymbol{B}\left(\nabla \cdot \boldsymbol{u} - \frac{\partial^2 s'}{\partial s \partial t}\right). \tag{3.17}$$

Finally, letting

$$\lambda = \nabla \cdot \boldsymbol{u} - \frac{\partial^2 s'}{\partial s \partial t}, \tag{3.18}$$

then 3.17 can be written as

$$\frac{\partial \boldsymbol{B}}{\partial t} = \nabla \times (\boldsymbol{u} \times \boldsymbol{B}) + \lambda \boldsymbol{B} \tag{3.19}$$

or equivalently, using Faraday's Law,

$$\nabla \times (\boldsymbol{E} + \boldsymbol{u} \times \boldsymbol{B}) + \lambda \boldsymbol{B} = 0. \tag{3.20}$$

The above two equivalent equations are a condition on velocity field $\boldsymbol{u}$ for a given divergenceless field $\boldsymbol{B}$, $\boldsymbol{u}$ is line-conserving if and only if it satisfies 3.19 where λ is an arbitrary, smooth function of space and time.

Equations 3.19 or 3.20 can be used with Ohm's Law to show that some nonideal effects are field line conserving. For example, when including the Hall Term, Ohm's Law can be written as

$$\boldsymbol{E} + \left(\boldsymbol{V} - \frac{1}{ne}\boldsymbol{J}\right) \times \boldsymbol{B} = 0, \tag{3.21}$$

which satisfies 3.20 by inspection with $\lambda = 0$ and velocity field $\boldsymbol{u} = \boldsymbol{V} - 1/ne\boldsymbol{J} \simeq v_e$. Here the magnetic field is convected with the electron velocity v_e, and topology is conserved. For magnetic field lines to be broken and reconnection to occur, additional physics beyond Hall MHD must be included.

3.3 Breaking the Frozen-In Law

Perhaps the simplest physics that can allow reconnection is in collisional plasmas, where ion-electron collisions are encapsulated as a resistivity term yielding the Resistive Ohm's Law equation

$$\boldsymbol{E} + \boldsymbol{V} \times \boldsymbol{B} = \eta_R \boldsymbol{J}. \tag{3.22}$$

Combining this expression with Faraday's Law and Ampere's Law

$$\nabla \times \boldsymbol{B} = \mu_0 \boldsymbol{J} \tag{3.23}$$

yields

$$\frac{\partial \boldsymbol{B}}{\partial t} - \nabla \times (\boldsymbol{V} \times \boldsymbol{B}) = \frac{\eta_R}{\mu_0} \nabla^2 \boldsymbol{B}. \tag{3.24}$$

With the exception of a decaying force-free (that is $\nabla \times \boldsymbol{B} = \alpha \boldsymbol{B}$ and $\boldsymbol{B} \cdot \nabla \alpha = 0$ for a spatially varying α) magnetic field geometry is changed by the diffusion term on the RHS. Typically, this term will only dominate the convection term near a region of stagnation flow where $\boldsymbol{V}$ is small. Generally, independent of the mechanism responsible, the region where field line breaking terms dominate is referred to the diffusion or dissipation region.

In weakly collisional plasmas, resistivity due to collisions is negligible, though other physical terms can be important to field line conservation. When including a gyrotropic (diagonal) electron pressure in addition to the Hall Term, after some manipulation, Ohm's Law can be written as

$$\begin{aligned} \boldsymbol{E} + \left(\boldsymbol{V} - \frac{1}{ne} \boldsymbol{J} \right) \times \boldsymbol{B} = - \frac{1}{ne} \Bigg[& \mathscr{F}_e \boldsymbol{J} \times \boldsymbol{B} + \left(\nabla p_{e\perp} + \mathscr{F}_e \nabla \tfrac{1}{2} B^2 \right) \cdot \left(\bar{\mathbf{I}} - \hat{b}\hat{b} \right) \\ & + \left(\nabla p_{e\parallel} - \mathscr{F}_e \nabla \tfrac{1}{2} B^2 \right) \cdot \hat{b}\hat{b} \Bigg], \end{aligned} \tag{3.25}$$

where $\mathscr{F}_e = \mu_0 (p_{e\parallel} - p_{e\perp}) / B^2$. Letting $\boldsymbol{C} = \nabla p_{e\perp} + \mathscr{F}_e \nabla \frac{1}{2} B^2$ and $\boldsymbol{D} = \nabla p_{e\parallel} - \mathscr{F}_e \nabla \frac{1}{2} B^2$ and using the identity $\left(\bar{\mathbf{I}} - \boldsymbol{BB} \right) \cdot \boldsymbol{C} = - \left(\boldsymbol{C} \times \boldsymbol{B} \right) \times \boldsymbol{B}$. Then this Ohm's Law can be written as

$$\boldsymbol{E} + \left\{ \boldsymbol{V} - \frac{1}{ne} \left[\left(1 - \mathscr{F}_e \right) \boldsymbol{J} - \frac{\boldsymbol{C} \times \boldsymbol{B}}{B^2} \right] \right\} \times \boldsymbol{B} = - \frac{1}{ne} \boldsymbol{D} \cdot \hat{b}\hat{b}. \tag{3.26}$$

By inspection, the RHS of this equation prohibits the existence of a topological preserving velocity. However, in many scenarios, gradients along field lines can be negligible, such that $\boldsymbol{D} \cdot \hat{b} \simeq 0$ or in reconnection, profiles achieve a relative extrema such that $D \simeq 0$ near the X-line . In these scenarios, inclusion of gyroscopic electron, magnetic field line is convected with velocity given inside the curly brackets of 3.26. This idea is useful in symmetric 2.5 dimensional reconnection with an guide-field in the out-of-plane direction. In this scenario, the field is in the out of plane direction

at X-lines. In this region, taking the curl of the RHS of 3.26 yields

$$-\nabla \times \left(\boldsymbol{D} \cdot \hat{b}\hat{b} \right) = \hat{b} \times \nabla \hat{b} \cdot \boldsymbol{D} = 0, \tag{3.27}$$

where the second equality is due to the mirror symmetry of the parallel and magnetic pressure in this region. The other terms from the first equality can be discarded because in this region, gradients along the magnetic field are zero. Once again in this scenario, field line topology is conserved locally near the X points.

The inclusion of electron inertia can also affect field line topology. Electron Ohm's Law

$$m_e n \left(\frac{\partial \boldsymbol{V}_e}{\partial t} + \boldsymbol{V}_e \cdot \nabla \boldsymbol{V}_e \right) = -ne \left(\boldsymbol{E} + \boldsymbol{V}_e \times \boldsymbol{B} \right) \tag{3.28}$$

can be combined with Faraday's Law to yield

$$\frac{\partial}{\partial t} \left(\boldsymbol{B} - \frac{m_e}{e} \nabla \times \boldsymbol{V}_e \right) = \nabla \times \left[\boldsymbol{V}_e \times \left(\boldsymbol{B} - \frac{m_e}{e} \nabla \times \boldsymbol{V}_e \right) \right]. \tag{3.29}$$

Comparing to 3.19, magnetic field line are broken by electron inertia but the quantity $\boldsymbol{B} - m_e/e \nabla \times \boldsymbol{V}_e$ is convected with the electron velocity $\boldsymbol{V}_e$. In ion-electron plasmas, since $m_i \gg m_e$, electron inertia is only relevant at the smallest scales.

Electron agyrotropy, which is a departure of electron motion from gyrotropic orbits and is represented by off-diagonal terms of the electron pressure tensor, can break magnetic field lines at larger scales than electron inertia and in symmetric geometries [2,137]. For the simple case of incompressible plasma where the off-diagonal terms can be modeled to lowest order as a fluid viscosity with a constant coefficient of viscosity, Ohm's Law can be written as

$$\boldsymbol{E} + \boldsymbol{V} \times \boldsymbol{B} = -\eta_H \nabla^2 \boldsymbol{J}, \tag{3.30}$$

where $\eta_H = m_e \nu_e / n_0$ is the hyper-resistivity and ν_e is the electron viscosity. This can

be combined with Faraday's Law to yield

$$\frac{\partial \boldsymbol{B}}{\partial t} = \nabla \times (\boldsymbol{V} \times \boldsymbol{B}) - \frac{\eta_H}{\mu_0} \nabla^4 \boldsymbol{B}. \tag{3.31}$$

Again, with the exception of a decaying force-free magnetic field, the second term of RHS, sometimes referred to as a biharmonic mixing (or biharmonic filtering) term, breaks magnetic topology. Due to the fourth-order differentiation associated with the term, biharmonic mixing affects small scale structures more and large scale structures less than diffusion [181], and is often employed in weakly collisional fluid reconnection simulations [133].

In the case of weak to moderate guide-fields, electron pressure agyrotropy is the dominant mechanism that breaks magnetic field line topology [2, 135–137]. The next section will use this mechanism in a simplified plasma model to find steady-state Sweet-Parker reconnection scalings.

3.4 Steady State Sweet-Parker Reconnection

A simple picture of steady-state two-dimensional magnetic reconnection is the Sweet-Parker reconnection model [7]. Reconnection is often studied in the steady-state because many astrophysical processes are essentially steady state [125]. The Sweet-Parker model assumes a geometry seen in Figure 3-1, with an inner reconnection region (region 2) of length $2l$ and thickness 2Δ embedded in an outer region (region 1) with magnetic shear. The direction of inflow is $\pm y$, while the outflow is $\pm x$. The magnetic field in far from the reconnection region is in the $\pm x$ direction, and gains a $\pm y$ component in the reconnection region. Reconnection models are often characterized by the reconnection rate, which a measure of the inflow plasma velocity normalized to the local Alfvén velocity, while the rate of magnetic flux reconnection, which is the rate at which flux conservation is violated, is given by the out-of-plane electric field E_z [182]. Sweet-Parker analysis allows an expression for the reconnection rate to be found, independent of the thickness of the reconnection region Δ.

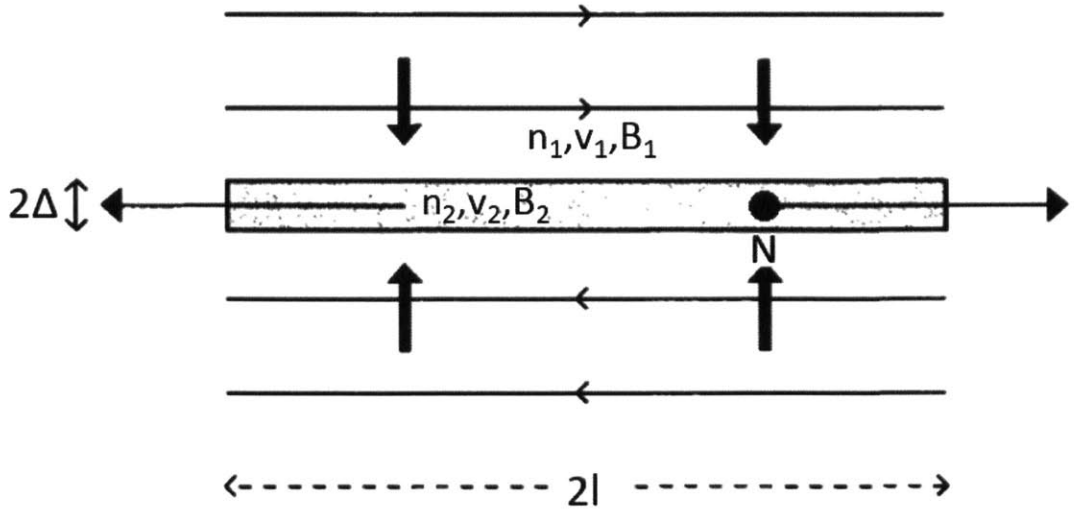

Figure 3-1: Sweet-Parker reconnection. The diffusion region is shaded with density n_2, magnetic field B_2 and velocity v_2 compared to n_1,B_1 and v_1 outside. Thick-headed arrows represent plasma flow while magnetic field lines are thin-headed arrows. The x-component of the plasma momentum equation is evaluated at point N. (Ref [3]).

This system can be modeled by compressible MHD with electron viscosity to allow magnetic field line topology changes. Viscosities and heat conduction are assumed small, so viscous heating can be ignored and pressure can be taken to be adiabatic. In steady state, the system is described by

$$\nabla \cdot (n\boldsymbol{V}) = 0 \tag{3.32}$$

$$\boldsymbol{E} + \boldsymbol{V} \times \boldsymbol{B} = -\frac{m_e \nu_e}{e} \nabla^2 \frac{\nabla \times \boldsymbol{B}}{\mu_0 n e} \tag{3.33}$$

$$m_i n \boldsymbol{V} \cdot \nabla \boldsymbol{V} = \frac{\nabla \times \boldsymbol{B}}{\mu_0} \times \boldsymbol{B} - \nabla p + m_i n \nu_i \left(\nabla^2 \boldsymbol{V} + \frac{1}{3} \nabla \nabla \cdot \boldsymbol{V} \right) \tag{3.34}$$

$$\frac{p}{n^\Gamma} = const \tag{3.35}$$

$$\nabla \cdot \boldsymbol{B} = 0, \tag{3.36}$$

where Γ is the ratio of specific heats. Furthermore, assume the density and pressure have constant values n_1 and p_1 outside the reconnection region and n_2 and p_2 inside the region (while the boundary has the average value), while flows v_1 and magnetic fields B_1 are constant outside the reconnection region, and vary linearly inside the

region. Under these assumptions, the continuity equation 3.32 yields

$$n_1 V_1 l = n_2 V_2 \Delta. \tag{3.37}$$

Since relevant plasmas are nearly ideal, the RHS of Ohm's Law 3.33 can be ignored in the outer region. In the inner region, the flow has nearly stagnated, so the $\boldsymbol{V} \times \boldsymbol{B} \simeq 0$ and the out-of-plane electric field is balanced by the RHS. In the inner diffusion region of resistive MHD, the electric field is balanced by resistivity leading to magnetic field diffusion. Equating the out-of-plane electric field in the outer and inner regions yields

$$E_z = -V_1 B_1 = -\frac{m_e \nu_e}{\mu_0 n_2 e^2 \Delta^3} \frac{2}{\frac{n_2}{n_1} + 1} B_1 = -\frac{d_{e2}^2 \nu_e}{\Delta^3} \frac{2}{\frac{n_2}{n_1} + 1} B_1, \tag{3.38}$$

where d_{e2} is the electron inertial length evaluated in the diffusion region. Expressions 3.37 and 3.38 can be combined to eliminate Δ, yielding

$$V_1^4 = \left(\frac{n_2}{n_1}\right)^3 \frac{d_{e2}^2 \nu_e}{l^3} \frac{2}{\frac{n_2}{n_1} + 1} V_2^3. \tag{3.39}$$

To find V_2, the x-component of 3.34 can be evaluated at a point N in Figure 3-1 along the x-axis halfway to the edge of the diffusion region:

$$m_i n_2 \frac{V_2}{2} \frac{V_2}{l} = \frac{B_1}{\mu_0 \Delta} \frac{B_2}{2} + m_i n_2 \nu_i \left(-\frac{\frac{1}{2} V_2}{\Delta^2}\right). \tag{3.40}$$

Since magnetic fields are divergenceless 3.36

$$\frac{B_1}{l} \sim \frac{B_2}{\Delta}, \tag{3.41}$$

while 3.37 and 3.38 can be combined to relate Δ and V_2. Then, 3.40 can be rewritten as

$$V_2^2 + \nu_i l \sqrt{\frac{\frac{n_2}{n_1}\left(\frac{n_2}{n_1} + 1\right)}{2 d_{e2}^2 \nu_e l}} V_2^{3/2} = \frac{B_1^2}{\mu_0 m_i n_2}. \tag{3.42}$$

To lowest order the outflow velocity is given by

$$V_2 \simeq \frac{B_1}{\sqrt{\mu_0 m_i n_1}} \sqrt{\frac{n_1}{n_2}} = V_{A1} \sqrt{\frac{n_1}{n_2}}, \tag{3.43}$$

where V_{A1} is the Alfvén velocity in the outer region. From 3.42, viscosity reduces outflow velocity, and from 3.43 compressibility can further reduce outflow velocity if $n_2 > n_1$. The compressibility can be found using the y-component of 3.34. Based on 3.39, the inflow speed can be assumed much less than the Alfvén speed, such that across the layer

$$\frac{\partial}{\partial y}\left(\frac{B^2}{2\mu_0} + p\right) \simeq 0 \Rightarrow p_1 + \frac{B_1^2}{2\mu_0} = p_2. \tag{3.44}$$

Combined with the adiabatic condition 3.35 yields

$$\left(1 + \frac{1}{\beta_1}\right)^{1/\Gamma} = \frac{n_2}{n_1} = N^{1/\Gamma}. \tag{3.45}$$

Finally combining 3.39, 3.43, and 3.45, the reconnection rate is

$$M_H = \frac{V_1}{V_{A1}} = \left(\frac{d_{e2}^2 \nu_e}{v_{A1} l^3}\right)^{1/4} \left(\frac{2N^{3/2\Gamma}}{N^{1/\Gamma}+1}\right)^{1/4} = \frac{1}{S_H^{1/4}} \left(\frac{2N^{3/2\Gamma}}{N^{1/\Gamma}+1}\right)^{1/4}, \tag{3.46}$$

where S_H is the hyper Lundquist number and is a measure of the hyper-resistivity of the system. The characteristic time for the Sweet-Parker estimated

$$\tau_{SP} = \frac{L}{V_1} = \frac{L}{V_{A1}} \frac{1}{M_H} = \frac{L}{V_{A1}} \left(\frac{N^{1/\Gamma}+1}{2N^{3/2\Gamma}}\right)^{1/4} S_H^{1/4}, \tag{3.47}$$

where L is the system size. In Sweet-Parker scaling, the layer length is the same order of the system size so $l \sim L$. For typical values of active regions of the solar corona, $n \sim 10^{15}$ m^{-3}, $B \sim 100$ G, $T \sim 100$ eV, $L \sim 10^8$ m, and collision time $\tau_{ee} \sim 10^{-2}$ s [183], the Sweet Parker time is $\tau_{SP} \sim 10^{10}$ s, compared to observed reconnection times of $\tau \sim 10^4$ s, a difference of many orders of magnitude.

Though reconnection rates predicted by Sweet-Parker models have been seen in numerical simulations [123] and in laboratory plasma [95,96], the Sweet-Parker model

is much too slow to account for many reconnection processes thought to occur in the solar system. Sweet-Parker models yield reconnection times on time scales of $\sqrt{\tau_A \tau_D}$ where τ_A is the Alfvén transit timescale and τ_D is a diffusive timescale for the magnetic field, where generally $\tau_D \ll \tau_A$. However, especially for astrophysical plasmas, Sweet-Parker reconnection is slow because of large system sizes and long collision times that characterize the systems. The next section will apply scaling arguments to the magnetic reconnection process using a different framework, the Electron Magnetohydrodynamic (EMHD) model.

3.5 Steady State Electron MHD Reconnection

The Electron Magnetohydrodynamic (EMHD) model is a single fluid formulation that describes plasma dynamics occurring on small spatial and temporal scales such that the ions are effectively immobile and act as a stationary, charge neutralizing background [184, 185]. The dynamics of the system are completely governed by the electron fluid, though quasi-neutrality eliminates electron density fluctuations as well. Plasma dynamics can be described using Faraday's Law 3.1, Ampere's Law 3.23, and a generalized Ohm's Law with plasma velocity $\boldsymbol{V} = 0$, pressure anisotropy, and constant density

$$en\boldsymbol{E} = \boldsymbol{J} \times \boldsymbol{B} - \nabla \cdot \left[p_{e\perp} \bar{\mathbf{I}} + \mathscr{F}_e \frac{\boldsymbol{B}\boldsymbol{B}}{\mu_0} \right] + \frac{m_e}{e} \left(\frac{\partial \boldsymbol{J}}{\partial t} - \frac{1}{ne} \boldsymbol{J} \cdot \nabla \boldsymbol{J} \right) - \frac{m_e \nu_e}{e} \nabla^2 \boldsymbol{J}. \quad (3.48)$$

Magnetic reconnection near an X-line can be studied in EMHD using scaling arguments in a similar manner to Sweet-Parker reconnection in MHD [186, 187]. Here, anisotropic gyrotropic electron pressure will be included. In steady state, discarding contributions from scalar potentials and electron convection, 3.48 can be written as

$$\boldsymbol{E} = \frac{1}{ne} \left((1 - \mathscr{F}_e) \frac{\boldsymbol{B} \cdot \nabla \boldsymbol{B}}{\mu_0} - \frac{\boldsymbol{B}\boldsymbol{B}}{\mu_0} \cdot \nabla \mathscr{F}_e - \frac{m_e \nu_e}{e} \nabla^2 \boldsymbol{J} \right). \quad (3.49)$$

The geometry of the EMHD reconnection region is depicted in Figure 3-2. Within a characteristic ion length (such as the ion inertial length or ion gyroradius) of the

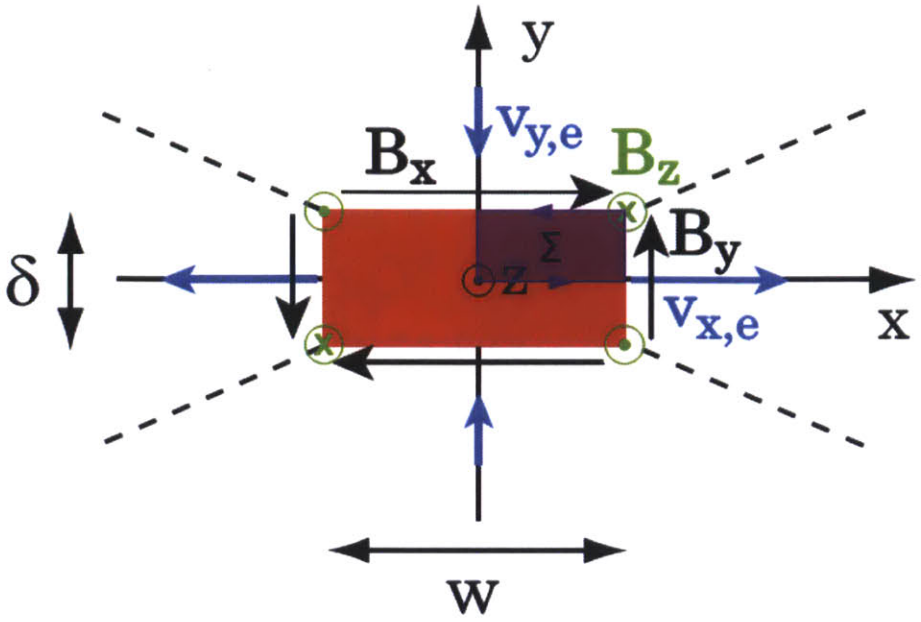

Figure 3-2: 2D EMHD reconnection geometry. Out-of-plane magnetic field develops due to assumed electron flow. The in-plane electric field is integrated around the shaded region Σ. (Ref [187]).

X-line, ion and electron motion decouple, and near the X-line, the plasma is described by EMHD. In addition to the in-plane magnetic fields of an X-line geometry, a quadrupolar out-of-plane field is generated due to ion-electron decoupling, though in this derivation the out-of-plane guide-field is taken to be zero far upstream from the X-line. This inner electron diffusion region has dimensions 2δ and $2w$ with estimates $\partial_x \sim 1/w$ and $\partial_y \sim 1/\delta$. From $\nabla \cdot \boldsymbol{B} = 0$,

$$\frac{B_x}{w} \sim \frac{B_y}{\delta} \tag{3.50}$$

and assuming $\delta < w$, then $|B_y| < |B_x|$ and $J_z \sim -B_x/\delta$. Equating out-of-plane electric field at the edge of the diffusion region at $(0, \delta)$ and the inner region at the X-line $(0, 0)$ yields

$$E_z \approx \frac{1}{ne}\left(1 - \mathscr{F}_e\right)\frac{B_x}{w}\frac{B_z}{\mu_0} = d_e^2 \nu_e \frac{B_x}{\delta^3}. \tag{3.51}$$

Using Faraday's Law 3.1 for static magnetic fields,

$$\frac{\partial B_z}{\partial t} = \nabla \times \boldsymbol{E}_p = 0. \tag{3.52}$$

Integrating 3.52 over a quarter of the region depicted in Figure 3-2, and using Stokes Theorem to transform the RHS yields

$$\iint_{\Sigma} \frac{\partial B_z}{\partial t} d\Sigma = \oint_{\partial\Sigma} \boldsymbol{E}_p \cdot d\boldsymbol{s} = 0. \tag{3.53}$$

Again, using scalings introduced above,

$$\frac{1}{ne}\left(1 - \tau\mathscr{F}_e\right)\left(\frac{B_x}{w} + \frac{B_y}{\delta}\right)\frac{B_x}{\mu_0} w = d_e^2 \nu_e \frac{B_z}{\delta^3} w, \tag{3.54}$$

with $\boldsymbol{B} \cdot \nabla \mathscr{F}_e \sim (\tau - 1)(B_x/w + B_y/\delta)\mathscr{F}$. Equations 3.51 and 3.54 can be combined to yield

$$\sqrt{\frac{2\left(1 - \tau\mathscr{F}_e\right)}{1 - \mathscr{F}_e}} B_x \approx B_z, \tag{3.55}$$

where $\tau \lesssim 1$. Then, from 3.51

$$\delta \approx \left(\frac{new\mu_0}{B_x} \frac{d_e^2 \nu_e}{1 - \mathscr{F}_e} \sqrt{\frac{1 - \mathscr{F}_e}{2\left(1 - \tau\mathscr{F}_e\right)}}\right)^{1/3} = \left(\frac{w d_e^2 \nu_e}{d_i V_{Ax}} \frac{1}{1 - \mathscr{F}_e} \sqrt{\frac{1 - \mathscr{F}_e}{2\left(1 - \tau\mathscr{F}_e\right)}}\right)^{1/3}. \tag{3.56}$$

Furthermore, since $\boldsymbol{V} = 0$ in EMHD, the electron velocities are given by

$$V_{ey} = -\frac{J_y}{ne} \approx \frac{B_z}{ne\mu_0 w} = \sqrt{\frac{2\left(1 - \tau\mathscr{F}_e\right)}{1 - \mathscr{F}_e}} \frac{d_i}{w} V_{Ax} \tag{3.57}$$

$$V_{ex} = -\frac{J_x}{ne} \approx \frac{B_z}{ne\mu_0 \delta} = \left(\frac{\left(1 - \tau\mathscr{F}_e\right)^2}{1 - \mathscr{F}_e} \frac{4 d_i^4 V_{Ax}}{w d_e^2 \nu_e}\right)^{1/3} V_{Ax}. \tag{3.58}$$

Finally using 3.51 and the above relations

$$E_z = \frac{d_i}{w} V_{Ax} B_x \sqrt{2\left(1 - \mathscr{F}_e\right)\left(1 - \tau\mathscr{F}_e\right)}. \tag{3.59}$$

In these expressions, $V_{Ax} = B_x/\sqrt{\mu_0 m_i n}$. In the isotropic scenario, $\mathscr{F}_e = 0$ and 3.56 allows both $\delta \sim w \sim \sqrt{d_e^2 \nu_e / d_i V_{Ax}}$ and $\delta \sim (d_e^2 \nu_e / d_i V_{Ax})^{1/3}$ [187]. The introduction of anisotropy allows more freedom in solutions. Particularly, considering the aspect ratio

$$\frac{\delta}{w} = \left(\frac{d_e^2 \nu_e}{w^2 d_i V_{Ax}} \frac{1}{1-\mathscr{F}_e} \sqrt{\frac{1-\mathscr{F}_e}{2\left(1-\tau \mathscr{F}_e\right)}} \right)^{1/3}, \tag{3.60}$$

reconnection rates can remain similar to isotropic cases if δ and w increase accordingly. In all the above expressions, the density n, magnetic field B_x and the layer width w are input parameters, and may be different from values far upstream of the reconnection in the MHD regime. These values are set by macroscopic physics, though the microscopic region near the X-line might also feedback into the macroscopic physics. Consequences of anisotropy in these expressions can be obscured since these values could change as a result of this feedback as well. Furthermore, the firehose ratio $\mathscr{F}_e$ used in the above expressions is evaluated at edge of the EMHD region, which may be different than the maximum value of the region.

An interesting result of EMHD reconnection scaling is that the inflow velocity 3.57 and out-of-plane electric field 3.59 do not explicitly depend on the electron viscosity, the mechanism that breaks the frozen-in condition. If resistivity is instead used as the mechanism to break the Frozen-In Law, the above arguments can be repeated with the substitution $d_e^2 \nu_e / \delta^2 \rightarrow \eta_R / \mu_0$ B_z and V_{ey} are the same as before, while

$$V_{ex} = -\frac{J_x}{ne} \approx \frac{B_z}{ne\mu_0 \delta} = 2\left(1-\tau \mathscr{F}_e\right) \frac{d_i V_{Ax}}{\eta_R/\mu_0} \frac{d_i}{w} V_{Ax} \tag{3.61}$$

$$E_z = \frac{d_i}{w} V_{Ax} B_x \sqrt{2\left(1-\tau \mathscr{F}_e\right)\left(1-\mathscr{F}_e\right)}. \tag{3.62}$$

Once again inflow velocity and the reconnection electric field are independent of the mechanism that breaks the frozen-in condition. This result has also been seen in simulations that include ion-electron decoupling effects [128, 131, 133].

It is useful to note that without electron viscosity, the aspect ratio in the resistive

case

$$\frac{\delta}{w} \approx \frac{\eta_R/\mu_0}{d_i V_{Ax}} \frac{1}{1-\mathscr{F}_e} \sqrt{\frac{1-\mathscr{F}_e}{2\left(1-\tau\mathscr{F}_e\right)}} \tag{3.63}$$

is independent of the layer length w. For a given aspect ratio (which would depend on macroscopic physics), the current layer can shrink without bound becoming singular, which has been observed in fluid simulations of magnetic reconnection [188]. Thus, for fluid simulations, electron viscosity or some electron hyperviscosity is necessary to smooth singularities at the stagnation point of the electron fluid.

Though EMHD descriptions of magnetic reconnection obtain the useful result of magnetic reconnection rates and electric fields independent of the dissipation mechanism, EMHD results still depend on macroscopic physics including ion dynamics. Though there has been some progress in coupling EMHD solutions to the macroscopic regime [189–192], the next section will instead describe a more qualitative picture of two-fluid MHD reconnection.

3.6 Two-Fluid MHD Reconnection

In plasma where collisions between ions and electrons are sufficiently weak, the large difference between their masses can allow motions of ion and electrons to decouple at small spatial and temporal scales [125]. In two-fluid MHD models, ions are governed by the ion momentum equation while the electron momentum equation is written as a generalized Ohm's Law [173]

$$\frac{m_e}{ne^2}\left[\frac{\partial \boldsymbol{J}}{\partial t} + \nabla\cdot\left(\boldsymbol{J}\boldsymbol{V} + \boldsymbol{V}\boldsymbol{J} - \frac{\boldsymbol{J}\boldsymbol{J}}{ne}\right)\right] = \boldsymbol{E} + \boldsymbol{V}\times\boldsymbol{B} - \frac{\boldsymbol{J}\times\boldsymbol{B}}{ne} - \frac{\nabla\cdot\bar{\mathbf{P}}_e}{ne} + \frac{m_e\nu_e}{e}\nabla^2\boldsymbol{J}, \tag{3.64}$$

where the electron pressure term is taken to be gyrotropic, electron viscosity has been included, and, for simplicity, the density is assumed uniform. Normalizing to some magnetic field B_0 and corresponding Alfvén velocity V_{A0}, spatial scale Δ, and

diffusive $\Delta^2/d_i V_A$ temporal scale, then 3.64 can be written

$$\begin{aligned} &\boldsymbol{E}' + \boldsymbol{V}' \times \boldsymbol{B}' - \frac{d_i}{\Delta}\left[\boldsymbol{J}' \times \boldsymbol{B}' - \frac{1}{2}\nabla' \cdot \bar{\beta}'_e\right] \\ &\quad = \frac{d_e^2}{\Delta^2}\left[\frac{d_i}{\Delta}\frac{\partial \boldsymbol{J}'}{\partial t'} + \nabla' \cdot \left(\boldsymbol{J}'\boldsymbol{V}' + \boldsymbol{V}'\boldsymbol{J}' - \frac{d_i}{\Delta}\boldsymbol{J}'\boldsymbol{J}'\right) - \frac{d_i}{\Delta}\nu'_e \nabla'^2 \boldsymbol{J}'\right], \end{aligned} \tag{3.65}$$

with the electron velocity is given by

$$\boldsymbol{V}'_e = \boldsymbol{V}' - \frac{d_i}{\Delta}\boldsymbol{J}', \tag{3.66}$$

where primed variables have been normalized.

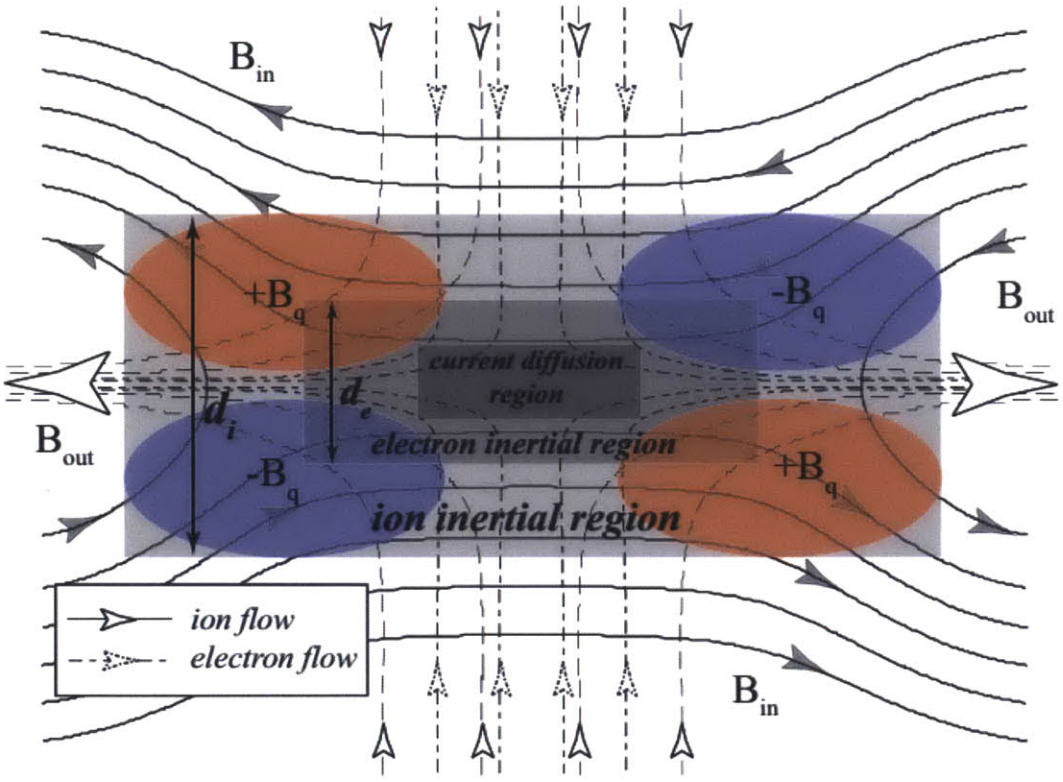

Figure 3-3: Schematic of two-fluid reconnection without guide-field with out-of-plane Hall magnetic field B_q. Here the viscous scale is assumed to be smaller than the electron inertial scale. (Ref [193]).

A two fluid reconnection region is depicted in Figure 3-3. At large scales with $\Delta \gg d_i$, the ions and electrons motion is strongly coupled since both $V'_i \simeq V'$ and $V'_e \simeq V' - J' d_i/\Delta \approx V'$. Magnetic field lines are frozen-in to both the electron and

ions fluids since 3.65 reduces to the scale invariant terms $\boldsymbol{E}' + \boldsymbol{V}' \times \boldsymbol{B}' \approx 0$. At the ion inertial scale where $\Delta \sim d_i$ (in the presence of a sufficient guide-field, the inertial scale is assumed to be $\Delta \sim \rho_s$ where $\rho_s = \sqrt{\beta_i} d_i$) ions and electrons decouple, with $V_e' \simeq V' - J'$. Ions are governed by charged fluid dynamics, while magnetic fields lines are frozen-in to the electron fluid. At the electron inertial scale $\Delta \sim d_e$, ions are nearly motionless compared to electrons with $V_i' \simeq V' \ll V_e' \simeq -J' d_i / d_e$, indicating the electron dynamics can be described by EMHD. At smaller scales is the current diffusion region, where 3.65 reduces to a forced convective-diffusion relation

$$\frac{\partial \boldsymbol{J}'}{\partial t'} - \nabla' \cdot (\boldsymbol{J}' \boldsymbol{J}') = \boldsymbol{E}' + \nu_e' \nabla'^2 \boldsymbol{J}'. \tag{3.67}$$

Simulations of two-fluid reconnection have found fast reconnection, independent of system size, with rates of order $M \sim .1$ [194–196]. This is on the order of rates observed during moderate to strong solar flares [197]. Note that the width of the current diffusion region is determined by the electron viscous scale δ_ν. If $\delta_\nu > d_e$, then the electron inertia region ceases to exist, and similarly, if $\delta_\nu > d_i$ the ion inertia region does not exist and reconnection proceeds in a Sweet-Parker manner.

In addition to allowing fast reconnection, the decoupling of ion and electron flow allows field and density structures to develop near the reconnection region not typically seen in collision-dominated single fluid plasmas. Out-of-plane quadrupolar magnetic field [125, 126], often called the Hall magnetic field, is generated by in-plane current loops produced by electrons flowing into and out of the reconnection region independent of ions. Hall magnetic fields are often used to diagnose weakly-collisional effects in laboratory [97] and magnetospheric [40, 41, 198, 199] plasma. The separation of electrons and ions can also generate an in-plane bipolar electric field, often call the Hall electric field, that has also been observed in the magnetosphere by spacecraft [33, 200, 201]. These fields are depicted in Figure 3-4. In the case of guide-field reconnection, the out-of-plane reconnecting electric field has a component parallel to the magnetic field, and this can also generate density cavities along the separators [202].

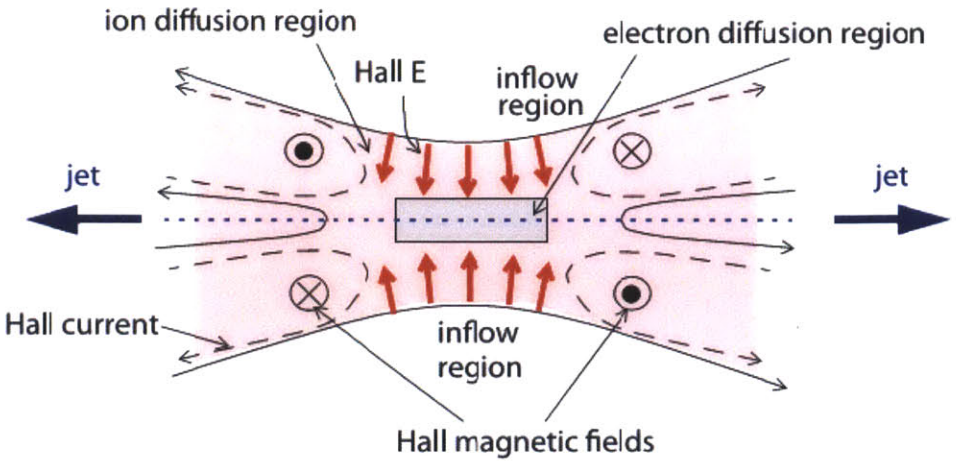

Figure 3-4: Diagram of fields within the ion dissipation (inertial) region. Jets represent plasma outflow while inflow is not depicted. (Ref [28]).

3.7 Summary

This chapter reviewed some concepts of steady state reconnection. In the ideal plasma limit, the Frozen-In Law constrains the evolution of magnetic field geometry. Non-ideal plasma may still preserve magnetic topology if the field evolution is governed by 3.19; otherwise magnetic field lines may be "broken" and magnetic reconnection can proceed. A simple picture of steady state reconnection is given by the Sweet-Parker model using single fluid MHD. The reconnection rate can be estimated, and while it is generally faster than diffusive evolution, the Sweet-Parker is much too slow to explain explosive reconnection observed in nature. Using similar arguments, the reconnection rate in EMHD can be much faster as it is independent of the global scales of the plasma, however, the validity of EMHD is limited to electron scales near the X-line. Two-fluid models of reconnection, which allow electron and ion motion to decouple at small scales, also allow fast reconnection, and influences the structure of the reconnection region.

Chapter 4

New Equations of State

This chapter introduces new Equations of State (EoS) derived by Egedal and Lê to properly account for the development of anisotropic electron pressure due to the trapping of electrons by electric and magnetic fields. This formulation is relevant to guide-field reconnection, where pressure anisotropy can having important consequences to the structure of the reconnection region. The EoS are first motivated by examining the evolution of the electron distribution function in a region of varying effective potential, after which the drift-kinetic equation is introduced and solved to lowest order. The EoS can be derived from moments of the solution. Finally, to ensure stable computer simulations, the EoS are modified to avoid the Firehose instability.

4.1 Anisotropic Electrons in Reconnection

Most fluid simulations rely on the assumption that, with the exception of near the X-line, electron pressure is nearly isotropic. However, in spacecraft observations and kinetic simulations, this is not often the case [47, 203–206] with strong electron pressure anisotropy ($p_{e\|} \gg p_{e\perp}$) developing in the reconnection region. Motivated by analysis of VTF experiments [103, 207, 208] and electron distributions observed by Wind spacecraft [5, 203], a new model of gyrotropic electron pressure has been derived [5,6] that accounts for the anisotropy due to the adiabatic trapping of electrons by electric and magnetic fields.

This model was derived by Egedal *et al.* [5] by considering the dynamics of magnetized electrons in a spatially and temporally varying effective potential, for example, when a magnetic flux tube expands as it approaches a reconnection region. Magnetic trapping can occur due the mirror effect where electrons are caught in a local minimum of the magnetic field density. In addition, a parallel electric field can create an effective potential (which is different from the electrostatic potential as the region has inductive fields) that could further trap electrons and produce strong parallel heating. Only particles with small velocity parallel to the magnetic field become trapped as the trapping wells develop slowly compared to a typical electron transit time of the region. Other particles are able to pass through, though their velocities change due to the electric and magnetic fields.

The effect of this process on the electron distribution in an expanded flux tube is illustrated in Figure 4-1. Passing particles (red and blue arrows) travel from one side to another, though they accelerate (decelerate) in the parallel direction as the enter (exit) the trapping region. In the region, the velocity distribution function of the passing electrons, which is assumed to be originally Maxwellian, is translated and distorted by fields. These particles are confined to regions of higher parallel velocity in phase space, shown by the red and blue shaded regions of the distribution function in Figure 4-1. Particles that become trapped (green double arrow) are also accelerated in the parallel direction, and occupy a larger extent of parallel velocity space in the trapping region, shown by the green shaded region of the distribution function in Figure 4-1. The net effect of the fields in this scenario is to increase parallel temperatures in the trapping region, indicated by the elongated distribution in Figure 4-1. This distribution has been used to develop Equations of State (EoS) for the anisotropic electron pressure by Lê *et al.* [6]. The details of this model, which are in excellent agreement with some spacecraft observations and kinetic simulations [5, 6, 203], will be discussed in section 4.3.

Strong parallel electric fields can be balanced by electron pressure anisotropy, and these fields can extend over macroscopic length scales [206], much greater than that allowed by Debye screening in isotropic plasmas. The value of this electric poten-

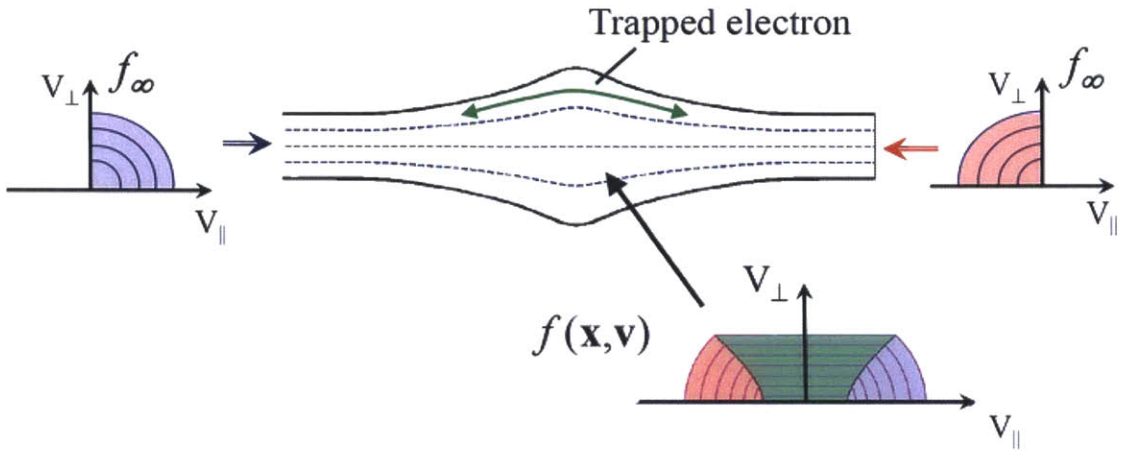

Figure 4-1: Development of anisotropic electron distribution in expanding flux tube. At the ends of the tube the distribution is isotropic but in the expanded region of the flux tube, electric and magnetic fields give rise to trapped particles and distorts passing particle distributions depicted in the distribution function at the bottom (Ref [209]).

tial can be inferred from observed electron distributions. An electron distribution observed by the Wind spacecraft during magnetotail reconnection is shown in Figure 4-2. Measured distribution density is depicted in color while the trapped-passing boundary is represented by the magenta lines. Theoretically predicted contour lines of constant density are in black. From the model, electric potentials of ~ 1 kV can be inferred. This model also accurately describes anisotropy in some kinetic simulations, as similar plots near a reconnection region of a kinetic simulation are shown in Figure 4-3d-g.

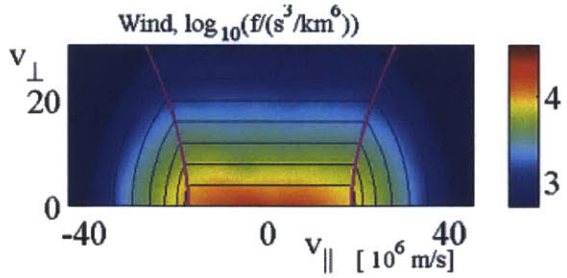

Figure 4-2: Color contour of electron distribution function measured by Wind spacecraft with overlaid with theoretically predicted isolines. The trapped passing boundary is represented by magenta lines (Ref [209]).

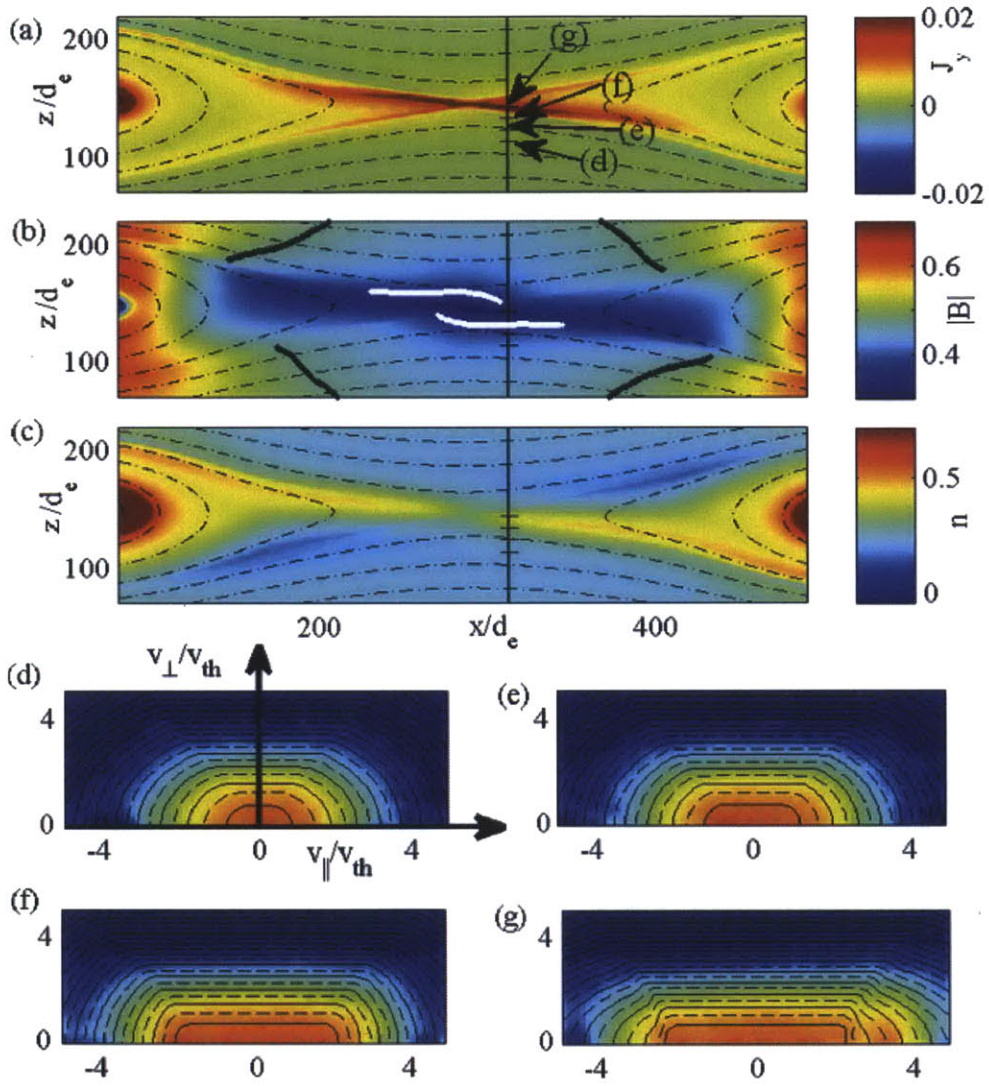

Figure 4-3: Particle-in-cell simulation of reconnection showing (a) out-of-plane current density, (b) magnetic field strength (with two isolines), and (c) density and the in-plane magnetic field lines (dashed lines). Distribution functions at locations (d-f) in (a) are shown below, with overlaid isolines of the theoretical predictions. (Ref [209]).

While the above arguments can be extended to heuristically determine the electron distribution function, a more rigorous formulation necessitates the introduction of the drift-kinetic equation.

4.2 The Drift-Kinetic Equation

Vlasov's equation can be solved to lowest order for the case of electrons in an expanding magnetic flux tube [5], which is analogous to an electron plasma approaching a reconnection site. The solution assumes the electrons remain magnetized, which is true as the electrons approach the reconnection region, and, in some cases, true throughout the reconnection regime [153].

The first step is to rewrite Vlasov's equation into a drift-kinetic form [210] that can take advantage of ordering relevant to reconnection. Starting with Vlasov's Equation (2.10)

$$\frac{\partial f}{\partial t} + \boldsymbol{v} \cdot \nabla f + \frac{Ze}{m}(\boldsymbol{E} + \boldsymbol{v} \times \boldsymbol{B}) \cdot \nabla_v f = 0, \tag{4.1}$$

cylindrical velocity-space coordinates $\left(v_\perp, \zeta, v_\parallel\right)$ can be introduced for $\boldsymbol{v} = \boldsymbol{v}_\parallel + \boldsymbol{v}_\perp = v_\parallel \hat{b} + v_\perp \hat{v}_\perp$. Radial and azimuthal vectors can be expressed using a local positive triplet $(\hat{e}_1, \hat{e}_2, \hat{b})$ and gyroangle ζ, such that

$$\hat{v}_\perp = \hat{e}_1 \cos\zeta + \hat{e}_2 \sin\zeta \qquad \text{and} \qquad \boldsymbol{\rho} = \hat{b} \times \frac{\boldsymbol{v}_\perp}{\Omega} = \rho\hat{\rho}.$$

Velocity-space coordinates can be changed from the parallel and perpendicular velocity to the first adiabatic invariant μ

$$\mu = \frac{mv_\perp^2}{2B} \tag{4.2}$$

and the particle energy $\mathcal{E}$

$$\mathcal{E} = \frac{mv^2}{2} + Ze\Phi, \tag{4.3}$$

where Φ is the electric potential. With these variables, Vlasov's equation can be

written as

$$\frac{\mathrm{D}f}{\mathrm{D}t} = \frac{\partial f}{\partial t} + \boldsymbol{v}\cdot\nabla f + \frac{\mathrm{d}\mu}{\mathrm{d}t}\frac{\partial f}{\partial \mu} + \frac{\mathrm{d}\mathcal{E}}{\mathrm{d}t}\frac{\partial f}{\partial \mathcal{E}} + \frac{\mathrm{d}\zeta}{\mathrm{d}t}\frac{\partial f}{\partial \zeta} = 0. \tag{4.4}$$

The time-derivative of the new velocity-space variables can be found by taking the dot product of the velocity-space acceleration equation

$$\frac{\mathrm{d}\boldsymbol{v}}{\mathrm{d}t} = \frac{\mathrm{d}}{\mathrm{d}t}\left(\boldsymbol{v}_\perp + v_\parallel \hat{b}\right) = \frac{Ze}{m}\boldsymbol{E} + \frac{Ze}{m}\boldsymbol{v}\times\boldsymbol{B} = \frac{Ze}{m}\boldsymbol{E} - v_\perp \Omega \hat{\rho} \tag{4.5}$$

with $m\boldsymbol{v}_\perp$, $m\boldsymbol{v}$, and $\hat{\rho}$. Dotting with $m\boldsymbol{v}_\perp$,

$$m\boldsymbol{v}_\perp \cdot \frac{\mathrm{d}}{\mathrm{d}t}\left(\boldsymbol{v}_\perp + v_\parallel \hat{b}\right) = \frac{\mathrm{d}}{\mathrm{d}t}\left(\frac{mv_\perp^2}{2}\right) + mv_\parallel \boldsymbol{v}_\perp \cdot \frac{\mathrm{d}\hat{b}}{\mathrm{d}t} = Ze\boldsymbol{v}_\perp \cdot \boldsymbol{E}, \tag{4.6}$$

and using

$$\frac{\mathrm{d}\mu}{\mathrm{d}t} = \frac{\mathrm{d}}{\mathrm{d}t}\left(\frac{mv_\perp^2}{2B}\right) = \frac{1}{B}\frac{\mathrm{d}}{\mathrm{d}t}\left(\frac{mv_\perp^2}{2}\right) - \frac{\mu}{B}\frac{\mathrm{d}B}{\mathrm{d}t}, \tag{4.7}$$

then

$$\frac{\mathrm{d}\mu}{\mathrm{d}t} = \frac{Ze}{B}\boldsymbol{v}_\perp \cdot \boldsymbol{E} - \frac{mv_\parallel}{B}\boldsymbol{v}_\perp \cdot \frac{\mathrm{d}\hat{b}}{\mathrm{d}t} - \frac{\mu}{B}\frac{\mathrm{d}B}{\mathrm{d}t}. \tag{4.8}$$

Dotting 4.5 with $m\boldsymbol{v}$ and using the time derivative of 4.3 yields

$$\frac{\mathrm{d}\mathcal{E}}{\mathrm{d}t} = Ze\left(\boldsymbol{v}\cdot\boldsymbol{E} + \frac{\mathrm{d}\Phi}{\mathrm{d}t}\right). \tag{4.9}$$

Finally, dotting 4.5 with $\hat{\rho}$ and using the definitions of $\hat{v}_\perp$ and $\hat{\rho}$, a short calculation yields

$$\hat{\rho}\cdot\frac{\mathrm{d}\boldsymbol{v}}{\mathrm{d}t} = v_\perp\frac{\mathrm{d}\zeta}{\mathrm{d}t} + v_\perp \hat{e}_2 \cdot \frac{\mathrm{d}\hat{e}_1}{\mathrm{d}t}\cos^2\zeta - v_\perp \hat{e}_1 \cdot \frac{\mathrm{d}\hat{e}_2}{\mathrm{d}t}\sin^2\zeta + v_\parallel \hat{\rho}\cdot\frac{\mathrm{d}\hat{b}}{\mathrm{d}t}, \tag{4.10}$$

so

$$\frac{\mathrm{d}\zeta}{\mathrm{d}t} = -\Omega + \frac{Ze}{mv_\perp}\hat{\rho}\cdot\boldsymbol{E} + \hat{e}_1\cdot\frac{\mathrm{d}\hat{e}_2}{\mathrm{d}t} - \frac{v_\parallel}{v_\perp}\hat{\rho}\cdot\frac{\mathrm{d}\hat{b}}{\mathrm{d}t}. \tag{4.11}$$

Putting the above expressions together, Vlasov's equation can now be written as

$$\frac{\partial f}{\partial t} + \boldsymbol{v}\cdot\nabla f + \left[\frac{Ze}{B}\boldsymbol{v}_\perp\cdot\boldsymbol{E} - \frac{mv_\parallel}{B}\boldsymbol{v}_\perp\cdot\frac{\mathrm{d}\hat{b}}{\mathrm{d}t} - \frac{\mu}{B}\frac{\mathrm{d}B}{\mathrm{d}t}\right]\frac{\partial f}{\partial \mu} + \left[Ze\left(\boldsymbol{v}\cdot\boldsymbol{E} + \frac{\mathrm{d}\Phi}{\mathrm{d}t}\right)\right]\frac{\partial f}{\partial \mathcal{E}} + \left[-\Omega + \frac{Ze}{mv_\perp}\hat{\rho}\cdot\boldsymbol{E} + \hat{e}_1\cdot\frac{\mathrm{d}\hat{e}_2}{\mathrm{d}t} - \frac{v_\parallel}{v_\perp}\hat{\rho}\cdot\frac{\mathrm{d}\hat{b}}{\mathrm{d}t}\right]\frac{\partial f}{\partial \zeta} = 0. \tag{4.12}$$

The next step is to introduce the gyro-average of a quantity Q

$$\langle Q\rangle = \frac{1}{2\pi}\int Q\mathrm{d}\zeta. \tag{4.13}$$

Then

$$\left\langle\frac{\mathrm{d}\mu}{\mathrm{d}t}\right\rangle = -\frac{\mu}{B}\frac{\partial B}{\partial t} \tag{4.14}$$

and

$$\left\langle\frac{\mathrm{d}\mathcal{E}}{\mathrm{d}t}\right\rangle = Ze\left[v_\parallel\hat{b}\cdot(\boldsymbol{E}+\nabla\Phi) + \frac{\partial\Phi}{\partial t}\right] = Ze\left[v_\parallel\hat{b}\cdot\boldsymbol{E}_{ind} + \frac{\partial\Phi}{\partial t}\right]. \tag{4.15}$$

Letting $f = \bar{f} + \tilde{f}$ where $\bar{f} = \langle f\rangle$ then 4.4 can be rewritten

$$\frac{\partial\bar{f}}{\partial t} + \boldsymbol{v}\cdot\nabla\bar{f} + \frac{\mathrm{d}\mu}{\mathrm{d}t}\frac{\partial\bar{f}}{\partial\mu} + \frac{\mathrm{d}\mathcal{E}}{\mathrm{d}t}\frac{\partial\bar{f}}{\partial\mathcal{E}} + \frac{\mathrm{D}\tilde{f}}{\mathrm{D}t} = 0. \tag{4.16}$$

The gyro-average of the above expression is the drift-kinetic equation introduced by Kulsrud [211]

$$\frac{\partial\bar{f}}{\partial t} + v_\parallel\hat{b}\cdot\nabla\bar{f} + \left\langle\frac{\mathrm{d}\mu}{\mathrm{d}t}\right\rangle\frac{\partial\bar{f}}{\partial\mu} + \left\langle\frac{\mathrm{d}\mathcal{E}}{\mathrm{d}t}\right\rangle\frac{\partial\bar{f}}{\partial\mathcal{E}} + \left\langle\frac{\mathrm{D}\tilde{f}}{\mathrm{D}t}\right\rangle = 0 \tag{4.17}$$

and taking their difference

$$\boldsymbol{v}_\perp\cdot\nabla\bar{f} + \left(\frac{\mathrm{d}\mu}{\mathrm{d}t} - \left\langle\frac{\mathrm{d}\mu}{\mathrm{d}t}\right\rangle\right)\frac{\partial\bar{f}}{\partial\mu} + \left(\frac{\mathrm{d}\mathcal{E}}{\mathrm{d}t} - \left\langle\frac{\mathrm{d}\mathcal{E}}{\mathrm{d}t}\right\rangle\right)\frac{\partial\bar{f}}{\partial\mathcal{E}} + \frac{\mathrm{D}\tilde{f}}{\mathrm{D}t} - \left\langle\frac{\mathrm{D}\tilde{f}}{\mathrm{D}t}\right\rangle = 0. \tag{4.18}$$

The drift-kinetic equation 4.17 is the gyro-average of Vlasov's equation 4.1. In certain scenarios, the drift-kinetic equation can be solved to obtain a species distribu-

tion function, providing fluid closure. In the next section, it is shown that in physical regimes relevant to magnetic reconnection, the drift-kinetic equation for the electrons can be solved, to lowest order, yielding the even part of the electron distribution function. The new EoS are calculated from the moments of the distribution function.

4.3 New Electron Equations of State

Following the analysis by Egedal *et al.* [209], we introduce an ordering relevant to electrons passing through an expanding flux tube

$$\nabla_\perp \sim \frac{1}{d}, \quad \nabla_\parallel \sim \frac{1}{L}, \quad v_\parallel \sim v_{Te}, \quad v_\perp \sim v_D, \quad \frac{\rho_e}{d} \sim \frac{d}{L} \sim \delta, \quad \frac{v_D}{v_{Te}} \sim \delta^2$$

$$\frac{\partial}{\partial t} \sim \frac{v_D}{d} \sim \delta \frac{v_{Te}}{L} \sim \delta^3 \Omega_e.$$

Here ρ_e is the electron gyro-radius, $v_D \sim E/B$ is the perpendicular drift velocity, and, v_{Te} the electron thermal velocity. Using this ordering,

$$\left\langle \frac{\mathrm{D}\tilde{f}}{\mathrm{D}t} \right\rangle \sim \delta^2 \Omega_e \tilde{f}$$

and using 4.18 reveals the ordering $\tilde{f} \sim \delta^2 \bar{f}$. Then at lowest order, the drift-kinetic equation 4.17 reduces to

$$v_\parallel \hat{b} \cdot \nabla \bar{f}_0 - e v_\parallel \hat{b} \cdot \boldsymbol{E}_{ind} \frac{\partial \bar{f}_0}{\partial \mathcal{E}} = 0, \tag{4.19}$$

where for electrons $Z = -1$ and $\boldsymbol{E}_{ind}$ is the inductive electric field. Introducing an acceleration potential $\Phi_\parallel$ such that

$$-\hat{b} \cdot \nabla \Phi_\parallel = \hat{b} \cdot \boldsymbol{E}_{ind}. \tag{4.20}$$

Then the general solution to 4.19 is $g(\mathcal{E} - e\Phi_\parallel)$ for any differentiable function g. If the electron distribution function is $f_\infty(\mathcal{E}_\parallel, \mathcal{E}_\perp)$ at the boundary of the flux tube, where

$\mathcal{E}_\parallel = mv_\parallel^2/2$ and $\mathcal{E}_\perp = mv_\perp^2/2$ then the solution is

$$f_0(\mathcal{E}_\parallel, \mathcal{E}_\perp) = f_\infty(\mathcal{E} - \mu B_\infty - e\Phi_\parallel, \mu B_\infty) \tag{4.21}$$

for electrons that pass through this region. Electrons can also be trapped in the developing magnetic potential well of an expanding flux tube. For this to occur, the initial transit time of these electrons should be less than the development time of the system, which is the inverse of the characteristic rate of change; denoting v_θ as the maximum transit velocity of trapped electrons then

$$\frac{d}{v_D} \sim \frac{L}{v_\theta} \Rightarrow v_\parallel \sim v_\theta \sim \delta v_{Te}. \tag{4.22}$$

Therefore, in the present ordering, trapped particles are characterized as having zero initial parallel energy. Then the distribution function for trapped electrons is

$$f_0(\mathcal{E}_\parallel, \mathcal{E}_\perp) = f_\infty(0, \mu B_\infty). \tag{4.23}$$

Finally, for an isotropic electron distribution at the boundary of the flux tube, 4.21 and 4.23 reduces to

$$f_0(\mathcal{E}_\parallel, \mathcal{E}_\perp) = \begin{cases} f_\infty(\mathcal{E} - e\Phi_\parallel), & \text{passing} \\ f_\infty(\mu B_\infty), & \text{trapped} \end{cases} \tag{4.24}$$

with the condition for passing electrons

$$\mathcal{E} - \mu B_\infty - e\Phi_\parallel \geq 0. \tag{4.25}$$

Assuming a Maxwellian electron distribution at the boundary of the flux tube, then

$$f_\infty = \frac{n_\infty}{(\sqrt{\pi} v_T)^3} e^{-v^2/v_T^2}, \tag{4.26}$$

where the electron temperature $T_{e\infty} = 1/2 m_e v_T^2$. The electron distribution function

for passing particles can then be written as

$$f_0(v_\parallel, v_\perp) = \frac{n_\infty}{\left(\sqrt{\pi} v_T\right)^3} e^{-v^2/v_T^2} e^{e\Phi_\parallel/T_e} \qquad \text{passing,} \tag{4.27}$$

and for trapped

$$f_0(v_\parallel, v_\infty) = \frac{n_\infty}{\left(\sqrt{\pi} v_T\right)^3} e^{-v_\perp^2 B_\infty/v_T^2 B} \qquad \text{trapped.} \tag{4.28}$$

In general the trapped-passing boundary condition can be written as

$$v_{b\parallel} = \sqrt{v_\Phi^2 + v_\perp^2 \left(\frac{B_\infty}{B} - 1\right)}, \tag{4.29}$$

where $v_\Phi^2 \equiv 2e\Phi/m_e$. The spatial density of this distribution is the given by

$$n = \int_0^\infty \mathrm{d}v_\perp \int_{v_{b\parallel}}^\infty 4\pi v_\perp f_{passing} \mathrm{d}v_\parallel + \int_0^\infty \mathrm{d}v_\perp \int_0^{v_{b\parallel}} 4\pi v_\perp f_{trapped} \mathrm{d}v_\parallel. \tag{4.30}$$

Let $h^2 = e\Phi_\parallel/T_e = v_\Phi^2/v_T^2$, $u_{b\parallel} = v_{b\parallel}/v_T$, $u_\perp = v_\perp/v_T$, $\tilde{n} = n/n_\infty$, and $\tilde{B} = B/B_\infty$ then integrating over $v_\parallel$ and dividing by n_∞ yields

$$\tilde{n} = \int_0^\infty \mathrm{d}u_\perp e^{h^2} \Big[1 - \mathrm{erf}(u_{b\parallel})\Big] 2u_\perp e^{-u_\perp^2} + \int_0^\infty \mathrm{d}u_\perp \left(\frac{2}{\sqrt{\pi}} u_{b\parallel}\right) 2u_\perp e^{-u_\perp^2/\tilde{B}}. \tag{4.31}$$

The parallel pressure can be calculated from the $m_e v_\parallel^2 = 2u_\parallel^2 T_e$ moment of the distribution, which, after integrating over $u_\parallel$ and dividing by $p_0 = n_\infty T_e$ yields

$$\begin{aligned} \tilde{p}_\parallel = \int_0^\infty \mathrm{d}u_\perp e^{h^2} \left[\frac{2}{\sqrt{\pi}} u_{b\parallel} e^{-u_{b\parallel}^2} + 1 - \mathrm{erf}\left(u_{b\parallel}\right)\right] 2u_\perp e^{-u_\perp^2} \\ + \int_0^\infty \mathrm{d}u_\perp \left(\frac{4}{3\sqrt{\pi}} u_{b\parallel}^3\right) 2u_\perp e^{-u_\perp^2/\tilde{B}} \end{aligned} \tag{4.32}$$

and the perpendicular pressure, which is calculated from the $1/2 m_e v_\perp^2 = u_\perp^2 T_e$ moment, yields

$$\tilde{p}_\perp = \int_0^\infty \mathrm{d}u_\perp e^{h^2} \Big[1 - \mathrm{erf}(u_{b\parallel})\Big] 2u_\perp^3 e^{-u_\perp^2} + \int_0^\infty \mathrm{d}u_\perp \left(\frac{2}{\sqrt{\pi}} u_{b\parallel}\right) 2u_\perp^3 e^{-u_\perp^2/\tilde{B}}, \tag{4.33}$$

where $\tilde{p}_\parallel = p_\parallel/p_0$ and $\tilde{p}_\perp = p_\perp/p_0$. Before presenting the new EoS, it is useful to examine the solution in the weak magnetic trapping regime ($\tilde{B} \simeq 1$). The trapped passing boundary becomes

$$u_{b\parallel} \simeq h. \tag{4.34}$$

The density is

$$\tilde{n} = e^{h^2}\Big(1 - \mathrm{erf}(h)\Big) + \frac{2}{\sqrt{\pi}} h\tilde{B}, \tag{4.35}$$

while the parallel and perpendicular pressures can be written as

$$\tilde{p}_\parallel = \tilde{n} + \frac{2}{\sqrt{\pi}} h\left(1 - \tilde{B}\right) + \frac{4}{3\sqrt{\pi}} h^3\tilde{B} \tag{4.36}$$

and

$$\tilde{p}_\perp = \tilde{n} + \frac{2}{\sqrt{\pi}} h\tilde{B}\left(\tilde{B} - 1\right). \tag{4.37}$$

Further, assuming weak electric trapping ($h \ll 1$) the density can be expressed as

$$\ln\tilde{n} = h^2 + \ln\left[1 + \frac{2h}{\sqrt{\pi}} \sum_{k=0}^{\infty} \frac{(-1)^k}{k!} \frac{2k\tilde{B}}{2k+1} h^{2k}\right]. \tag{4.38}$$

Then, to lowest order, the pressures are given by $\tilde{p}_\parallel = \tilde{p}_\perp = \tilde{n}$ that is, the pressure is isothermal. This is due to the majority of electrons can pass through the flux tube, allowing for high heat conductivity.

In the strong trapping limit, $h \gg 1$, and the density can be expressed as

$$\tilde{n} = \frac{2\tilde{B}}{\sqrt{\pi}} h + \frac{1}{h\sqrt{\pi}} \sum_{k=0}^{\infty} \frac{(2k)!}{4^k k!} \frac{1}{h^{2k}}. \tag{4.39}$$

To lowest order, $h = \sqrt{\pi}\tilde{n}/2\tilde{B}$ and the pressures are

$$\tilde{p}_\parallel = \frac{\pi}{6} \frac{\tilde{n}^3}{\tilde{B}^2} \qquad \text{and} \qquad \tilde{p}_\perp = \tilde{n}\tilde{B}.$$

In the strong trapping limit, the pressures resemble the CGL closure. In this limit, the majority of electrons are trapped by the acceleration potential, causing the elec-

tron to have very low heat conductivity. Based on these to limits, it is apparent that the development of an acceleration potential allows the electron pressure to transition from the isothermal limit to the CGL limit. To obtain the new EoS, the electron pressure distribution can be integrated using 4.29 the general trapped-passing boundary condition to find an expression for the density $\tilde{n}(\Phi_\parallel, \tilde{B})$, which can be inverted for the acceleration potential

$$\tilde{n} = \tilde{n}(\Phi_\parallel, \tilde{B}) \rightarrow \Phi_\parallel(\tilde{n}, \tilde{B}). \tag{4.40}$$

This expression can then be used to express the parallel and perpendicular pressures as functions of the density and the magnetic field

$$\tilde{p}_\parallel = \tilde{p}_\parallel(\Phi_\parallel(\tilde{n}, \tilde{B}), \tilde{B}) \rightarrow \tilde{p}_\parallel(\tilde{n}, \tilde{B}) \tag{4.41}$$

$$\tilde{p}_\perp = \tilde{p}_\parallel(\Phi_\parallel(\tilde{n}, \tilde{B}), \tilde{B}) \rightarrow \tilde{p}_\perp(\tilde{n}, \tilde{B}). \tag{4.42}$$

This procedure was done numerically [6] and the resulting expressions for the electron pressures were fitted as

$$\tilde{p}_\parallel = \frac{\tilde{n}}{1 + \frac{1}{2}\alpha} + \frac{\pi}{6}\frac{\alpha}{1 + \frac{1}{2\alpha}} \tag{4.43}$$

$$\tilde{p}_\perp = \frac{\tilde{n}}{1 + \alpha} + \frac{\tilde{n}\tilde{B}}{1 + \frac{1}{\alpha}}, \tag{4.44}$$

where

$$\alpha = \frac{\tilde{n}^3}{\tilde{B}^2}. \tag{4.45}$$

Notice that for small α, the pressure fit approaches the isotropic limit, and for high α, the pressure fit approaches the CGL limit. These EoS have also been shown to match the parallel and perpendicular electron pressures in kinetic simulations of magnetic reconnection, which solve the relativistic Boltzmann Equation [6]. In addition, the electron distributions on which the equations were based match distributions measured by spacecraft during magnetic reconnection [5].

Thus far, solving the drift-kinetic equation to lowest order for the distribution

function of electrons in an expanding flux tube yielded new EoS that closed the diagonal terms of the electron fluid pressure. This closure allows pressure anisotropy to develop, as seen in kinetic simulations. However, these equations allow this anisotropy to increase without bound, such that the system can become unstable. The next section will discuss this instability, the Firehose Instability, and modifications to the EoS to maintain stability.

4.4 Modified Equations of State

A notable feature of the new EoS is that the pressure is allowed to be anisotropic. For low $\tilde{B}$, α is large and $\tilde{p}_{\parallel} \gg \tilde{p}_{\perp}$, which can lead to the Firehose Instability. This instability is similar to the erratic motion observed after perturbing of a gardenhose (or firehose) with rapid water flow.

The instability condition can be found using linear theory for an incompressible, isothermal, ideal MHD plasma with electron pressure anisotropy. This ion motion can be modeled as

$$\nabla \cdot \boldsymbol{V} = 0 \tag{4.46}$$

$$mn\frac{\mathrm{d}\boldsymbol{V}}{\mathrm{d}t} = \boldsymbol{J} \times \boldsymbol{B} - \nabla\left(nT_i + p_{e\perp}\right) - \nabla \cdot \left[\left(p_{e\parallel} - p_{e\perp}\right)\hat{b}\hat{b}\right] \tag{4.47}$$

and combined with Ideal MHD equations

$$\boldsymbol{E} + \boldsymbol{V} \times \boldsymbol{B} = 0$$

$$\nabla \cdot \boldsymbol{B} = 0$$

$$\frac{\partial \boldsymbol{B}}{\partial t} = -\nabla \times \boldsymbol{E}$$

$$\nabla \times \boldsymbol{B} = \mu_0 \boldsymbol{J}$$

to describe the system. From the incompressible flow condition 4.46, the number density n is constant. Each quantity can be expanded as $Q \simeq Q_0 + Q_1$ where Q_0 is the equilibrium value, Q_1 the perturbed value, and $Q_0 \gg Q_1$. If spatial variations

are only along the equilibrium magnetic field $\boldsymbol{B}_0$ and since $\nabla \cdot \boldsymbol{B}_1 = 0$, $\boldsymbol{B}_0 \cdot \boldsymbol{B}_1 = 0$. For an homogeneous equilibrium with no plasma flow, using the relation $\boldsymbol{J} \times \boldsymbol{B} = \nabla \cdot \boldsymbol{B}\boldsymbol{B}/\mu_0 - \nabla B^2/2\mu_0$, the first order momentum equation 4.47 can be rewritten as

$$mn_0 \frac{\partial \boldsymbol{V}_1}{\partial t} = \left(1 - \mathscr{F}_e\right) \frac{\boldsymbol{B}_0 \cdot \nabla \boldsymbol{B}_1}{\mu_0}, \tag{4.48}$$

where $\mathscr{F}$ is the Firehose ratio

$$\mathscr{F}_s = \frac{p_{s\parallel} - p_{s\perp}}{B^2/\mu_0}. \tag{4.49}$$

Combing Faraday's Law and the Ideal Ohm's law yields

$$\frac{\partial \boldsymbol{B}_1}{\partial t} = \nabla \times (\boldsymbol{V}_1 \times \boldsymbol{B}_0) \Rightarrow \frac{\partial \boldsymbol{B}_1}{\partial t} = \boldsymbol{B}_0 \cdot \nabla \boldsymbol{V}_1. \tag{4.50}$$

Assuming wave like perturbations, $Q_1 = \check{Q}_1 \exp[i(k_\parallel \cdot \boldsymbol{x} - \omega t)]$, then expressions 4.48 and 4.50 admit the dispersion relation

$$\omega^2 = v_A^2 \left(1 - \mathscr{F}_e\right) k_\parallel^2. \tag{4.51}$$

Parallel pressure anisotropy tends to slow Alfvén waves, and when $\mathscr{F} > 1$ the waves become unstable. Then the Firehose Instability condition is

$$p_{e\parallel} - p_{e\perp} - \frac{B^2}{2\mu_0} \geq 0, \tag{4.52}$$

where equality represents the point when the tension force along magnetic field lines goes to zero.

The Firehose instability tends to cause kinks in magnetic field lines. Particles then scatter due to these kinks, which decreases the anisotropy, which will decrease or quench the instability (Drake 2012). However, the physics of particle scattering due to magnetic geometry is not included in the new EoS, so the instability would grow unabated in fluid models that include this electron closure.

The EoS can be modified to limit the Firehose ratio such that $\mathscr{F} \leq 1$. The value

of α in equations 4.43 and 4.44, which directly correlates the Firehose ratio, can be bounded by limiting the $\tilde{n}$ used in its calculation. This amounts to changing α to

$$\alpha = g(\tilde{n}^3, \tilde{n}_M^3) f_B(\tilde{B}), \tag{4.53}$$

where $\tilde{n}_M$ is the limiting value of the density, $g(x, y)$ is a function that returns the minimum value of x and y, and $f_B(\tilde{B}) = 1/\tilde{B}^2$ from above. The minimum value function can be approximated as

$$g(x, y) = \frac{xy}{(x^p + y^p)^{1/p}}, \tag{4.54}$$

where $p = 2$. The limiting value, $\tilde{n}_M$, can be found using the large α limit of the EoS in the Firehose condition. In this limit, $\tilde{p} \simeq B^2/\mu_0$, then

$$\frac{\pi}{6} \tilde{n}_M^3 f_B(\tilde{B}) n_0 T_e = \frac{B^2}{\mu_0} \tag{4.55}$$

and

$$\tilde{n}_M^3 = \frac{6}{\pi} \frac{\tilde{B}^2}{f_B} \frac{B_0^2}{\mu_0 n_0 T_e} N_f^3, \tag{4.56}$$

where N_f^3 is a scalar factor that can be used to further capture adjust the limit.

This ad-hoc fix removes the Firehose instability in the case of $\alpha \gg 1$ but allows the instability in the limit $\alpha \ll 1$ while $\tilde{n} \gg 1$ or $\tilde{B} \ll 1$. In this case, $\tilde{n} > \tilde{n}_M$, $\tilde{p}_\parallel - \tilde{p}_\perp \simeq 1/2\tilde{n}\alpha$ the Firehose instability condition is

$$p_\parallel - p_\perp - \frac{B^2}{\mu_0} \simeq \left(\frac{3}{\pi} \tilde{n} N_f^3 - 1 \right) \frac{B^2}{\mu_0} \geq 0, \tag{4.57}$$

which can be easily satisfied when $\tilde{n} > \pi/3N_f^3$. A simple fix for this instability regime is to change the isotropic term of the perpendicular pressure to match that of the parallel pressure in the EoS. Finally, it is desirable that for $\tilde{n} = \tilde{B} = 1$, $\tilde{p}_\perp = 1$. This can be implemented by modifying the denominator of the CGL term of the

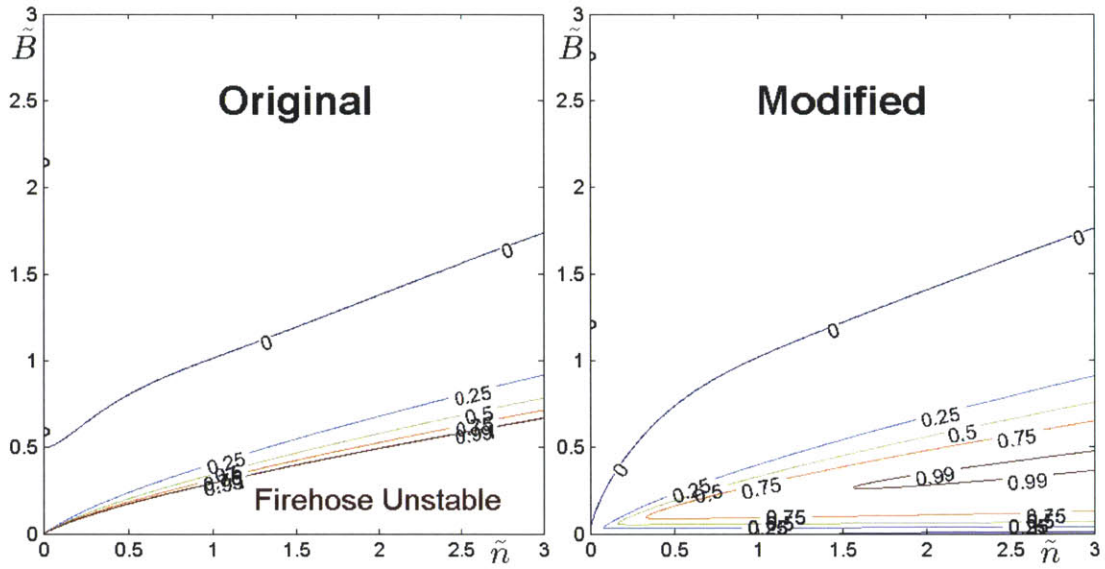

Figure 4-4: Contour plot of the Firehose ratio for the (a) original and (b) modified equations of state as a function of $\tilde{n}$ along the horizontal axis and $\tilde{B}$ along the vertical axis

perpendicular pressure. Summarizing, the modified EoS can be written as

$$\tilde{p}_\perp = \frac{\tilde{n}}{1+\frac{1}{2}\alpha} + \frac{\tilde{n}\tilde{B}}{1+\frac{2}{\alpha}} \tag{4.58}$$

$$\tilde{p}_\parallel = \frac{\tilde{n}}{1+\frac{1}{2}\alpha} + \frac{\pi}{6}\frac{\alpha}{1+\frac{1}{2\alpha}}, \tag{4.59}$$

where

$$\alpha = \frac{\tilde{n}^3\tilde{n}_M^3}{\sqrt{\tilde{n}^6+\tilde{n}_M^6}}\frac{1}{\tilde{B}^2} \tag{4.60}$$

and

$$\tilde{n}_M^3 \doteq \frac{12}{\pi\beta_{e0}}\tilde{B}^4 N_f^3, \tag{4.61}$$

with $\beta_{e0} = 2\mu_0 n_0 T_e/B_0^2$. Figure 4-4 shows contour plots of the Firehose ratio for the original (a) and modified (b) EoS as functions of $\tilde{n}$ and $\tilde{B}$. The original equations are firehose unstable for low $\tilde{B}$, the bottom region of the plot. The modified EoS, however, are stable for all $\tilde{n}$ and $\tilde{B}$. Contours of low $\mathscr{F}$ are not strongly affected by the modifications.

4.5 Summary

This chapter discussed new Equations of State (EoS) that describe the development of electron pressure anisotropy due to the adiabatic trapping of magnetized electrons in an expanding magnetic flux tube. The EoS can be derived by closing the electron fluid using the lowest-order solution of the drift-kinetic equation, as described by Egedal. These EoS were then modified to avoid the firehose instability, which goes unabated in this fluid formulation. Using the EoS, the anisotropic fluid model that will be used in this dissertation, including optional resistivity, can be summarized below:

$$\frac{\mathrm{d}n}{\mathrm{d}t} + n\nabla\cdot\boldsymbol{V} = 0 \tag{4.62}$$

$$mn\frac{\mathrm{d}\boldsymbol{V}}{\mathrm{d}t} = \boldsymbol{J}\times\boldsymbol{B} - \nabla p_i - \nabla p_{e\perp} - \nabla\cdot\left[\left(p_{e\parallel}-p_{e\perp}\right)\hat{b}\hat{b}\right] - \nabla\cdot\bar{\boldsymbol{\Pi}}_V \tag{4.63}$$

$$\frac{\mathrm{d}p_i}{\mathrm{d}t} + \frac{5}{3}p_i\nabla\cdot\boldsymbol{V} + \frac{2}{3}\bar{\boldsymbol{\Pi}}_V : \nabla\boldsymbol{V} = \frac{2}{3}\nabla\cdot\left(n\kappa\nabla\frac{p_i}{n}\right) \tag{4.64}$$

$$\begin{aligned}\boldsymbol{E}+\boldsymbol{V}\times\boldsymbol{B} = \frac{1}{ne}\Big\{\boldsymbol{J}\times\boldsymbol{B} - \nabla p_{e\perp} - \nabla\cdot\left[\left(p_{e\parallel}-p_{e\perp}\right)\hat{b}\hat{b}\right] - \nabla\cdot\bar{\boldsymbol{\Pi}}_J\Big\} \\ + \frac{m_e}{e}\frac{\partial}{\partial t}\left(\frac{\boldsymbol{J}}{ne}\right) - \frac{m_e}{e}\frac{\boldsymbol{J}}{ne}\cdot\nabla\frac{\boldsymbol{J}}{ne} + \eta_R\boldsymbol{J}\end{aligned} \tag{4.65}$$

$$\frac{\partial\boldsymbol{B}}{\partial t} = -\nabla\times\boldsymbol{E} \tag{4.66}$$

$$\mu_0\boldsymbol{J} = \nabla\times\boldsymbol{B} \tag{4.67}$$

$$\frac{p_{e\perp}}{p_0} = \frac{\tilde{n}}{1+\frac{1}{2}\alpha} + \frac{\tilde{n}\tilde{B}}{1+\frac{2}{\alpha}} \tag{4.68}$$

$$\frac{p_{e\parallel}}{p_0} = \frac{\tilde{n}}{1+\frac{1}{2}\alpha} + \frac{\pi}{6}\frac{\alpha}{1+\frac{1}{2\alpha}} \tag{4.69}$$

where

$$\alpha = \frac{\tilde{n}^3\tilde{n}_M^3}{\sqrt{\tilde{n}^6+\tilde{n}_M^6}}\frac{1}{\tilde{B}^2} \tag{4.70}$$

and

$$\tilde{n}_M^3 = \frac{12}{\pi\beta_{e0}}\tilde{B}^4N_f^3 \tag{4.71}$$

where

$$\bar{\mathbf{\Pi}}_U = -m_U n \nu_U \left[\nabla \boldsymbol{U} + (\nabla \boldsymbol{U})^T - \frac{2}{3} (\nabla \cdot \boldsymbol{U}) \bar{\mathbf{I}} \right] \tag{4.72}$$

with $m_U = m$, $\nu_U = \nu_i$ and $\boldsymbol{U} = \boldsymbol{V}$ for $\bar{\mathbf{\Pi}}_V$ and $\nu_U = \nu_e$ and $\boldsymbol{U} = -\boldsymbol{J}/ne$ for $\bar{\mathbf{\Pi}}_J$. The approximation $-\nabla \cdot \bar{\mathbf{\Pi}}_U = m_U n \nu_U \left(\nabla^2 \boldsymbol{U} + 1/3 \nabla \nabla \cdot \boldsymbol{U} \right)$ is used for simplicity. The isotropic fluid formulation has

$$\frac{p_{e\perp}}{p_0} = \frac{p_{e\parallel}}{p_0} = \tilde{n}. \tag{4.73}$$

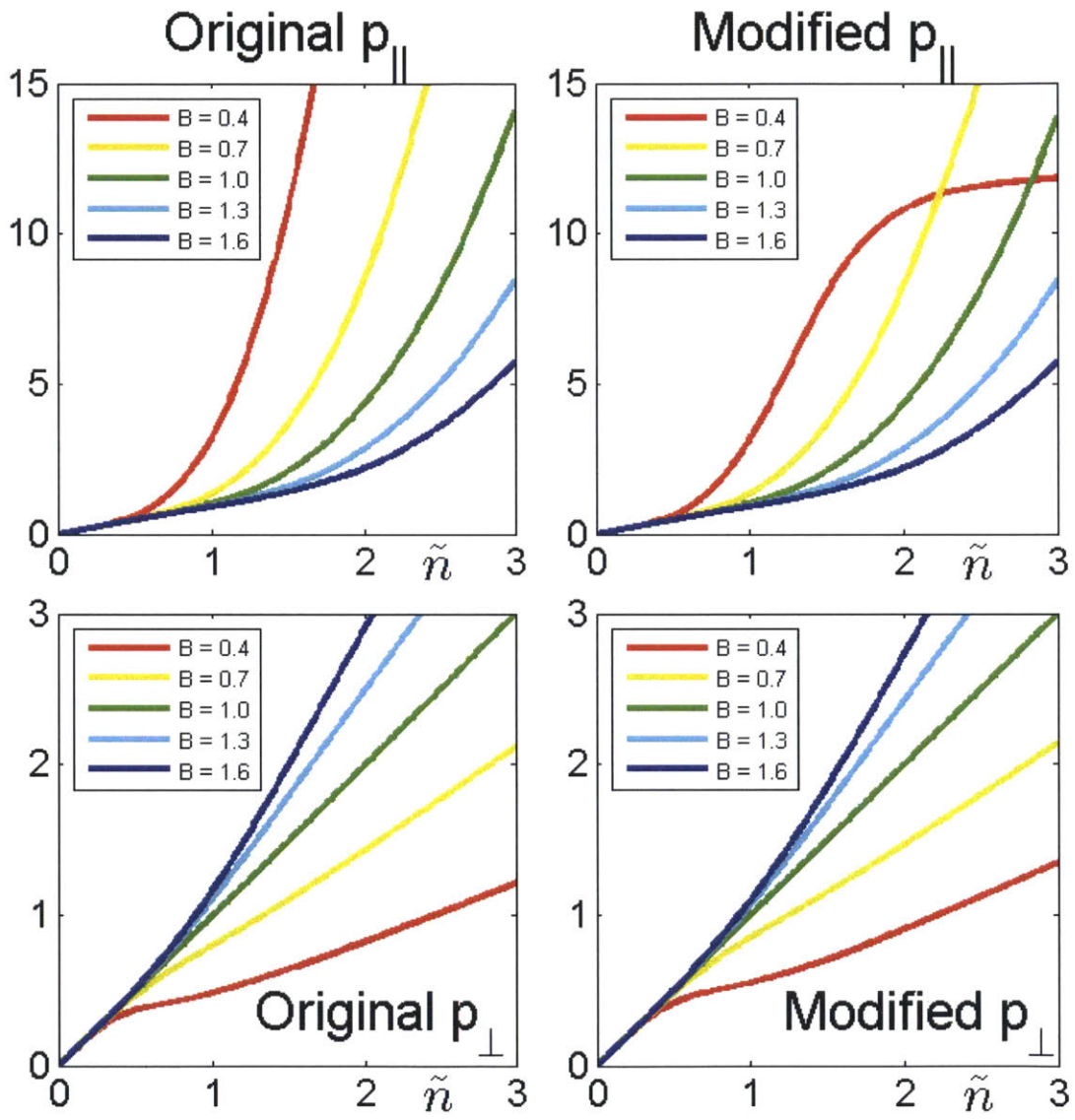

Figure 4-5: Plots of (a) the original parallel pressure (b) the original perpendicular pressure (c) the modified parallel pressure (d) the modified perpendicular pressure as a function of $\tilde{n}$ when $\tilde{B} = .4$ (red), .7 (yellow), 1.0 (green), 1.3 (cyan) and 1.6 (blue)

Chapter 5

Simulation Setup

This chapter describes the simulation systems used to model magnetic reconnection in this dissertation. Fluid simulations were built using the HiFi framework, which had been previously developed to solve coupled differential equations on massively parallel computer systems. The fluid model with the new Equations of State (EOS) is described as implemented in HiFi; the results of simulations of this model are compared to an isotropic model also implemented in HiFi and a kinetic simulation.

5.1 Description of HiFi Code Framework

The HiFi code framework was developed, in part, by Lukin [193,212] for solving systems of partial differential equations (PDEs) in arbitrary domains on large parallel computer systems using an implicit, high-order spectral element method. The publicly available Portable Extensible Toolkit for Scientific Computation (PETSc) [213] library is used to solve, in parallel, the large linear systems generated.

As described by Lukin, the system of M coupled PDEs to be solved for primary dependent variables $\{U(\boldsymbol{x},t)\}_{i=1,M}$ must be expressible in the flux-source form

$$\left\{\frac{\partial Q^k}{\partial t}+\nabla\cdot\boldsymbol{F}^k=S^k\right\}, \tag{5.1}$$

where

$$Q^k = \sum_{i=1,M} \left[A^{ki}(\boldsymbol{x}) + \boldsymbol{B}^{ki}(\boldsymbol{x}) \cdot \nabla \right] U^i, \tag{5.2}$$

$$\boldsymbol{F}^k = \boldsymbol{F}^k \left(t, \boldsymbol{x}, \left\{ U^i \right\}_{i=1,M}, \left\{ \nabla_{\mathbf{x}} U^i \right\}_{i=1,M} \right), \tag{5.3}$$

$$S^k = S^k \left(t, \boldsymbol{x}, \left\{ U^i \right\}_{i=1,M}, \left\{ \nabla_{\mathbf{x}} U^i \right\}_{i=1,M} \right), \tag{5.4}$$

and A^{ki}, $\boldsymbol{B}^{ki}$, $\boldsymbol{F}^k$, and S^k are arbitrary differentiable functions while $\boldsymbol{x}$ denotes a point in physical space. The physical space $\mathcal{X}$ in which the PDEs are expressed can be represented by a wide range of coordinate systems including those that yield grids of nonuniform density. This property allows the density of the physical grid to vary with the feature size of the solution, increasing computational efficiency. Computations are performed in a uniform, square "logical space" $\Xi = [0,1] \times [0,1]$, and physical geometries are implemented by specifying a mapping $\mathcal{M} : \Xi \to \mathcal{X}$.

Spatial discretization is handled using the spectral element method. The computational domain is subdivided into coarse elements; within each element, the primary dependent variables are represented by linear combination of a set of basis functions such that

$$U(\boldsymbol{x}(\boldsymbol{\xi}), t) = \sum u_i(t) \alpha_i(\boldsymbol{\xi}), \tag{5.5}$$

where $\boldsymbol{\xi}$ denotes a point in logical space. These functions are local to the element; they are zero in all other elements. This method allows for parallelization by domain decomposition and the exponential spatial convergence of spectral methods. In the HiFi code framework, two linear elements and the Jacobi polynomials up to order $n_p - 1$, with $n_p = 8$, are taken as the basis set $\lambda_j(\xi)$. The Jacobi polynomials are zeroed at the boundary of the element, while the linear elements are zeroed at opposite ends of the boundary. The linear elements ensure continuity and allow coupling of the solution across elements. The basis functions are formed by the Cartesian products of the basis set such that $\alpha_i(\boldsymbol{\xi}) = \lambda_j(\xi_1)\lambda_k(\xi_2)$. Multiplying 5.1 by α_i and, after integrating by parts and some manipulations, yields the matrix expression

$$\mathbb{M} \frac{\mathrm{d}\boldsymbol{u}}{\mathrm{d}t} = \mathbb{F}\left(t, \boldsymbol{u}\right), \tag{5.6}$$

where $\boldsymbol{u}$ are the coefficients of the expansion in 5.5. Also note that $\mathbb{F}$ depends on boundary conditions.

HiFi allows for many time advancement schemes, including the Crank-Nicholson method, which is the scheme used in this dissertation. In this method, equation 5.6 is discretized as

$$\mathbb{M}\left(\frac{\boldsymbol{u}^{n+1}-\boldsymbol{u}^{n}}{\Delta t}\right)=\frac{1}{2}\mathbb{F}\left(t+\Delta t,\boldsymbol{u}^{n+1}\right)+\frac{1}{2}\mathbb{F}\left(t,\boldsymbol{u}^{n}\right), \tag{5.7}$$

where $\Delta t \equiv t^{n+1}-t^{n}$ is the time step between the current time t^{n} and the next time point t^{n+1}, while $\boldsymbol{u}^{n}$ are the values of the expansion coefficients at t^{n} and $\boldsymbol{u}^{n+1}$ are the values at time point t^{n+1}. The expansion coefficients are implicitly defined in 5.7; they can be found using the Newton's Iteration Method. Defining $\boldsymbol{u}_{j}^{n+1}$ as the jth iteration of the expansion coefficients with $\boldsymbol{u}_{0}^{n+1}=\boldsymbol{u}^{n}$ and $\delta\boldsymbol{u}_{j}\equiv\boldsymbol{u}_{j+1}^{n+1}-\boldsymbol{u}_{j}^{n+1}$, letting

$$\mathbb{M}\boldsymbol{u}^{n+1}-\frac{\Delta t}{2}\mathbb{F}\left(t+\Delta t,\boldsymbol{u}^{n+1}\right)-\mathbb{M}\boldsymbol{u}^{n}-\frac{\Delta t}{2}\mathbb{F}\left(t,\boldsymbol{u}^{n}\right)\equiv\mathbf{R}\left(\boldsymbol{u}^{n+1}\right) \tag{5.8}$$

and

$$\left.\frac{\partial\mathbf{R}}{\partial\boldsymbol{u}}\right|_{(t+\Delta t,\boldsymbol{u}_{j}^{n+1})}=\mathbb{M}-\frac{\Delta t}{2}\left.\frac{\partial\mathbb{F}}{\partial\boldsymbol{u}}\right|_{(t+\Delta t,\boldsymbol{u}_{j}^{n+1})}\equiv\mathbb{J}, \tag{5.9}$$

equation 5.7 can be iterated as

$$\begin{aligned}\mathbf{R}\left(\boldsymbol{u}_{j}^{n+1}\right)+\mathbb{J}\delta\boldsymbol{u}_{j}\Rightarrow\delta\boldsymbol{u}_{j}&=\mathbb{J}^{-1}\mathbf{R}\left(\boldsymbol{u}_{j}^{n+1}\right)\\ \Rightarrow\boldsymbol{u}_{j+1}^{n+1}&=\boldsymbol{u}_{j}^{n+1}+\delta\boldsymbol{u}_{j}\\ j\Rightarrow j+1&\end{aligned} \tag{5.10}$$

until the condition $\left\|\mathbf{R}\left(\boldsymbol{u}_{j}^{n+1}\right)\right\|_{2}\leq n_{tol}\left\|\mathbf{R}\left(\boldsymbol{u}_{0}^{n+1}\right)\right\|_{2}$ is satisfied, where n_{tol} is a tolerance parameter. The time step Δt is dynamically adapted such that it increases if the iterations converge too quickly and decreases if too many iterations are required, increasing computational efficiency. Newton's iteration method also requires (approximately) inverting the matrix $\mathbb{J}$, which describes the coupling of the basis functions. However, since only basis functions that are linear in at least one direction couple

across elements, the static condensation procedure can be employed to separate these cross-element couplers from the element interiors. This reduces the size of the matrix and improves parallel efficiency. To use this procedure, $\mathbb{J}$ must be calculated explicitly by specifying the analytical derivatives of $\boldsymbol{F}^k$ and S^k with respect to $\{U^i\}_{i=1,M}$ and $\{\nabla_{\mathbf{x}} U^i\}_{i=1,M}$.

As noted before, boundary conditions are incorporated into 5.6. Quantities are advanced in time on the boundary and the interior in a single time step. However, boundary conditions are described by a separate system of PDEs. HiFi allows for many types of boundary conditions, including periodic, "natural", and "explicit-local" boundary conditions. A periodic condition ensures the left and right and/or top and bottom boundaries have the same value, which is determined by the interior PDE system. A natural condition evaluates the interior PDE at the boundary as well. In an explicit-local condition, the solution on the boundary satisfy the conditions

$$\left\{\left[A^{ki}\frac{\partial U^i}{\partial t} + \boldsymbol{B}^{ki}\cdot\nabla\left(\frac{\partial U^i}{\partial t}\right)\right] = S^k\right\}_{k=1,M} \tag{5.11}$$

$$S^k = S^k\left(t, \hat{n}, \boldsymbol{x}, \left\{U^i, \nabla_x U^i, \nabla_{xx} U^i\right\}_{i=1,M}\right), \tag{5.12}$$

where $A^{ki} = A^{ki}(\hat{n}, \boldsymbol{x})$, $\boldsymbol{B}^{ki} = \boldsymbol{B}^{ki}(\hat{n}, \boldsymbol{x})$, and S^k are arbitrary differentiable functions and $\hat{n}$ denotes and outward unit vector normal to the boundary. Robin boundary conditions are a case of the explicit-local conditions.

The HiFI framework provides a straight-forward platform for solving coupled non-linear PDEs using parallel computer systems. However, the equations to be solved must be expressible in the flux-source form 5.1. The next section details how to express a 2-D plasma model with the modified EoS in HiFi.

5.2 Plasma Model with Anisotropic Electron Pressure

Following from section 4.5, plasma dynamics can be modeled as

$$\frac{\mathrm{d}n}{\mathrm{d}t} + n\nabla\cdot\boldsymbol{V} = 0 \tag{5.13}$$

$$mn\frac{\mathrm{d}\boldsymbol{V}}{\mathrm{d}t} = \boldsymbol{J}\times\boldsymbol{B} - \nabla p_i - \nabla p_{e\perp} - \nabla\cdot\left[\left(p_{e\parallel}-p_{e\perp}\right)\hat{b}\hat{b}\right] - \nabla\cdot\bar{\boldsymbol{\Pi}}_V \tag{5.14}$$

$$\frac{\mathrm{d}p_i}{\mathrm{d}t} + \frac{5}{3}p_i\nabla\cdot\boldsymbol{V} + \frac{2}{3}\bar{\boldsymbol{\Pi}}_V : \nabla\boldsymbol{V} = \frac{2}{3}\nabla\cdot\left(n\kappa\nabla\frac{p_i}{n}\right) \tag{5.15}$$

$$\begin{aligned}\boldsymbol{E}+\boldsymbol{V}\times\boldsymbol{B} = \frac{1}{ne}\Big\{&\boldsymbol{J}\times\boldsymbol{B} - \nabla p_{e\perp} - \nabla\cdot\left[\left(p_{e\parallel}-p_{e\perp}\right)\hat{b}\hat{b}\right] - \nabla\cdot\bar{\boldsymbol{\Pi}}_J\Big\}\\ &+\frac{m_e}{e}\frac{\partial}{\partial t}\left(\frac{\boldsymbol{J}}{ne}\right) - \frac{m_e}{e}\frac{\boldsymbol{J}}{ne}\cdot\nabla\frac{\boldsymbol{J}}{ne} + \eta_R\boldsymbol{J}\end{aligned} \tag{5.16}$$

$$\frac{\partial\boldsymbol{B}}{\partial t} = -\nabla\times\boldsymbol{E} \tag{5.17}$$

$$\mu_0\boldsymbol{J} = \nabla\times\boldsymbol{B} \tag{5.18}$$

$$\frac{p_{e\perp}}{p_0} = \frac{\tilde{n}}{1+\frac{1}{2}\alpha} + \frac{\tilde{n}\tilde{B}}{1+\frac{2}{\alpha}} \tag{5.19}$$

$$\frac{p_{e\parallel}}{p_0} = \frac{\tilde{n}}{1+\frac{1}{2}\alpha} + \frac{\pi}{6}\frac{\alpha}{1+\frac{1}{2\alpha}}, \tag{5.20}$$

where

$$\alpha = \frac{\tilde{n}^3\tilde{n}_M^3}{\sqrt{\tilde{n}^6+\tilde{n}_M^6}}\frac{1}{\tilde{B}^2}, \tag{5.21}$$

$$\tilde{n}_M^3 = \frac{12}{\pi\beta_{e0}}\tilde{B}^4N_f^3, \tag{5.22}$$

$$\bar{\boldsymbol{\Pi}}_U = -m_Un\nu_U\left[\nabla\boldsymbol{U} + (\nabla\boldsymbol{U})^T - \frac{2}{3}(\nabla\cdot\boldsymbol{U})\,\bar{\mathbf{I}}\right], \tag{5.23}$$

with $m_U = m$, $\nu_U = \nu_i$ and $\boldsymbol{U} = \boldsymbol{V}$ for $\bar{\boldsymbol{\Pi}}_V$ and $\nu_U = \nu_e$ and $\boldsymbol{U} = -\boldsymbol{J}/ne$ for $\bar{\boldsymbol{\Pi}}_J$. Note the approximation $-\nabla\cdot\bar{\boldsymbol{\Pi}}_U \simeq m_Un\nu_U\left(\nabla^2\boldsymbol{U} + 1/3\nabla\nabla\cdot\boldsymbol{U}\right)$ is used for simplicity.

This system can be normalized by

$$n = n_0\tilde{n},\ \boldsymbol{B} = B_0\tilde{\boldsymbol{B}},\ \boldsymbol{V} = V_A\tilde{\boldsymbol{V}},\ \nabla = \frac{1}{d_i}\nabla',\ \frac{\partial}{\partial t} = \Omega_i$$

where n_0 is the background density, and B_0 is the upstream reconnecting field. Pressures are normalized to B_0^2/μ_0. Dissipation parameters are normalized as $\nu_i = V_A d_i \tilde{\nu}_i$, $\nu_e = V_A d_i \tilde{\nu}_e$, $\kappa = V_A d_i \tilde{\kappa}$, and $\eta_R = V_A d_i \mu_0 \tilde{\eta}_R$ and once again $\xi = m_e/m_i$. Combining 5.16 and 5.17, which disregards electron potential flow independent of ions, the model becomes

$$\frac{\partial \tilde{n}}{\partial \tilde{t}} + \nabla \cdot \left(\tilde{n}\tilde{\boldsymbol{V}}\right) \tag{5.24}$$

$$\frac{\partial \tilde{\boldsymbol{V}}}{\partial \tilde{t}} = -\tilde{\boldsymbol{V}} \cdot \nabla'\tilde{\boldsymbol{V}} + \frac{1}{\tilde{n}}\tilde{\boldsymbol{J}} \times \tilde{\boldsymbol{B}} - \frac{1}{\tilde{n}}\nabla\left(\tilde{p}_i + \tilde{p}_{e\perp}\right) - \frac{1}{\tilde{n}}\nabla \cdot \left(\mathscr{F}\tilde{\boldsymbol{B}}\tilde{\boldsymbol{B}}\right) + \tilde{\nu}_i\nabla'^2\tilde{\boldsymbol{V}} + \frac{1}{3}\tilde{\nu}_i\nabla\nabla \cdot \tilde{\boldsymbol{V}} \tag{5.25}$$

$$\frac{\partial \tilde{p}_i}{\partial \tilde{t}} + \tilde{\boldsymbol{V}} \cdot \nabla\tilde{p}_i + \frac{5}{3}\tilde{p}_i\nabla \cdot \tilde{\boldsymbol{V}} - \frac{2}{3}\tilde{n}\tilde{\nu}_i\left[\left(\nabla'\tilde{\boldsymbol{V}}\right)^2 + \nabla'\tilde{\boldsymbol{V}} : \left(\nabla'\tilde{\boldsymbol{V}}\right)^T - \frac{2}{3}\left(\nabla' \cdot \tilde{\boldsymbol{V}}\right)^2\right] = \frac{2}{3}\nabla' \cdot \left(\tilde{n}\tilde{\kappa}\nabla'\frac{\tilde{p}_i}{\tilde{n}}\right) \tag{5.26}$$

$$\frac{\partial}{\partial \tilde{t}}\left[\tilde{\boldsymbol{B}} + \xi\nabla' \times \frac{\tilde{\boldsymbol{J}}}{\tilde{n}}\right] = \nabla' \times \left\{\tilde{\boldsymbol{V}} \times \tilde{\boldsymbol{B}} - \frac{1}{\tilde{n}}\left[\tilde{\boldsymbol{J}} \times \left(\tilde{\boldsymbol{B}} + \xi\nabla' \times \frac{\tilde{\boldsymbol{J}}}{\tilde{n}}\right) - \nabla' \cdot \left(\mathscr{F}\tilde{\boldsymbol{B}}\tilde{\boldsymbol{B}}\right) - \nabla'\tilde{p}_{e\perp}\right] - \nabla' \times \left(\tilde{\eta}_R\tilde{\boldsymbol{B}} + \xi\tilde{\nu}_e\nabla' \times \frac{\tilde{\boldsymbol{J}}}{\tilde{n}}\right)\right\} \tag{5.27}$$

$$\tilde{\boldsymbol{J}} = \nabla' \times \tilde{\boldsymbol{B}}, \tag{5.28}$$

where $\mathscr{F}$ is the firehose ratio $\mu_0(p_{e\parallel} - p_{e\perp})/B_0^2$. For 2.5-dimensional magnetic reconnection with (x, y) as the in-plane cartesian coordinates, $\partial_z Q \equiv z \cdot \nabla Q = 0$ for any quantity Q. The magnetic field can therefore be written as

$$\tilde{\boldsymbol{B}} = \hat{z} \times \nabla'\tilde{\psi} + \tilde{\zeta}\hat{z}, \tag{5.29}$$

where the out-of-plane component of the magnetic vector potential is given by $\tilde{A}_z =$

$-\tilde{\psi}$. The requirement that dependent variables have at most second-order spatial derivatives necessitates the introduction of auxiliary dependent variables. Let

$$\tilde{\lambda} = \frac{\nabla'^2 \tilde{\psi}}{\tilde{n}} \tag{5.30}$$

$$\tilde{\chi} = \nabla' \cdot \left(\frac{\nabla' \tilde{\zeta}}{\tilde{n}} \right) \tag{5.31}$$

$$\tilde{\theta} = \frac{1}{2} \left(\nabla' \tilde{\psi} \right)^2 \tag{5.32}$$

and $\tilde{\boldsymbol{V}} = \tilde{u}\hat{x} + \tilde{v}\hat{y} + \tilde{w}\hat{z}$. Then the ten equations describing the ten dependent variables can be written in flux-source form:

$$M + \nabla' \cdot (F_1 \hat{x} + F_2 \hat{y}) = S \tag{5.33}$$

$\tilde{n}$:

$$M = \frac{\partial \tilde{n}}{\partial t} \tag{5.34}$$

$$F_1 = \tilde{n}\tilde{u} \tag{5.35}$$

$$F_2 = \tilde{n}\tilde{v} \tag{5.36}$$

$$S = 0 \tag{5.37}$$

$\tilde{u}$:

$$M = \frac{\partial \tilde{u}}{\partial t} \tag{5.38}$$

$$F_1 = -\frac{1}{3}\tilde{\nu}_i \left(4\tilde{u}_x + \tilde{v}_y \right) \tag{5.39}$$

$$F_2 = -\tilde{\nu}_i \tilde{u}_y \tag{5.40}$$

$$\begin{aligned} S = &-\tilde{u}\tilde{u}_x - \tilde{v}\tilde{u}_y - \frac{1}{\tilde{n}}\tilde{\zeta}\tilde{\zeta}_x - \left(1 - \mathscr{F}\right)\tilde{\lambda}\tilde{\psi}_x - \frac{1}{\tilde{n}}\left(\tilde{p}_{ix} + \tilde{p}_{e\perp x}\right) \\ &+ \frac{1}{\tilde{n}}\left(\mathscr{F}_y \tilde{\psi}_x - \mathscr{F}_x \tilde{\psi}_y\right)\tilde{\psi}_y - \frac{\mathscr{F}}{\tilde{n}}\tilde{\theta}_x \end{aligned} \tag{5.41}$$

$\tilde{v}$:

$$M = \frac{\partial \tilde{v}}{\partial t} \tag{5.42}$$

$$F_1 = -\tilde{\nu}_i \tilde{v}_x \tag{5.43}$$

$$F_2 = -\frac{1}{3}\tilde{\nu}_i \left(4\tilde{v}_y + \tilde{u}_x\right) \tag{5.44}$$

$$\begin{aligned} S = &-\tilde{u}\tilde{v}_x - \tilde{v}\tilde{v}_y - \frac{1}{\tilde{n}}\tilde{\zeta}\tilde{\zeta}_y - \left(1 - \mathscr{F}\right)\tilde{\lambda}\tilde{\psi}_y - \frac{1}{\tilde{n}}\left(\tilde{p}_{iy} + \tilde{p}_{e\perp y}\right) \\ &- \frac{1}{\tilde{n}}\left(\mathscr{F}_y\tilde{\psi}_x - \mathscr{F}_x\tilde{\psi}_y\right)\tilde{\psi}_x - \frac{\mathscr{F}}{\tilde{n}}\tilde{\theta}_y \end{aligned} \tag{5.45}$$

$\tilde{w}$:

$$M = \frac{\partial \tilde{w}}{\partial t} \tag{5.46}$$

$$F_1 = -\tilde{\nu}_i \tilde{w}_x \tag{5.47}$$

$$F_2 = -\tilde{\nu}_i \tilde{w}_y \tag{5.48}$$

$$S = -\tilde{u}\tilde{w}_x - \tilde{v}\tilde{w}_y - \left(1 - \mathscr{F}\right)\left(\tilde{\zeta}_y\tilde{\psi}_x - \tilde{\zeta}_x\tilde{\psi}_y\right) - \frac{1}{\tilde{n}}\left(\mathscr{F}_y\tilde{\psi}_x - \mathscr{F}_x\tilde{\psi}_y\right)\tilde{\zeta} \tag{5.49}$$

$\tilde{p}_i$:

$$M = \frac{\partial \tilde{p}_i}{\partial t} \tag{5.50}$$

$$F_1 = -\frac{2}{3}\tilde{\kappa}\left(\tilde{p}_{ix} - \frac{\tilde{p}_i}{\tilde{n}}\tilde{n}_x\right) \tag{5.51}$$

$$F_2 = -\frac{2}{3}\tilde{\kappa}\left(\tilde{p}_{iy} - \frac{\tilde{p}_i}{\tilde{n}}\tilde{n}_y\right) \tag{5.52}$$

$$S = -\tilde{u}\tilde{p}_{ix} - \tilde{v}\tilde{p}_{iy} - \frac{5}{3}\tilde{p}_i\left(\tilde{u}_x + \tilde{v}_y\right) + \frac{2}{3}\tilde{n}\tilde{\nu}_i\left[\frac{4}{3}\left(\tilde{u}_x^2 + \tilde{v}_y^2 - \tilde{u}_x\tilde{v}_y\right) + \left(\tilde{u}_y + \tilde{v}_x\right)^2 + \tilde{w}_x^2 + \tilde{w}_y^2\right] \tag{5.53}$$

$\tilde{\zeta}$:

$$M = \frac{\partial}{\partial t}\left[\tilde{\zeta} - \xi\tilde{\chi}\right] \tag{5.54}$$

$$F_1 = \tilde{w}\tilde{\psi}_y + \tilde{u}\tilde{\zeta} - \tilde{\lambda}\left(\tilde{\psi}_y - \xi\tilde{\lambda}_y\right) - \frac{1}{\tilde{n}}\tilde{\zeta}_y\left(\tilde{\zeta} - \xi\tilde{\chi}\right) + \mathscr{F}\left(\tilde{\lambda}\tilde{\psi}_y - \frac{1}{\tilde{n}}\tilde{\theta}_y\right) + \frac{1}{\tilde{n}}\left(\mathscr{F}_y\tilde{\psi}_x - \mathscr{F}_x\tilde{\psi}_y\right)\tilde{\psi}_x - \frac{1}{\tilde{n}}\tilde{p}_{e\perp y} - \left(\tilde{\eta}_R\tilde{\zeta}_x - \xi\tilde{\nu}_e\tilde{\chi}_x\right) \tag{5.55}$$

$$F_2 = -\tilde{w}\tilde{\psi}_x + \tilde{v}\tilde{\zeta} + \tilde{\lambda}\left(\tilde{\psi}_x - \xi\tilde{\lambda}_x\right) + \frac{1}{\tilde{n}}\tilde{\zeta}_x\left(\tilde{\zeta} - \xi\tilde{\chi}\right) - \mathscr{F}\left(\tilde{\lambda}\tilde{\psi}_y - \frac{1}{\tilde{n}}\tilde{\theta}_y\right) + \frac{1}{\tilde{n}}\left(\mathscr{F}_y\tilde{\psi}_x - \mathscr{F}_x\tilde{\psi}_y\right)\tilde{\psi}_y + \frac{1}{\tilde{n}}\tilde{p}_{e\perp x} - \left(\tilde{\eta}_R\tilde{\zeta}_y - \xi\tilde{\nu}_e\tilde{\chi}_y\right) \tag{5.56}$$

$$S = 0 \tag{5.57}$$

$\tilde{\psi}$:

$$M = \frac{\partial}{\partial t}\left[\tilde{\psi} - \xi\tilde{\lambda}\right] \tag{5.58}$$

$$F_1 = -\tilde{\eta}_R\tilde{\psi}_x + \xi\tilde{\nu}_e\tilde{\lambda}_x \tag{5.59}$$

$$F_2 = -\tilde{\eta}_R\tilde{\psi}_y + \xi\tilde{\nu}_e\tilde{\lambda}_y \tag{5.60}$$

$$S = -\tilde{u}\tilde{\psi}_x - \tilde{v}\tilde{\psi}_y + \frac{1}{\tilde{n}}\left[\left(\tilde{\psi}_x - \xi\tilde{\lambda}_x\right)\tilde{\zeta}_y - \left(\tilde{\psi}_y - \xi\tilde{\lambda}_y\right)\tilde{\zeta}_x\right] - \frac{\mathscr{F}}{\tilde{n}}\left(\tilde{\psi}_x\tilde{\zeta}_y - \tilde{\psi}_y\tilde{\zeta}_x\right) - \frac{1}{\tilde{n}}\left(\mathscr{F}_y\tilde{\psi}_x - \mathscr{F}_x\tilde{\psi}_y\right)\tilde{\zeta}$$

$\tilde{\lambda}$:

$$M = 0 \tag{5.61}$$

$$F_1 = \tilde{\psi}_x \tag{5.62}$$

$$F_2 = \tilde{\psi}_y \tag{5.63}$$

$$S = \tilde{n}\tilde{\lambda} \tag{5.64}$$

$\tilde{\chi}$

$$M = 0 \tag{5.65}$$

$$F_1 = \frac{\tilde{\psi}_x}{\tilde{n}} \tag{5.66}$$

$$F_2 = \frac{\tilde{\psi}_y}{\tilde{n}} \tag{5.67}$$

$$S = \tilde{\chi} \tag{5.68}$$

$\tilde{\theta}$:

$$M = 0 \tag{5.69}$$

$$F_1 = 0 \tag{5.70}$$

$$F_2 = 0 \tag{5.71}$$

$$S = \tilde{\theta} - \left(\tilde{\psi}_x^2 + \tilde{\psi}_y^2\right). \tag{5.72}$$

The pressure terms are implemented as described by 5.19 - 5.22 with $\tilde{B} = \sqrt{2\tilde{\theta} + \tilde{\zeta}^2}$. A traditional plasma model with isothermal-isotropic electron pressure can be implemented with $\tilde{p}_{e\perp} = \tilde{p}_{e\parallel} = \tilde{n}\tilde{T}_e$ and $\mathscr{F} = 0$. As mentioned in 5.1, analytical derivatives of all the equations with respect to the dependent variables and their first spatial derivatives must be inputted into HiFi to use the static condensation procedure.

Using the flux-source form, the plasma model is able to be implemented in the HiFi code framework. The next section will compare the results of three simulations: a fluid magnetic reconnection simulation using isothermal-isotropic electron pressure, a simulation using the new EoS and a fully kinetic simulation.

5.3 Simulation Comparisons

Magnetic reconnection has been widely studied through fluid-based models. Isotropic, two-fluid plasma models are sufficient to reproduce fast reconnection and characteristic "Hall" magnetic field structures in weakly collisional regimes [133], which have been observed by spacecraft in Earth's magnetosphere [199] and in laboratory experiments [97]. However, these models predict substantially different structure of the reconnection region compared to kinetic simulations, which are based on first-principles. For the generic reconnection scenario including an out-of-plane guide magnetic field, kinetic simulations often predict elongated and asymmetric current layers, compared

to conventional isotropic simulations with short and mainly symmetric current layers. These long layers can be unstable to secondary reconnection instabilities, which could be essential to correctly modeling the reconnection process. Spacecraft observations and kinetic simulations also have seen electron pressure anisotropy in the vicinity of the reconnection, something that cannot be captured by simple isotropic models. However, the new EoS can accurately account for the anisotropic electron pressure that can develop in the reconnection region due to electric and magnetic trapping of electrons. To test if the new EoS captures the relevant physics that determine the structure of the reconnection region, fluid simulations using isotropic electrons pressure, the new EoS, and a fully-kinetic simulation were performed.

Kinematic simulations model weakly-collisional plasma by attempting to solve Vlasov's equation for the time-dependent distribution function of the plasma. In particular, the particle-in-cell (PIC) method self-consistently represents plasma as a large sample of computational particles, and Vlasov's equation for the distribution function is found by computing their trajectories. Typically in this method, the computational domain is divided into a mesh of cells, where each cell contains many particles. Fields are defined on the cell mesh. Particle motions are determined based on these fields and collisional effects, while smooth charge and current densities are computed from these particles. Field evolution is determined by Maxwell's equation using these charges and currents. Though computationally expensive, PIC simulations give insight many phenomena that are not correctly modeled by traditional approximate methods.

In this dissertation, the particle-in-cell code VPIC was used to implement the corresponding kinetic simulations. VPIC is a first principles, 3D electromagnetic, relativistic kinetic PIC code. Fluid simulations were built using the HiFi framework described above.

For ease of comparison, the three simulations were all applied to the same 2.5 dimensional system, where the half dimension is in the out-of-plane direction and is taken to mean that quantities have no gradients in this direction. In the following simulation comparison, the half dimension was in the y-direction. The simulations were performed in a doubly-periodic domain of size $L_x \times L_z = 48d_i \times 32d_i$ where

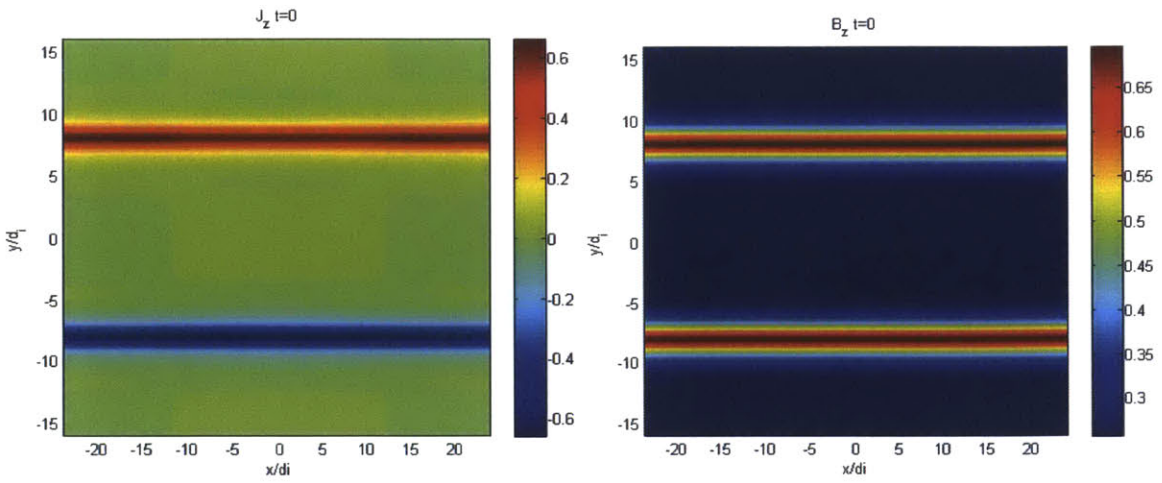

(a) (b)

Figure 5-1: (a) Initial out-of-plane current density profile and for all three simulations. (b) Initial out-of-plane magnetic field profile for all three simulations

$d_i = \sqrt{m_i/\mu_0 n_0 e^2}$ is the ion inertial length. The fluid simulations had 84 grid points per d_i while the kinetic simulations had 192 points. The initial configuration for the simulations was a double, force-free current sheet with magnetic fields given by

$$B_x(\boldsymbol{x}, 0) \simeq B_0 \left[\tanh\left(\frac{z + \frac{1}{4}L_z}{\lambda}\right) - \tanh\left(\frac{z - \frac{1}{4}L_z}{\lambda}\right) - 1 \right], \tag{5.73}$$

and

$$B_y(\boldsymbol{x}, 0) = \sqrt{B_0^2 - B_x^2(\boldsymbol{x}, 0) + B_{0y}^2}. \tag{5.74}$$

The initial out-of-plane current profile is shown in Figure 5-1a and the initial out-of-plane magnetic field profile is shown in Figure 5-1b. Lengths were normalized to d_i, while velocities and times were normalized to the Alfvén speed $V_A = B_0/\sqrt{\mu_0 m_i n_0}$ and the ion cyclotron time $\tau_{ci} \equiv 1/\Omega_i = m_i/eB_0$, respectively. The initial current sheet half-thickness was $\lambda = 1$, and the initial upstream guide magnetic field, $B_{0y} = 0.4B_0$. The ion and electron pressures were initially uniform with normalized values $\beta_{i0} = 2p_i\mu_0/B_0^2 = 0.30$ and $\beta_{e0} = 2p_{||}\mu_0/B_0^2 = 2p_\perp\mu_0/B_0^2 = .26$. The mass ratio was $m_i/m_e = 400$. In these fluid simulations, the normalized dissipation parameters were $\eta_H = 1.5 \times 10^{-5}$, $\nu_i = 3.9 \times 10^{-2}$ and $\kappa_i = 1.2 \times 10^{-2}$. The fluid simulation were not sensitive to moderate changes in these parameters; low values hasten

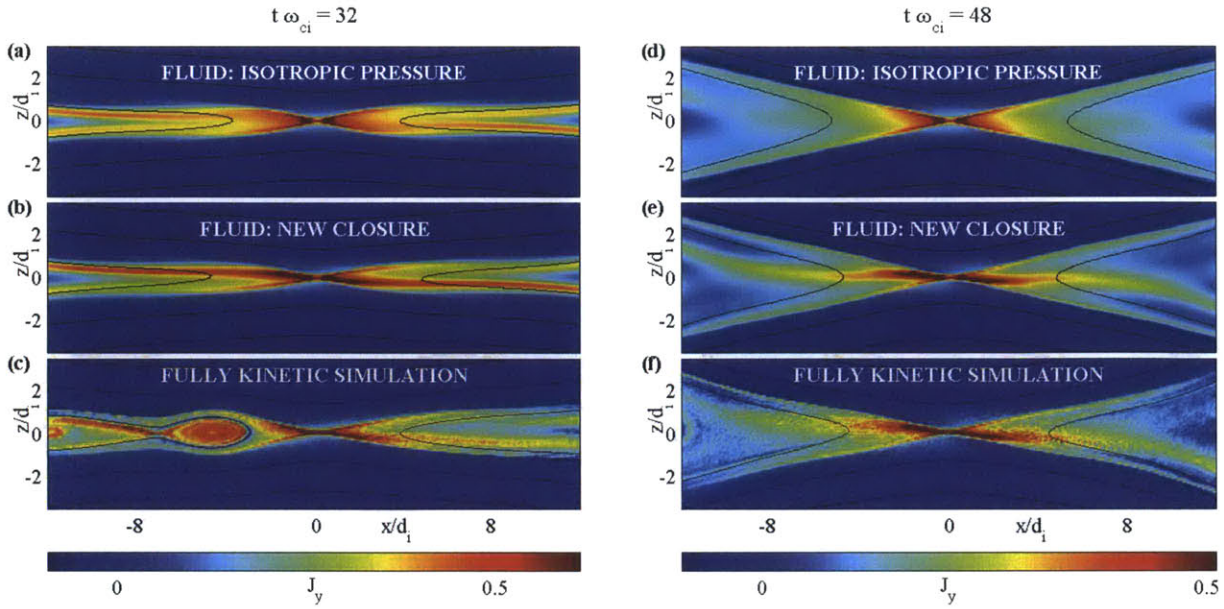

Figure 5-2: Out-of-plane current density profiles for all three simulations at two different simulation times. Solid line represent in-plane magnetic field lines. (a-c) Profiles evaluated at $t\,\Omega_{ci} = 32$. (d-f) Profiles evaluated at $t\,\Omega_{ci} = 48$.

the onset of physical and numerical instabilities and high values resemble collisional regimes. Reconnection was seeded with a single X-line using an in-plane magnetic field perturbation of amplitude 2.1×10^{-2}

Before the onset of fast reconnection, the fluid runs yielded nearly identical profiles of all quantities independent of the closure used for the electrons, but significant differences developed at later times characterized by fast reconnection. At this later stage, all profiles of the fluid simulation with anisotropic pressure were in excellent agreement with the kinetic simulation results. As an example, 5-2 provides two sets of time slices of the out-of-plane current density, J_y, obtained from the three simulations schemes outlined above.

The profiles in 5-2a-c were obtained at $t\Omega_i = 32$, just after the onset of fast reconnection. At this time, the profiles for the fluid runs were still similar but differences are emerging in the inner reconnection region. Partly due to the intrinsically higher level of numerical noise in kinetic simulations, the onset of reconnection in the kinetic run included the random formation of a magnetic island that is ejected in the $x < 0$ direction of the exhaust. Despite the differences introduced by the island, the profiles

Figure 5-3: Ratio of parallel to perpendicular electron pressure $p_{||}/p_{\perp}$ for (a) the anisotropic simulation and (b) the particle simulation. Solid lines represent in-plane magnetic field lines.

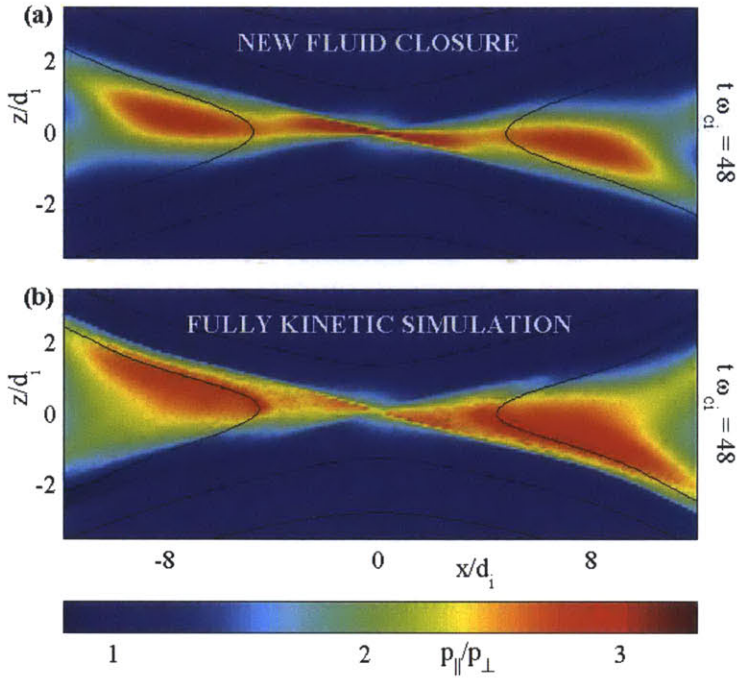

of the kinetic run and the anisotropic fluid run were in good agreement for $x > 0$.

For the profiles in 5-2d and 5-2e, evaluated at $t\Omega_i = 48$, the differences in J_y between the fluid simulations were more dramatic. For the isotropic run, the previously observed symmetric structure of the current layer is reproduced, limited in size to a few d_i centered on the X-line. In contrast, for the fluid run with the anisotropic pressure, an extended and asymmetric current layer was observed, which matched the current layer of the fully kinetic simulations (compare 5-2e and 5-2f).

The agreement between the new fluid model and the kinetic simulation demonstrates that fluid simulations with the new EOS correctly models much of the physics in kinetic reconnection simulations and that the electron pressure anisotropy is responsible for elongated electron current layers.

The profiles of the pressure anisotropy, $p_{||}/p_{\perp}$, for $t\Omega_i = 48$ are shown in 5-3 as obtained with the new fluid model and the kinetic simulation. Both simulations yielded profiles which were slightly asymmetric towards the diagonal along two of

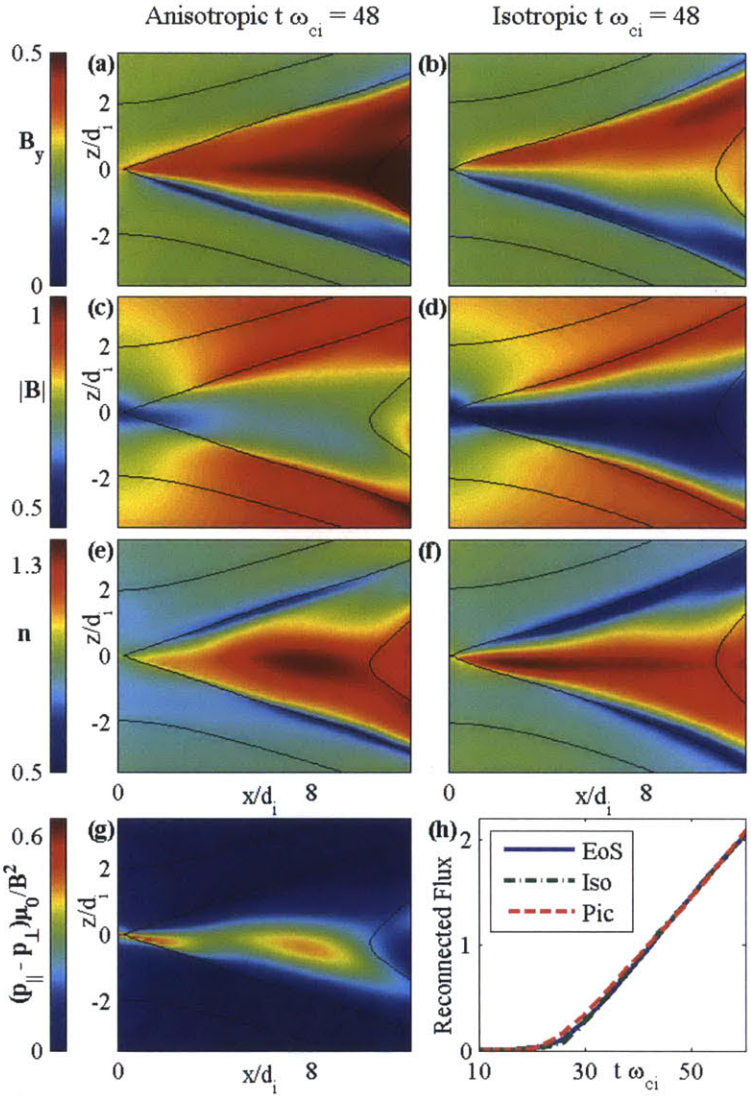

Figure 5-4: Comparison between isotropic and anisotropic simulation results of (a,b) the out-of-plane magnetic field, (c,d) the total magnetic field strength, (e,f) the plasma density and (g) Firehose stability criterion. For the firehose stability criterion, a ratio greater than one indicates the region is firehose unstable. Solid lines represent in-plane magnetic field lines. (h) Time evolution of the reconnected magnetic flux in the fluid simulation with the new Equations of State (blue solid line), the isotropic fluid simulation (grean dash-dotted line), and the kinetic PIC simulation (red dashed line).

the four separators. Furthermore, the profiles demonstrated good agreement in the magnitude of $p_{||}/p_{\perp}$. This agreement was confirmed in other simulations with varying initial plasma parameters as well.

The asymmetric structure of $p_{||}/p_{\perp}$ develops due to the density and magnetic profiles in hall reconnection. Figure 5-4, obtained at $t\Omega_i = 48$ from the fluid simulations, displays profiles of B_y, B, and n. Pressure balance in the z direction requires $Bv^2/2\mu_0 + p_{\perp} + p_i \simeq const$ which regulates the density profile such that n is increased where B is small. The asymmetries in the profiles of B and n shown in Figures 5-4c-f are directly related to the asymmetries in how the "Hall" magnetic field adds and subtracts from the background guide-field. In turn, because $p_{||}$ and $p_{\perp}$ profiles are related to n and B through the EOS, this asymmetry is also observed in the pressure profiles.

The pressure anistropy drives perpendicular currents in the X-line region through the additional current term $J_{\perp extra} = [(p_{||} - p_{\perp})/B]\hat{b} \times \hat{b} \cdot \nabla \hat{b}$. Since, in MHD models, $\nabla \cdot \boldsymbol{J} = 0$, parallel current is generated such that $d(J_{||extra}/B)/dl = (\nabla \cdot J_{\perp extra})/B$. These additional currents influence the magnetic geometry, allowing the magnetic field to simply rotate in the exhaust with a smaller reduction in B compared to isotropic reconnection. This increased value of B also reduces the anisotropy as predicted by the EOS, which will be further explored in subsequent chapters. In this simulation, the feedback between anisotropy and the magnetic field in the layer allows the exhaust region to regulate the anisotropy and settle near the firehose criterion shown in Figure 5-4g. In kinetic simulations, anisotropy is also regulated through pitch angle scattering. While the pressure anisotropy is important for the structures of the reconnection region, it does not influence the rate of reconnection, as seen in Figure 5-4h.

5.4 Summary

This chapter described the simulation systems used to model magnetic reconnection in this dissertation. Fluid simulations were built using the HiFi framework, which had

been developed to solve coupled differential equations on massively parallel computer systems. Two 2.5 dimensional, Hall-MHD plasma models, one that includes the new Equations of State (EoS) to model electron pressure anisotropy and another that assumes isotropic electron pressure, were implemented in HiFi. Magnetic reconnection simulations using these codes were compared to a similar fully kinetic simulation. The results of the comparisons demonstrated that the new EoS correctly captured much of the relevant physics in ion-electron magnetic reconnection, and that electron pressure anisotropy is responsible for current layer elongation seen in kinetic simulations.

Chapter 6

Magnetic Reconnection Simulations with New Equations of State

Simulations from the previous chapter demonstrated that the new Equations of State (EoS) that allow electron pressure anisotropy capture essential physics of magnetic reconnection, including the formation of elongated current layers seen in spacecraft observations and kinetic simulations.

This chapter discusses the regimes where the new EoS are valid and introduces a series of simulations that explore the structure of the reconnection region. A model predicting current layer conditions is developed and applied to simulation results. Finally, simulations comparing two mass ratios on a larger domain are presented.

6.1 Regimes of Validity

The formulation of the new Equations of State (EoS) necessitates the adiabatic invariance of the magnetic moment $\mu = mv_\perp^2/2B$ which, for electrons, requires $\rho_e/R_c \ll 1$ [214] where $\rho_e \equiv `mv_\perp/eB$ is electron Larmor radius and $R_c = |\hat{b} \cdot \nabla \hat{b}|^{-1}$ is the magnetic field line radius of curvature. For anti-parallel and weak guide-field reconnection, this condition is violated near the X-line and pitch angle isotropization

due to nonadiabatic particle motion occurs. In higher guide-fields, electrons remain magnetized and the magnetic moment is conserved, so the downstream electron pressure may remain anisotropic. Lê introduced a parameter K [153] with

$$K^2 = \min\left(\frac{R_c}{\rho_{eff}}\right), \tag{6.1}$$

where the effective Larmor radius $\rho_{eff} = \sqrt{m_e T_{eff}}/eB$ depends on total energy through $T_{eff} = \mathrm{Tr}\left(\bar{\mathbf{P}}_e\right)/3n$. The K parameter characterizes regimes of the electron diffusion region through associated classes of particle orbits, and is related to the κ parameter used in earlier literature [214].

Using a series of kinetic simulation that varied the guide-magnetic field, upstream electron pressure, and ion-electron mass ratio, it was observed that electrons remain in a fully magnetized regime when $K \gtrsim 2.5$. As reconnection proceeds, electron energization has been shown to scale with the ratio of electron to magnetic pressure, β_e, as $\Delta E \propto \beta_e^{-1/2}$ [206, 215] such that stronger guide-field is required to maintain electron magnetization at lower upstream pressure, contrary to what initial inspection of 6.1 might suggest. Figure 6-1 illustrates the boundary between the unmagnetized and magnetized exhaust regimes. Above the dashed curve where $K \sim 2.5$, the exhaust is magnetized.

The various regimes and their dependence on ion-electron mass ratio for upstream $\beta_e = .03$ is shown in Figure 6-2. In regime (1), $K \lesssim 1$ and has an unmagnetized exhaust with inner electron electron jets and is characterized by meandering thermal electron orbits. Regime (2) with $1 \lesssim K \lesssim 2.5$ also has an unmagnetized exhaust except no inner jets form and electron orbits are chaotic. In regimes (3) and (4), the exhaust remains fully magnetized with $K \gtrsim 2.5$, as mentioned above. In regime (3), the guide-field is sufficiently weak to also allow the layer to approach the marginal firehose condition, and an elongated current layer forms in this regime. In regime (4), the large magnetic tension due to the high guide-field restricts the layer from reaching the marginal firehose condition, an elongated layer does not form, and current is along the separator. The dependence of K on the mass ratio through ρ_{eff} is evident in 6-2

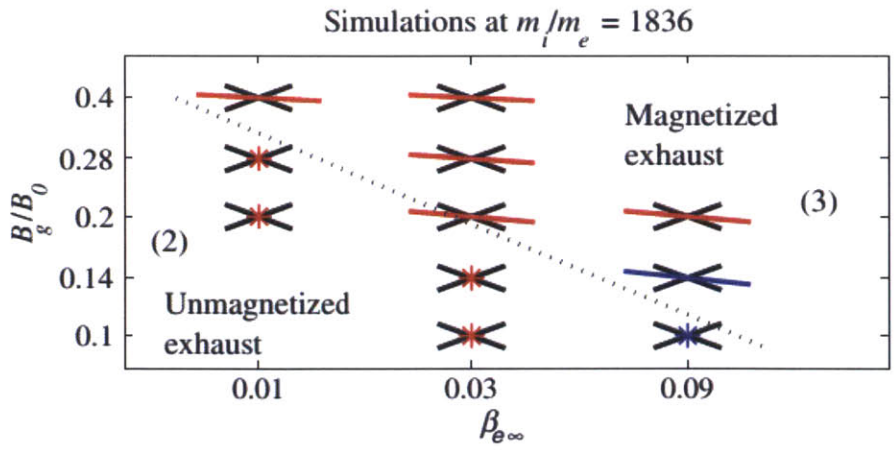

Figure 6-1: Classification of simulation runs as a function of upstream $\beta_{e\infty} = 2\mu_0 p_{e\infty}/B_0^2$ and guide-field B_g/B_0 where B_0 is the reconnecting field, at mass ratio $m_i/m_e = 1836$. Symbols indicate the electron current structure. Along the dashed curve, $K \sim 2.5$ (Ref [153])

as well.

In kinetic simulations, higher mass ratios are necessary to observe the elongated current layers. However since the EoS assume adiabatic electron trajectories, fluid simulations with the EoS will always have magnetized exhausts, independent of the mass ratio, upstream electron pressure, or the guide-field. The independence of the mass ratio can potentially allow much more efficient fluid simulations of magnetic reconnection, as full mass ratio kinetic simulations can be very expensive. From Figure 6-1, anisotropic fluid simulations with $\beta_e \gtrsim .03$ require guide-fields of $B_g \gtrsim .2B_0$ to remain physically relevant. This condition dictates the parameters used in the rest of the simulations presented in this dissertation. In the next section, a series of simulations that scan of the guide-field strength and upstream electron temperature is used to explore the structure of the reconnection region.

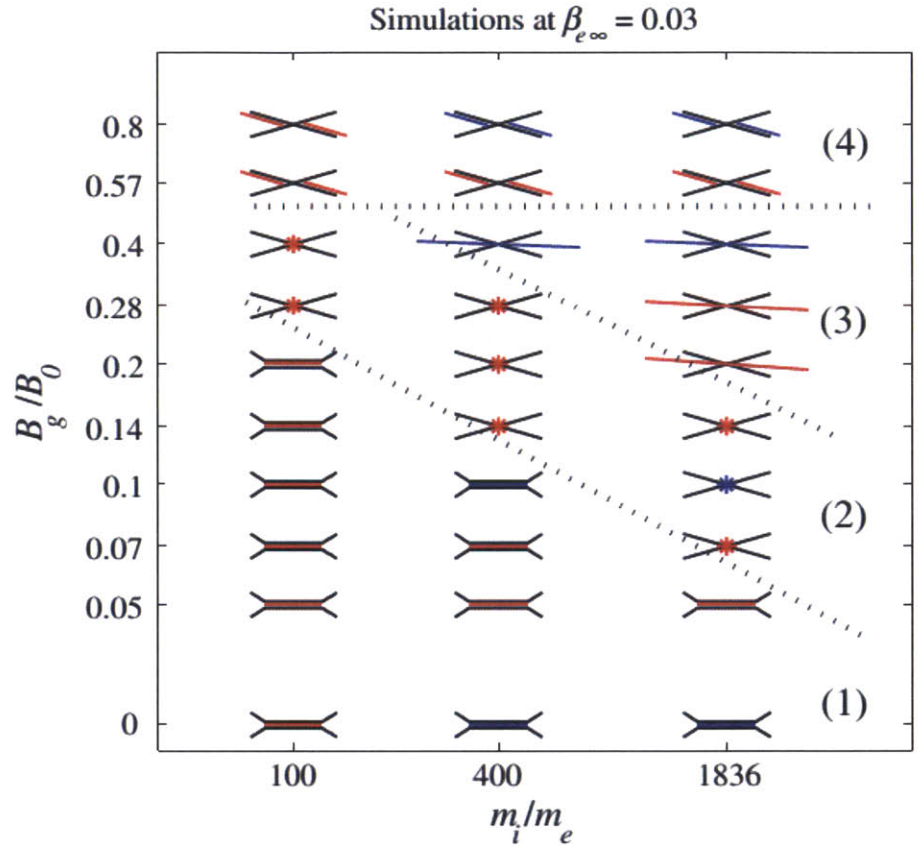

Figure 6-2: Classification of simulations runs as a function of upstream mass ratio m_i/m_e and B_g/B_0 where B_0 is the reconnecting field at $\beta_{e\infty} = .03$. Symbols indicate the electron current structure in each of the four regimes. (1) Inner electron jets and unmagnetized exhaust at $K \lesssim 1$. (2) No inner jets and unmagnetized at $1 \lesssim K \lesssim 2.5$. (3) Magnetized exhaust with elongated current layer at $K \gtrsim 2.5$. (4) Magnetized exhaust without elongated current layer but current along separators. (Ref [153]).

6.2 Anisotropic Current Layers

As seen in the previous section, the structure of the reconnection region in kinetic simulations is heavily influenced by the guide-field strength and the upstream electron temperature. Since the EoS are not influenced by mass ratio, this dependence is readily explored using fluid simulations. Towards this goal, a series of fluid simulations have been performed with a range of temperatures and guide-fields. The simulation domain is 2.5 dimensional and does not depend on the out-of-plane z-direction. The domain has size $L_x \times L_y = 48d_i \times 32d_i$ where $d_i = \sqrt{m_i/\mu_0 n_0 e^2}$ is the ion inertial length. Grid points are uniformly distributed in the x-direction with 72 grid points per d_i, while in the y-direction the grid point density is peaked at the center with 68.5 grid points per d_i and 11 grid points per d_i at the boundaries. The domain is periodic in the x-direction and has conducting wall boundaries in the y-direction, such that the out-of-plane vector potential A_z and current density J_z are held fixed, the y-component of the plasma velocity V_y is zeroed, and other quantities have zero y-derivatives at the boundary. The initial equilibrium is a force-free current sheet with magnetic fields given by

$$B_x(\boldsymbol{x}, 0) = B_0 \tanh\left(\frac{y}{\lambda}\right) \tag{6.2}$$

$$B_z(\boldsymbol{x}, 0) = \sqrt{B_0^2 - B_x^2(\boldsymbol{x}, 0) + B_{0z}^2}. \tag{6.3}$$

Lengths are normalized to d_i, velocities to the Alfvén speed $V_A = B_0/\sqrt{\mu_0 m_i n_0}$, and times to the ion cyclotron time $\tau_{ci} \equiv 1/\Omega_i = m_i/eB_0$. The initial current sheet half-thickness $\lambda = 1$, ion-electron mass ratio $m_i/m_e = 100$, ion viscosity $\nu_i = 2.5 \times 10^{-2}$, ion heat diffusion $\kappa_i = 7.5 \times 10^{-3}$, and hyper-resistivity $\eta_H \equiv d_e^2 \nu_e = 2.5 \times 10^{-4}$. Ion viscous heating was removed to simplify analysis as this effect has minimal impact on layer dynamics. Reconnection was seeded with a single X-line using an in-plane magnetic field perturbation

$$\tilde{B}_x(\boldsymbol{x}, 0) = \epsilon B_0 \frac{\pi}{L_y} \cos\left(\frac{2\pi x}{L_x}\right) \sin\left(\frac{\pi y}{L_y}\right) \tag{6.4}$$

$$\tilde{B}_y(\boldsymbol{x}, 0) = -\epsilon B_0 \frac{2\pi}{L_x} \sin\left(\frac{2\pi x}{L_x}\right) \cos\left(\frac{\pi y}{L_y}\right) \tag{6.5}$$

with $\epsilon = .2524$. Additionally, a secondary perturbation of the magnetic field with a strength of 6% of the perturbing field is included to break the left-right symmetry of the simulation and allow magnetic islands, if they form, to be ejected from the reconnection region.

The species temperatures and upstream initial guide-field vary in each simulation, though the ratio of upstream ion-electron temperature remains at $T_i/T_e = 4$ with the electron pressure is assumed isotropic upstream from the reconnection region with $p_{e||\infty} = p_{e\perp\infty} = p_e$. Four different values of guide-field $B_g/B_0 = .28, .40, .57, .81$ and three values of $\beta_e = 2\mu_0 p_e/(B_0^2 + B_g^2) = .03, .08, .19$ (p_e is adjusted accordingly) are simulated. In addition, corresponding isotropic simulations are also performed.

In the simulations, the x-position of the dominant X-line x_0 is defined as the minimum of the function [149]

$$\Phi_B(x, t) = \int_{L_y/2}^{L_y/2} |B_x| \, \mathrm{d}y, \tag{6.6}$$

while the y position is defined as the minimum of $|B_x(x_0, y)|$. The rate of magnetic flux reconnection $R = E_z/V_{Arec}B_{rec}$ at the X-line is shown for all runs with $\beta_e = .03$ in Figure 6-3. Here, it is shown that the rate dramatically increases at the onset of fast reconnection. After this period the layer reaches a relative steady state. The rates are nearly independent of guide-field and anisotropy, though the time of the transition to fast reconnect appears to have some dependence on both. Magnetic flux reconnection rates are also shown in Figures 6-4 and 6-5 for simulations with guide-fields of $B_g = .4$ and $B_g = .81$ respectively. From the figures, higher β_e corresponds with a quicker transition to fast reconnection. For the highest β_e, the rate continues to gradually increase during fast reconnection, until the rate drops as the layer approaches a new equilibrium.

The out-of-plane reconnecting electric field at the x-line for runs with $\beta_e = .03$ is plotted in Figure 6-6. Here the electric field peaks and begins to decline as the

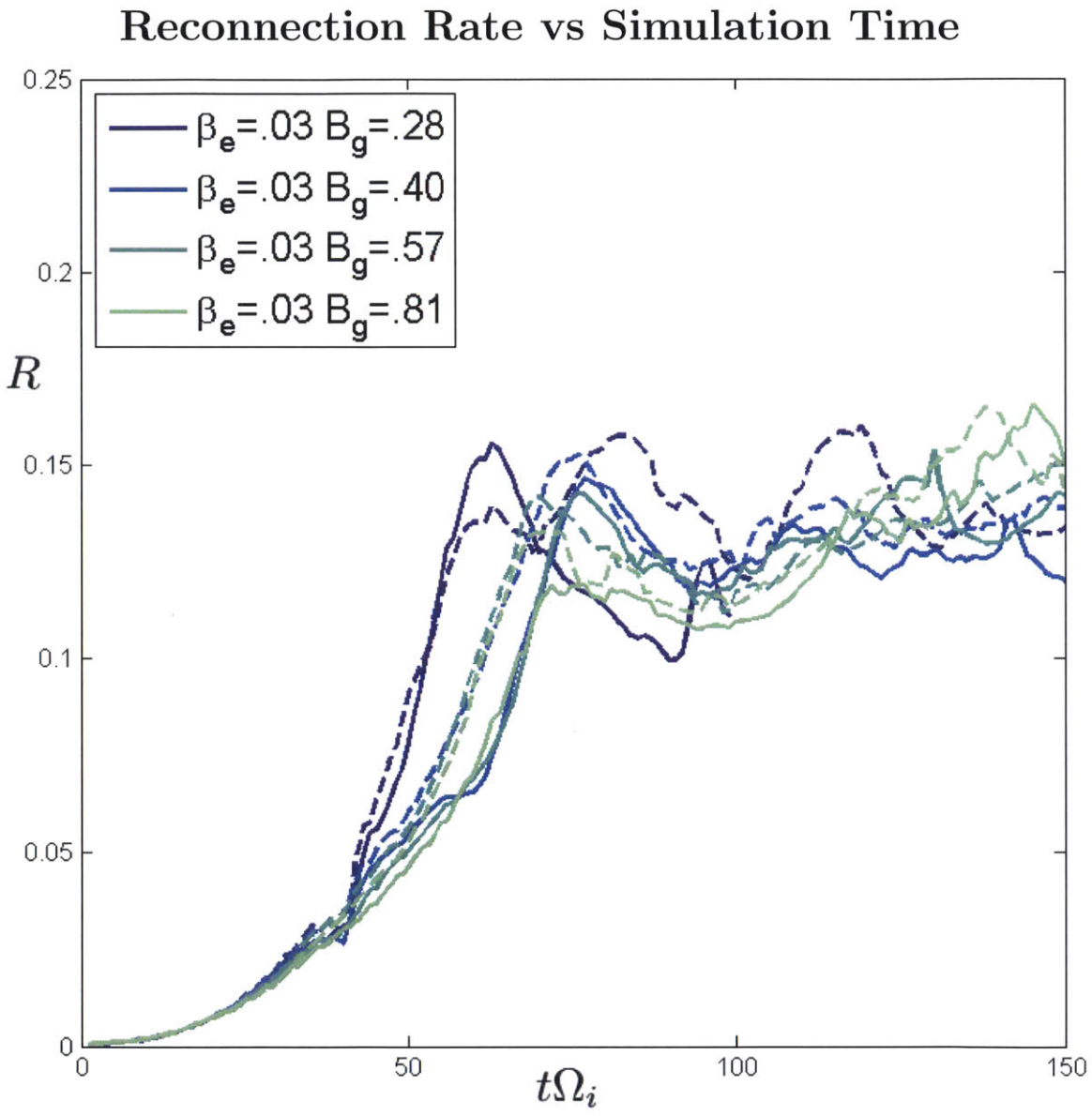

Figure 6-3: Rate of magnetic flux reconnection $R = E_z/V_{Arec}B_{rec}$ as a function of ion gyrotime. Solid and dashed lines indicate anisotropic and isotropic electron pressure, respectively.

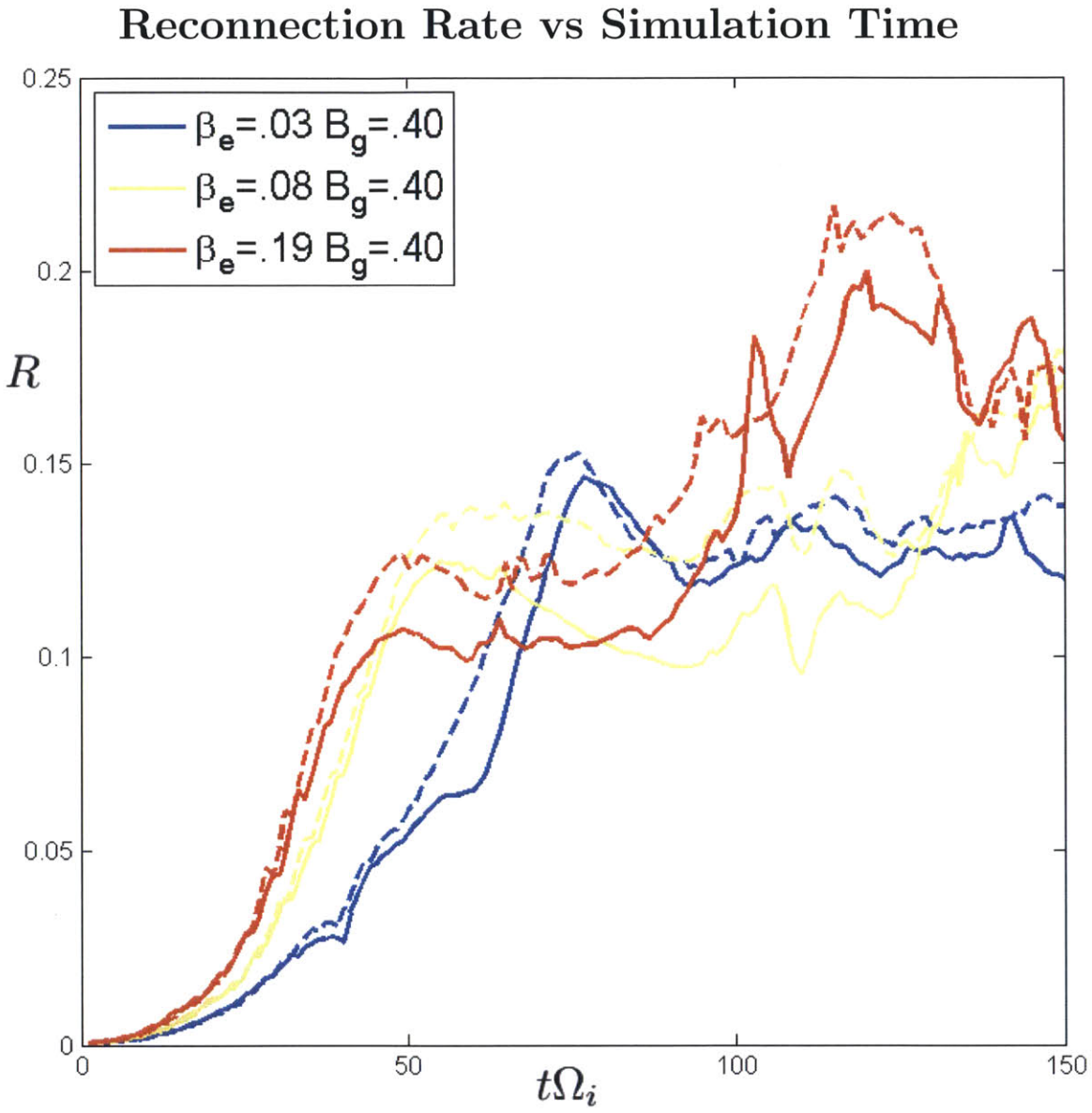

Figure 6-4: Rate of magnetic flux reconnection $R = E_z/V_{Arec}B_{rec}$ as a function of ion gyrotime. Solid and dashed lines indicate anisotropic and isotropic electron pressure, respectively.

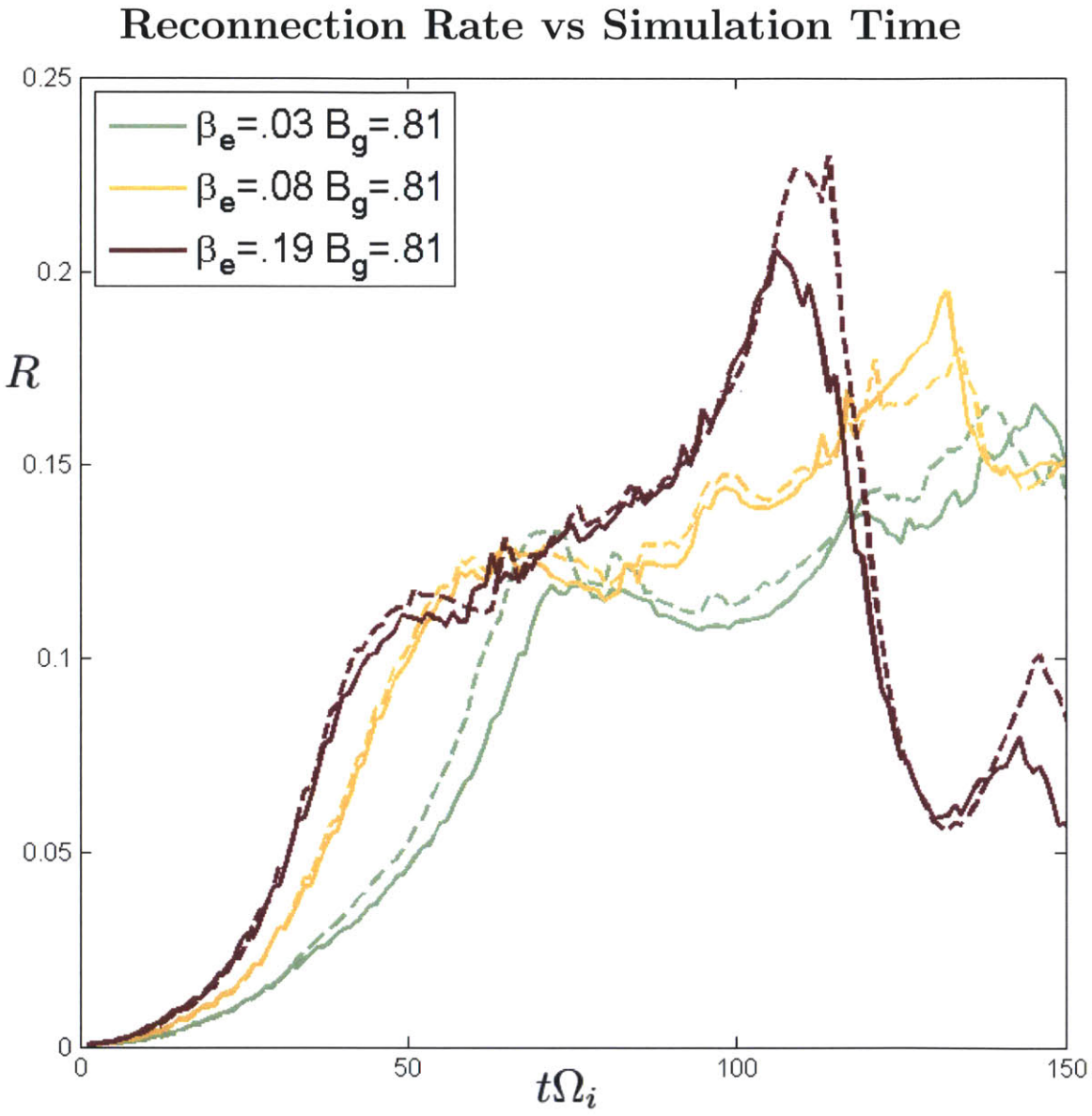

Figure 6-5: Rate of magnetic flux reconnection $R = E_z/V_{Arec}B_{rec}$ as a function of ion gyrotime. Solid and dashed lines indicate anisotropic and isotropic electron pressure, respectively.

simulation becomes limited by effects of the boundary. The peak electric field appears nearly independent of anisotropy and weakly dependent on guide-field. The electric field of runs with $B_g = .4$ and $B_g = .81$ are shown in Figures 6-7 and 6-8, respectively. From these figures, it can be inferred that some of the difference in the observed flux reconnection rates is due to differences in the upstream normalization parameters.

Comparing current layers in anisotropic simulations, a strong dependence of the guide-field on the current layer structure is seen, demonstrated in Figures 6-9a-d at $t\Omega_i = 87$. Lower guide-fields result in elongated current layers aligned between the magnetic separators, while higher guide-fields result in current more concentrated at the X-line and along the magnetic separators. This matches results seen in full mass ratio particle-in-cell simulations [153]. Figures 6-9e-g show the results from corresponding isotropic runs. Here, guide-field does not appear to strongly affect the structure of the current layers, with current concentrated at the X-line and along the magnetic separators like in the high guide-field, anisotropic simulations.

Returning to the anisotropic simulations, Figures 6-10a-d show the ratio of parallel to perpendicular electron pressure $p_{e\parallel}/p_{e\perp}$, depicted using a log color scale. There is a strong, inverse correlation between guide-field and electron pressure anisotropy for this range of fields. From the EoS, this is due to the decreasing relative importance of the reconnecting field in the current layer as the guide-field is increased, such that the normalized magnetic field $\tilde{B} = B/B_\infty \rightarrow 1$ as seen in Figures 6-10e-g. The normalized density, depicted in Figures 6-11a-d, does not exhibit a definitive trend between density and guide-field.

The firehose ratio $\mu_0(p_{e\parallel} - p_{e\perp})/B^2$ for the different guide-fields is shown in Figures 6-11e-g. In runs with guide-field $B_g = .28B_0, .40B_0$, this ratio approaches, and may exceed, unity near the X-line. Here magnetic field lines are able to rotate around the current layer due to the decreased magnetic tension. In runs at guide-field $B_g = .81B_0$, pressure anisotropy does not significantly affect magnetic tension, and the current layer strongly resembles isotropic simulations.

Upstream values of β_e do not have as significant of an effect on current layer structure as guide-field values. Figures 6-12a-c show current layers with $B_g = .28B_0$

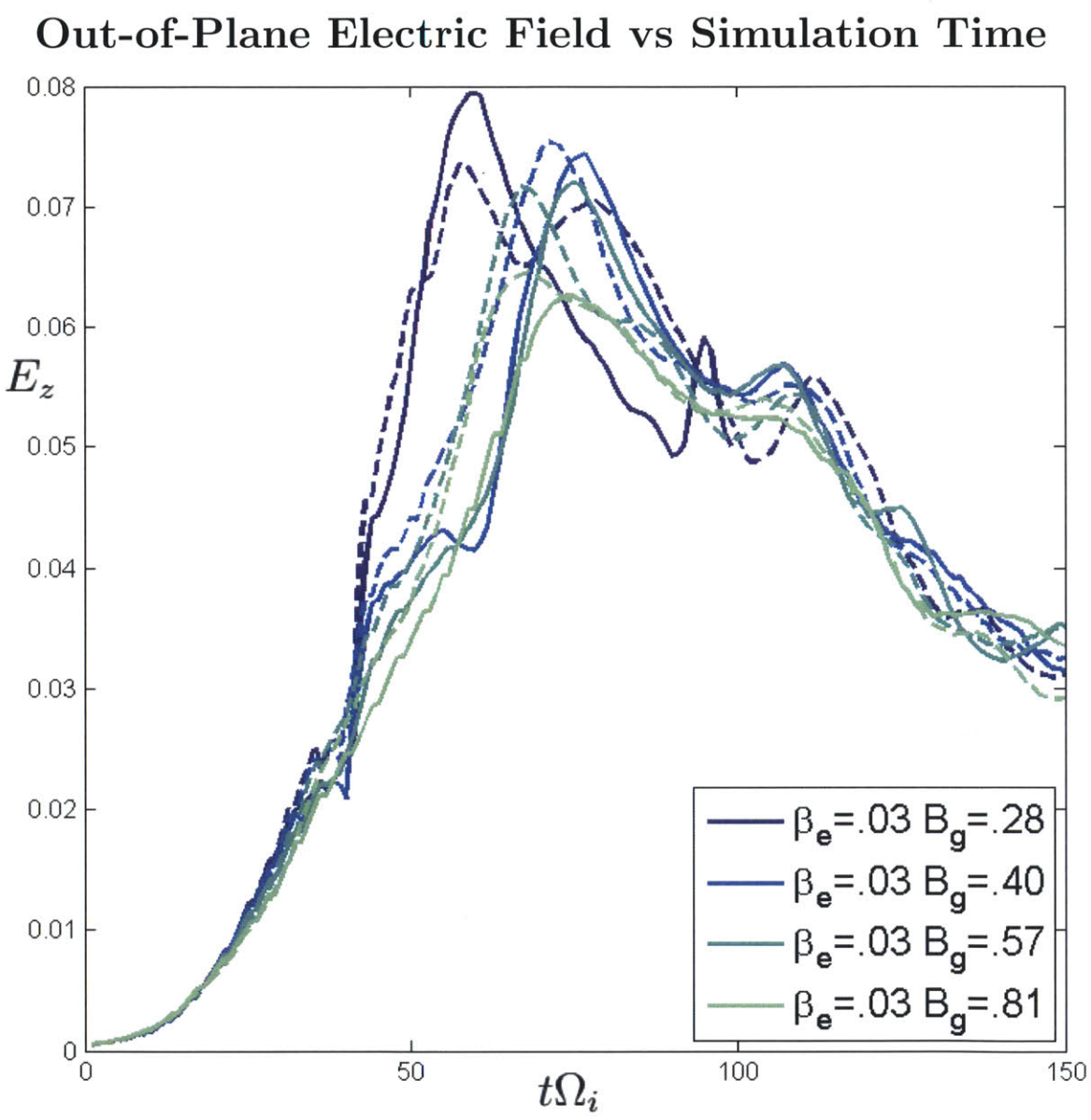

Figure 6-6: Out-of-plane electric field at the x-line as a function of ion gyrotime. Solid and dashed lines indicate anisotropic and isotropic electron pressure, respectively.

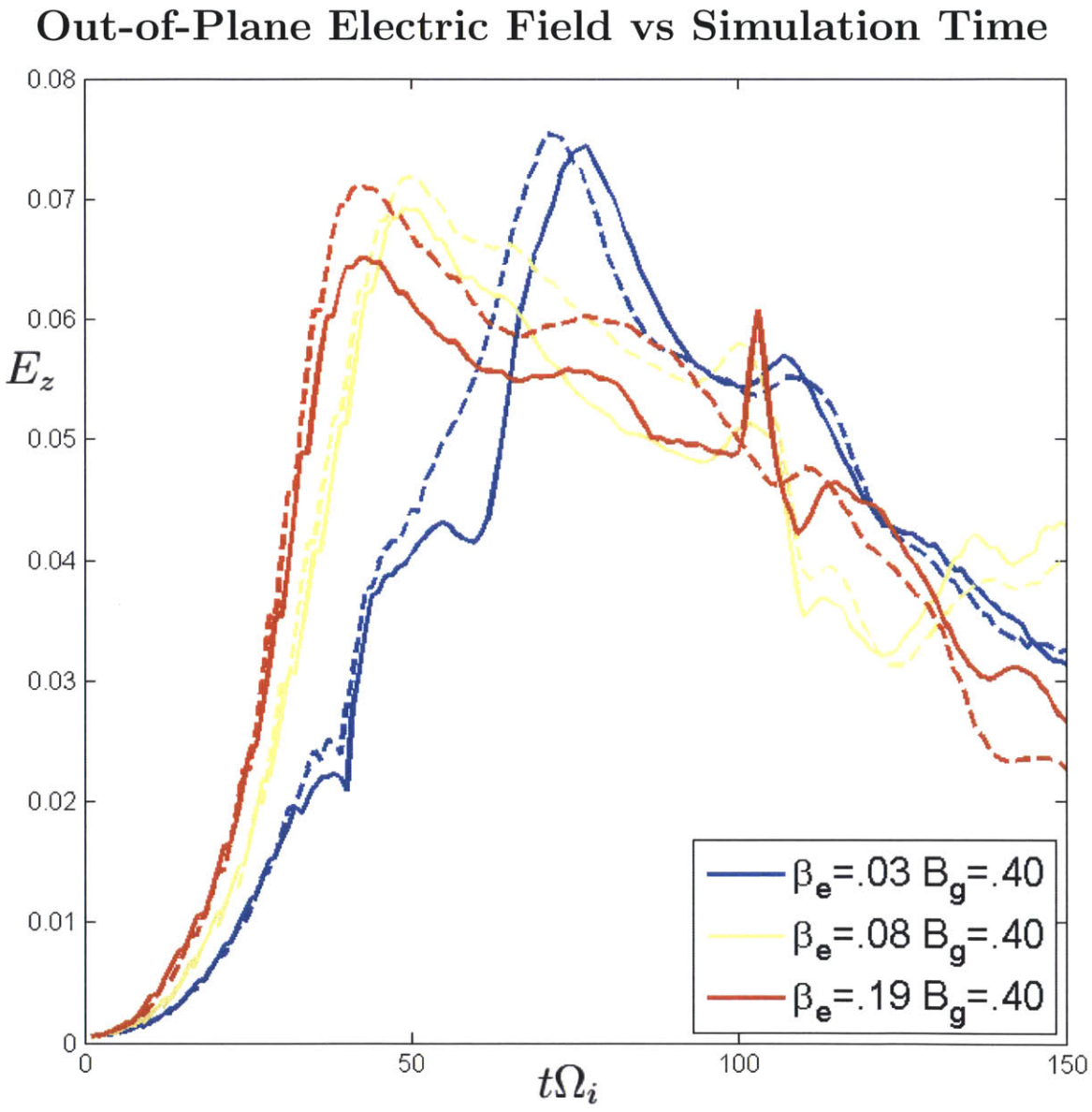

Figure 6-7: Out-of-plane electric field at the x-line as a function of ion gyrotime. Solid and dashed lines indicate anisotropic and isotropic electron pressure, respectively.

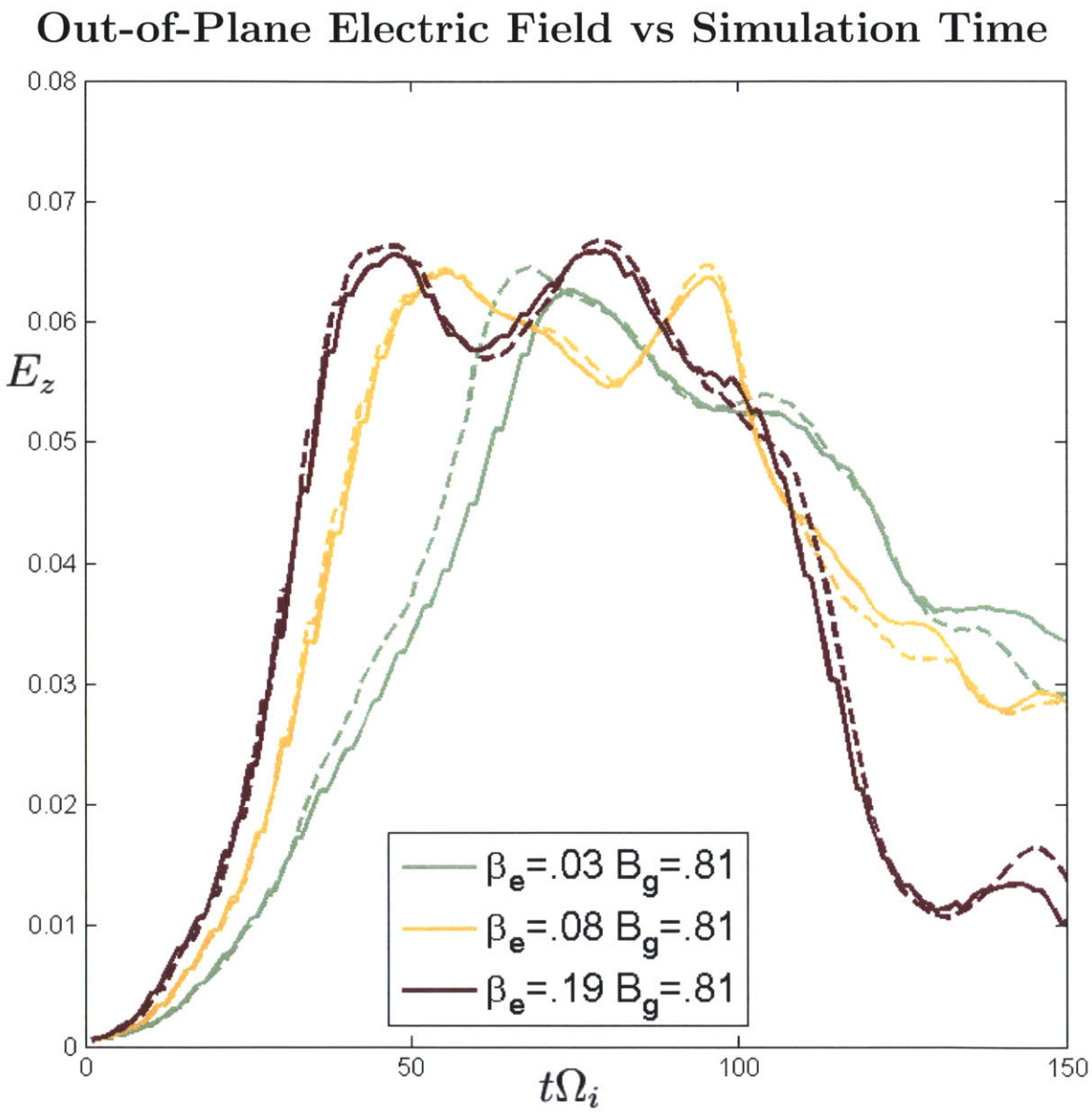

Figure 6-8: Out-of-plane electric field at the x-line as a function of ion gyrotime. Solid and dashed lines indicate anisotropic and isotropic electron pressure, respectively.

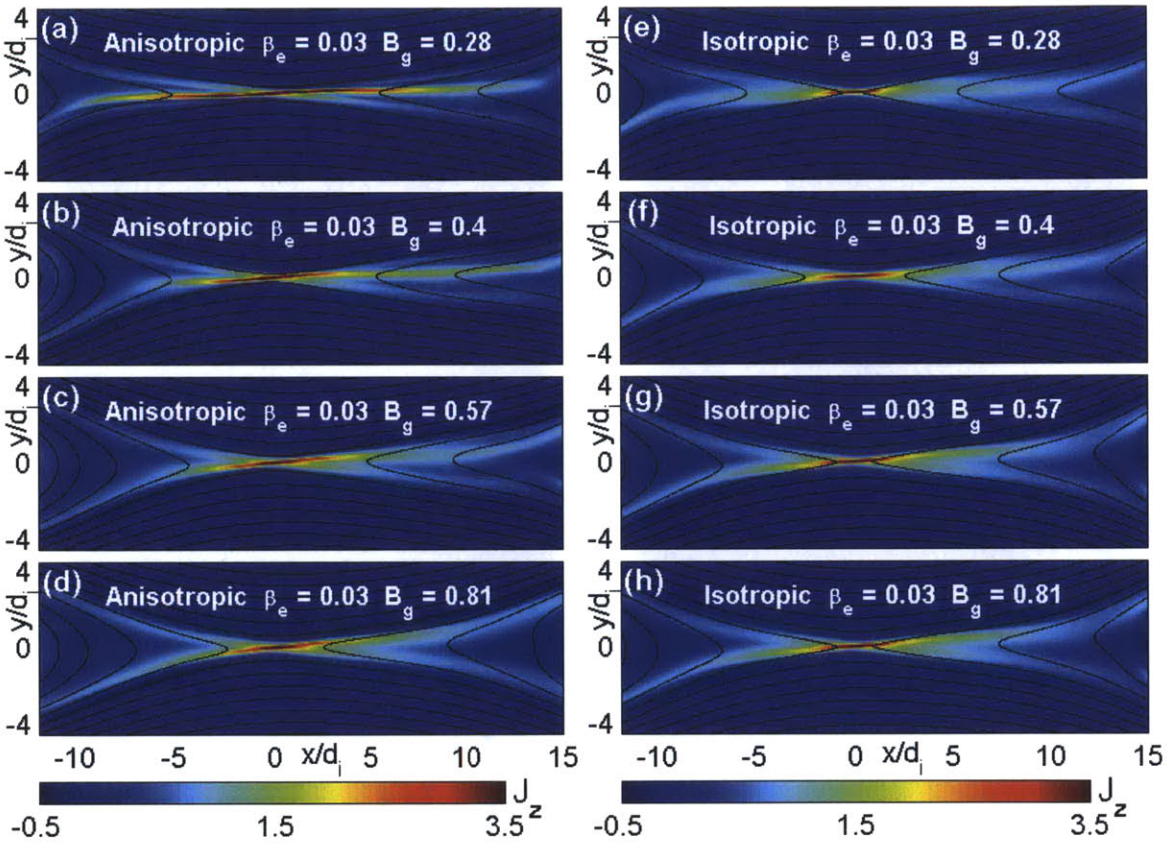

Figure 6-9: Out-of-plane current density J_z and superimposed in-plane magnetic field lines in reconnection simulations with (a-d) the new Equations of State and (e-g) isotropic electrons for $\beta_e = .03$ at $t\Omega_i = 87$ with guide-fields of $B_g/B_0 = .28, .40, .57, .81$ where B_0 is the initial upstream reconnecting field.

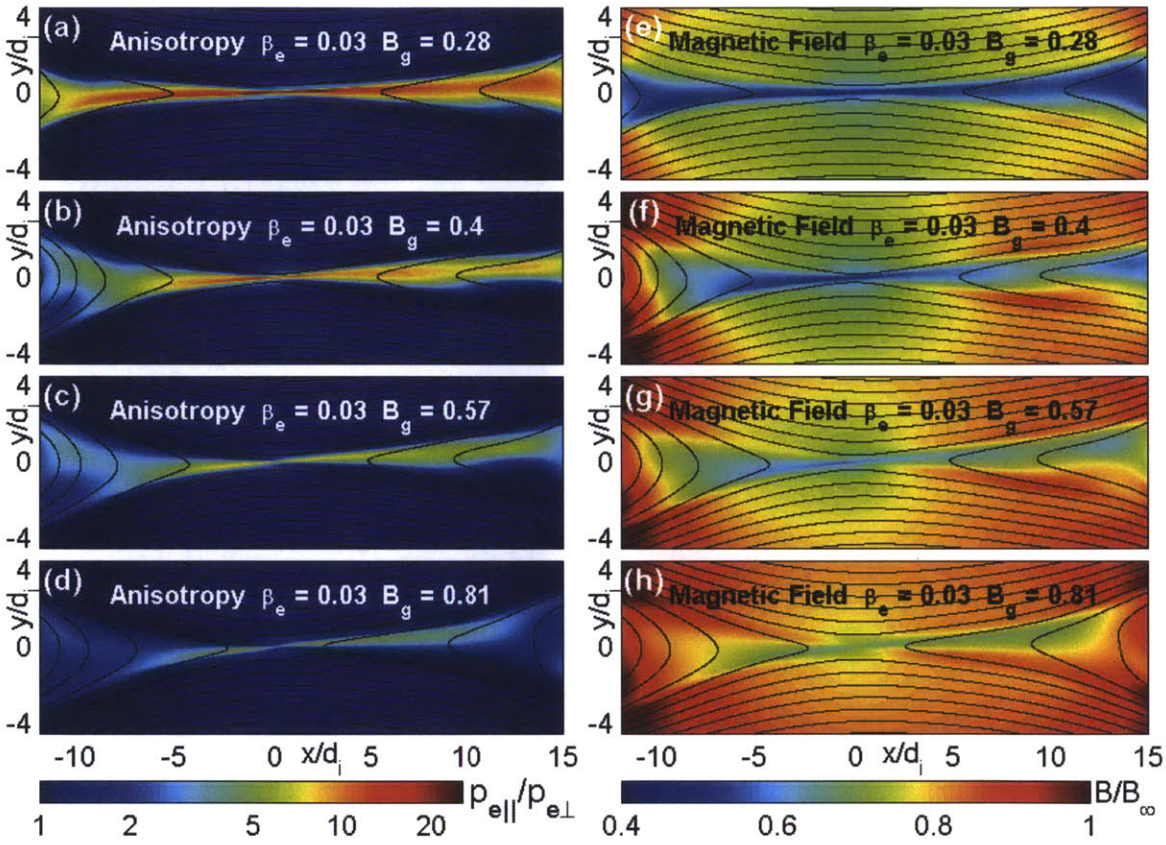

Figure 6-10: (a-d) Ratio of parallel to perpendicular electron pressure $p_{e\|}/p_{e\perp}$ on a logarithmic scale and (e-g) magnetic field strength normalized to the far upstream value with superimposed in-plane magnetic field lines in reconnection simulations with the new Equations of State for $\beta_e = .03$ at $t\Omega_i = 87$ with guide-fields of $B_g/B_0 = .28, .40, .57, .81$ where B_0 is the initial upstream reconnecting field.

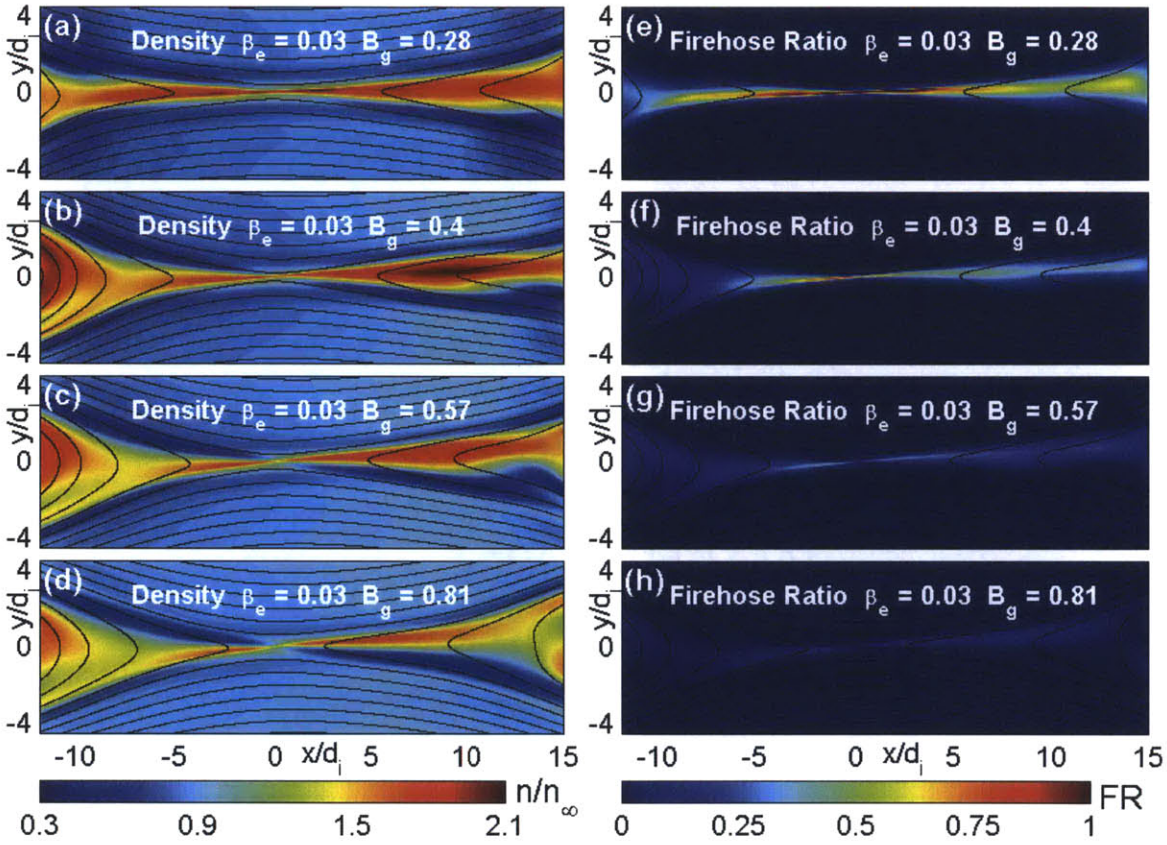

Figure 6-11: (a-d)Density normalized to the far upstream value and (e-g) firehose ratio $\mathscr{F}_e = \mu_0 p_{e\parallel} - p_{e\perp}/B^2$ with superimposed in-plane magnetic field lines in reconnection simulations with the new Equations of State for $\beta_e = .03$ at $t\Omega_i = 87$ with guide-fields of $B_g/B_0 = .28, .40, .57, .81$ where B_0 is the initial upstream reconnecting field.

for the three different values of $\beta_e = .03, .08, .19$ at $t\Omega_i = 87, 83, 65$ respectively. Though there appears to be a correlation between the length of the layers and β_e, this may have to do with the expansion of the magnetic islands that bound the current layers, which is an artifice of the periodic boundaries. As expected, these layers are in stark contrast to corresponding low guide-field isotropic simulations, which do not exhibit signs of current layer elongation, shown in Figures 6-12d-f. Anisotropic simulations with $B_g = .81B_0$ are shown in Figures 6-13a-c, and once again these are similar to the corresponding isotropic current layers shown in Figure 6-13d-f.

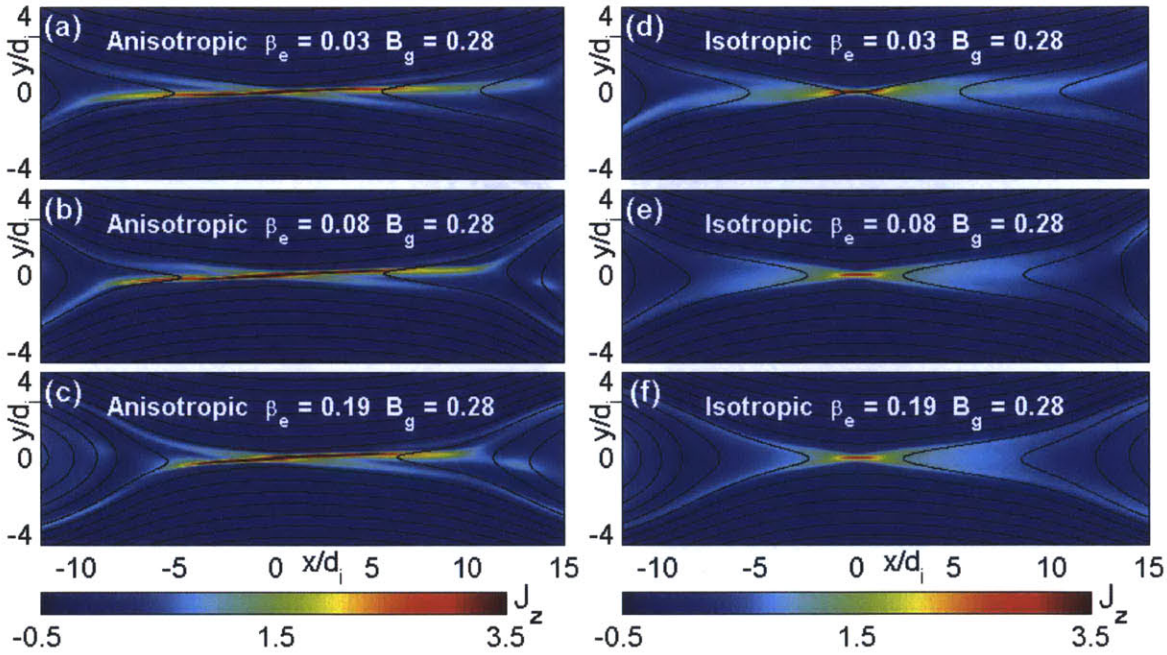

Figure 6-12: Out-of-plane current density J_z and superimposed in-plane magnetic field lines in reconnection simulations with (a-c) the new Equations of State and (d-f) isotropic electrons for $B_g = .28B_0$, where B_0 is the initial upstream reconnecting field, with $\beta_e = .03, .08, .19$ at $t\Omega_i = 87, 83, 65$, respectively.

The ratio $p_{e\parallel}/p_{e\perp}$ for the different values of β_e at low guide-field $B_g = .28B_0$ is shown in Figures 6-14a-c plotted, with a logarithmic color scale. A strong inverse dependence of β_e on anisotropy is observed, as expected from the derivation of the EoS where electron trapping decreases with increasing temperature since the thermal energy increases compared to the trapping potential. In these simulations, this dependence is due to the correlation between β_e and normalized density, depicted in

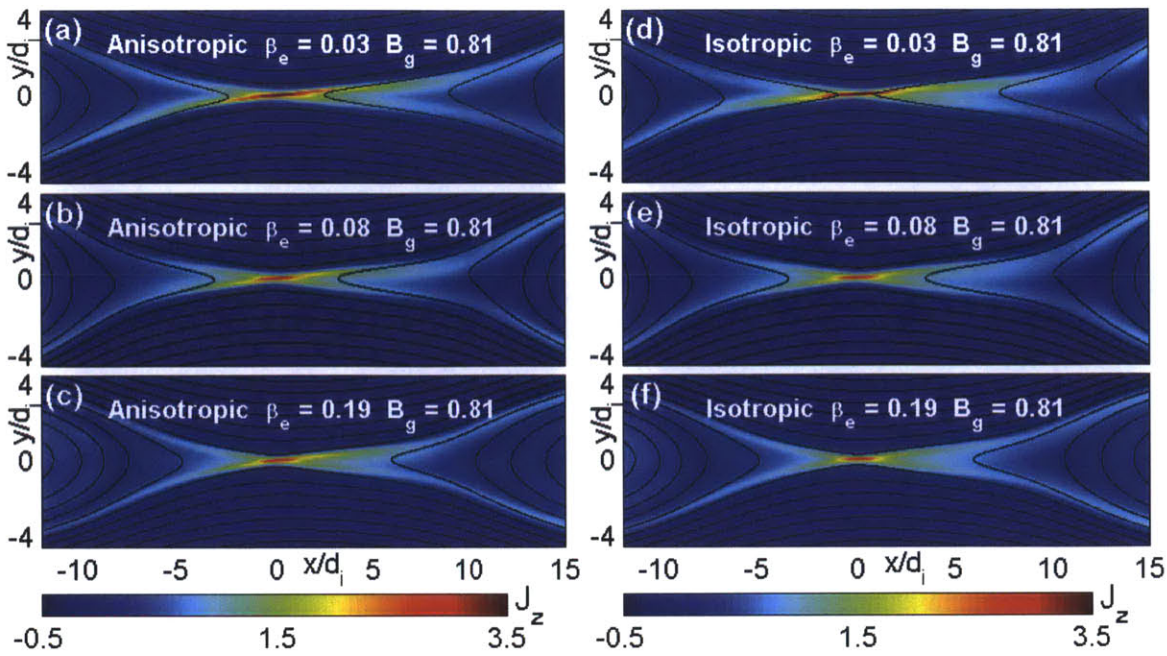

Figure 6-13: Out-of-plane current density J_z and superimposed in-plane magnetic field lines in reconnection simulations with (a-c) the new Equations of State and (d-f) isotropic electrons for $B_g = .28B_0$, where B_0 is the initial upstream reconnecting field, with $\beta_e = .03, .08, .19$ at $t\Omega_i = 87, 83, 65$, respectively.

Figures 6-15a-c. With the constancy of T_i/T_e, magnetic pressure variations are balanced by ion pressure, such that $\Delta BB/\mu_0 \sim \Delta nT_i$ and density variations are reduced at higher temperatures. In contrast, the normalized magnetic field is not significantly affected by β_e, as depicted in Figures 6-16a-c. These trends are also observed in runs with high guide-field $B_g = .81B_0$. The anisotropy ratio $p_{e\|}/p_{e\perp}$ is shown in Figures 6-14d-f, normalized density in Figures 6-15d-f and normalized magnetic field in Figures 6-16d-f.

In contrast to the anisotropy shown above, the firehose ratio of the current layer, shown in Figures 6-17a-c for low guide-field $B_g = .28B_0$, does not strongly depend on the value of β_e. The increasing β_e is somewhat negated by the decreasing anisotropy seen above, such that the firehose ratios in these runs are similar. This is also the case in high guide-field runs with $B_g = .81B_0$, as shown in Figures 6-17d-f, except here the ratio remains low for different values of β_e.

Further comparison between anisotropic and isotropic simulations shows electron

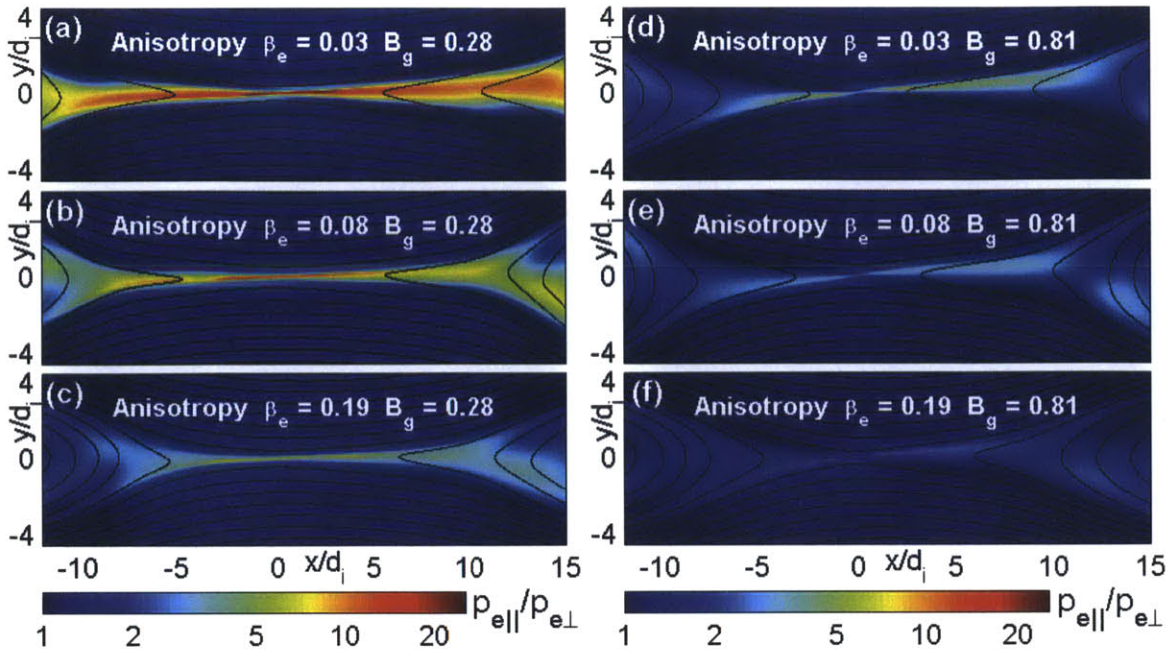

Figure 6-14: Anisotropy $p_{e\|}/p_{e\perp}$ and superimposed in-plane magnetic field lines in reconnection simulations with the new Equations of State for (a-c) $B_g = .28B_0$ and (d-f) $B_g = .81B_0$, where B_0 is the initial upstream reconnecting field, with $\beta_e = .03, .08, .19$ at $t\Omega_i = 87, 83, 65$, respectively.

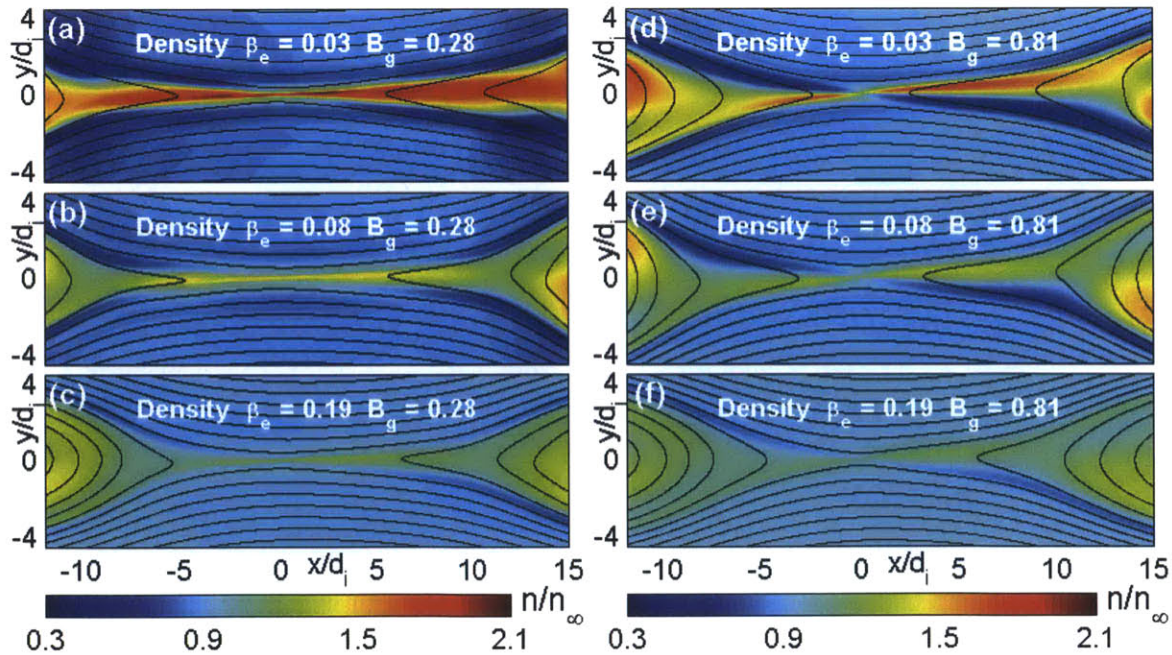

Figure 6-15: Density normalized to the far upstream value and superimposed in-plane magnetic field lines in reconnection simulations with the new Equations of State for (a-c) $B_g = .28B_0$ and (d-f) $B_g = .81B_0$, where B_0 is the initial upstream reconnecting field, with $\beta_e = .03, .08, .19$ at $t\Omega_i = 87, 83, 65$, respectively.

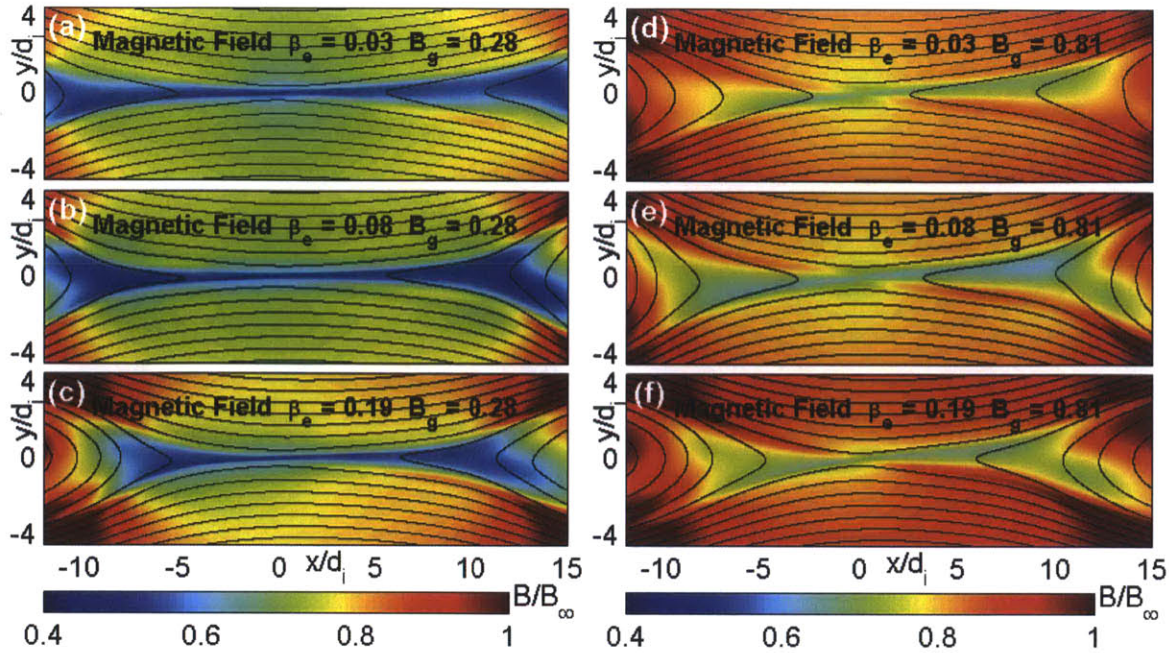

Figure 6-16: Magnetic field strength normalized to the far upstream value and superimposed in-plane magnetic field lines in reconnection simulations with the new Equations of State for (a-c) $B_g = .28B_0$ and (d-f) $B_g = .81B_0$, where B_0 is the initial upstream reconnecting field, with $\beta_e = .03, .08, .19$ at $t\Omega_i = 87, 83, 65$, respectively.

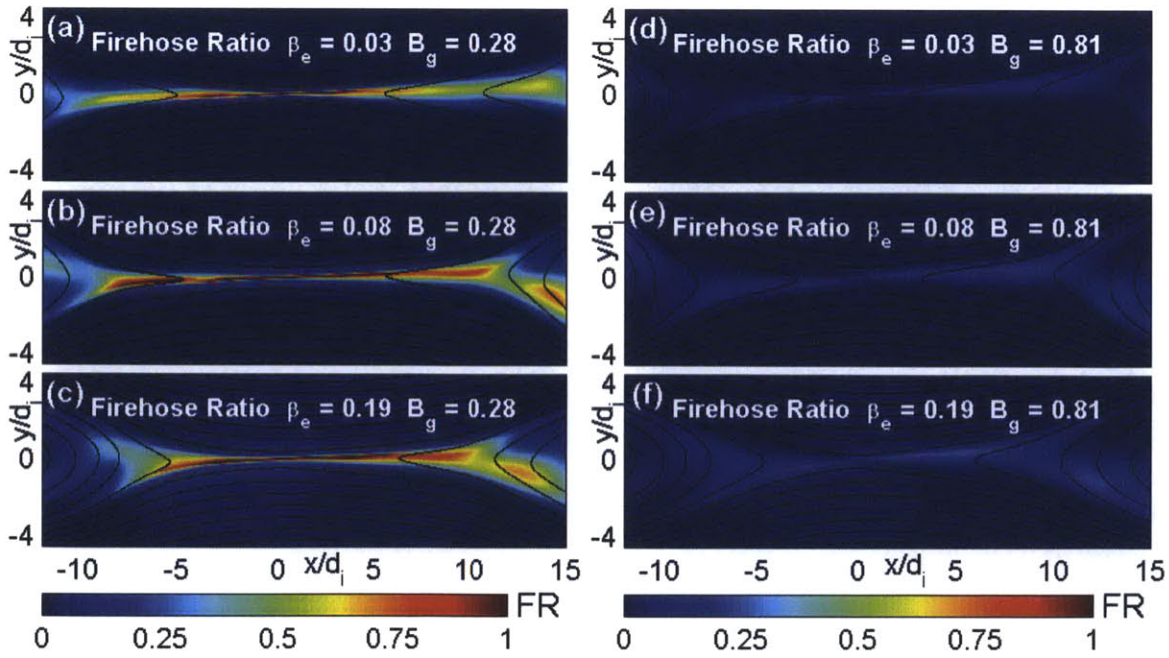

Figure 6-17: Firehose ratio $\mu_0 p_{e\parallel} - p_{e\perp}/B^2$ and superimposed in-plane magnetic field lines in reconnection simulations with the new Equations of State for (a-c) $B_g = .28B_0$ and (d-f) $B_g = .81B_0$, where B_0 is the initial upstream reconnecting field, with $\beta_e = .03, .08, .19$ at $t\Omega_i = 87, 83, 65$, respectively.

pressure anisotropy affects the structure of the reconnection region outside of elongated current layers at lower guide-fields. The normalized magnetic field strength of the reconnection region both anisotropic and isotropic simulations for low $B_g = .28B_0$ and low $\beta_e = .03$ is shown in Figure 6-18. The field in the isotropic simulation is considerably lower than that in the anisotropic simulation. This drop is reproduced not only in runs with higher β_e, but also, to a lesser extent, in runs with higher guide-fields as well, an example of which is shown in Figure 6-19. The higher field strengths seen in anisotropic simulations are due, in part, to extra perpendicular current driven by pressure anisotropy given by $\boldsymbol{J}_{\perp ext} = \boldsymbol{B} \times \mathscr{F}_e \boldsymbol{\kappa}/\mu_0$ with $\boldsymbol{\kappa} = \hat{b} \cdot \nabla \hat{b} = -\hat{R}_c/R_c$ where R_c is the local radius of magnetic curvature and $\hat{R}_c$ is a unit vector from the center of curvature to the point on the magnetic field line. Presuming $\nabla \cdot \boldsymbol{J}_{ext} = 0$, additional parallel current satisfies the equality $d(J_{||extra}/B)/dl = (\nabla \cdot \boldsymbol{J}_{\perp extra})/B$. This current generates additional field that increases the magnetic field strength in the region and decrease the overall variation of the magnetic pressure. In these simulations, plasma pressure variation, which balances magnetic field pressure, is also decreased and, correspondingly, density variation is also reduced in anisotropic simulations. The normalized densities of the reconnection regions are shown in Figure 6-20 for $B_g = .28B_0$ and low $\beta_e = .03$. Once again, the density variation is much larger in the isotropic simulation and this effect is also seen in higher guide-fields as well. The change in normalized density is much less severe at higher temperatures, as shown in Figure 6-21 for $\beta_e = .19$.

The result of the collusion of these two effects is the self-regulation of pressure anisotropy in the reconnection region. However, in these simulations, this regulation is not perfect, and other processes not included in the fluid model can also temper the anisotropy. The self-regulation of anisotropy in the reconnection can be seen by comparing the anisotropy seen in anisotropic simulations with the values predicted by the new EoS using the density and magnetic field of isotropic simulations. This comparison is shown in Figure 6-22 for low $\beta_e = .03$ and low $B_g = .28B_0$ plotted using a logarithmic color scale. Here, the predicted anisotropy using isotropic values can be as much as 20 times greater than what is observed in anisotropic simulations.

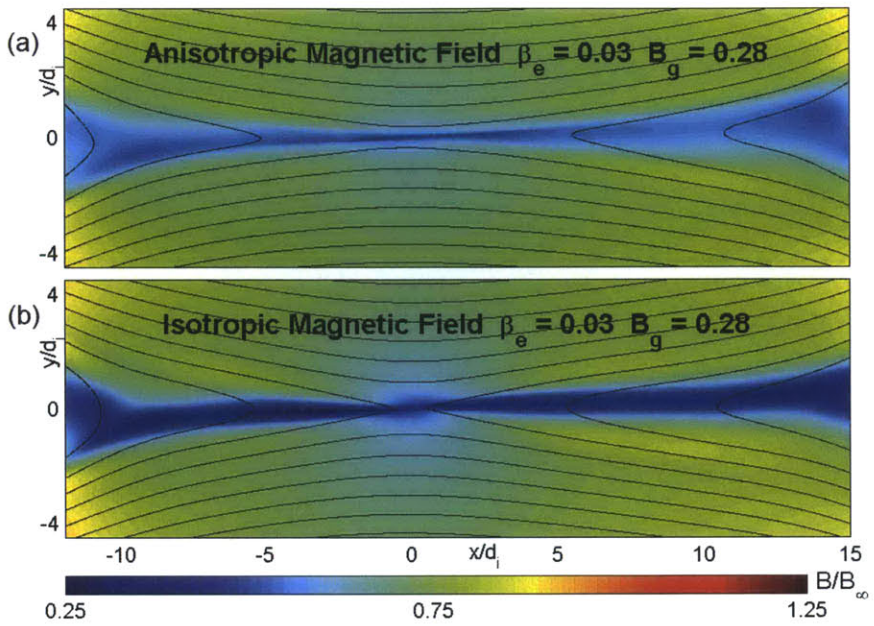

Figure 6-18: Magnetic field strength normalized to the far upstream value and superimposed in-plane magnetic field lines for $\beta_e = .03$, $B_g = .28B_0$, where B_0 is the initial upstream reconnecting field, at $t\Omega_i = 87$ in reconnection simulations with (a) the new Equations of State and (b) isotropic electron pressure.

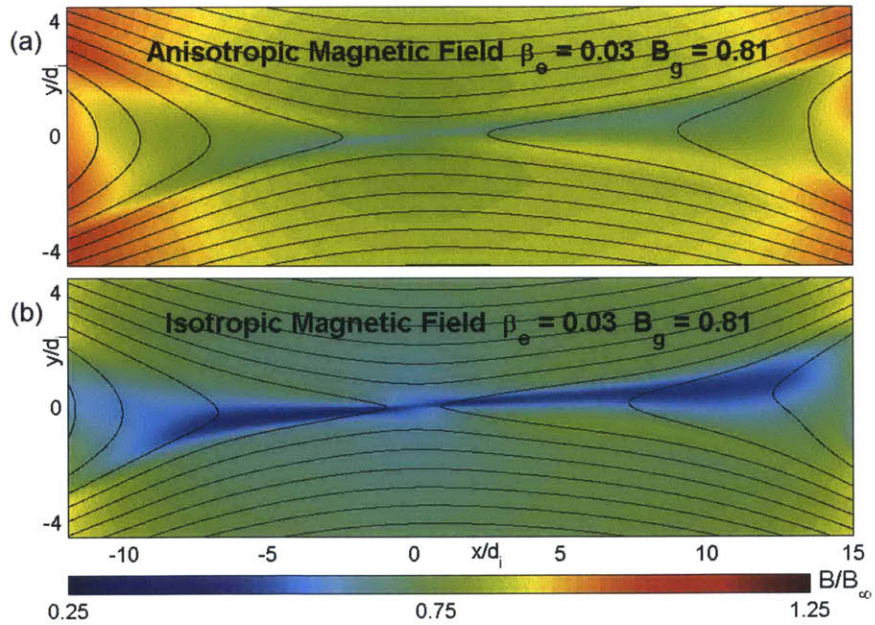

Figure 6-19: Magnetic field strength normalized to the far upstream value and superimposed in-plane magnetic field lines for $\beta_e = .03$, $B_g = .81B_0$, where B_0 is the initial upstream reconnecting field, at $t\Omega_i = 87$ in reconnection simulations with (a) the new Equations of State and (b) isotropic electron pressure.

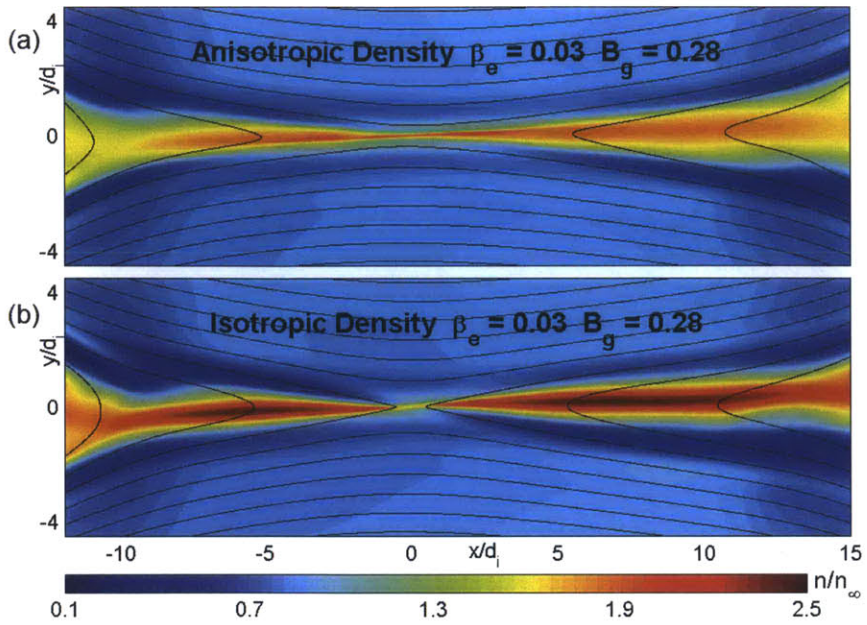

Figure 6-20: Density normalized to the far upstream value and superimposed in-plane magnetic field lines for $\beta_e = .03$, $B_g = .28B_0$, where B_0 is the initial upstream reconnecting field, at $t\Omega_i = 87$ in reconnection simulations with (a) the new Equations of State and (b) isotropic electron pressure.

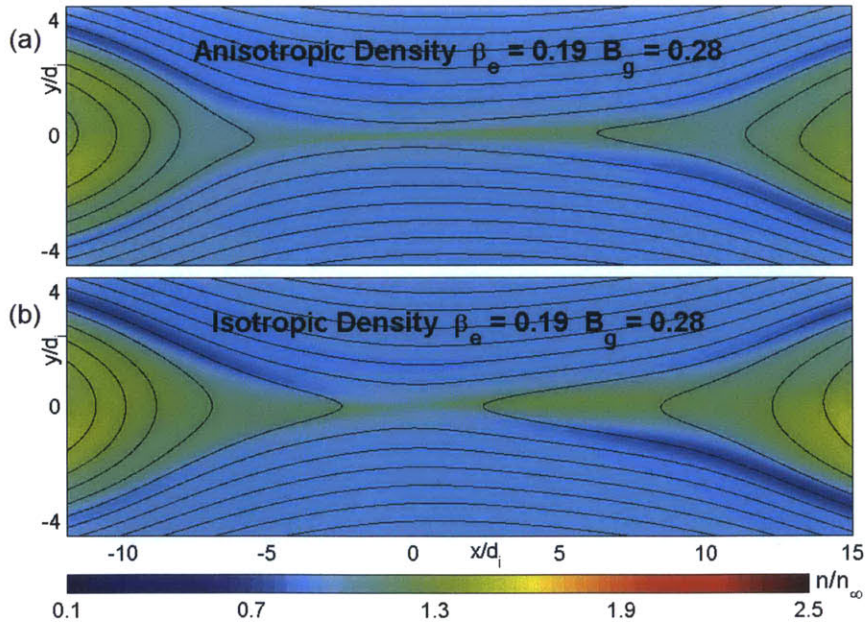

Figure 6-21: Density to the far upstream value and superimposed in-plane magnetic field lines for $\beta_e = .19$, $B_g = .28B_0$, where B_0 is the initial upstream reconnecting field, at $t\Omega_i = 65$ in reconnection simulations with (a) the new Equations of State and (b) isotropic electron pressure.

Increasing B_g or β_e decreases the predicted anisotropy down to a 50% increase at the highest $\beta_e = .19$ and $B_g = .81B_0$.

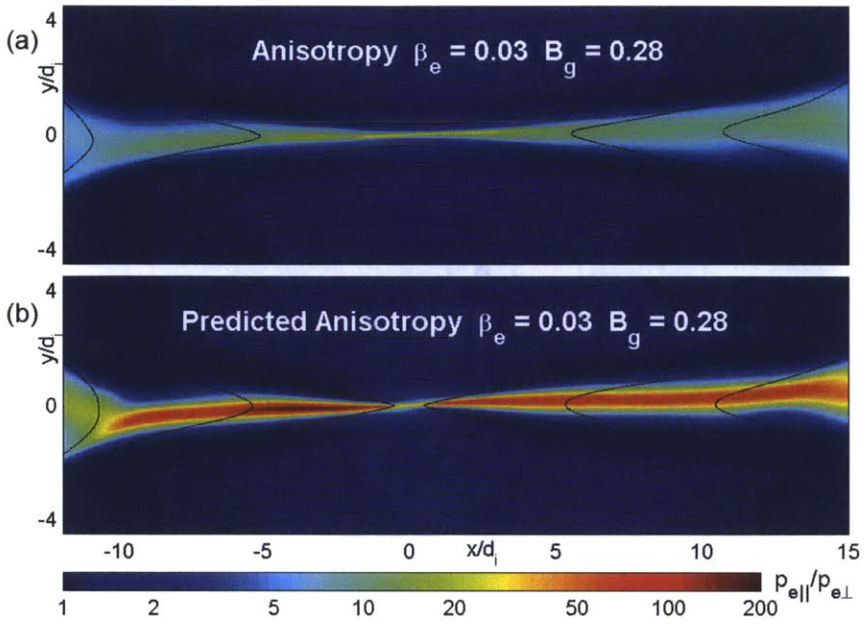

Figure 6-22: Anisotropy $p_{e\|}/p_{e\perp}$ and superimposed in-plane magnetic field lines in reconnection simulations for $\beta_e = .03$, $B_g = .28B_0$, where B_0 is the initial upstream reconnecting field, and $t\Omega_i = 87$. (a) An anisotropic reconnection simulation using the new Equations of State. (b) Predicted value using the density and magnetic field found in an isotropic simulation as inputs to the new Equations of State.

An effect of this self-regulation is to mollify the firehose ratio $\mathscr{F}_e$ of the reconnection region. The predicted value of the firehose ratio from for isotropic simulations can also be calculated using density and magnetic field values with the new Equations of State. In all but runs with $\beta_e = .08, .19$ at the highest guide-field $B_g = .81B_0$, the marginal firehose condition $\mathscr{F}_e = 1$ is greatly exceeded, even when $\beta_e = .03$ and $B_g = .81B_0$, as shown in Figure 6-23.

The effect of pressure anisotropy can also be seen by studying the terms of the normalized general Ohm's Law

$$\boldsymbol{E} = -\left(\boldsymbol{V} - \frac{\boldsymbol{J}}{n}\right) \times \boldsymbol{B} + \xi \frac{\partial}{\partial t}\left(\frac{\boldsymbol{J}}{ne}\right) - \xi \frac{\boldsymbol{J}}{ne} \cdot \nabla \frac{\boldsymbol{J}}{ne} - \eta_H \nabla^2 \frac{\boldsymbol{J}}{n} - \frac{1}{n}\left[\nabla p_{e\perp} + \nabla \cdot (\mathscr{F}_e \boldsymbol{B}\boldsymbol{B})\right], \tag{6.7}$$

where $\xi \equiv m_e/m_i$. Figure 6-24 is a plot of the various components of the out-of-

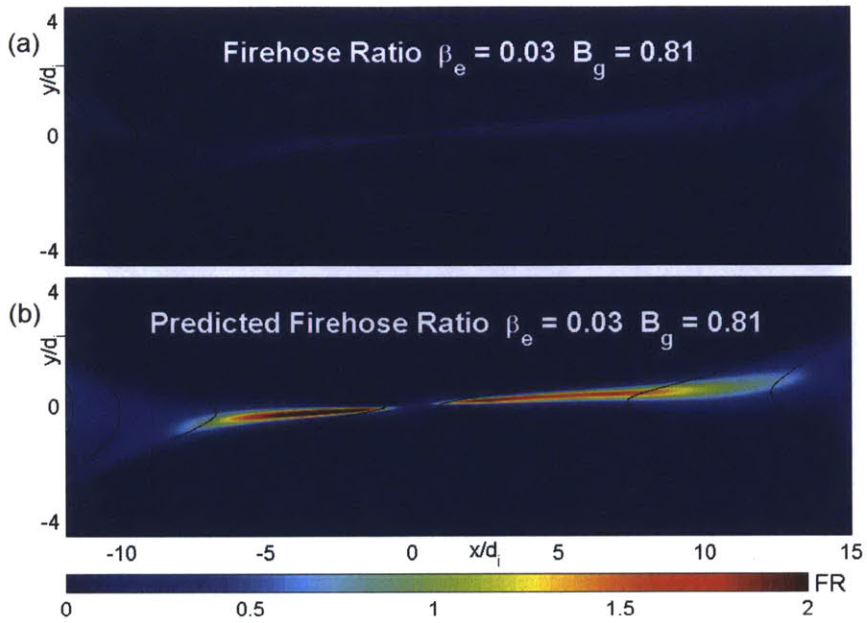

Figure 6-23: Firehose ratio $\mathscr{F}_e = \mu_0 p_{e\parallel} - p_{e\perp}/B^2$ and superimposed in-plane magnetic field lines in reconnection simulations for $\beta_e = .03$, $B_g = .81B_0$, where B_0 is the initial upstream reconnecting field, and $t\Omega_i = 87$. (a) An anisotropic reconnection simulation using the new Equations of State. (b) Predicted value using the density and magnetic field found in an isotropic simulation as inputs to the new Equations of State.

plane electric field E_z plotted across the layer along the line $y = 0$, for $\beta_e = .03$ and $B_g = .28B_0$ at $t\Omega_i = 87$. For simplicity, the electron term $\boldsymbol{V}_e \times \boldsymbol{B} \equiv (\boldsymbol{V} - \boldsymbol{J}/n) \times \boldsymbol{B}$ is plotted instead of the Hall term $\boldsymbol{J} \times \boldsymbol{B}/n$. In the plot, the regions where the plasma and electron fluids are frozen-in can be seen as where the nearly constant electric field is balanced as $E_z = -(V \times B)_z$ and $E_z = -(V_e \times B)_z$, respectively. The overshoot of this balance is likely due to the laplacian in the viscous and hyper-resistive terms. Near the X-line at $y = 0$, hyper-resistivity nearly balances the electric field and breaks the frozen-in condition. Though the anisotropy term is small in Figure 6-24, E_z is about 10% weaker than the field of the corresponding isotropic simulation, shown in Figure 6-25, while the current diffusion region is slightly wider in the anisotropic simulation.

A clearer picture of the importance electron pressure, inertia, and hyper-resistivity is obtained by transforming the electric field into an inertial reference frame moving at the local electron fluid velocity $\boldsymbol{V}_e$. In the non-relativistic limit, the electric field

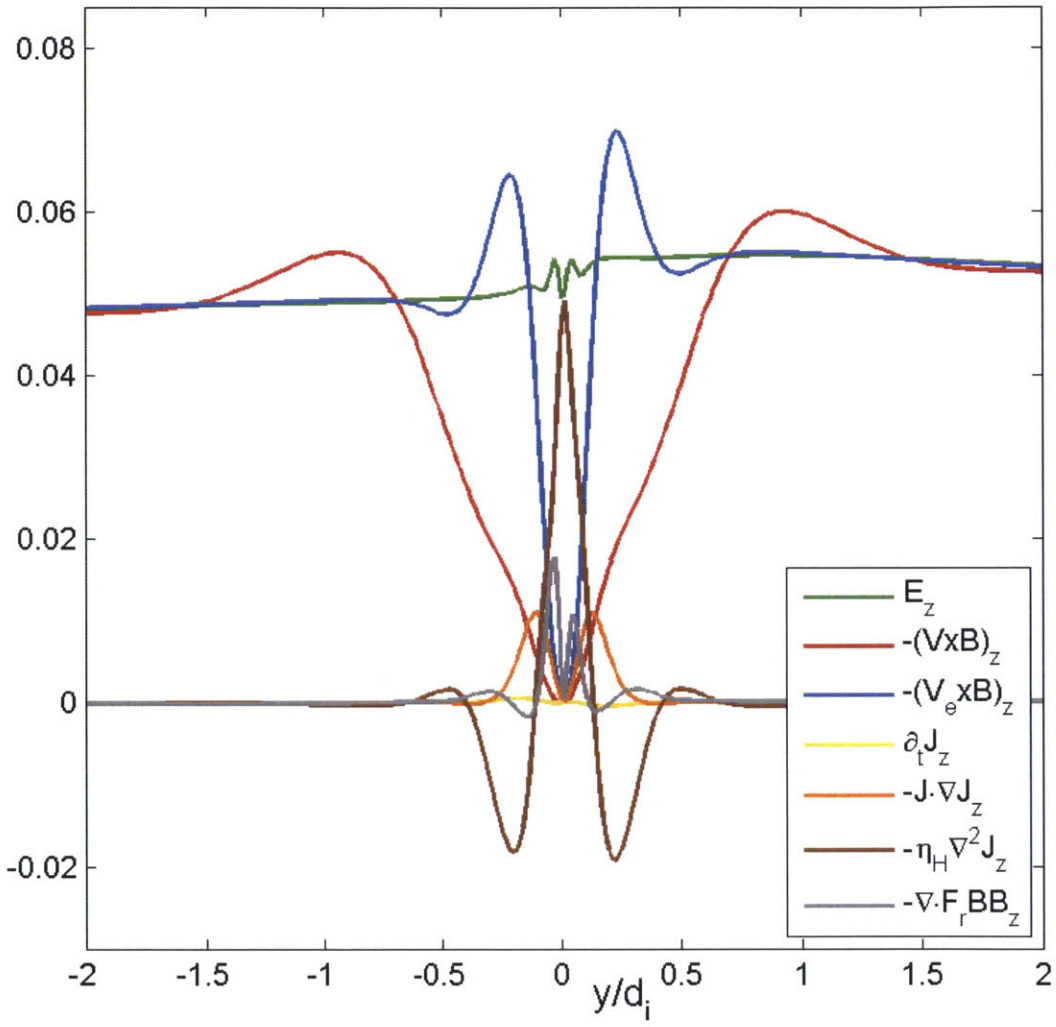

Figure 6-24: Cut across the x-line of the anisotropic simulation for $\beta_e = .03$ and $B_g = .28B_0$ at $t\Omega_i = 87$, showing the contributions to the out-of-plane electric field using the generalized Ohm's Law 6.7

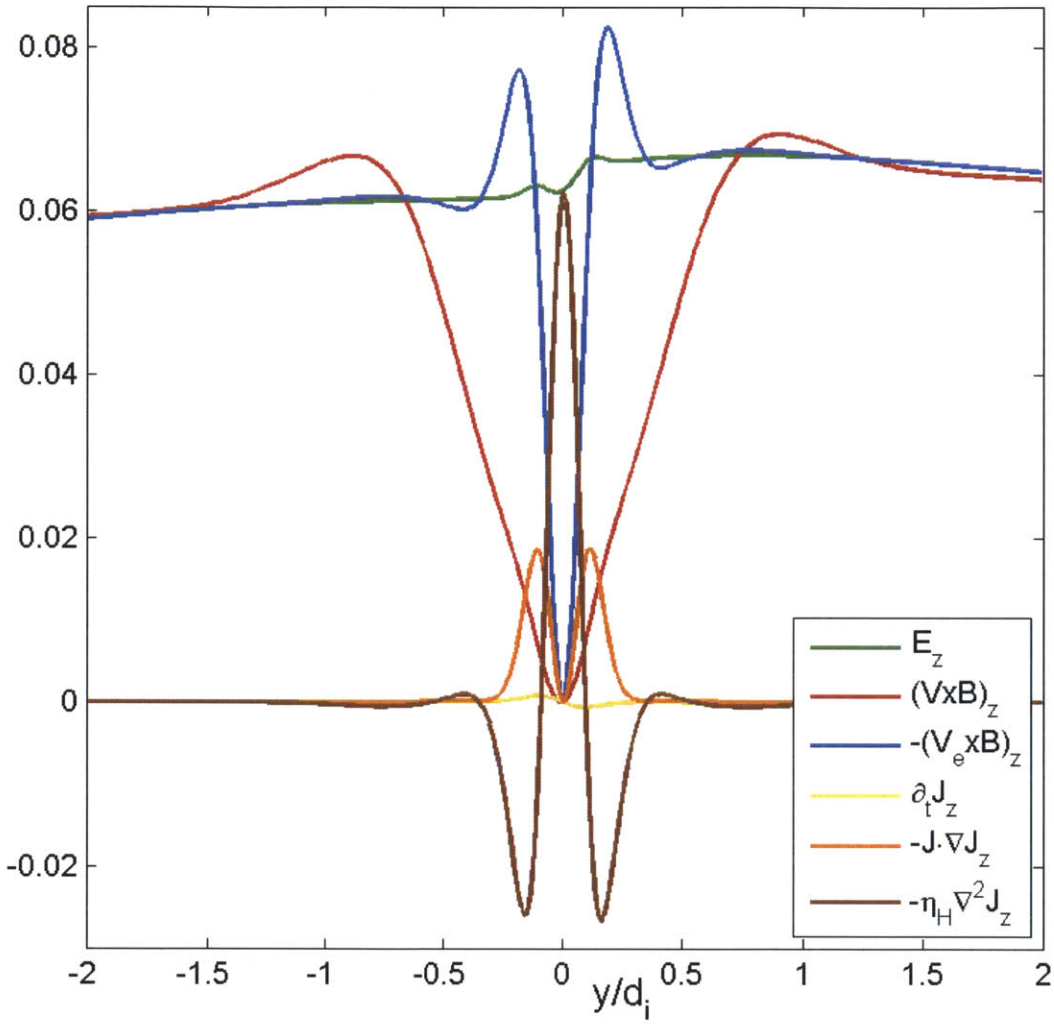

Figure 6-25: Cut across the x-line of the isotropic simulation for $\beta_e = .03$ and $B_g = .28B_0$ at $t\Omega_i = 87$, showing the contributions to the out-of-plane electric field using generalized Ohm's Law

$\boldsymbol{E}'$ in electron fluid reference frame is given by

$$\boldsymbol{E}' \approx \boldsymbol{E} + \boldsymbol{V}_e \times \boldsymbol{B}. \tag{6.8}$$

Note that parallel electric fields are unaffected by this transformation. Ohm's Law 6.7 reduces to

$$\boldsymbol{E}' = \xi \frac{\partial}{\partial t}\left(\frac{\boldsymbol{J}}{ne}\right) - \xi \frac{\boldsymbol{J}}{ne} \cdot \nabla \frac{\boldsymbol{J}}{ne} - \eta_H \nabla^2 \frac{\boldsymbol{J}}{n} - \frac{1}{n}\Big[\nabla p_{e\perp} + \nabla \cdot (\mathscr{F}_e \boldsymbol{B}\boldsymbol{B})\Big]. \tag{6.9}$$

Figure 6-26 is a similar plot of the out-of-plane electric field in the electron fluid reference frame across the layer along the line $y = 0$. The current diffusion region and the role of hyper-resistivity on the fluid-frame electric field is evident.

The dominant terms of the fluid-frame electric field can also be studied along the layer. Here, the path along the layer $y_p = s(x)$ is defined by the maximum total electron fluid speed such that $V_e(x, y_p)$ is a maximum for a given x-position. A plot of $s(x)$ for the anisotropic isotropic simulation is shown in Figure 6-27. The isotropic path is not smooth further from the x-line because these simulations typically have very short current layers concentrated near the x-line. Data along both paths is smoothed in an attempt to remove artificial noise generated by down-sampling simulation results.

The terms of the z-component of the fluid-frame electric field E'_z for the anisotropic simulation is plotted in Figure 6-28. Near the x-line at $x = 0$, E'_z is dominated by off-diagonal components of the electron pressure, represented by hyper-resistivity, while further from the x-line, the gyrotropic pressure, represented by the new EoS, dominates. Surprisingly, the hyper-resistivity remains significant away from the x-line and appears necessary to temper the contributions from the gyrotropic electron pressure. Further investigation is necessary to determine if off-diagonal pressure plays a similar role in kinetic simulations. A similar plot of E'_z is shown in Figure 6-29 for a corresponding isotropic simulation. Here, the fluid-frame electric field is confined to the region near the x-line, and the hyper-resistivity term is much smaller than in the anisotropic run.

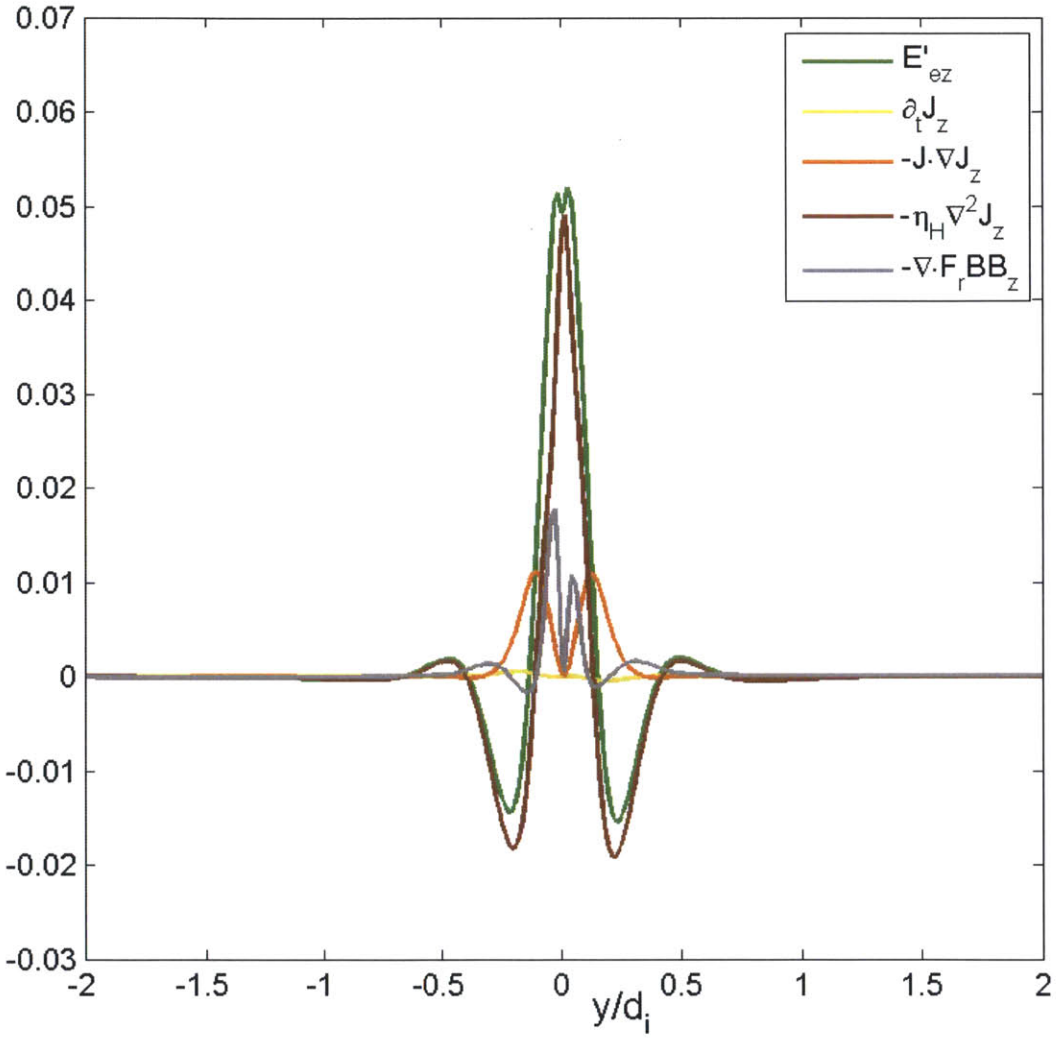

Figure 6-26: Cut across the x-line of the anisotropic simulation for $\beta_e = .03$ and $B_g = .28B_0$ at $t\Omega_i = 87$, showing the contributions to the electron frame, out-of-plane electric field using the transformed Ohm's Law 6.9

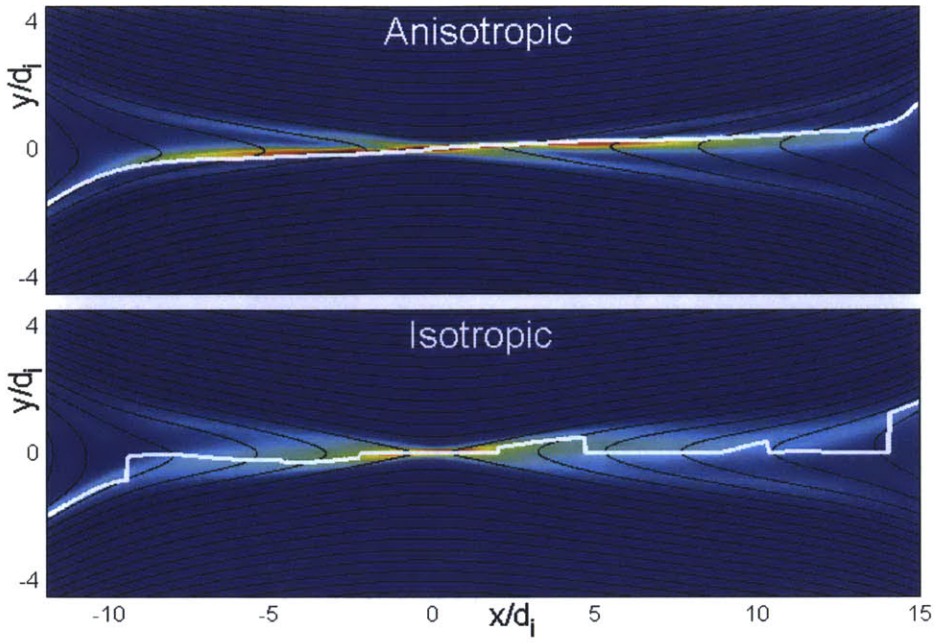

Figure 6-27: Out-of-plane current density of simulations for $\beta_e = .03$ and $B_g = .28B_0$ at $t\Omega_i = 87$ with superimposed path defined by the maximum total electron speed.

The fluid-frame electric field along the layer E'_s and its component terms are plotted in Figure 6-30. Here, very near the x-line, the gyrotropic pressure dominates, while further away it still remains significant. However, hyper-resistivity is the dominant term downstream for the x-line. Once again, kinetic simulation are needed to further investigate this phenomena. A similar plot E'_s is shown in Figure 6-31 for a corresponding isotropic simulation. Once again, the fluid-frame electric field is confined to the region near the x-line, and the hyper-resistivity term is much smaller than in the anisotropic run.

These types of plots can also be used to determine the dominant terms of the gyrotropic part of the electron pressure. The divergence of the diagonal part of the electron pressure can be written as

$$\nabla \cdot \left[p_{e\perp} \bar{\mathbf{I}} + \mathscr{F} \frac{\boldsymbol{B}\boldsymbol{B}}{\mu_0} \right] = \mathscr{F}_e \boldsymbol{J} \times \boldsymbol{B} + \left(\nabla p_{e\perp} + \mathscr{F}_e \nabla \tfrac{1}{2} B^2 \right) \cdot \left(\bar{\mathbf{I}} - \hat{b}\hat{b} \right) + \left(\nabla p_{e\parallel} - \mathscr{F}_e \nabla \tfrac{1}{2} B^2 \right) \cdot \hat{b}\hat{b}. \tag{6.10}$$

The different contributions to the parallel electric field $E_\parallel$ along the layer are shown in

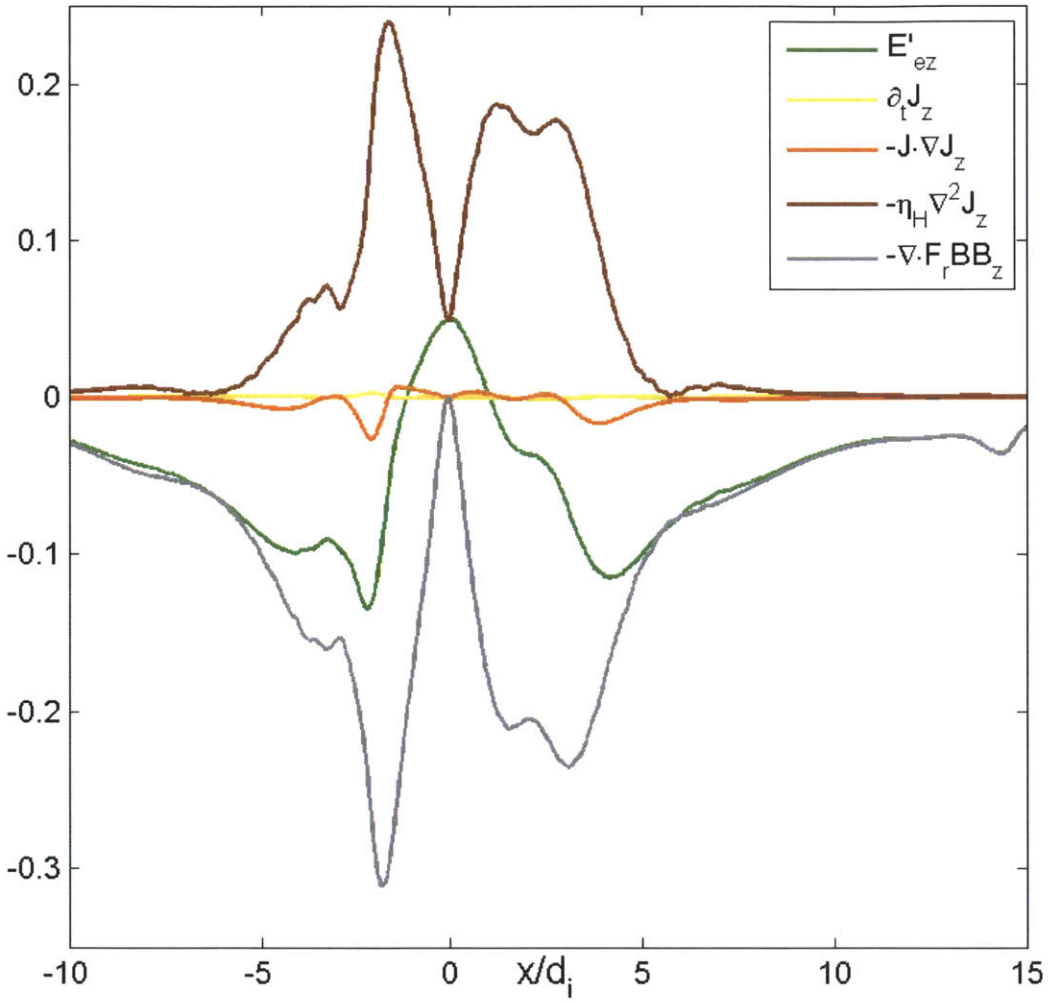

Figure 6-28: Cut along the layer of the anisotropic simulation for $\beta_e = .03$ and $B_g = .28B_0$ at $t\Omega_i = 87$, showing the contributions to the electron frame, out-of-plane electric field using the transformed Ohm's Law 6.9

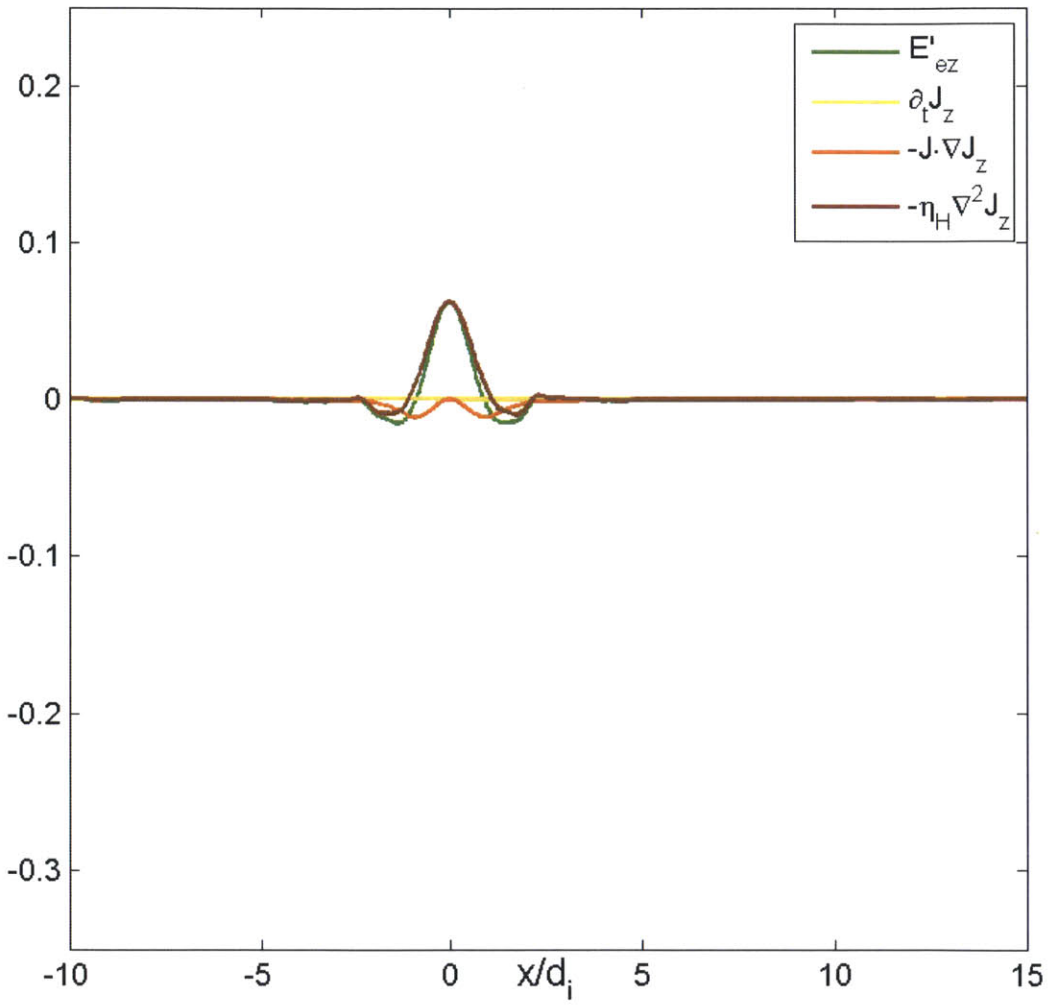

Figure 6-29: Cut along the layer of the isotropic simulation for $\beta_e = .03$ and $B_g = .28B_0$ at $t\Omega_i = 87$, showing the contributions to the electron frame, out-of-plane electric field using the transformed Ohm's Law

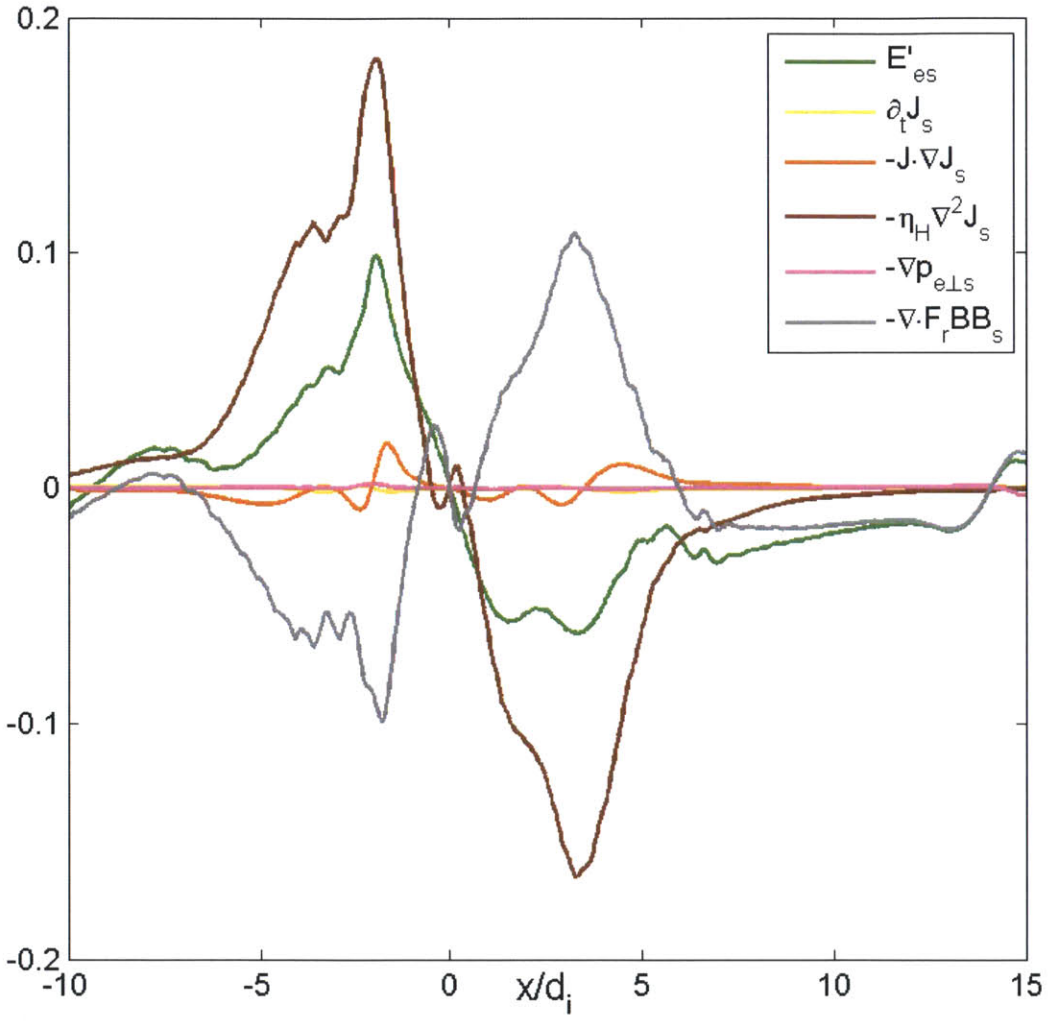

Figure 6-30: Cut along the layer of the anisotropic simulation for $\beta_e = .03$ and $B_g = .28B_0$ at $t\Omega_i = 87$, showing the contributions to the electron frame electric field along the layer using the transformed Ohm's Law 6.9

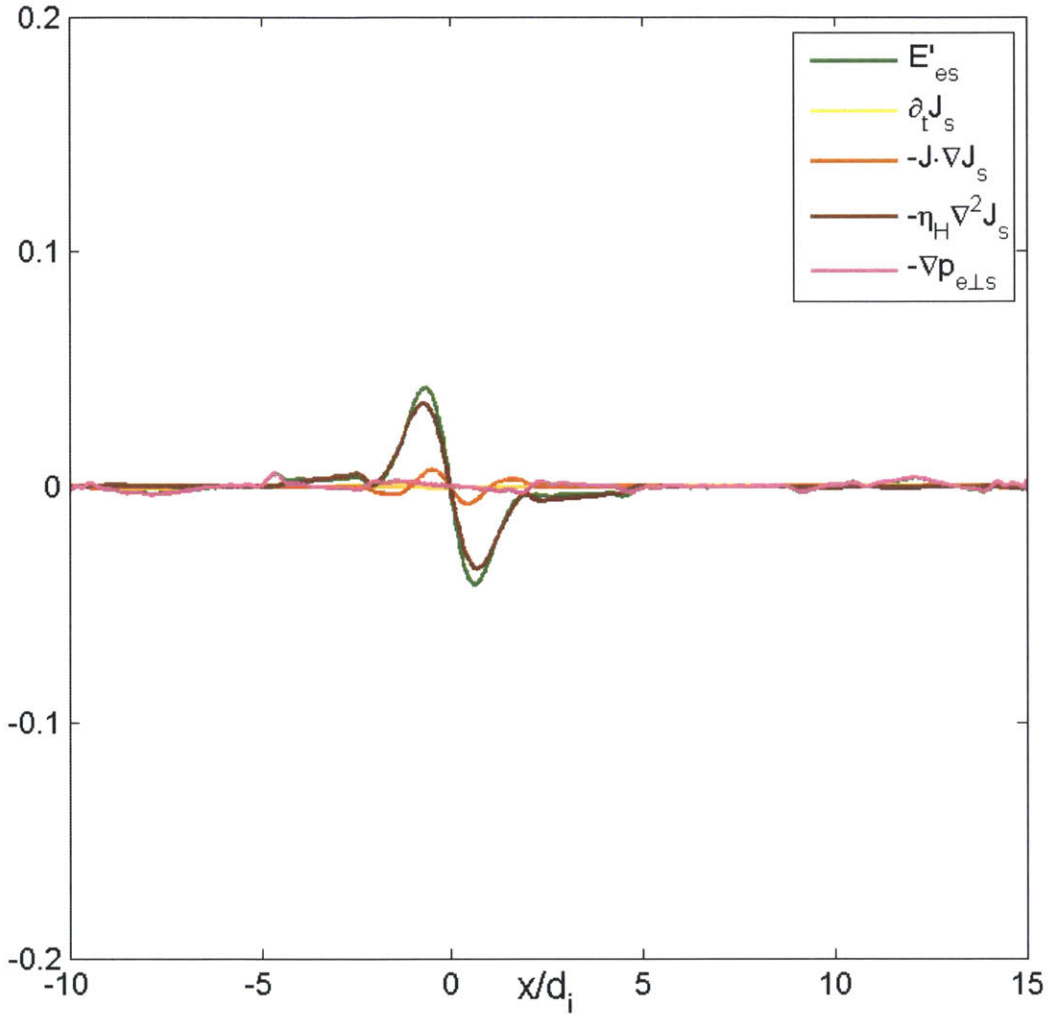

Figure 6-31: Cut along the layer of the isotropic simulation for $\beta_e = .03$ and $B_g = .28B_0$ at $t\Omega_i = 87$, showing the contributions to the electron frame electric field along the layer using the transformed Ohm's Law

Figure 6-32 where the electron pressure term has been separated as shown in 6.10. In Figure 6-32, the dominant component of the diagonal electron pressure is the $\hat{b}\hat{b}\cdot\nabla p_{e\|}$ which is nearly balanced by the hyper-resistivity.

Different contributions to the component of plasma frame electric field $\boldsymbol{E}'' = \boldsymbol{E} + \boldsymbol{V}\times\boldsymbol{B}$ in the $\boldsymbol{J}\times\boldsymbol{B}$ direction are plotted in Figure 6-33 where the electron pressure term has been separated as in 6.10. Here the dominant contributions include the $\mathscr{F}_e\boldsymbol{J}\times\boldsymbol{B}$ and $\mathscr{F}_e\left(\bar{\mathbf{I}}-\hat{b}\hat{b}\right)\cdot\nabla\frac{1}{2}B^2$ in addition to the Hall term.

In contrast to the previous two components, neither the electric field nor any terms from the generalized Ohm's Law 6.7 are found to be significant in the $\boldsymbol{B}\times(\boldsymbol{J}\times\boldsymbol{B})$. Based on Figures 6-32 and 6-33, it appears the Hall and gyrotropic pressure terms during steady reconnection may be approximated as

$$\begin{aligned}\boldsymbol{J}\times\boldsymbol{B}-\nabla\cdot\left[p_{e\perp}\bar{\mathbf{I}}+\mathscr{F}\frac{\boldsymbol{B}\boldsymbol{B}}{\mu_0}\right] &\approx(1-\mathscr{F}_e)\,\boldsymbol{J}\times\boldsymbol{B}-\mathscr{F}_e\left(\bar{\mathbf{I}}-\hat{b}\hat{b}\right)\cdot\nabla\tfrac{1}{2}B^2-\hat{b}\hat{b}\cdot\nabla p_{e\|}\\ &\approx-\mathscr{F}_e\left(\bar{\mathbf{I}}-\hat{b}\hat{b}\right)\cdot\nabla\tfrac{1}{2}B^2-\hat{b}\hat{b}\cdot\nabla p_{e\|},\end{aligned}\tag{6.11}$$

where the second relation holds if $\mathscr{F}_e\sim 1$. Fluid simulation which make use of this simplification could examine if this is sufficient for fast reconnection.

This section examined the structure of the reconnection current layer as it depends on the guide-field strength and upstream electron temperature. The next section will examine these parameters in relation to electron temperature of the reconnection region.

6.3 Scaling Laws for Anisotropic Current Layers

During magnetic reconnection in weakly collisional plasmas, the EoS relates the development of anisotropic electron pressure to the density and magnetic field. In steady reconnection, the value of these quantities can be calculated by appealing to the conservation of plasma momentum across and along the current layer.

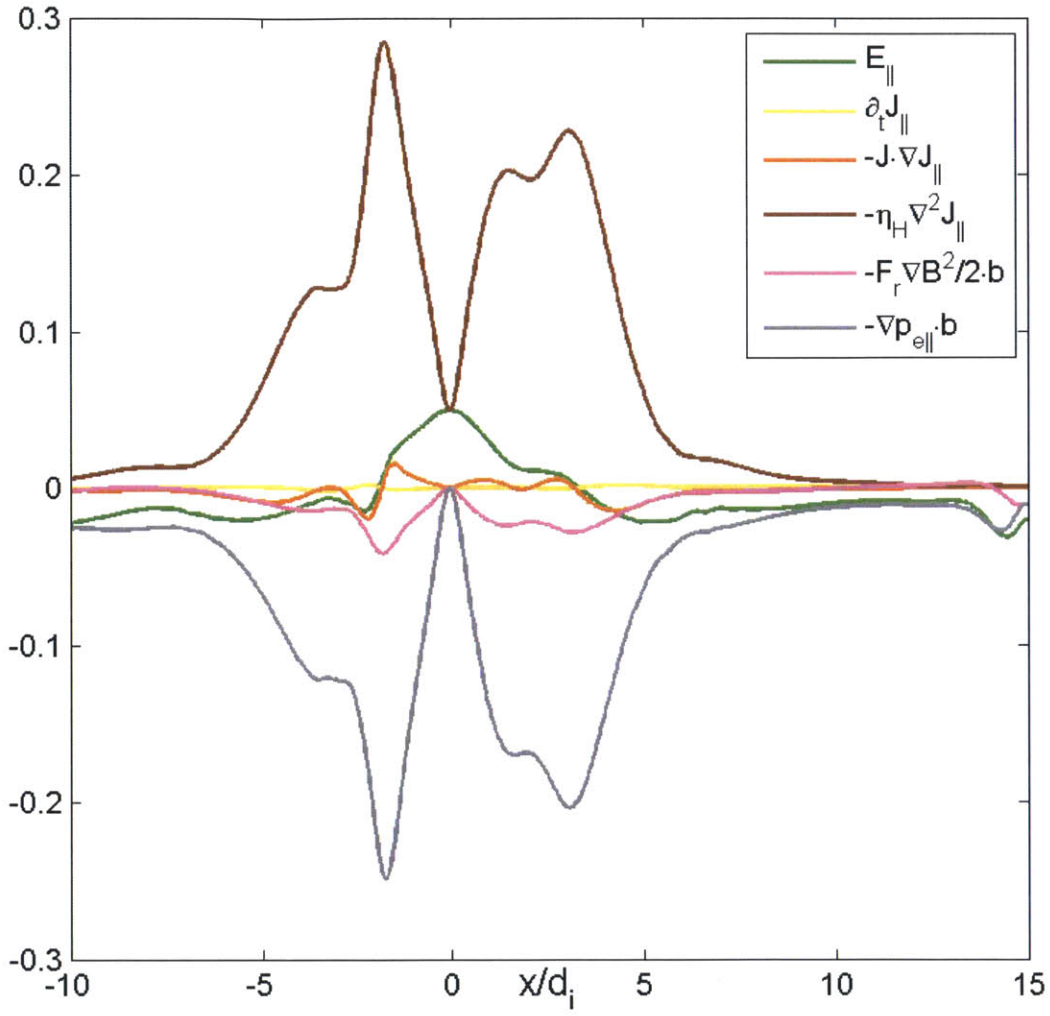

Figure 6-32: Cut along the layer of the anisotropic simulation for $\beta_e = .03$ and $B_g = .28B_0$ at $t\Omega_i = 87$, showing the contributions to the parallel electric field using generalized Ohm's Law 6.7 and the decomposition 6.10

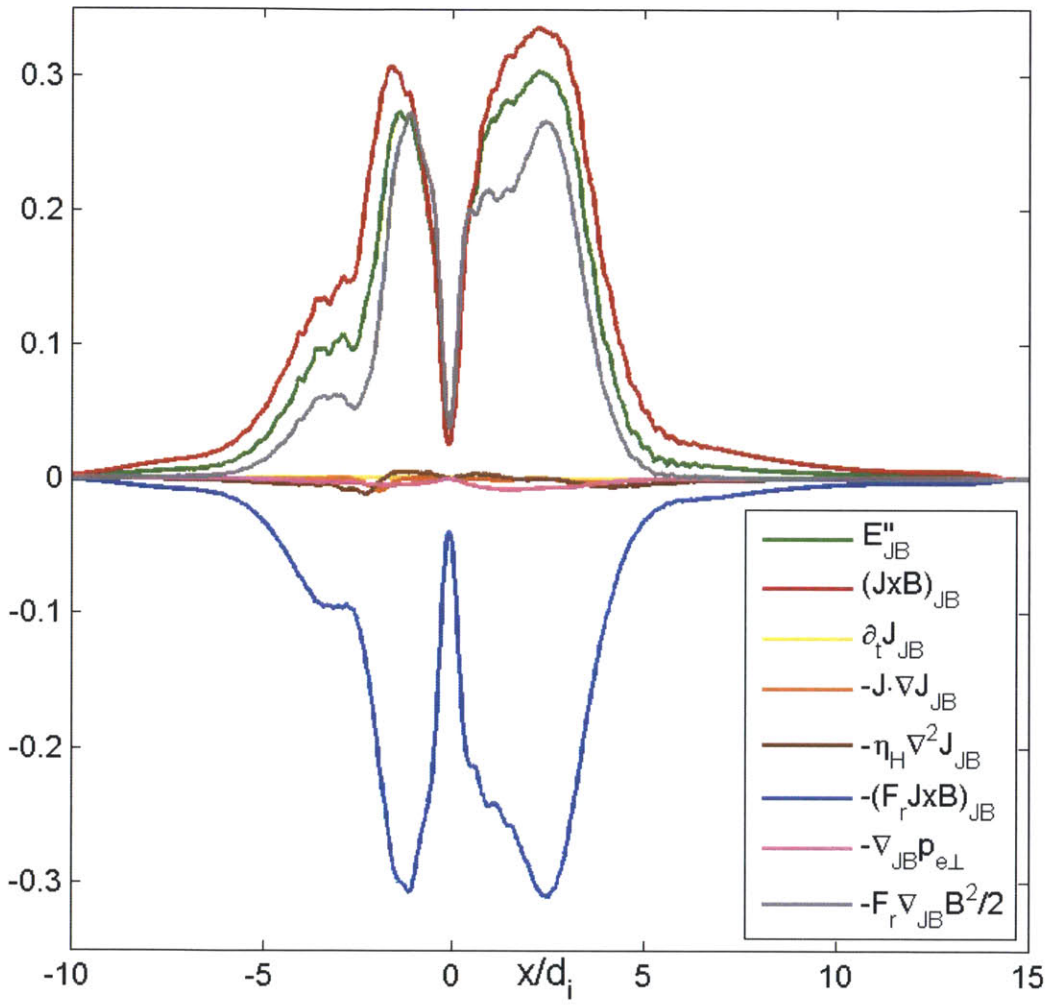

Figure 6-33: Cut along the layer of the anisotropic simulation for $\beta_e = .03$ and $B_g = .28B_0$ at $t\Omega_i = 87$, showing the contributions to the plasma frame, electric field in the $\boldsymbol{J} \times \boldsymbol{B}$ direction using generalized Ohm's Law 6.7 and the decomposition 6.10

In steady state, total momentum equation can be written as

$$\nabla \cdot \bar{\mathbf{T}} = 0, \tag{6.12}$$

where

$$\bar{\mathbf{T}} = mn\boldsymbol{V}\boldsymbol{V} + \left(p_i + p_{e\perp} + \frac{B^2}{2\mu_0}\right)\bar{\mathbf{I}} - (1 - \mathscr{F}_e)\frac{\boldsymbol{B}\boldsymbol{B}}{\mu_0} - mn\nu_i\left[\nabla\boldsymbol{V} + (\nabla\boldsymbol{V})^T - \frac{2}{3}(\nabla\cdot\boldsymbol{V})\bar{\mathbf{I}}\right]. \tag{6.13}$$

This expression can be applied to a 2.5 dimensional system with a reversing component of the magnetic field and a current sheet centered about the neutral sheet as dictated by Ampere's Law. Using the same coordinates as those used in the simulations, the neutral sheet is located at $y = 0$ and the system is symmetric about this plane as well. The reversing magnetic field component is taken to be in the x direction, and B_x is the upstream value of the reversing magnetic field. Let λ be the current sheet half-thickness and L_x be the scale of variation along the x direction. Integrating the x-component of 6.12 from the neutral line $y = 0$ to $y = \lambda$

$$\int_0^\lambda \mathrm{d}y\, \nabla \cdot \bar{\mathbf{T}} \cdot \hat{x} = \int_0^\lambda \mathrm{d}y\, \nabla \cdot \left(\bar{\mathbf{T}} \cdot \hat{x}\right) = 0 \tag{6.14}$$

yields

$$mnV_yV_x - (1 - \mathscr{F}_e)\frac{B_yB_x}{\mu_0} - mn\nu_i\left(\partial_yV_x + \partial_xV_y\right) + \int_0^\lambda \mathrm{d}y\, \frac{\partial}{\partial x}\Bigg\{mnV_x^2 + \left(p_i + p_{e\perp} + \frac{B_T^2}{2\mu_0}\right) - (1 - \mathscr{F}_e)\frac{B_x^2}{\mu_0} - \frac{2}{3}mn\nu_i\left(2\,\partial_xV_x - \partial_yV_y\right)\Bigg\} = 0, \tag{6.15}$$

where B_x, V_y, ∂_xV_y, and ∂_yV_x vanish when $y = 0$ by symmetry and quantities outside an integral are evaluated at $y = \lambda$. Similarly, the y component of 6.12 can be

integrated yielding

$$
\begin{aligned}
&mnV_y^2 + \left(p_i + p_{e\perp} + \frac{B^2}{2\mu_0}\right) - (1-\mathscr{F}_e)\frac{B_y^2}{\mu_0} - \frac{2}{3}mn\nu_i\Big(2\,\partial_y V_y - \partial_x V_x\Big) \\
&\quad + \int_0^{\lambda} \mathrm{d}y\, \frac{\partial}{\partial x}\left\{ mnV_yV_x - (1-\mathscr{F}_e)\frac{B_yB_x}{\mu_0} - mn\nu_i\Big(\partial_y V_x + \partial_x V_y\Big)\right\} \\
&\quad = \left\{ mnV_y^2 + \left(p_i + p_{e\perp} + \frac{B^2}{2\mu_0}\right) - (1-\mathscr{F}_e)\frac{B_y^2}{\mu_0} - \frac{2}{3}mn\nu_i\Big(2\,\partial_y V_y - \partial_x V_x\Big)\right\}\Bigg|_{y=0}.
\end{aligned}
\tag{6.16}
$$

Assuming thin current sheets such that at $y = \lambda$

$$
\frac{\lambda}{L_x} \ll \frac{B_y}{B_x}, \tag{6.17}
$$

the integrals in 6.15 and 6.16 are small compared to the evaluated terms. In addition taking $V < V_A$ at $y = \lambda$ and negligible viscosity, 6.15 reduces to $(1-\mathscr{F}_e)B_yB_x/\mu_0 \simeq 0$, and for nonzero B_x and B_y

$$
\frac{B^2}{\mu_0} - \left(p_{e\parallel} - p_{e\perp}\right) \simeq 0. \tag{6.18}
$$

This is the marginal firehose condition. Here the magnetic tension is balanced by electron pressure anisotropy. In the case of isotropic plasma, this condition is far from satisfied and magnetic tension is balanced by pressure gradients along the neutral sheet, such that 6.17 is also not satisfied and the system is inherently two-dimensional. Using the same assumptions as before, including 6.17 and 6.18, 6.16 reduces to

$$
p_i + p_{e\perp} + \frac{B^2}{2\mu_0} = \frac{1}{2}K_{yy}. \tag{6.19}
$$

This is an equations of perpendicular pressure balance, where K_{yy} is a constant, and is approximately twice the perpendicular pressure at the neutral sheet. These conditions were first derived to describe magnetotail equilibria [216,217], and can be found directly by assuming one dimensional equilibrium [218].

During steady reconnection, plasma flows are also nearly steady such that

$$\nabla \cdot \bar{\mathbf{T}} = \frac{\partial}{\partial t}(mn\boldsymbol{V}) \simeq 0. \tag{6.20}$$

Therefore, in reconnection scenarios where strong anisotropy develops, 6.18 and 6.19 should still nearly hold. The elongated current sheets seen in anisotropic reconnection scenarios are a result of the existence of 1D equilibria similar to steady reconnection. Using the new EoS for electron pressure and assuming ions behave adiabatically yields a system of equations for the density and magnetic field near the neutral sheet. In the large anisotropy limit, $\tilde{n}^3/\tilde{B}^2 \gg 1$ and the electron pressure is approximately

$$\tilde{p}_{e\parallel} \simeq \frac{\pi}{6}\left(\frac{\tilde{n}^3}{\tilde{B}^2} - \frac{1}{2}\right) \tag{6.21}$$

$$\tilde{p}_{e\perp} \simeq \tilde{n}\tilde{B}, \tag{6.22}$$

where for quantity Q, $\tilde{Q} = Q/Q_\infty$ and Q_∞ is the value of the quantity far upstream from the current sheet. Adiabatic ion pressure is approximated as

$$\frac{p_i}{n^\Gamma} \simeq \frac{p_{i\infty}}{n_\infty^\Gamma} \Rightarrow \tilde{p}_i \simeq \tilde{n}^\Gamma, \tag{6.23}$$

where Γ is the adiabatic index, and taken to be 5/3. Inserting these expressions into 6.18 and 6.19 yields

$$\tilde{B}^2 - \left[\frac{\pi}{12}\left(\frac{\tilde{n}^3}{\tilde{B}^2} - \frac{1}{2}\right)\beta_{e\infty} - \frac{1}{2}\tilde{n}\tilde{B}\beta_{e\infty}\right] = \tilde{F} \tag{6.24}$$

$$\frac{1}{2}\tilde{n}^\Gamma R_\infty \beta_{e\infty} + \frac{1}{2}\tilde{n}\tilde{B}\beta_{e\infty} + \frac{\tilde{B}^2}{2} = \tilde{\alpha}\left(\frac{1}{2}\beta_{i\infty} + \frac{1}{2}\beta_{e\infty} + \frac{1}{2}\right), \tag{6.25}$$

where the expressions have been normalized by B_∞^2/μ_0, $\beta_{e\infty} = 2\mu_0 p_{e\infty}/B_\infty^2$, $R_\infty = p_{i\infty}/p_{e\infty}$, $\tilde{F}$ represents a small deviation from the marginal firehose condition, and $\tilde{\alpha}$ represents the ratio of the total perpendicular pressure of the neutral sheet to its

upstream value. Assuming $\beta_{e\infty}^{2/3} \ll 1$, then, to lowest order,

$$\tilde{B} \simeq \left[\tilde{\alpha}\frac{1+(1+R_\infty)\,\beta_{e\infty}}{1+c_0^\Gamma \beta_{e\infty}^{4/9} R_\infty}\right]^{1/2} \simeq \left[\frac{\tilde{\alpha}}{1+c_0^\Gamma \beta_{e\infty}^{4/9} R_\infty}\right]^{1/2} \tag{6.26}$$

$$\tilde{n} \simeq \frac{c_0}{\beta_{e\infty}^{1/3}}\left[\tilde{\alpha}\frac{1+(1+R_\infty)\,\beta_{e\infty}}{1+c_0^\Gamma \beta_{e\infty}^{4/9} R_\infty}\right]^{2/3} \simeq \frac{c_0}{\beta_{e\infty}^{1/3}}\left[\frac{\tilde{\alpha}}{1+c_0^\Gamma \beta_{e\infty}^{4/9} R_\infty}\right]^{2/3}, \tag{6.27}$$

where $c_0 = (12/\pi)^{1/3}$. Note the weak dependence on R_∞. Decreasing this ratio increases both the parallel and perpendicular pressures in the layer region, while slightly decreasing their ratio. The net result is that the layer more readily satisfies the marginal firehose condition 6.18.

The above analysis can also be applied to the simulations performed above. Using the full EoS in the marginal firehose condition and perpendicular force balance equations yields

$$\frac{B^2}{\mu_0} - \left[p_{e\parallel}(\tilde{n},\tilde{B}) - p_{e\perp}(\tilde{n},\tilde{B})\right] = \tilde{F} \tag{6.28}$$

$$\tilde{n}^\Gamma p_{i\infty} + p_{e\perp}(\tilde{n},\tilde{B}) + \frac{B^2}{2\mu_0} = \tilde{\alpha}\left(p_{i\infty} + p_{e\infty} + \frac{B_\infty^2}{2\mu_0}\right). \tag{6.29}$$

Expressions for $\tilde{n}$ and $\tilde{B}$ are obtained by numerically solving this system of equations. The solutions are compared to values obtained from simulation results. For each integer ion gyrotime, quantities are binned by spatially averaging over small regions of size $.8d_e \times 3d_e$ along the layer; the span of one such bin is depicted by the white box in Figure 6-34. Only values from bins where the (averaged) normalized value of the firehose condition satisfies $F < .1$ are retained. Simulations at guide-field $B_g = .81$ did not yield bins that satisfied the firehose constraint.

A plot of the normalized firehose condition versus alpha factor for all bins at all times is shown in Figure 6-35. The variation of the data from the marginal firehose condition is due in part to the strength of condition 6.17, that is, the layer is not strictly one dimensional. Also, though the firehose condition is violated in some simulations, indicating these layers are firehose unstable, the instability is not observed to grow significantly in all these simulations for a number of reasons. The

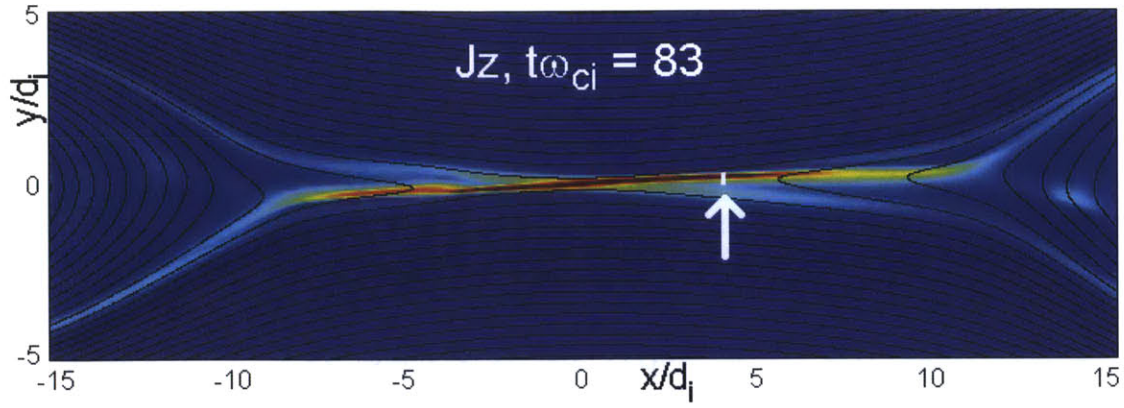

Figure 6-34: Out-of-Plane current density with in-plane magnetic field lines. The white box depicts a region over which quantities are spatially averaged to obtain one current-layer bin at $t\Omega_i = 83$.

MHD firehose instability growth rate depends on the parallel wavevector and in the layer, the magnetic field has a significant component in the out-of-plane, ignorable, direction. Also dissipative terms can dampen the instability. Finally, the EMHD description does not permit the firehose instability, so fluid models that reduce to EMHD descriptions at the smallest scales may not develop the instability if firehose unstable regions are confined to small scales.

Plots of bin data for the density, magnetic field, parallel and perpendicular electron pressures, and the pressure anisotropy ratio $p_{e\parallel}/p_{e\perp}$ for all times versus α are shown in Figures 6-36, 6-37, 6-38, 6-39, and 6-40, respectively. Lines represent predicted values of quantities for different levels of the firehose condition. Data from bins are mostly confined within the range of predicted values, in a similar manner to the actual firehose values of the bins, depicted in Figure 6-35.

The use of nominal values of the firehose value F and the α parameter in 6.28 and 6.29 allow the prediction of layer conditions based on upstream values of density, magnetic field, and species temperatures. In Figure 6-41, nominal values of $F = .09$ and $\alpha = .5$ are used to calculate predicted values of layer density, magnetic field, and electron pressures as functions of electron beta with $T_{i\infty}/T_{e\infty} = 4$ and compared to bins within $\pm 5\%$ of these values. Values found from simulation are in good agreement with predicted values.

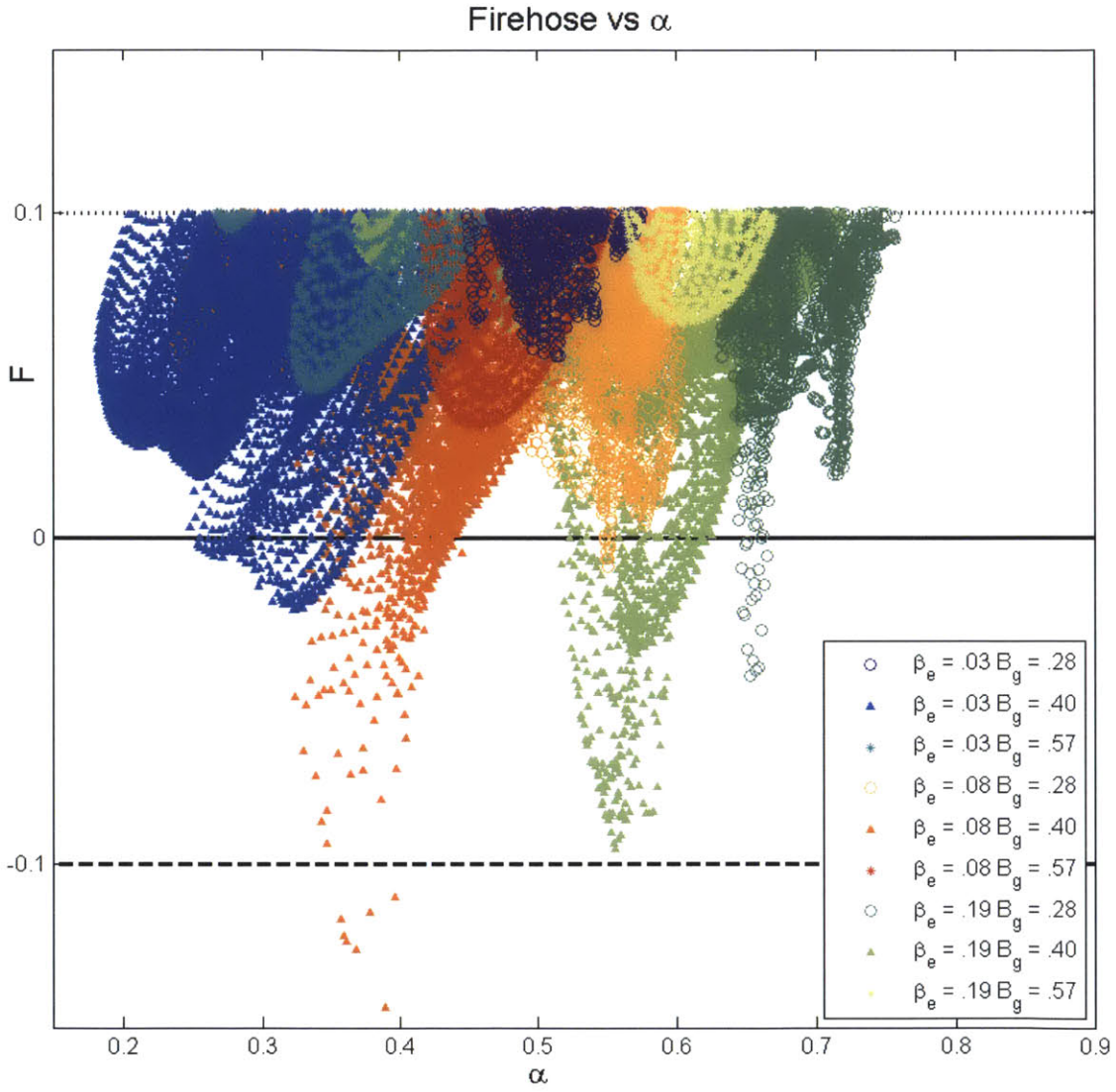

Figure 6-35: Firehose value of layer bins as a function of α.

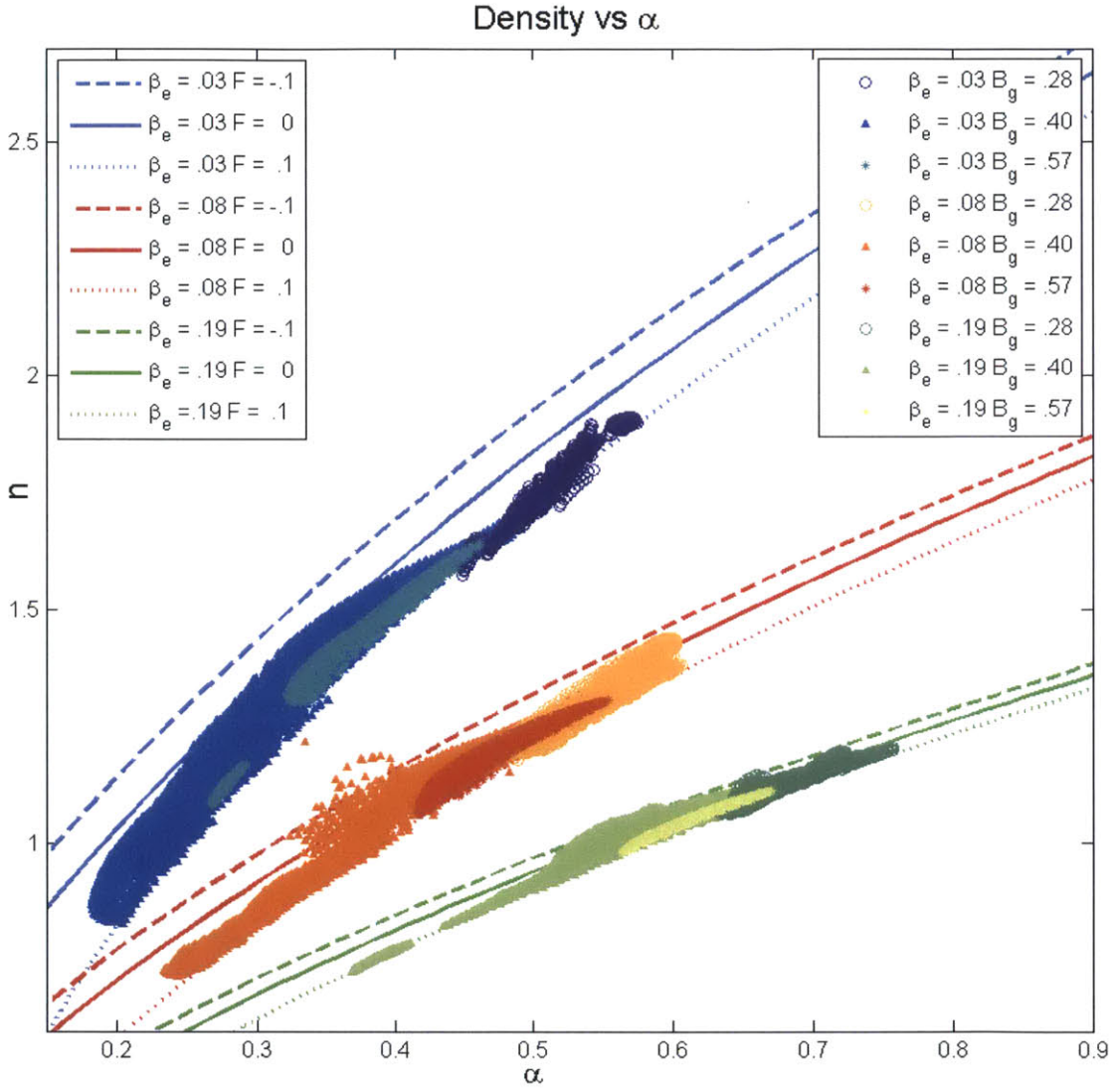

Figure 6-36: Density of layer bins as a function of α. Dotted, solid, and dashed lines indicates value predicted with firehose value of $F = .1$, $F = 0$, and $F = -.1$ respectively.

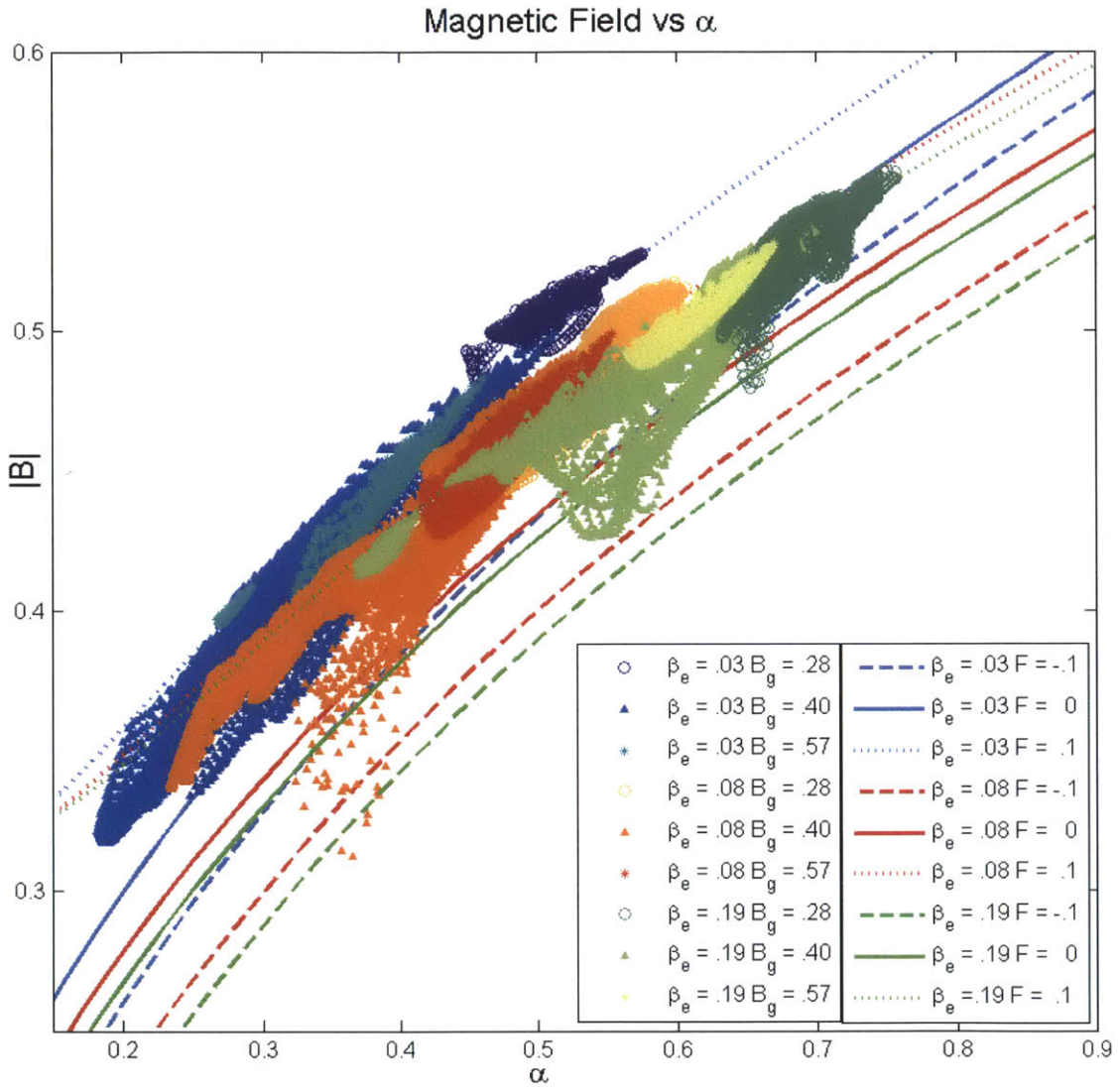

Figure 6-37: Magnetic Field of layer bins as a function of α. Dotted, solid, and dashed lines indicates value predicted with firehose value of $F = .1$, $F = 0$, and $F = -.1$ respectively.

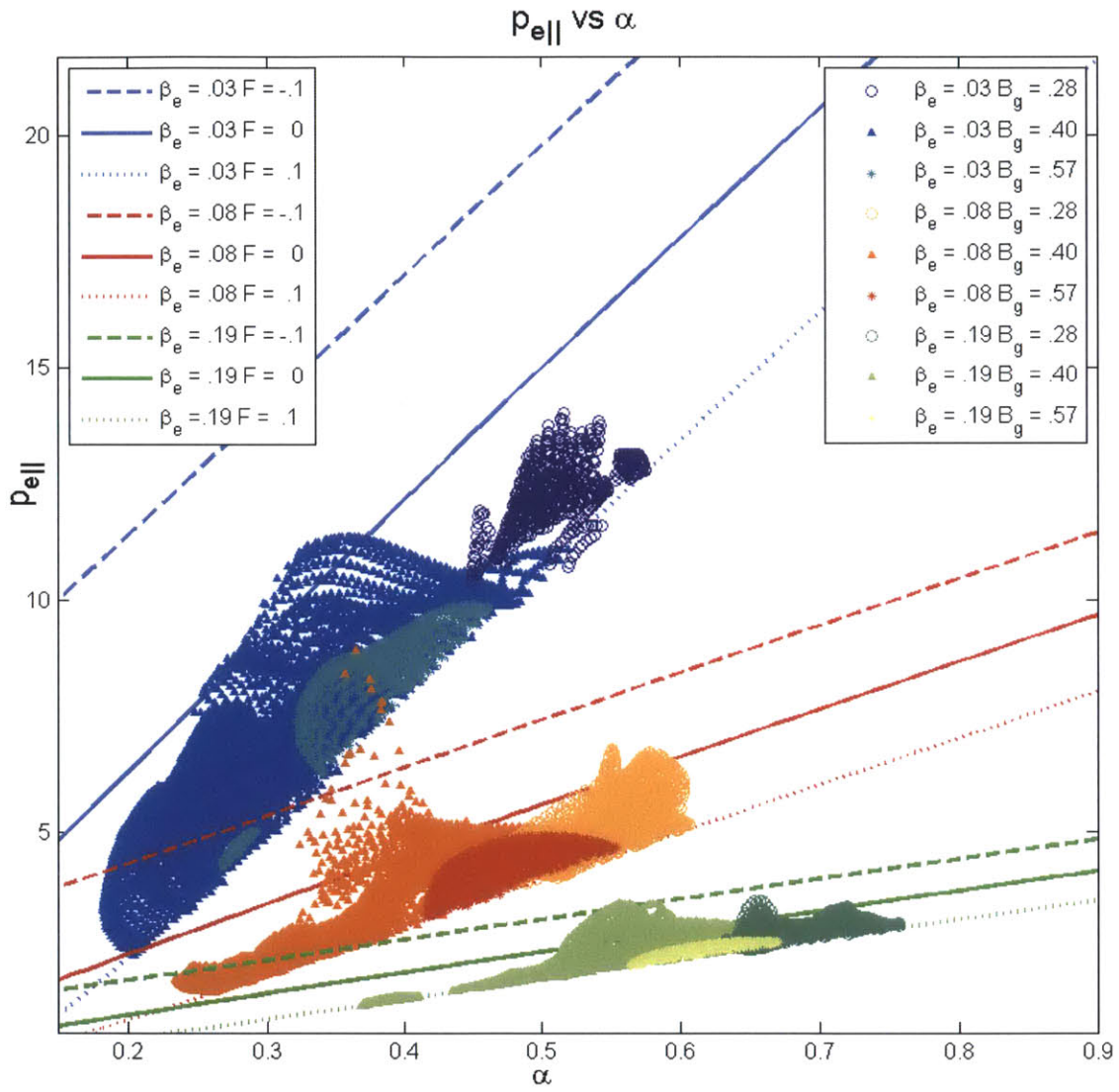

Figure 6-38: Parallel electron pressure of layer bins as a function of α. Dotted, solid, and dashed lines indicates value predicted with firehose value of $F = .1$, $F = 0$, and $F = -.1$ respectively.

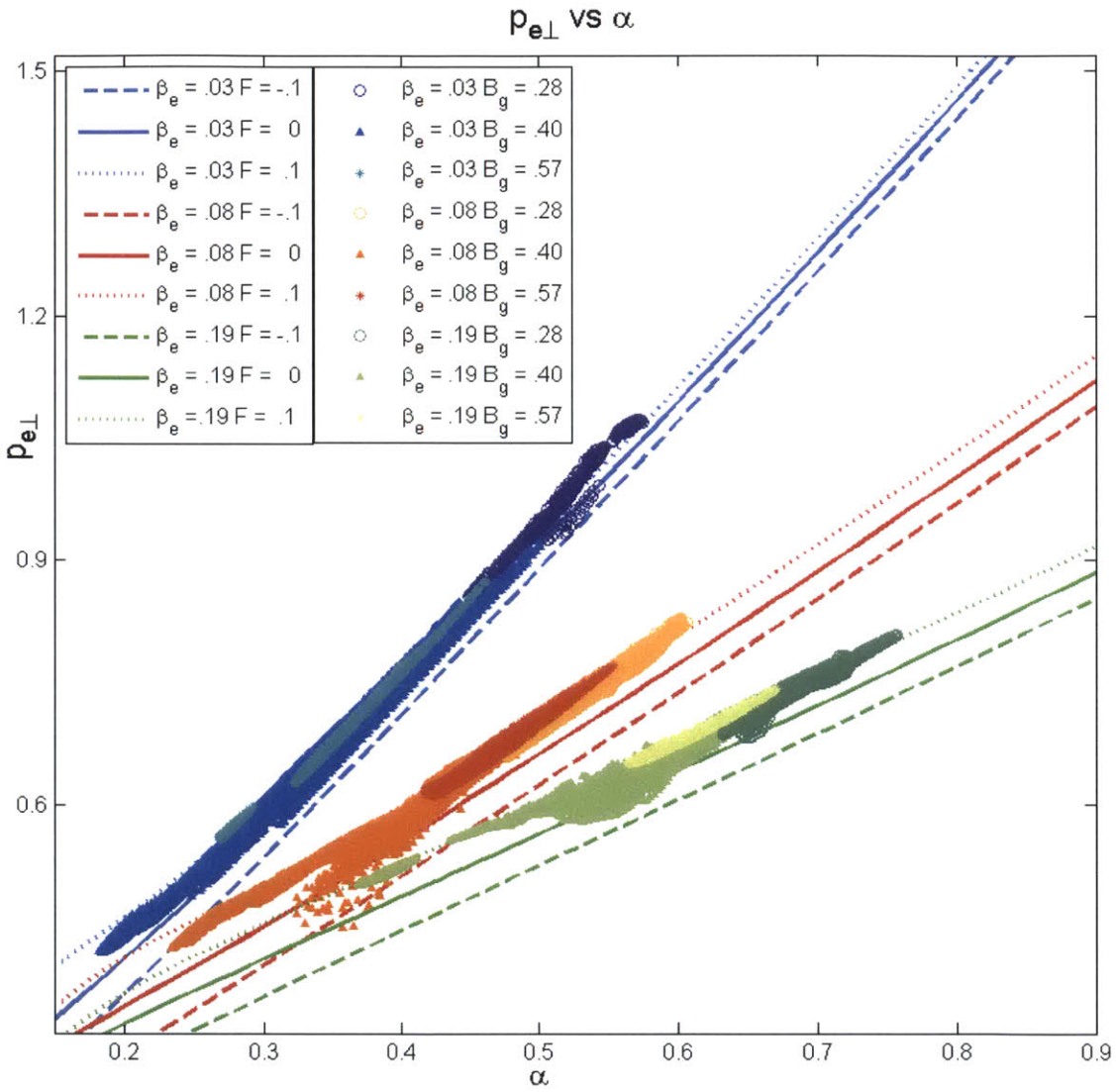

Figure 6-39: Perpendicular electron pressure of layer bins as a function of α. Dotted, solid, and dashed lines indicates value predicted with firehose value of $F = .1$, $F = 0$, and $F = -.1$ respectively.

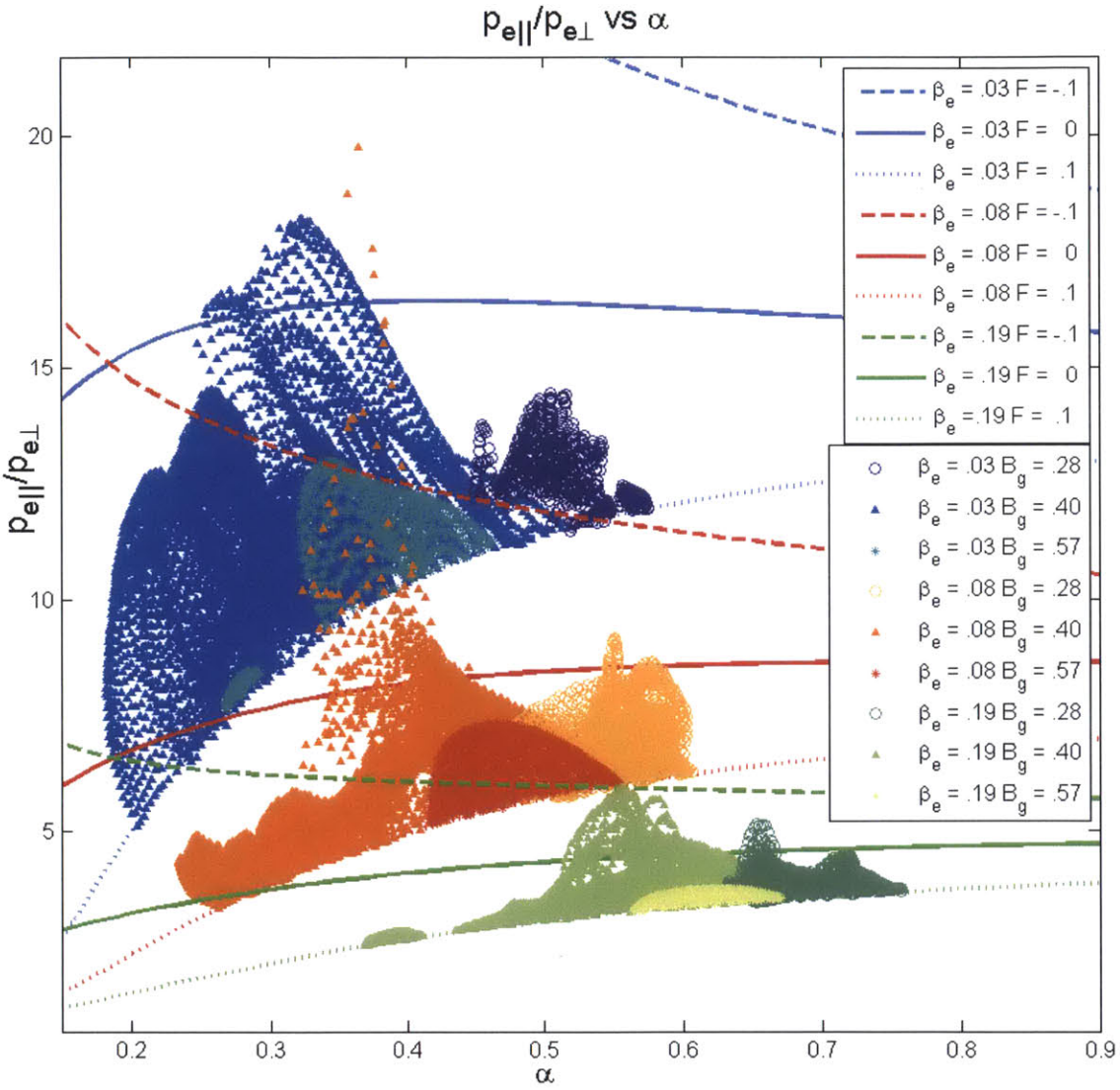

Figure 6-40: Parallel to perpendicular electron pressure ratio of layer bins as a function of α. Dotted, solid, and dashed lines indicates value predicted with firehose value of $F = .1$, $F = 0$, and $F = -.1$ respectively.

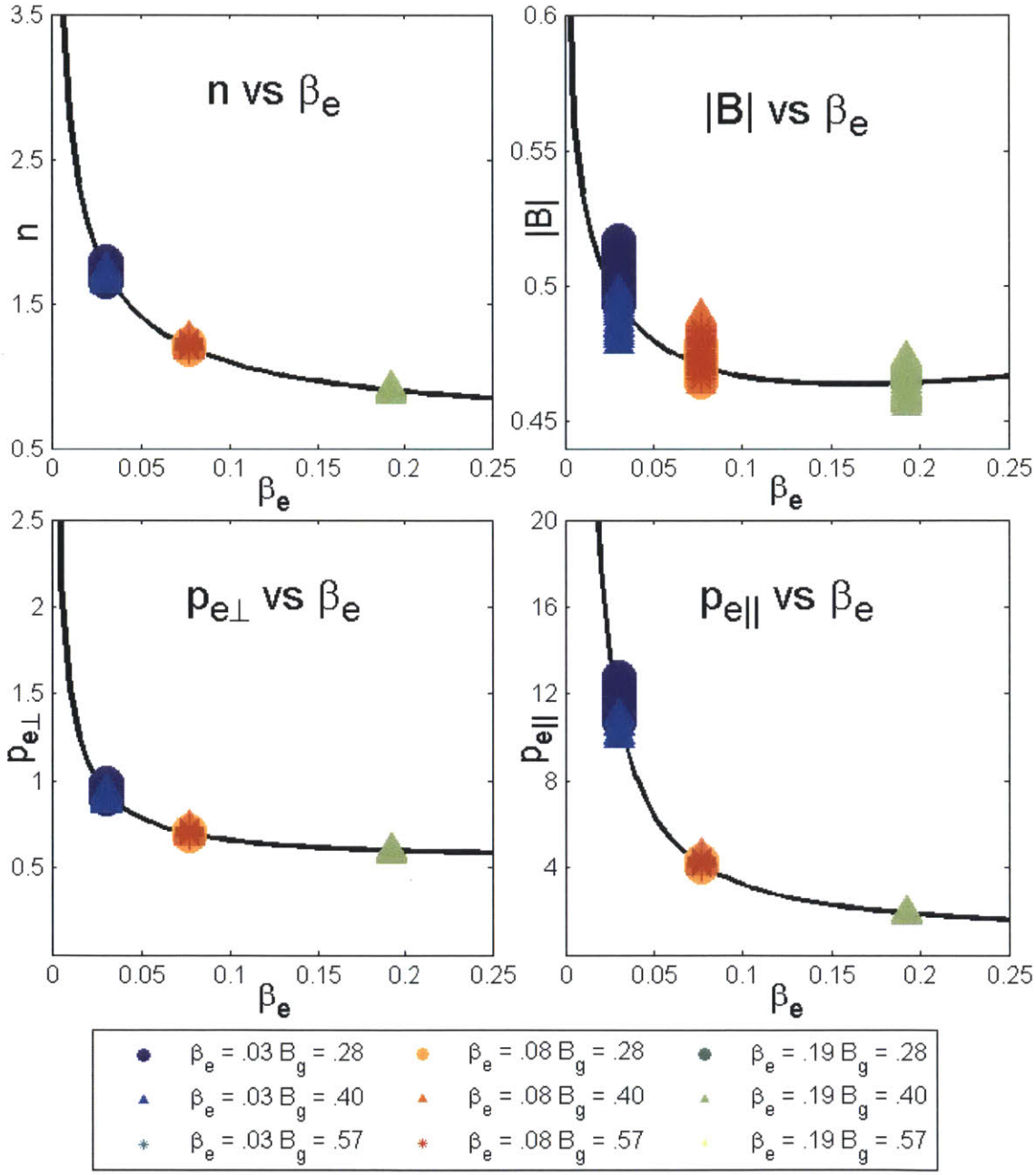

Figure 6-41: Layer density, magnetic field and perpendicular and parallel electron pressures as functions of upstream electron beta, assuming $T_{i\infty}/T_{e\infty} = 4$. Line indicates predicted value using firehose condition $F = .09$ and force balance parameter $\alpha = .5$. Simulation data was chosen to be within $\pm 5\%$ of these values.

Additional reconnection simulations have been performed to confirm the validity of ion-electron temperature dependence of the force-balance model. Specifically, runs with $T_i/T_e = 1, .25$ have been performed to complement selected runs described above with $T_i/T_e = 4$. These values are motivated by the casual observation that kinetic simulations with reduced ion-electron temperature ratio appeared to more readily form elongated layers (W. Daughton, private communication). This behavior may also be inferred from the lowest order solutions for the normalized magnetic field 6.26 and density 6.27.

Although simulations at $\beta_{e\infty} = .03$ were attempted, these runs became numerically unstable before the layer was able to fully develop. Instead simulations at $\beta_{e\infty} = .19$ for guide-field of $B_g/B_0 = .40, .57, .81$ were completed. The guide-field of $B_g/B_0 = .28$ also became numerically unstable before the layer was able to fully develop. Layer quantities are obtained in the same manner as described above, averaging data over bins of size $.8d_e \times 3d_e$. Simulations at guide-field $B_g = .81$ did not yield bins that satisfied the firehose constraint $F < .1$ and therefore are not included in plots below.

A plot of of the normalized firehose condition versus the alpha factor is shown in Figure 6-42. Here the firehose condition parameter appears to decrease with decreasing ion-electron temperature ratio, notably for the smallest value when $T_i/T_e = .25$

Plots of the normalized density, magnetic field, and parallel and perpendicular electron pressures compared to predicted values are shown in Figures 6-43, 6-44, 6-45, and 6-46, respectively. As predicted by lowest order solutions 6.26 and 6.27, both the normalized density and magnetic field increased with decreasing ion-electron temperature ratio, with the net effect of these changes increasing the parallel and perpendicular electron pressures. However, the response of the anisotropy ratio $p_{e\parallel}/p_{e\perp}$ to ion-electron temperature, depicted in Figure 6-47 does not appear to be captured by the lowest order solutions.

Finally, simulations which include viscous ion heating and limits the electron pressure anisotropy to the marginal firehose condition, as described in 4.4, have been performed. These domain for these simulations has size $L_x \times L_y = 64d_i \times 32d_i$. Grid points are uniformly distributed in the x-direction with 42 grid points per d_i, while

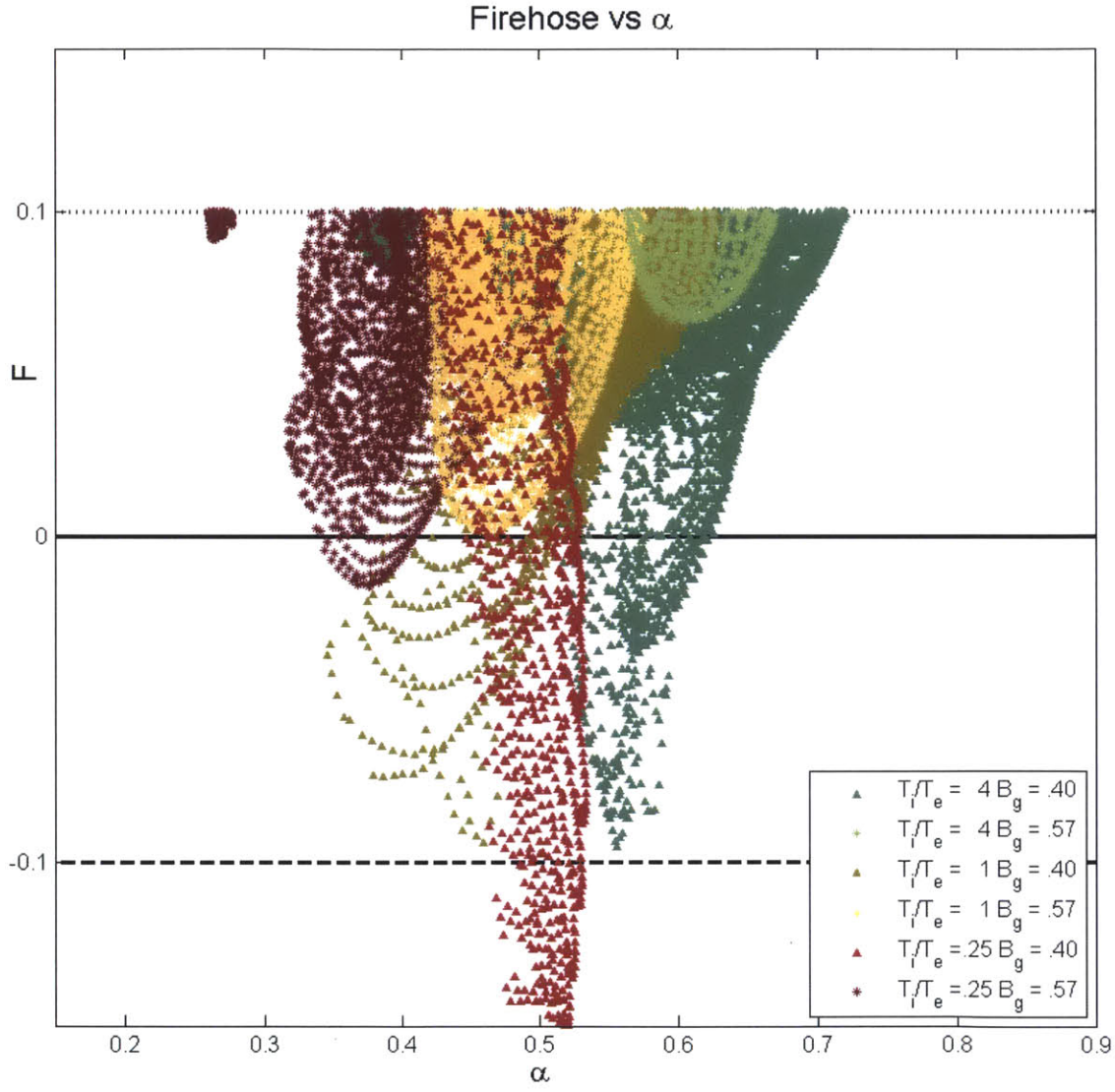

Figure 6-42: Firehose value of layer bins as a function of α for $\beta_e = .19$.

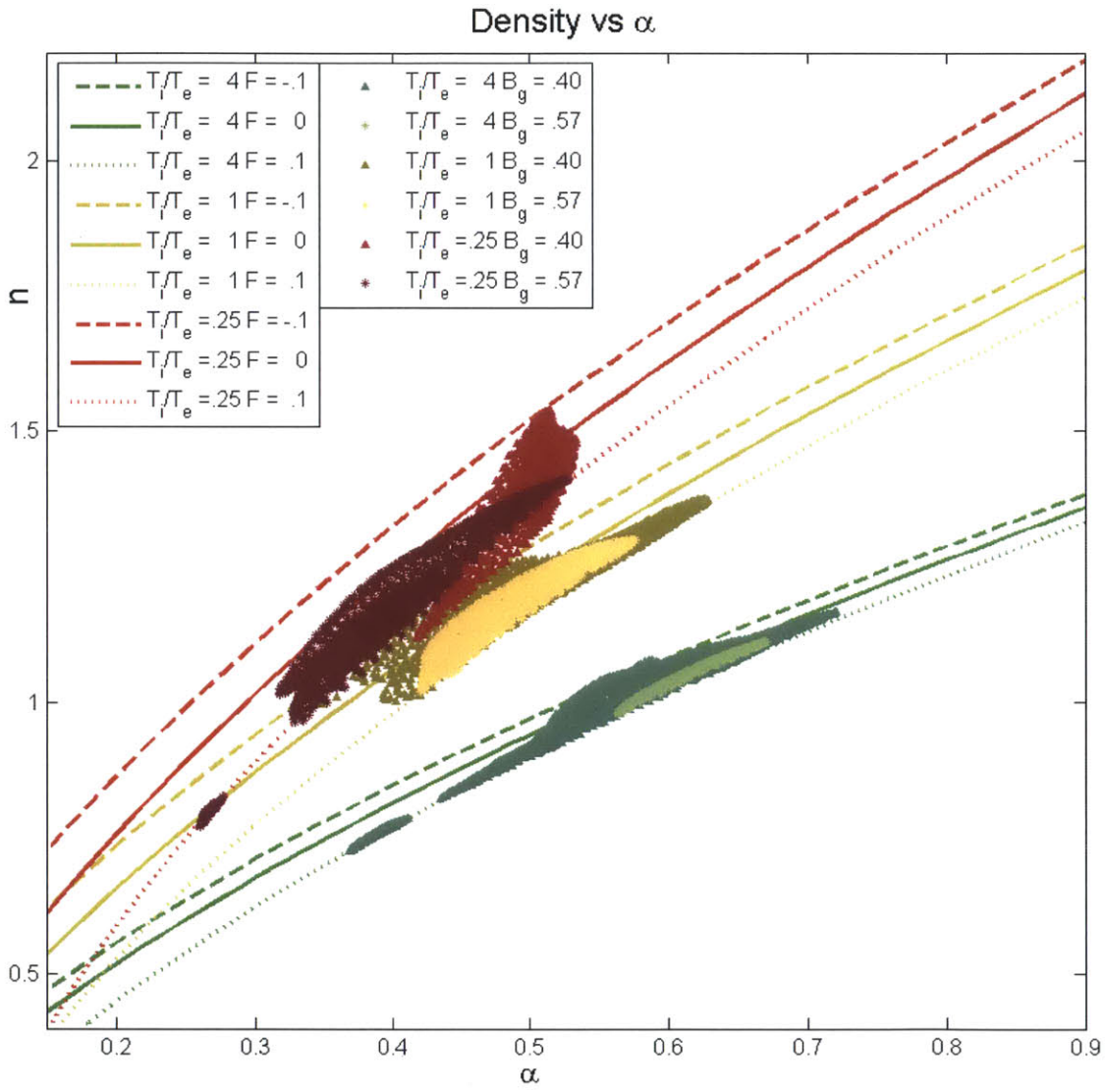

Figure 6-43: Density of layer bins as a function of α for $\beta_e = .19$. Dotted, solid, and dashed lines indicates value predicted with firehose value of $F = .1$, $F = 0$, and $F = -.1$ respectively.

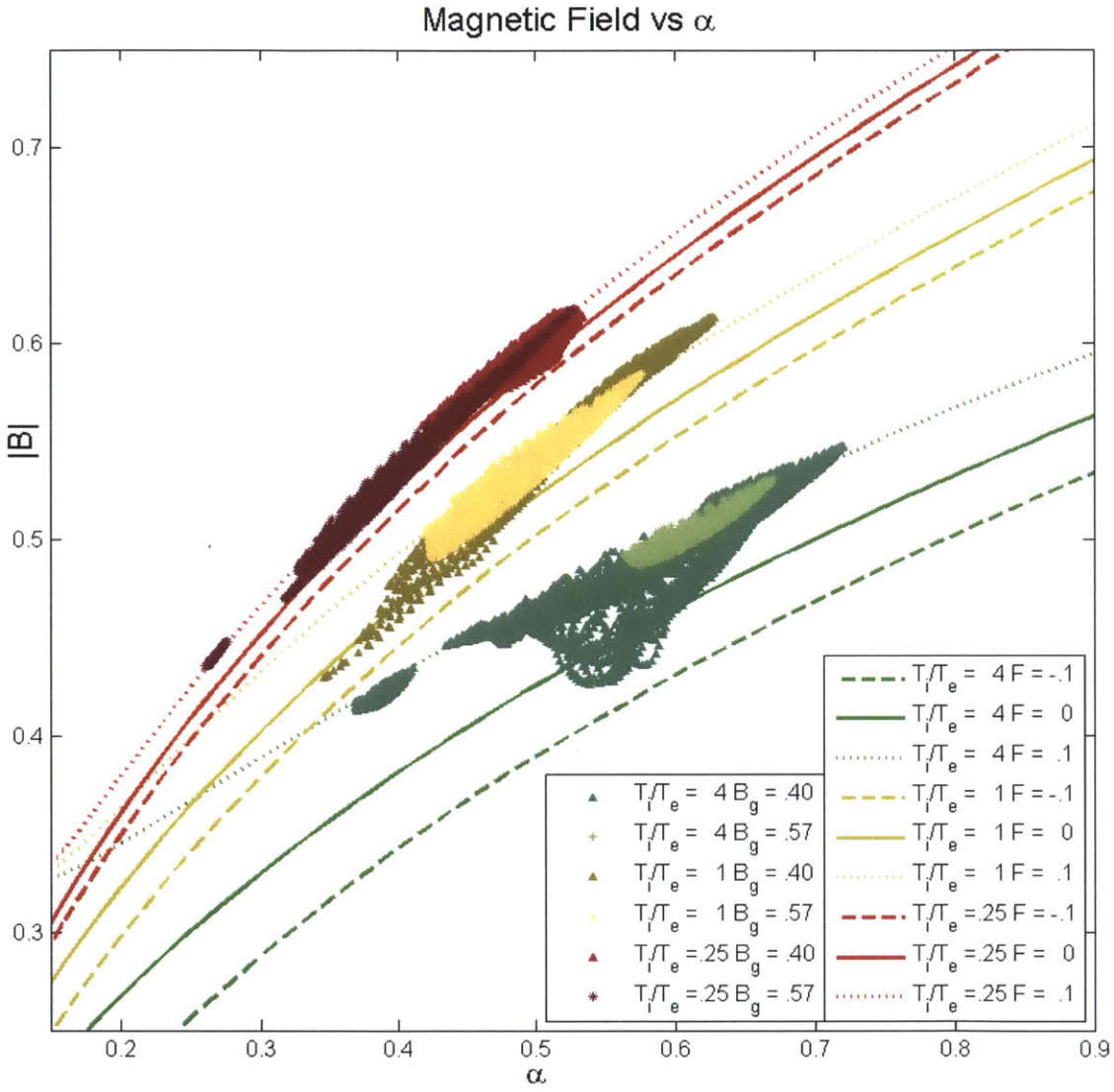

Figure 6-44: Magnetic Field of layer bins as a function of α for $\beta_e = .19$. Dotted, solid, and dashed lines indicates value predicted with firehose value of $F = .1$, $F = 0$, and $F = -.1$ respectively.

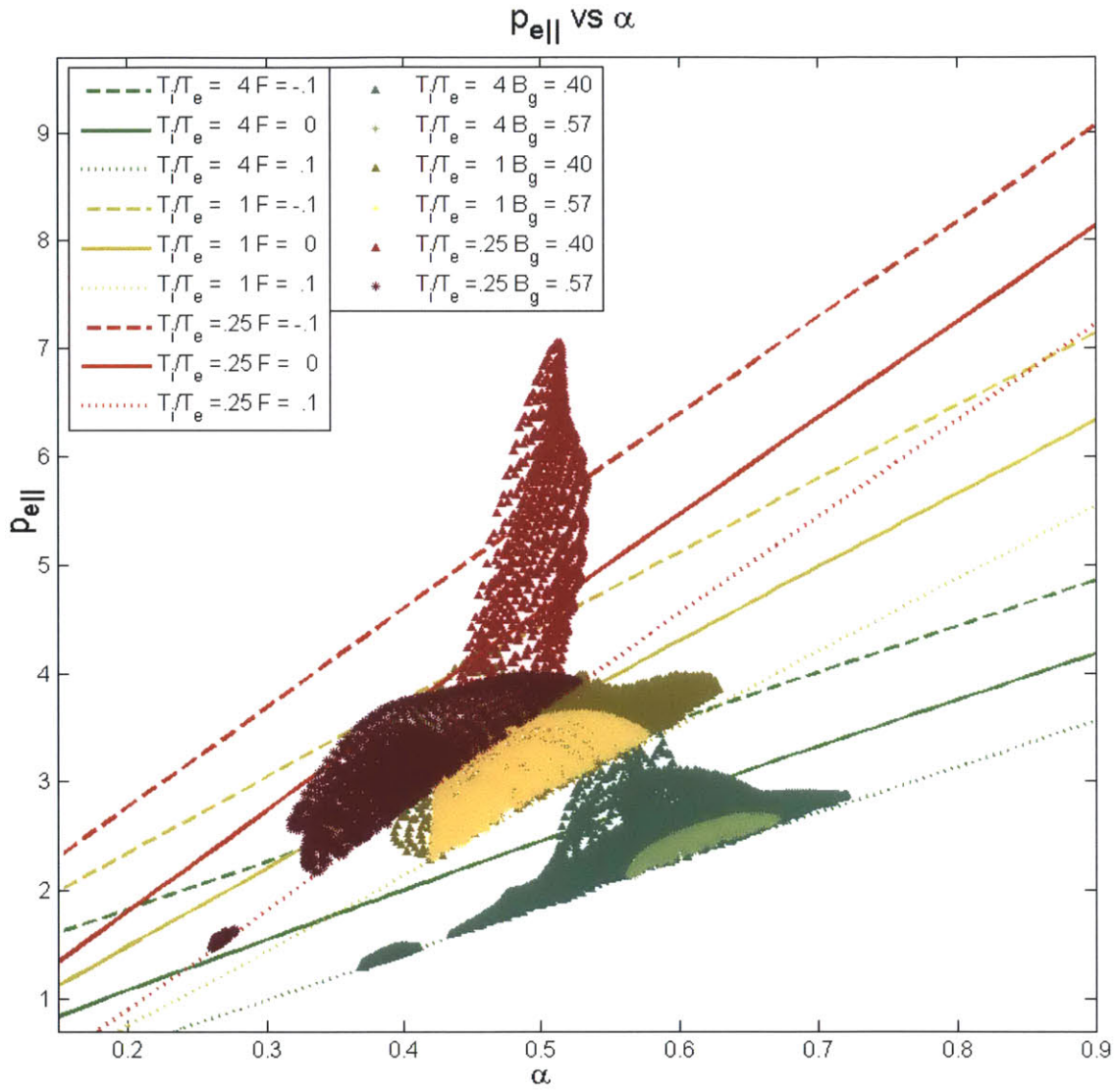

Figure 6-45: Parallel electron pressure of layer bins as a function of α for $\beta_e = .19$. Dotted, solid, and dashed lines indicates value predicted with firehose value of $F = .1$, $F = 0$, and $F = -.1$ respectively.

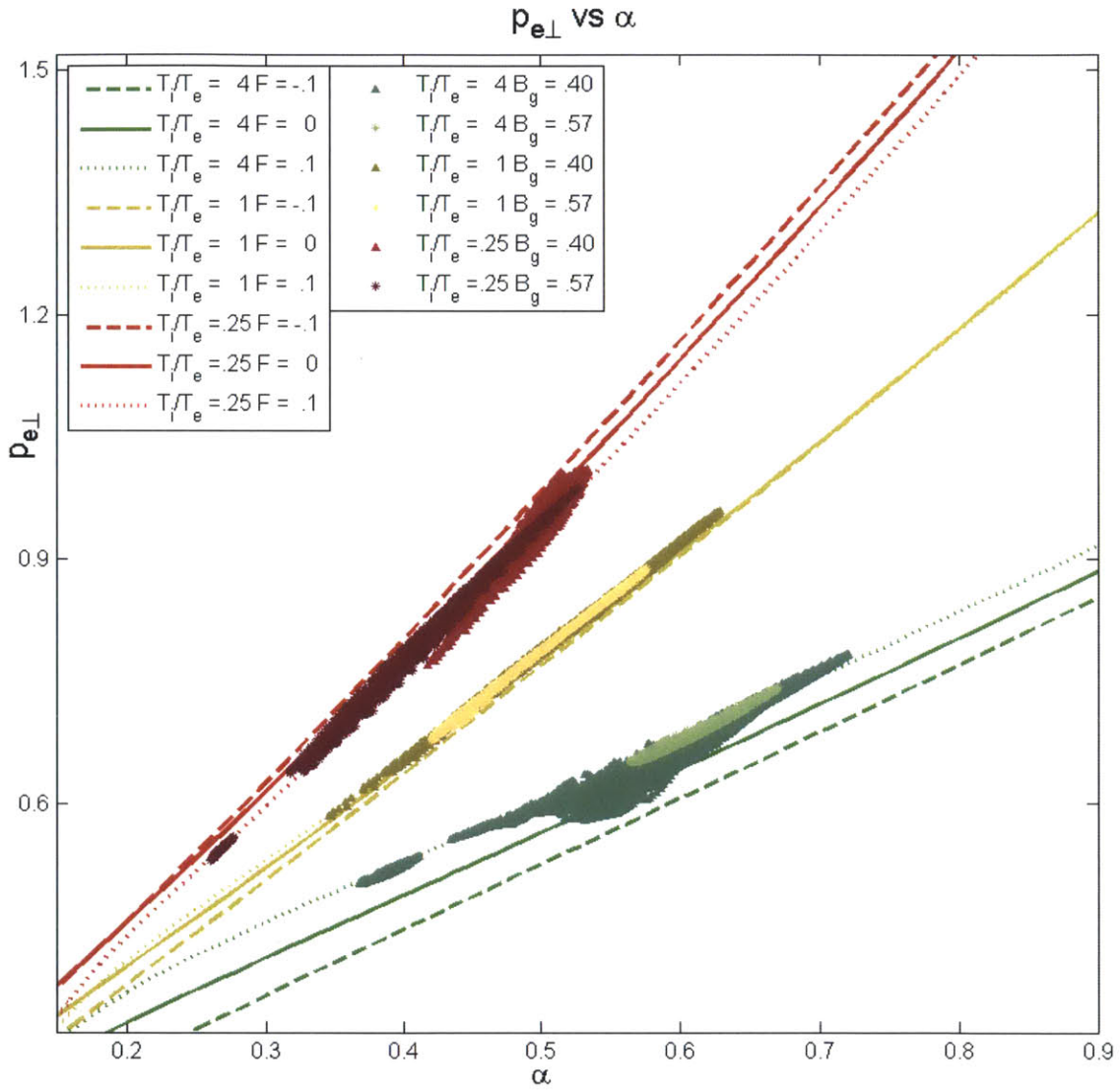

Figure 6-46: Perpendicular electron pressure of layer bins as a function of α for $\beta_e = .19$. Dotted, solid, and dashed lines indicates value predicted with firehose value of $F = .1$, $F = 0$, and $F = -.1$ respectively.

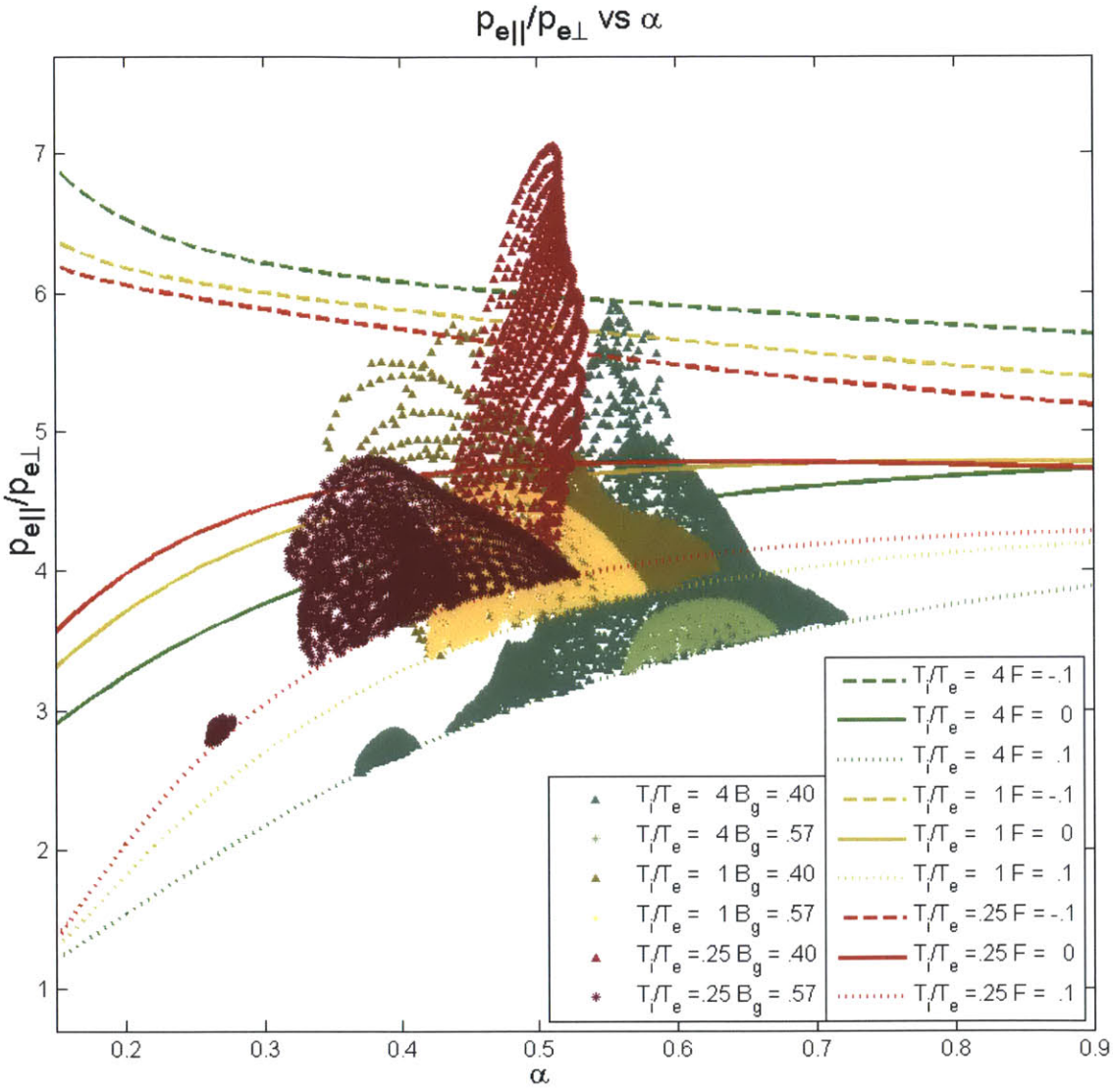

Figure 6-47: Parallel to perpendicular electron pressure ratio of layer bins as a function of α for $\beta_e = .19$. Dotted, solid, and dashed lines indicates value predicted with firehose value of $F = .1$, $F = 0$, and $F = -.1$ respectively.

in the y-direction the grid point density is peaked at the center with 35.2 grid points per d_i and 5.7 grid points per d_i at the boundaries. The boundary conditions are the same as the simulations described above with periodic boundaries in the x-direction and conducting wall boundaries in the y-direction. The initial equilibrium is once again a force-free current sheet with half-thickness of one ion inertial length. The mass ratio is once again $m_i/m_e = 100$, ion viscosity $\nu_i = 4 \times 10^{-2}$, ion heat diffusion $\kappa_i = 7.5 \times 10^{-3}$, and hyper-resistivity $\eta_H \equiv d_e^2 \nu_e = 4 \times 10^{-4}$. The perturbation is the same as described above, as are the normalization factors. The ion-electron temperature ratio is once again $T_i/T_e = 4$, and the three beta values presented are again $\beta_e = .03, .08, .19$. The guide-field is $B_g = .2B_0$.

To accurately apply the force-balance model to simulations with viscous ion heating, the ion temperature increase of the layer is estimated. Near the x-line, $\boldsymbol{V} \cdot \nabla n \simeq 0$ and $\boldsymbol{V} \cdot \nabla p_i \simeq 0$. For a nearly one dimensional layer, this would be true along the layer as well. During steady reconnection $\nabla \cdot \boldsymbol{V} \simeq 0$ along the layer from the conservation of density. Then during steady reconnection, taking the density to be constant within the layer, the normalized ion energy equation 5.26 reduces to

$$-\tilde{\nu}_i \left[\nabla' \tilde{\boldsymbol{V}} + \left(\nabla' \tilde{\boldsymbol{V}} \right)^T \right] : \nabla' \tilde{\boldsymbol{V}} = \tilde{\kappa} \nabla'^2 \tilde{T}_{i*}, \tag{6.30}$$

that is, viscous heating is balanced by thermal diffusion, where $\tilde{T}_{i*}$ is the difference between the layer temperature and upstream temperature. Assuming velocity gradients and temperature gradient have about the same scale then

$$\tilde{T}_{i*} \approx \frac{2\tilde{\nu}_i}{\tilde{\kappa}} \tilde{V}_{in}^2 \sim .02 \frac{\tilde{\nu}_i}{\tilde{\kappa}}, \tag{6.31}$$

where normalized inflow velocity $\tilde{V}_{in} \sim .1$ during fast reconnection. Evaluating this expression using the simulation parameters yields $\tilde{T}_{i*} \sim 8/75$. This is the value used in subsequent plots.

Plots of the normalized density, magnetic field, parallel and perpendicular electron pressures, and anisotropy compared to predicted values are shown in Figures 6-48, 6-49, 6-50, 6-51, and 6-52, respectively. Instead of averaging over a small box like

in previous analysis, direct values along the layer where the modifications to the EoS only weakly temper the anisotropy are used in these plots. Though the modified EoS are used in simulations, the untempered EoS are used in the force balance model. Despite the limits of the simple estimation of viscous heating, the force-balance model appears to be in agreement with simulation values.

This section developed a model predicting density, magnetic fields, and anisotropic electron pressures in the reconnection region based on upstream values. The next section examines fluid simulations with the new equations of state on larger domains and at lower mass ratios.

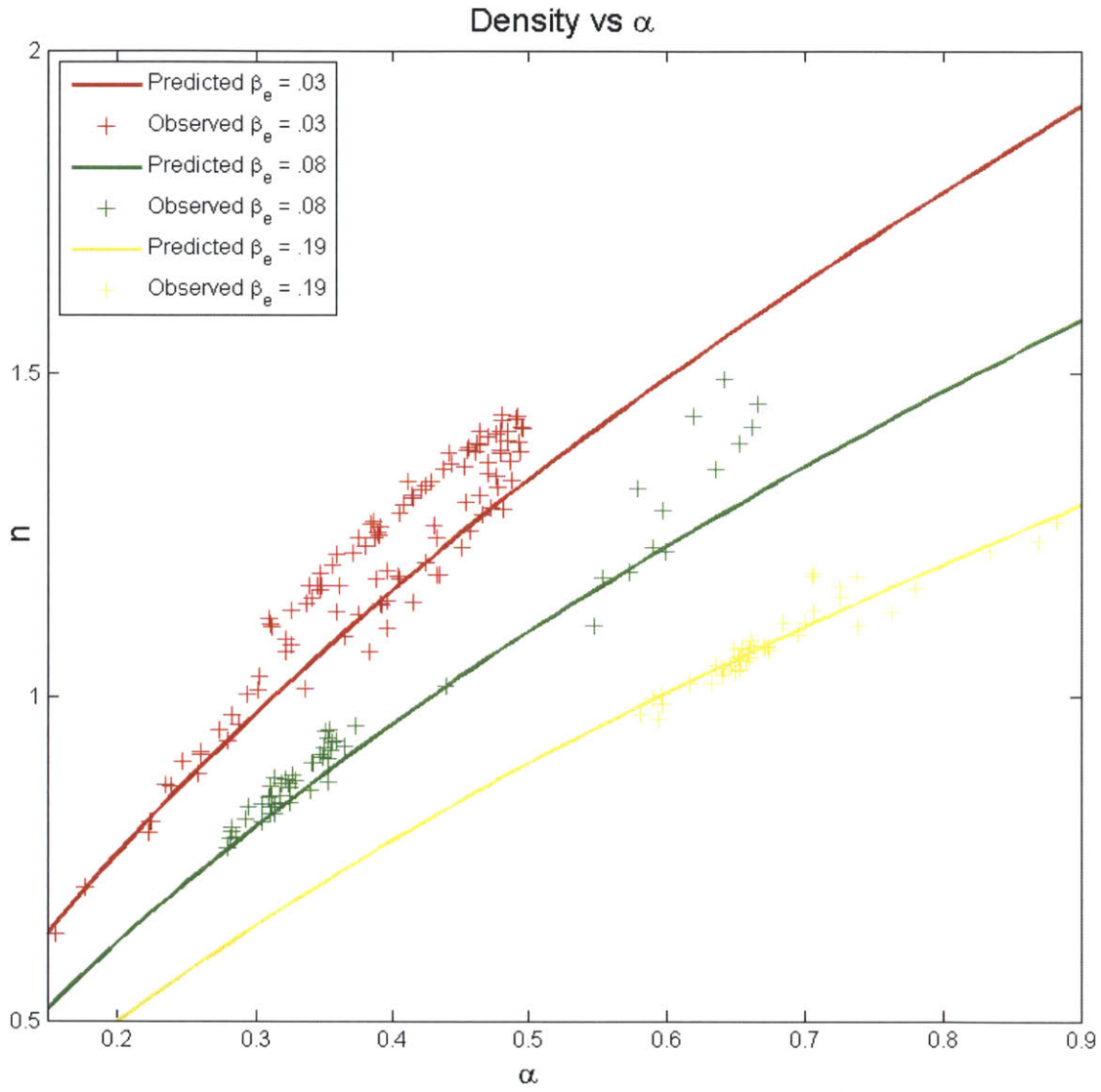

Figure 6-48: Density of layer bins as a function of α for $B_g = .2B_0$ in simulations using the modified EoS and an estimation of viscous heating within the layer. The line indicates the predicted value at the marginal firehose condition.

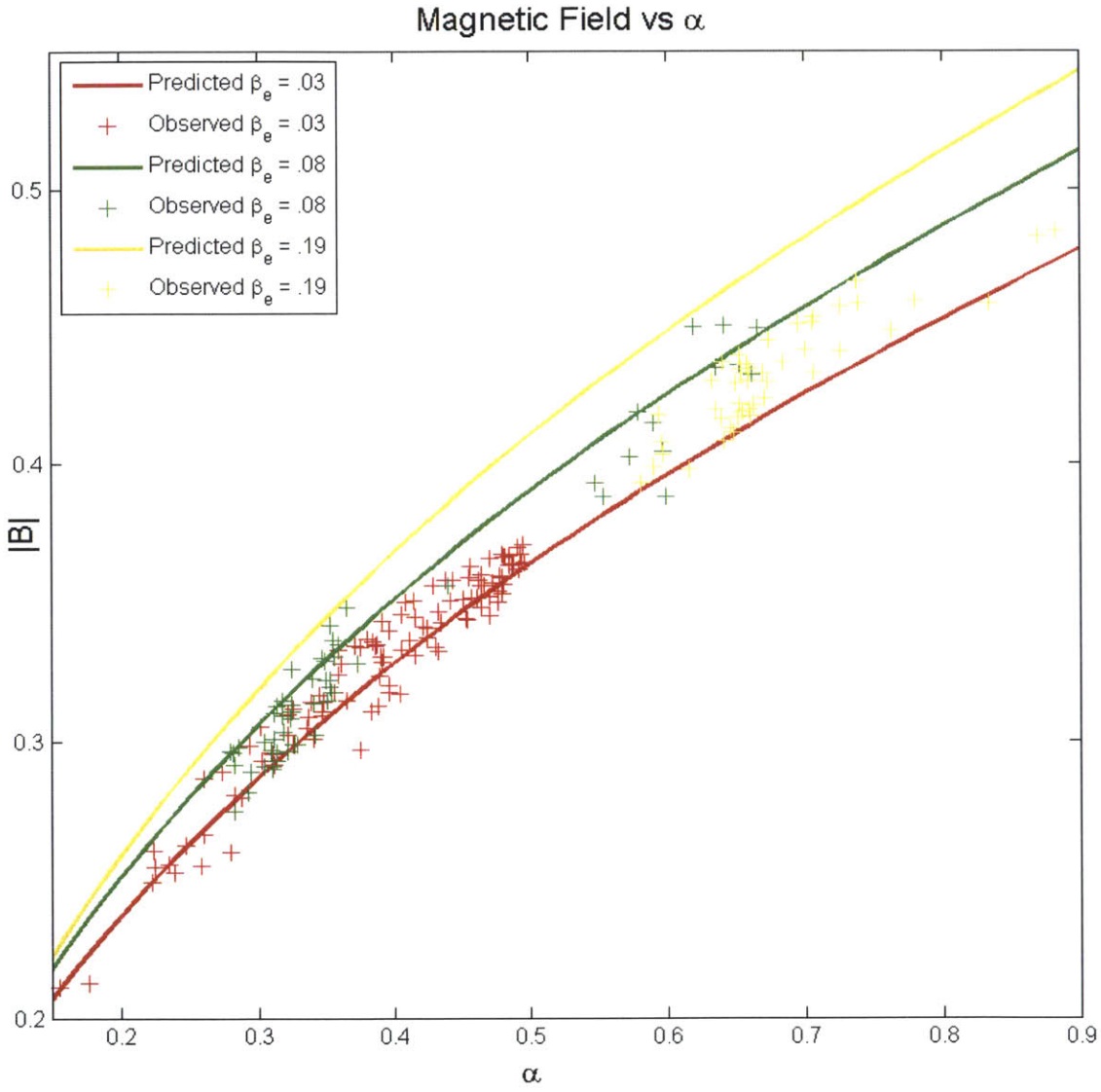

Figure 6-49: Magnetic Field of layer bins as a function of α for $B_g = .2B_0$ in simulations using the modified EoS and an estimation of viscous heating within the layer. The line indicates the predicted value at the marginal firehose condition.

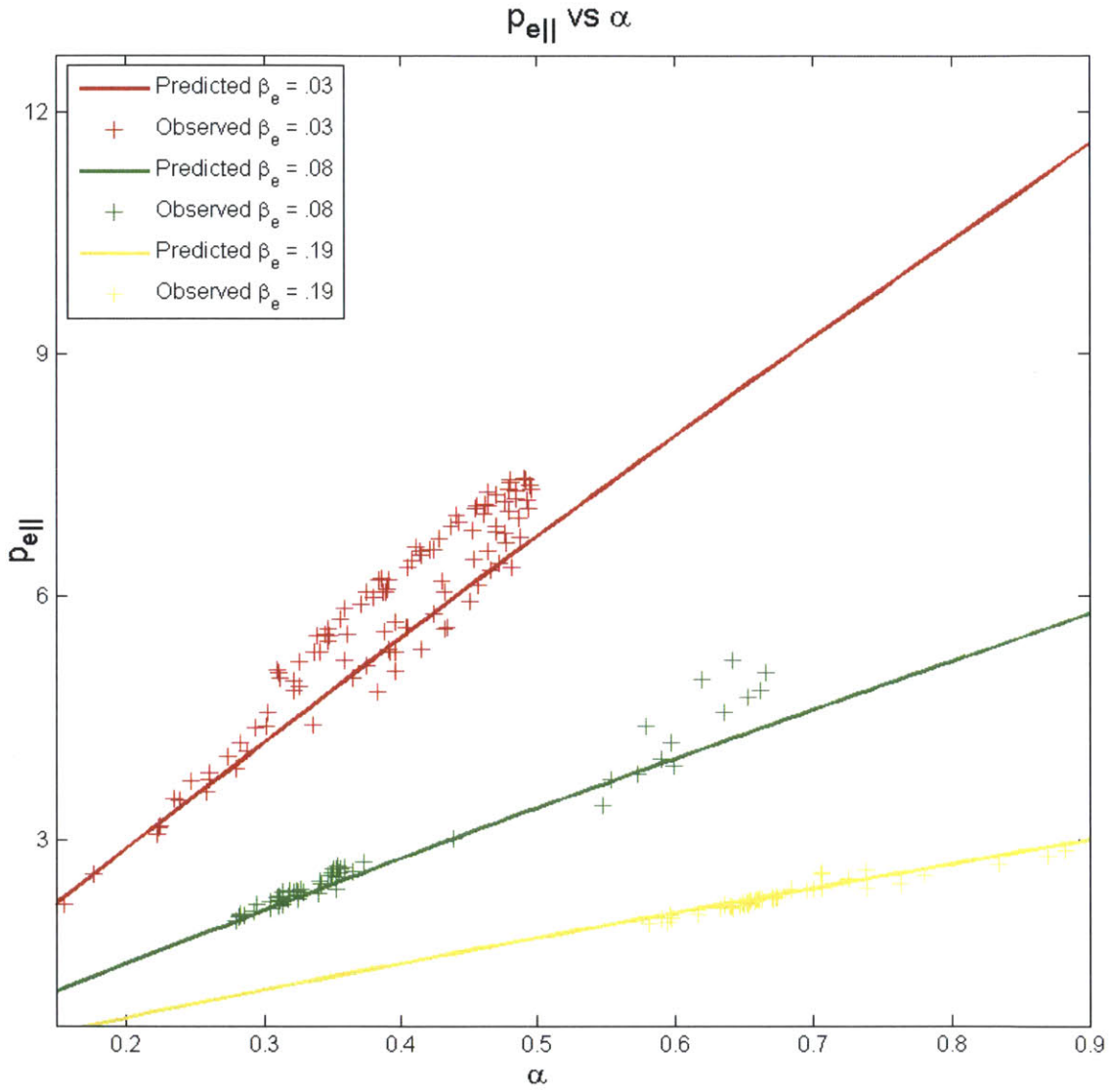

Figure 6-50: Parallel electron pressure of layer bins as a function of α for $B_g = .2B_0$ in simulations using the modified EoS and an estimation of viscous heating within the layer. The line indicates the predicted value at the marginal firehose condition.

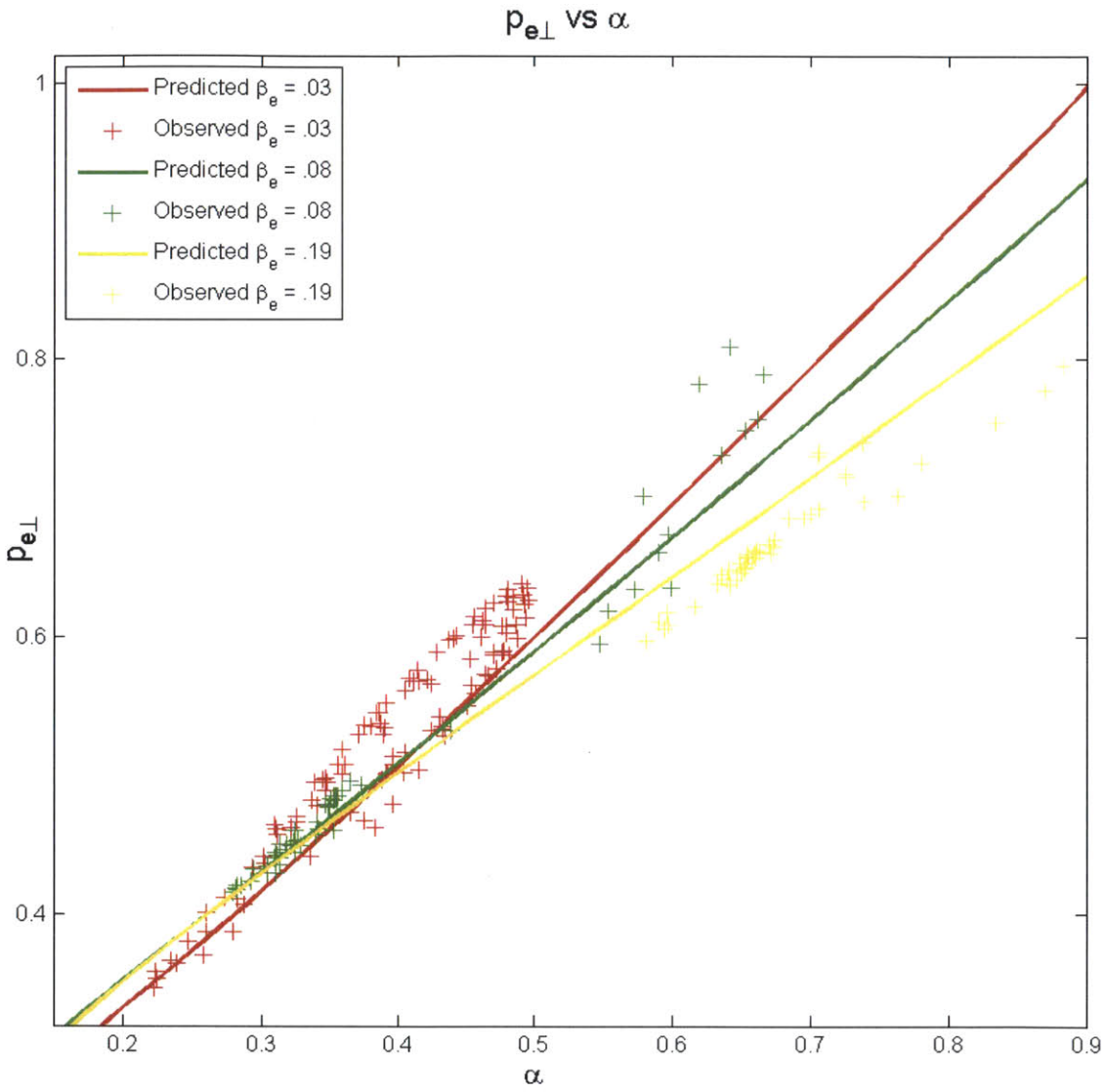

Figure 6-51: Perpendicular electron pressure of layer bins as a function of α for $B_g = .2B_0$ in simulations using the modified EoS and an estimation of viscous heating within the layer. The line indicates the predicted value at the marginal firehose condition.

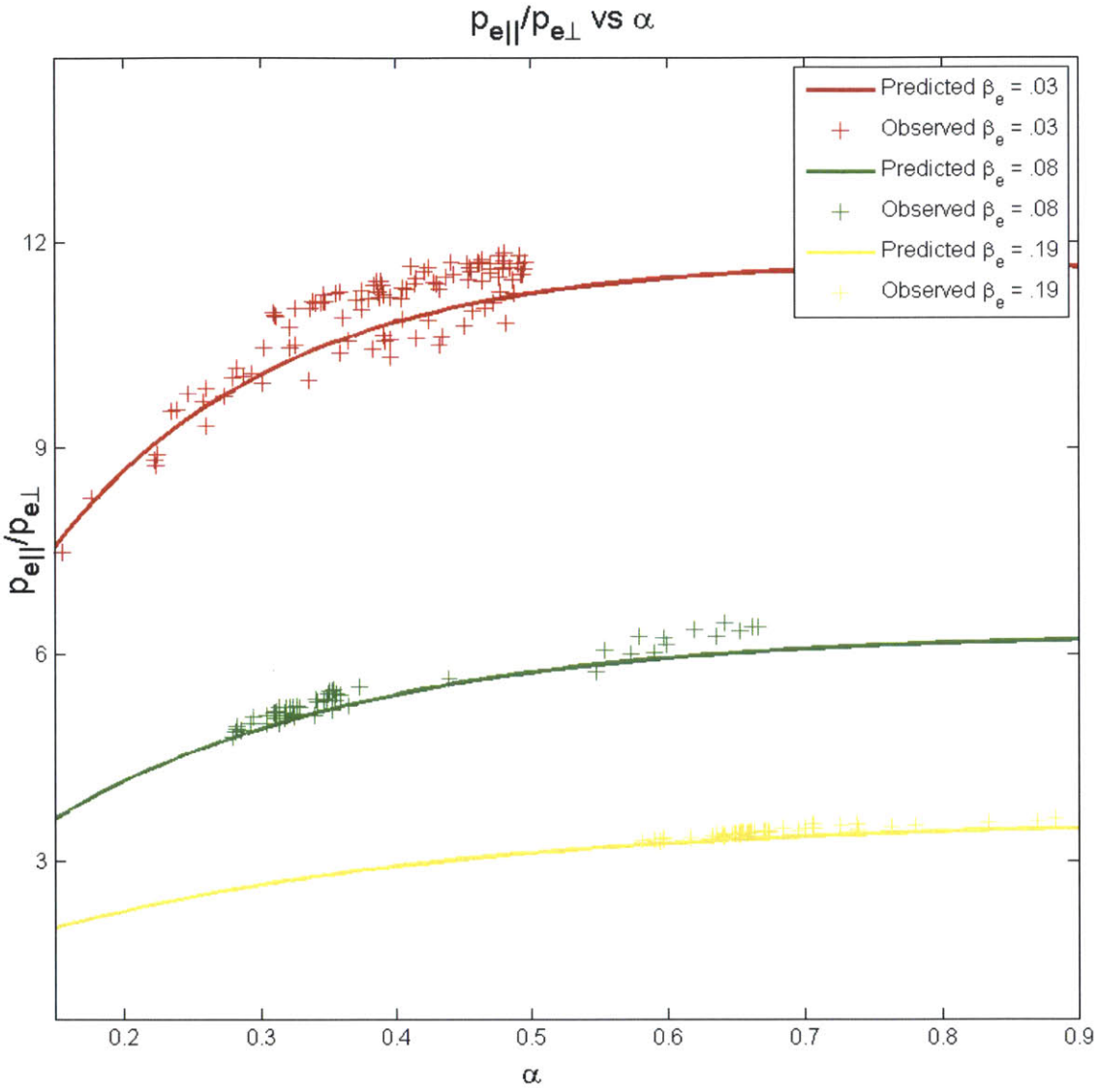

Figure 6-52: Parallel to perpendicular electron pressure ratio of layer bins as a function of α for $B_g = .2B_0$ in simulations using the modified EoS and an estimation of viscous heating within the layer. The line indicates the predicted value at the marginal firehose condition.

6.4 Large Scale Current Layer

The new EoS hold the promise of being able to allow large three dimensional simulations of magnetic reconnection that accurately capture the development of electron pressure anisotropy. As evident in Figure 6-2, kinetic simulation results are strongly dependent ion-electron mass ratio, and to access the elongated layer Regime 3, which describes some plasmas relevant to magnetospheric reconnection, large mass ratios are required to correctly model system dynamics. This requirement limits kinetic simulation performed on even the most powerful computer systems to relatively small domain sizes. However, since the EoS are derived assuming large mass ratios and magnetic moment conservation, fluid simulation that describe electron pressure using the EoS remain in Regimes 3 and 4 at any mass ratio. To test the independence of mass ratio on layer structure and electron pressure anisotropy in fluid simulations, two 2.5 dimensional simulations with mass ratios $m_i/m_e = 100$ and $m_i/m_e = 25$ have been performed on a relatively large domain size of $L_x \times L_y = 144d_i \times 96d_i$. Both simulations are periodic in the x-direction and have conducting wall boundaries in the y-direction. The simulation with $m_i/m_e = 100$ has uniform distribution of grid points in the x-direction with 42 points per d_i, while in the y-direction the grid point density is peaked at the center with 35.2 points per d_i and 5.6 points per d_i at the boundaries. The simulation with $m_i/m_e = 25$ also has uniform distribution of grid points in the x-direction with 21.3 points per d_i, while in the y-direction the grid point density is peaked at the center with 17.6 points per d_i and 2.8 points per d_i at the boundaries. The initial equilibriums and single x-line perturbations are the same as described above. In these simulations, $\beta_e = .03$, $B_g = .2B_0$, $T_i/T_e = 4$, $\nu_i = 4 \times 10^{-2}$, and $\kappa_i = 7.5 \times 10^{-3}$. Normalized hyper-resistivity depends on the inverse of the mass ratio, for $m_i/m_e = 100$, $\eta_H = 4 \times 10^{-4}$ and for $m_i/m_e = 25$, $\eta_H = 1.6 \times 10^{-3}$. Both simulations used the modified EoS of section 4.4 where the firehose ratio is limited to $\mathscr{F}_e \leq .87$.

Since results of these simulations are retroactively compared to spacecraft observations, it is necessary to transform the coordinate system used in the simulations

to one that aligns with the LMN boundary coordinate system used in magnetopause observations, where the reconnecting field is along L, the guide-field is along M, and N traverses the layer. A simple way to align the computational XYZ coordinates with the LMN coordinates is to use the "mirror image" of the computational results through the parity transformation where

$$(x, y, z) \rightarrowtail (-x, -y, -z).$$

This transformation changes the handedness of the coordinate system from right to left. To complete the transformation, the plasma velocity and current density vectors change sign under the inversion such that $\{\boldsymbol{V}, \boldsymbol{J}\} \rightarrowtail \{-\boldsymbol{V}, -\boldsymbol{J}\}$ while the magnetic field, a being a pseudovector, does not.

Plots of the current layers are shown in Figure 6-53. Contrary to kinetic simulations, elongated current layers are seen at the very low mass ratios as well. Though the current layer at $m_i/m_e = 25$ is thicker, the two layers have a similar appearance. The current layers in these simulations are seen to exceed $60d_i$ in length and appear to be limited by system size. The magnetic islands that bound the layer grow continuously in time, eventually constricting the layer. Note that while secondary islands formed and were ejected earlier during the layer, island production appears to subside at later times after the layer is fully developed.

Plots of the anisotropy are shown in Figure 6-54. Near the x-line, the anisotropy appears similar in both simulations. Further from the x-line, near magnetic islands that bound the layer, pockets of low anisotropy appear. These locations are where the modifications to the EoS dominate, allowing the simulation to remain numerically stable.

This section described the setup and some results of fluid simulations on relatively large domain sizes. As predicted, current layer structure and anisotropy are nearly independent of simulation mass ratio. The next section compares simulation results with spacecraft observations of the magnetospheric reconnection.

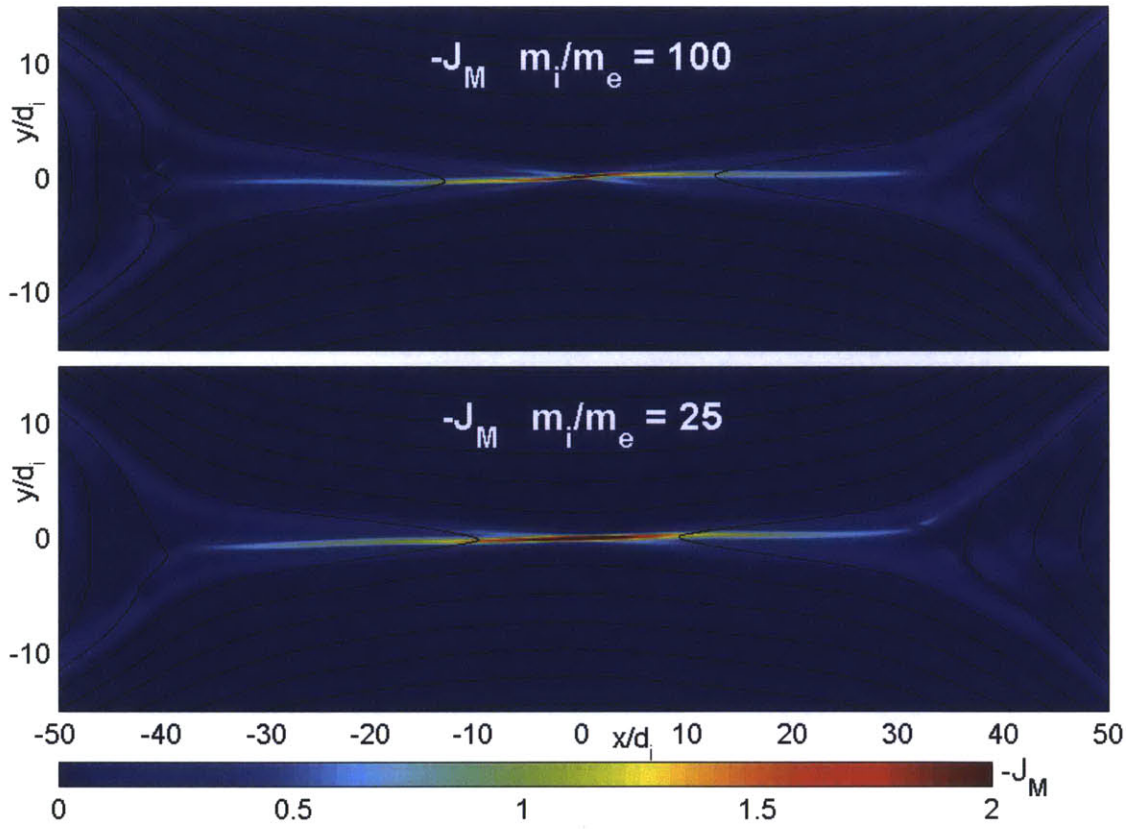

Figure 6-53: Out-of-plane current density J_M and superimposed in-plane magnetic field lines in reconnection simulations with the new Equations of State for $\beta_e = .03$ and $B_g = .2B_0$, where B_0 is the initial upstream reconnecting field at two different mass ratios.

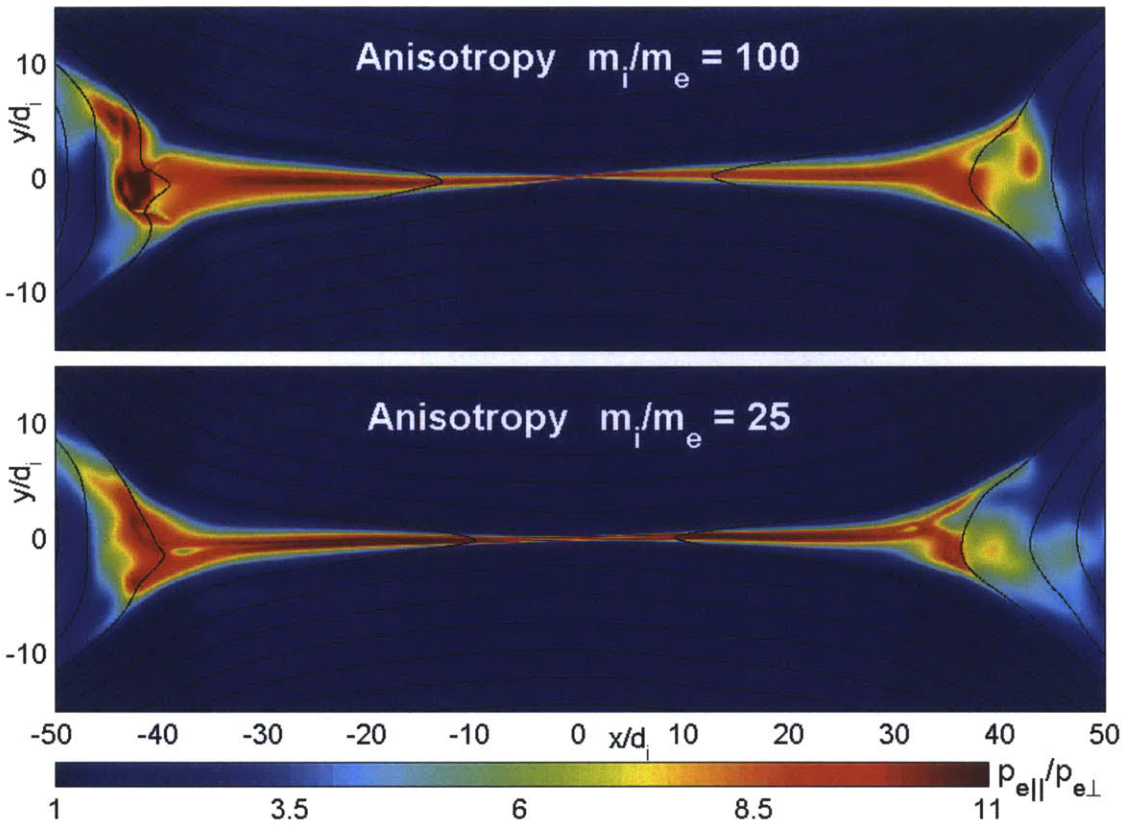

Figure 6-54: Anisotropy $p_{e\|}/p_{e\perp}$ and superimposed in-plane magnetic field lines in reconnection simulations for $\beta_e = .03$ and $B_g = .2B_0$, where B_0 is the initial upstream reconnecting field at two different mass ratios.

6.5 Comparison with Spacecraft Data

The fluid simulations presented above can be compared to *in situ* observations of a reconnection exhaust by the Cluster spacecraft [53]. The guide-field of this observation was $B_g = .15B_0$ with a 10% density asymmetry across the current sheet. The upstream electron temperature was not reported in the papers published. A schematic of the spacecrafts trajectory is shown in Figure 6-55. Plasma and field data observed by the spacecraft is shown in Figure 6-56 [143].

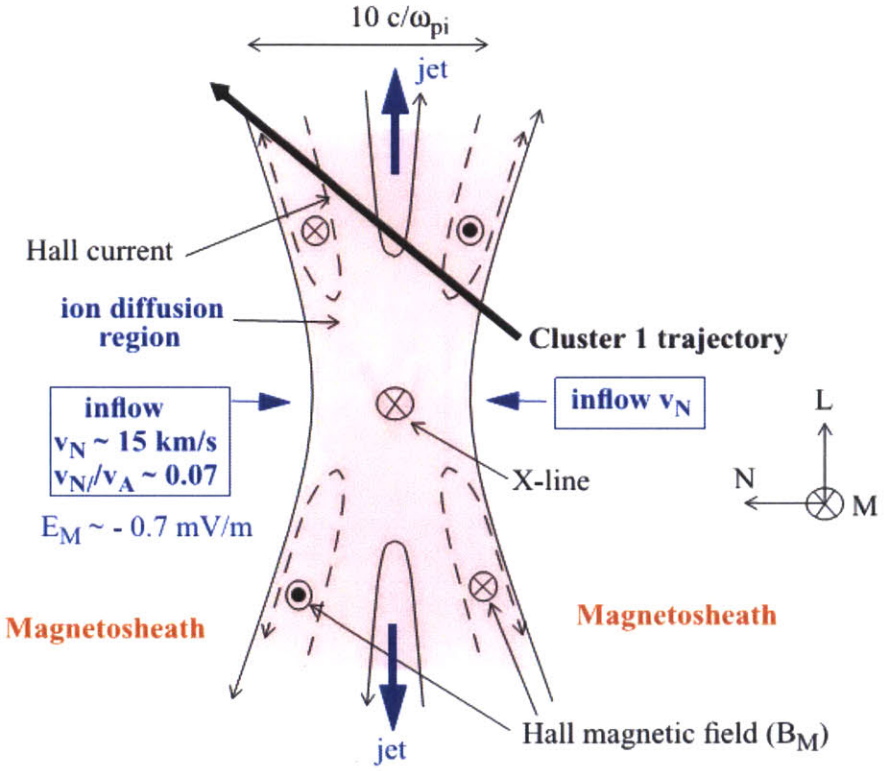

Figure 6-55: Schematic of the Cluster crossing of reconnection layer in the LMN coordinates. The sketch is for idealized symmetric boundary conditions, whereas a slight density asymmetry was observed (Ref [53]).

Plots of the Hall magnetic fields from from both simulations with a superimposed trajectory estimated to be similar to that of the spacecraft [143] 6-57. This virtual trajectory crosses the exhaust closer to the x-line than in observations due to limitations of the system size. Plasma fields and profiles from along the path are shown in Figures 6-58 and 6-59 for mass ratio $m_i/m_e = 100$ and $m_i/m_e = 25$, respectively. De-

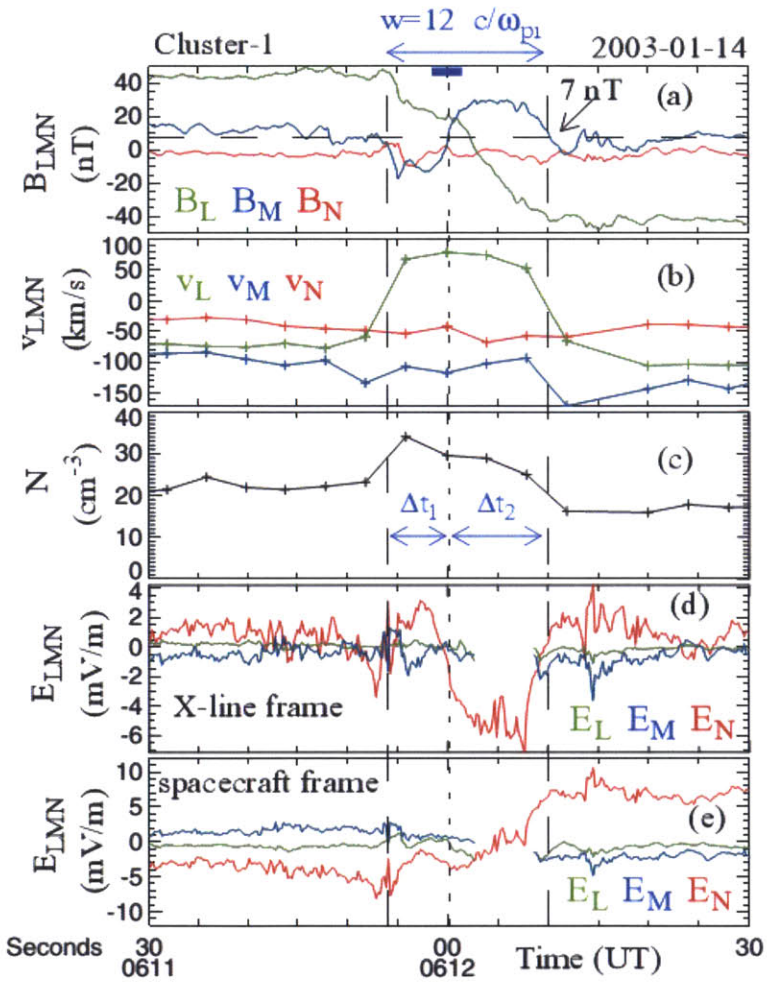

Figure 6-56: Plasma and field profiles observed during Cluster crossing of reconnection layer. Shown are the (a) Magnetic field, (b) ion bulk flow, (c) ion density, and (d) electric field components in the x-line frame (Ref [143]).

spite difference in upstream parameters including upstream density asymmetry, there is some agreement between simulations and observations. The difference between the widths of the Hall electric and magnetic fields between simulations and observations is like due to the proximity of the cut to the x-line while differences in gradients may be due to dissipation parameters needed for numerical stability. Comparing the simulations, there is some difference between profiles due to the $m_i/m_e = 25$ simulation reaching steady reconnection at a later ion-gyrotime time then the higher mass ratio simulation. The overall characteristics of the profiles, however, are similar.

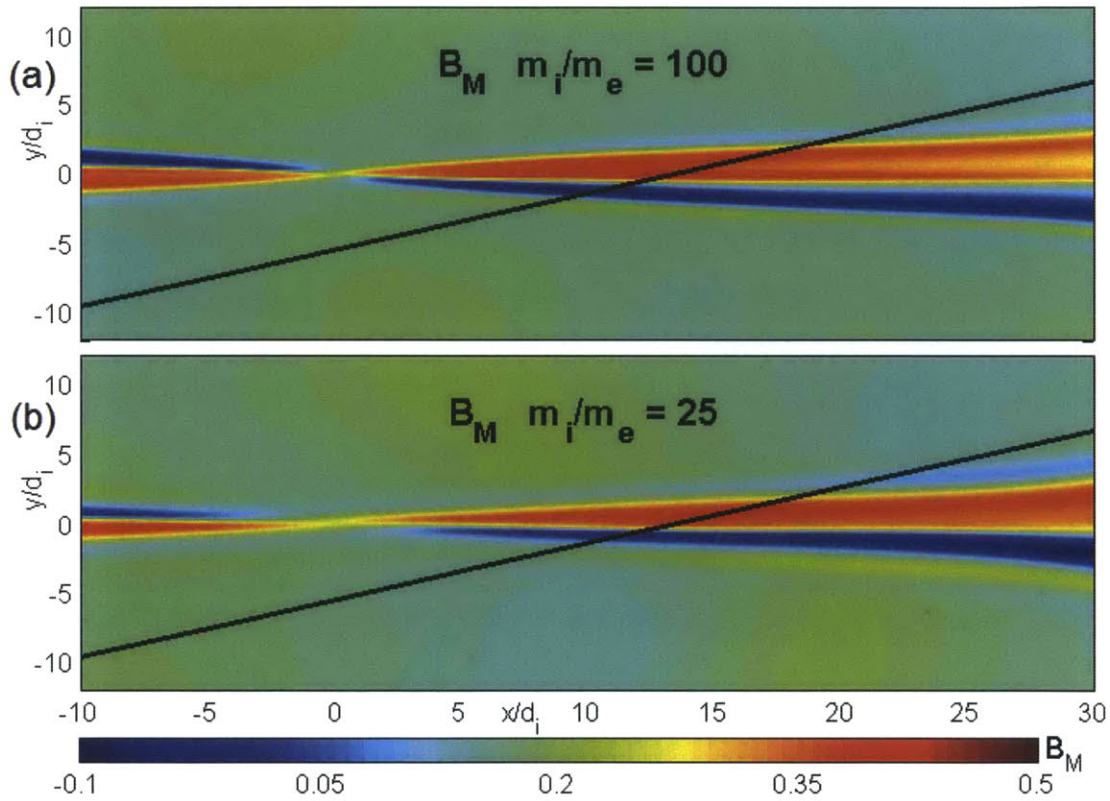

Figure 6-57: Hall reconnection field B_M from simulations at (a) $m_i/m_e = 100$ and (b) $m_i/m_e = 25$. Superimposed is a virtual trajectory similar to that of the Cluster spacecraft.

6.6 Summary

This chapter reviewed the regimes where fluid simulation with the new equations of state are physically valid and uses this criteria as a parameter guide for a series of

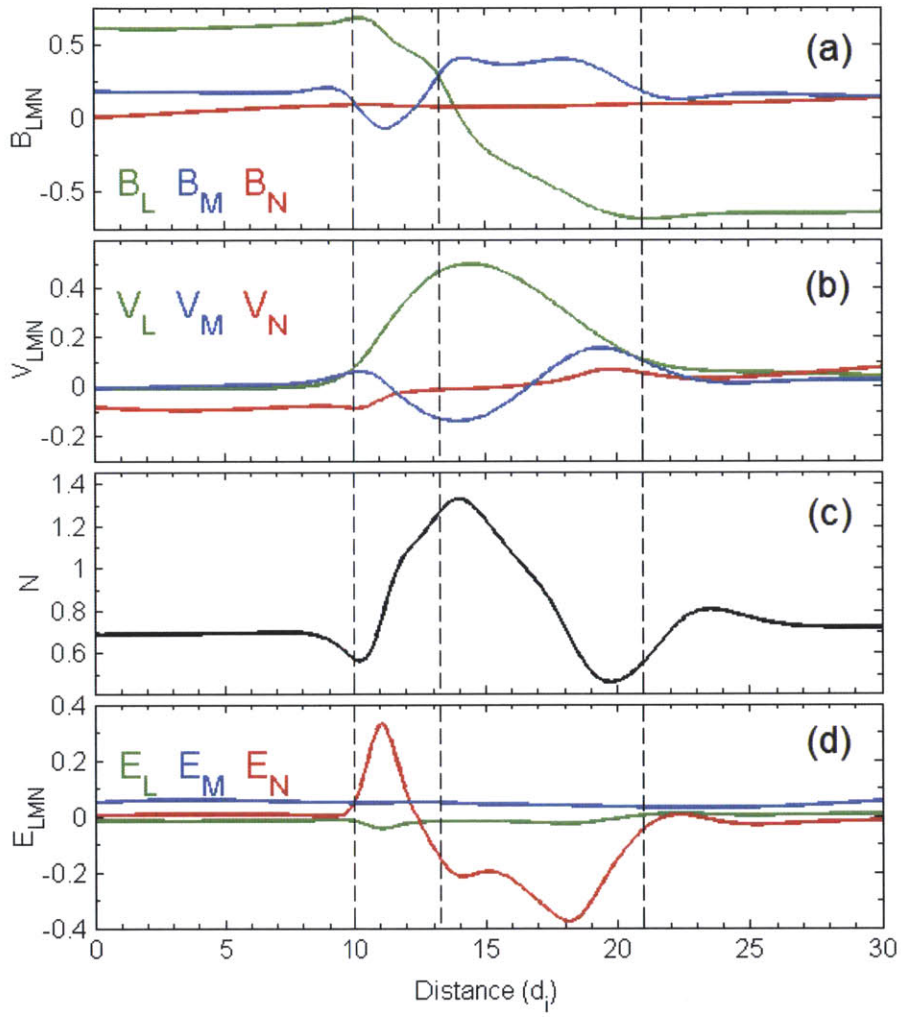

Figure 6-58: Simulation results at $m_i/m_e = 100$ of plasma and field profiles along a virtual crossing of reconnection layer. Shown are the (a) Magnetic field, (b) ion bulk flow, (c) ion density, and (d) electric field components in the x-line frame.

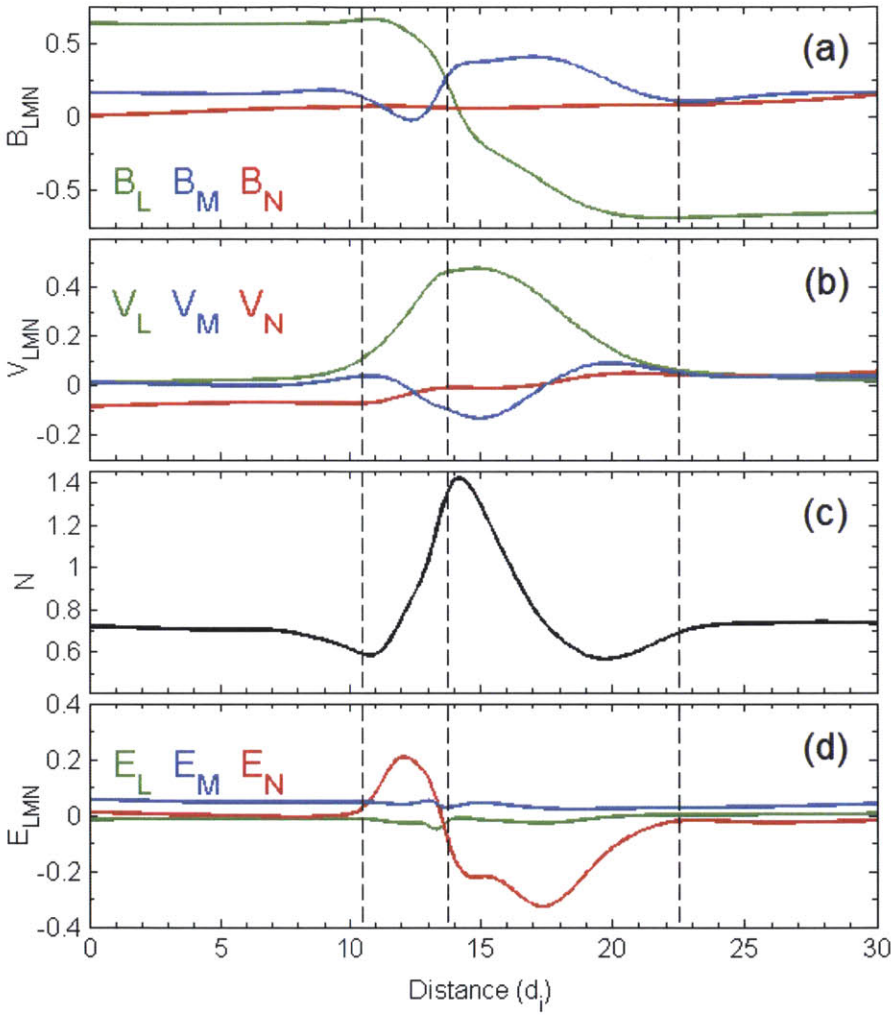

Figure 6-59: Simulation results at $m_i/m_e = 25$ of plasma and field profiles along a virtual crossing of reconnection layer. Shown are the (a) Magnetic field, (b) ion bulk flow, (c) ion density, and (d) electric field components in the x-line frame.

simulations. These simulations showed both the transition from elongated current layers to currents along the separators as the guide-field increased, and the inverse dependence of anisotropy on β_e. Comparisons to isotropic simulations revealed the additional current driven by anisotropy provides negative feedback on layer anisotropy, and tempers the firehose ratio of the layer $\mathscr{F}_e$. Examination of the components of the parallel electric field along the layer in fluid simulations revealed the gytropic electron pressure and hyper-resistivity, which represents off-diagonal components of electric pressure, mainly balanced one another, but this has not been tested in kinetic simulations. Using the Equations of State and balance of forces in a nearly 1D current layer, a model predicting the plasma density, magnetic field and electron pressures of the layer based on upstream plasma conditions was also developed and successfully applied to simulation results with moderate guide-fields. Finally, simulations at lower mass ratio on larger domains are explored, and compared to one another and to spacecraft observations. Despite some differences between upstream conditions of the simulations and spacecraft observations, simulation results and density, field and velocity measurements from a reconnection event observed by Cluster share many qualitative similarities.

Chapter 7

Summary of New Results

This dissertation presents the implementation of new Equations of State (EoS) into a fluid simulation. The EoS describe the development of anisotropic electron pressure in conditions typical of weakly-collisional reconnection. The implementation of this kinetic process in a fluid code allows reconnection to be accurately simulated using less computationally intensive fluid codes. The key new results are listed below:

Elongated current layers can develop in anisotropic fluid simulations of magnetic reconnection. In reconnection scenarios with sufficient guide-field to magnetize the exhaust plasma, fluid models based on the equations of state properly describe electron pressure anisotropy and can develop elongated layers which have been observed by spacecraft and in kinetic simulations. Due to the EoS, the observed anisotropy is independent of mass ratio allowing fluid simulations to more readily study the stability of these layers. In fact, in future implementations of the code, this provides a unique possibility for studying these layers in 3D.

Self-regulation tempers anisotropy in current layers. In addition to the fire-hose instability, which will quench anisotropy, the reconnection region exhibits some self-regulation to temper anisotropy. Pressure anisotropy along bent magnetic field, characteristic of reconnection regions drives additional current. This current generates magnetic field, increasing the total field and decreasing den-

sity variations. This decreases anisotropy as predicted by the EoS and can even limit the onset of the firehose instability.

Layer conditions may be predicted using upstream values. In reconnection scenarios with moderate guide fields, the elongated layers that typically form can be characterized by simplified force balances across and along the layer. When combined with the equations of state, layer conditions maybe predicted using upstream values. Estimating electron heating maybe be useful for spacecraft data analysis as a signature of weakly-collisional reconnection.

Future developments to the fluid code could include introducing the dynamic electron pressure into the two-fluid model which could allow an, albeit crude, pitch angle scattering and hyper-resistive heating. Also, the Braginskii formulation of ion gyro-viscosity could be added as an approximation for finite Larmor Radius effects.

Future work using this model could include the development of a 3D fluid simulation accurately study reconnection structure on a larger domain. This could be useful for more systematic comparison to spacecraft data, including from the upcoming MMS mission, and may provide more insight about signatures of reconnection.

Bibliography

[1] J. W. Dungey. Conditions for the occurence of electrical discharges in astrophysical systems. *Philosophical Magazine*, 44(354):725–738, JUL 1953.

[2] V. M. Vasyliunas. Theoretical models of magnetic field line merging. *Reviews of Geophysics*, 13(1):303–336, FEB 1975.

[3] E. R. Priest and T. G. Forbes. *Magnetic Reconnection.* Cambridge University Press, 2000.

[4] M. Yamada, R. M. Kulsrud, and H. Ji. Magnetic reconnection. *Reviews of Modern Physics*, 82:603–664, Mar 2010.

[5] J. Egedal, W. Fox, N. Katz, M. Porkolab, M. Øieroset, R. P. Lin, W. Daughton, and J. F. Drake. Evidence and theory for trapped electrons in guide field magnetotail reconnection. *Journal of Geophysical Research: Space Physics (1978–2012)*, 113(A12), 2008.

[6] A. Lê, J. Egedal, W. Daughton, W. Fox, and N. Katz. Equations of state for collisionless guide-field reconnection. *Physical Review Letters*, 102(8):085001, 2009.

[7] E. N. Parker. Sweet's mechanism for merging magnetic fields in conducting fluids. *Journal of Geophysical Research*, 62(4):509–520,. 1957.

[8] G. Paschmann. Space physics: Breaking through the lines. 439(7073):144–145.

[9] IEA. Key world energy statistics 2012.

[10] R. G. Giovanelli. A theory of chromospheric flares. *Nature*, 158:81, 1946.

[11] R. G. Giovanelli. Magnetic and electric phenomena in the sun's atmosphere associated with sunspots. *Monthly Notices of the Royal Astronomical Society*, 107:338, 1947.

[12] J. W. Dungey. *Cosmic electrodynamics.* University Press Cambridge, 1958.

[13] P. A. Sweet. The neutral point theory of solar flares. In *Electromagnetic phenomena in cosmical physics*, volume 6, page 123, 1958.

[14] S. Tsuneta, H. Hara, T. Shimizu, L. W. Acton, K. T. Strong, H. S. Hudson, and Y. Ogawara. Observation of a solar flare at the limb with the yohkoh soft x-ray telescope. *Publications of the Astronomical Society of Japan*, 44:L63–L69, 1992.

[15] S. Masuda, T. Kosugi, H. Hara, S. Tsuneta, and Y. Ogawara. A loop-top hard x-ray source in a compact solar flare as evidence for magnetic reconnection. 1994.

[16] B. J. Thompson, S. P. Plunkett, J. B. Gurman, J. S. Newmark, O. C. St Cyr, and D. J. Michels. Soho/eit observations of an earth-directed coronal mass ejection on may 12, 1997. *Geophysical Research Letters*, 25(14):2465–2468, 1998.

[17] N. Nishizuka, H. Takasaki, A. Asai, and K. Shibata. Multiple plasmoid ejections and associated hard x-ray bursts in the 2000 november 24 flare. *The Astrophysical Journal*, 711(2):1062, 2010.

[18] D. E. McKenzie. Observational studies of reconnection in the solar corona. *Physics of Plasmas (1994-present)*, 18(11):111205, 2011.

[19] R. P. Lin and H. S. Hudson. 10–100 kev electron acceleration and emission from solar flares. *Solar Physics*, 17(2):412–435, 1971.

[20] R. A. Kopp and G. W. Pneuman. Magnetic reconnection in the corona and the loop prominence phenomenon. *Solar Physics*, 50(1):85–98, 1976.

[21] D. E. Innes, B. Inhester, W. I. Axford, and K. Wilhelm. Bi-directional plasma jets produced by magnetic reconnection on the sun. 1997.

[22] J. W. Dungey. Interplanetary magnetic field and the auroral zones. *Physical Review Letters*, 6:47–48, 1961.

[23] B. Coppi, G. Laval, and R. Pellat. Dynamics of the geomagnetic tail. *Physical Review Letters*, 16(26):1207–1210, JUN 1966.

[24] V. Angelopoulos, J. P. McFadden, D. Larson, C. W. Carlson, S. B. Mende, H. Frey, T. D. Phan, D. G. Sibeck, K-H. Glaßmeier, U. Auster, et al. Tail reconnection triggering substorm onset. *Science*, 321(5891):931–935, 2008.

[25] W. J. Hughes. The magnetopause, magnetotail, and magnetic reconnection. In Margaret G Kivelson and Christopher T Russell, editors, *Introduction to space physics*, pages 227–287. Cambridge university press, 1995.

[26] G. Paschmann, J. R. Asbridge, J. T. Gosling, and R. C. Elphic. Plasma acceleration at the earth's magnetopause- evidence for reconnection. 1979.

[27] B. U. Ö. Sonnerup, G. Paschmann, I. Papamastorakis, N. Sckopke, G. Haerendel, S. J. Bame, J. R. Asbridge, J. T. Gosling, and C. T. Russell. Evidence for magnetic field reconnection at the earth's magnetopause. *Journal of Geophysical Research: Space Physics (1978–2012)*, 86(A12):10049–10067, 1981.

[28] G. Paschmann. Recent in-situ observations of magnetic reconnection in near-earth space. *Geophysical Research Letters*, 35(19), 2008.

[29] G. Paschmann, M. Øieroset, and T. D. Phan. In-situ observations of reconnection in space. In *Microphysics of Cosmic Plasmas*, pages 309–341. Springer, 2014.

[30] T. D. Phan, L. M. Kistler, B. Klecker, G. Haerendel, G. Paschmann, B. U. Ö. Sonnerup, W. Baumjohann, M. B. Bavassano-Cattaneo, C. W. Carlson, A. M. DiLellis, et al. Extended magnetic reconnection at the earth's magnetopause from detection of bi-directional jets. *Nature*, 404(6780):848–850, 2000.

[31] J. T. Gosling, M. F. Thomsen, S. J. Bame, T. G. Onsager, and C. T. Russell. The electron edge of low latitude boundary layer during accelerated flow events. *Geophysical Research Letters*, 17(11):1833–1836, 1990.

[32] S. A. Fuselier, D. M. Klumpar, and E. G. Shelley. Ion reflection and transmission during reconnection at the earth's subsolar magnetopause. *Geophysical Research Letters*, 18(2):139–142, 1991.

[33] F. S. Mozer, S. D. Bale, and T. D. Phan. Evidence of diffusion regions at a subsolar magnetopause crossing. *Physical Review Letters*, 89(1):015002, 2002.

[34] A. Vaivads, A. Retinò, Y. V. Khotyaintsev, and M. André. The alfvén edge in asymmetric reconnection. *Annales Geophysicae (09927689)*, 28(6), 2010.

[35] A. Nishida, H. Hayakawa, and E. W. Hones. Observed signatures of reconnection in the magnetotail. *Journal of Geophysical Research: Space Physics (1978–2012)*, 86(A3):1422–1436, 1981.

[36] A. Nishida. Reconnection in earth's magnetotail: An overview. *Geophysical Monograph Series*, 30:159–167, 1984.

[37] T. Nagai, K. Takahashi, H. Kawano, T. Yamamoto, S. Kokubun, and A. Nishida. Initial geotail survey of magnetic substorm signatures in the magnetotail. *Geophysical Research Letters*, 21(25):2991–2994, 1994.

[38] V. A. Sergeev, V. Angelopoulos, D. G. Mitchell, and C. T. Russell. In situ observations of magnetotail reconnection prior to the onset of a small substorm. *Journal of Geophysical Research: Space Physics (1978–2012)*, 100(A10):19121–19133, 1995.

[39] T. Nagai, M. Fujimoto, Y. Saito, S. Machida, T. Terasawa, R. Nakamura, T. Yamamoto, T. Mukai, A. Nishida, and S. Kokubun. Structure and dynamics of magnetic reconnection for substorm onsets with geotail observations. *Journal of Geophysical Research: Space Physics (1978–2012)*, 103(A3):4419–4440, 1998.

[40] M. Øieroset, T. D. Phan, M. Fujimoto, R. P. Lin, and R. P. Lepping. In situ detection of collisionless reconnection in the earth's magnetotail. *Nature*, 412(6845):414–417, 2001.

[41] T. Nagai, I. Shinohara, M. Fujimoto, M. Hoshino, Y. Saito, S. Machida, and T. Mukai. Geotail observations of the hall current system: Evidence of magnetic reconnection in the magnetotail. *Journal of Geophysical Research: Space Physics (1978–2012)*, 106(A11):25929–25949, 2001.

[42] A. Runov, R. Nakamura, W. Baumjohann, R. A. Treumann, T. L. Zhang, M. Volwerk, Z. Vörös, A. Balogh, K-H. Glaßmeier, B. Klecker, et al. Current sheet structure near magnetic x-line observed by cluster. *Geophysical Research Letters*, 30(11), 2003.

[43] R. Nakamura, W. Baumjohann, Y. Asano, A. Runov, A. Balogh, C. J. Owen, A. N. Fazakerley, M. Fujimoto, B. Klecker, and H. Rème. Dynamics of thin current sheets associated with magnetotail reconnection. *Journal of Geophysical Research: Space Physics (1978–2012)*, 111(A11), 2006.

[44] A. Vaivads, Y. Khotyaintsev, M. André, A. Retinò, S. C. Buchert, B. N. Rogers, P. Décréau, G. Paschmann, and T. D. Phan. Structure of the magnetic reconnection diffusion region from four-spacecraft observations. *Physical Review Letters*, 93(10):105001, 2004.

[45] J. P. Eastwood, M. A. Shay, T. D. Phan, and M. Øieroset. Asymmetry of the ion diffusion region hall electric and magnetic fields during guide field reconnection: Observations and comparison with simulations. *Physical Review Letters*, 104(20):205001, 2010.

[46] J. P. Eastwood, T. D. Phan, M. Øieroset, and M. A. Shay. Average properties of the magnetic reconnection ion diffusion region in the earth's magnetotail: The 2001–2005 cluster observations and comparison with simulations. *Journal of Geophysical Research: Space Physics (1978–2012)*, 115(A8), 2010.

[47] M. Øieroset, R. P. Lin, T. D. Phan, D. E. Larson, and S. D. Bale. Evidence for electron acceleration up to 300 k e v in the magnetic reconnection diffusion region of earths magnetotail. *Physical Review Letters*, 89(19):195001, 2002.

[48] D. N. Baker, W. K. Peterson, S. Eriksson, X. Li, J. B. Blake, J. L. Burch, P. W. Daly, M. W. Dunlop, A. Korth, E. Donovan, et al. Timing of magnetic reconnection initiation during a global magnetospheric substorm onset. *Geophysical Research Letters*, 29(24):43–1, 2002.

[49] S. Curtis. The magnetospheric multiscale mission... resolving fundamental processes in space plasmas. In *The magnetospheric multiscale mission: resolving fundamental processes in space plasmas: report of the NASA Science and Technology Definition Team for the Magnetospheric Multiscale (MMS) Mission/S.*

Curtis. Greenbelt, Md.: National Aeronautics and Space Administration, Goddard Space Flight Center, 1999.(NASA/TM; 2000-209883), volume 1, 1999.

[50] A. S. Sharma and S. A. Curtis. Magnetospheric multiscale mission. In *Nonequilibrium Phenomena in Plasmas*, pages 179–195. Springer, 2005.

[51] S. A. Fuselier and W. S. Lewis. Properties of near-earth magnetic reconnection from in-situ observations. *Space Science Reviews*, 160(1-4):95–121, 2011.

[52] A. Retinò, D. Sundkvist, A. Vaivads, F. S. Mozer, M. André, and C. J. Owen. In situ evidence of magnetic reconnection in turbulent plasma. *Nature Physics*, 3(4):236–238, 2007.

[53] T. D. Phan, G. Paschmann, C. Twitty, F. S. Mozer, J. T. Gosling, J. P. Eastwood, M. Øieroset, H. Reme, and E. A. Lucek. Evidence for magnetic reconnection initiated in the magnetosheath. *Geophysical Research Letters*, 34(14), 2007.

[54] J. A. Slavin, M. H. Acuña, B. J. Anderson, D. N. Baker, M. Benna, G. Gloeckler, R. E. Gold, G. C. Ho, R. M. Killen, H. Korth, et al. Mercury's magnetosphere after messenger's first flyby. *Science*, 321(5885):85–89, 2008.

[55] J. A. Slavin, M. H. Acuña, B. J. Anderson, D. N. Baker, M. Benna, S. A. Boardsen, G. Gloeckler, R. E. Gold, G. C. Ho, H. Korth, et al. Messenger observations of magnetic reconnection in mercurys magnetosphere. *Science*, 324(5927):606–610, 2009.

[56] J. P. Eastwood, D. A. Brain, J. S. Halekas, J. F. Drake, T. D. Phan, M. Øieroset, D. L. Mitchell, R. P. Lin, and M. H. Acuña. Evidence for collisionless magnetic reconnection at Mars. *Geophysical Research Letters*, 35(2), 2008.

[57] J. S. Halekas, J. P. Eastwood, D. A. Brain, T. D. Phan, M. Øieroset, and R. P. Lin. In situ observations of reconnection hall magnetic fields at Mars: Evidence for ion diffusion region encounters. *Journal of Geophysical Research: Space Physics (1978–2012)*, 114(A11), 2009.

[58] T. L. Zhang, Q. M. Lu, W. Baumjohann, C. T. Russell, A. Fedorov, S. Barabash, A. J. Coates, A. M. Du, J. B. Cao, R. Nakamura, et al. Magnetic reconnection in the near venusian magnetotail. *Science*, 336(6081):567–570, 2012.

[59] C. T. Russell, K. K. Khurana, D. E. Huddleston, and M. G. Kivelson. Localized reconnection in the near jovian magnetotail. *Science*, 280(5366):1061–1064, 1998.

[60] A. Radioti, D. Grodent, J-C. Gérard, B. Bonfond, and J. T. Clarke. Auroral polar dawn spots: Signatures of internally driven reconnection processes at jupiter's magnetotail. *Geophysical Research Letters*, 35(3), 2008.

[61] C. M. Jackman, C. T. Russell, D. J. Southwood, C. S. Arridge, N. Achilleos, and M. K. Dougherty. Strong rapid dipolarizations in saturn's magnetotail: In situ evidence of reconnection. *Geophysical Research Letters*, 34(11), 2007.

[62] H. J. McAndrews, C. J. Owen, M. F. Thomsen, B. Lavraud, A. J. Coates, M. K. Dougherty, and D. T. Young. Evidence for reconnection at saturn's magnetopause. *Journal of Geophysical Research: Space Physics (1978–2012)*, 113(A4), 2008.

[63] J. D. Richardson, J. W. Belcher, R. S. Selesnick, M. Zhang, G. L. Siscoe, and A. Eviatar. Evidence for periodic reconnection at uranus? *Geophysical Research Letters*, 15(8):733–736, 1988.

[64] D. E. Huddleston, C. T. Russell, G. Le, and A. Szabo. Magnetopause structure and the role of reconnection at the outer planets. *Journal of Geophysical Research: Space Physics (1978–2012)*, 102(A11):24289–24302, 1997.

[65] J. T. Gosling, R. M. Skoug, D. J. McComas, and C. W. Smith. Direct evidence for magnetic reconnection in the solar wind near 1 au. *Journal of Geophysical Research: Space Physics (1978–2012)*, 110(A1), 2005.

[66] T. D. Phan, J. T. Gosling, M. S. Davis, R. M. Skoug, M. Øieroset, R. P. Lin, R. P. Lepping, D. J. McComas, C. W. Smith, H. Reme, et al. A magnetic reconnection x-line extending more than 390 earth radii in the solar wind. *Nature*, 439(7073):175–178, 2006.

[67] M. S. Davis, T. D. Phan, J. T. Gosling, and R. M. Skoug. Detection of oppositely directed reconnection jets in a solar wind current sheet. *Geophysical Research Letters*, 33(19), 2006.

[68] H. Tian, S. Yao, Q. Zong, J. He, and Y. Qi. Signatures of magnetic reconnection at boundaries of interplanetary small-scale magnetic flux ropes. *The Astrophysical Journal*, 720(1):454, 2010.

[69] J. T. Gosling. Magnetic reconnection in the solar wind. *Space Science Reviews*, 172(1-4):187–200, 2012.

[70] I. T. Chapman. Controlling sawtooth oscillations in tokamak plasmas. *Plasma Physics and Controlled Fusion*, 53(1):013001, 2011.

[71] S. Von Goeler, W. Stodiek, and N. Sauthoff. Studies of internal disruptions and m= 1 oscillations in tokamak discharges with soft-x-ray tecniques. *Physical Review Letters*, 33:1201–1203, 1974.

[72] B. B. Kadomtsev. On disruptive instability in tokamaks. *Soviet Journal of Plasma Physics*, 1:710–715, 1975.

[73] A. W. Edwards, D. J. Campbell, W. W. Engelhardt, H-U. Fahrbach, R. D. Gill, R. S. Granetz, S. Tsuji, B. J. D. Tubbing, A. Weller, J. Wesson, et al. Rapid collapse of a plasma sawtooth oscillation in the jet tokamak. *Physical Review Letters*, 57(2):210, 1986.

[74] J. Wesson. *Tokamaks*, volume 149. Oxford University Press, 2011.

[75] M. Yamada, F. M. Levinton, N. Pomphrey, R. Budny, J. Manickam, and Y. Nagayama. Investigation of magnetic reconnection during a sawtooth crash in a high-temperature tokamak plasma. *Physics of Plasmas (1994-present)*, 1(10):3269–3276, 1994.

[76] N. A. Uckan, J. Galambos, J. Wesley, D. Boucher, F. Perkins, D. Post, and S. Putvinski. Iter-eda physics design requirements and plasma performance assessments. Technical report, Oak Ridge National Lab., TN (United States), 1996.

[77] A. H. Morton. Disruptive instability mode structure in the lt-3 tokamak. *Nuclear Fusion*, 16(4):571, 1976.

[78] N. R. Sauthoff, S. Von Goeler, and W. Stodiek. A study of disruptive instabilities in the plt tokamak using x-ray techniques. *Nuclear Fusion*, 18(10):1445, 1978.

[79] J. B. Taylor. Relaxation of toroidal plasma and generation of reverse magnetic fields. *Physical Review Letters*, 33(19):1139, 1974.

[80] J. B. Taylor. Relaxation and magnetic reconnection in plasmas. *Reviews of Modern Physics*, 58(3):741, 1986.

[81] R. G. Watt and R. A. Nebel. Sawteeth, magnetic disturbances, and magnetic flux regeneration in the reversed-field pinch. *Physics of Fluids (1958-1988)*, 26(5):1168–1170, 1983.

[82] D. A. Baker. The role of magnetic reconnection phenomena in the reversed-field pinch. *Geophysical Monograph Series*, 30:332–340, 1984.

[83] J. H. Hammer. Reconnection in spheromak formation and sustainment. In E. W. Hones Jr, editor, *Magnetic Reconnection in Space and Laboratory Plasmas*, volume 30, pages 319–331. American Geophysical Union, 1984.

[84] T. R. Jarboe. Review of spheromak research. *Plasma physics and controlled fusion*, 36(6):945, 1994.

[85] A. Bratenahl and C. M. Yeates. Experimental study of magnetic flux transfer at the hyperbolic neutral point. *Physics of Fluids*, 13:2696–2709, 1970.

[86] S. I. Syrovatskii, A. G. Frank, and Khodzhaev A. Z. Current distribution near the null line of a magnetic field and turbulent plasma resistance. *Soviet Physics - Technical Physics English Translation*, 18:580–586, 1973.

[87] P. J. Baum and A. Bratenahl. Mass motion and heating in a magnetic neutral point system. *Journal of Plasma Physics*, 11(01):93–98, 1974.

[88] P. J. Baum and A. Bratenahl. Magnetic reconnection experiments. In L. Marton and C. Marton, editors, *Advances in Electronics and Electron Physics*, volume 54, pages 1–61. Academic Press, 1980.

[89] A. G. Frank. Experimental study of the conditions for the appearance of a neutral current sheet in a plasma: Some characteristics of the sheet. In N.G. Basov, editor, *Neutral Current Sheets in Plasmas*, volume 74 of *The Lebedev Physics Institute Series*, pages 107–163. Springer US, 1976.

[90] S. I. Syrovatskii. Pinch sheets and reconnection in astrophysics. *Annual Review of Astronomy and Astrophysics*, 19:163–229, 1981.

[91] R. L. Stenzel and W. Gekelman. Magnetic field line reconnection experiments 1. field topologies. *Journal of Geophysical Research: Space Physics*, 86(A2):649–658, 1981.

[92] W. Gekelman and R. L. Stenzel. Magnetic field line reconnection experiments 2. plasma parameters. *Journal of Geophysical Research: Space Physics*, 86(A2):659–666, 1981.

[93] R. L. Stenzel, W. Gekelman, and N. Wild. Magnetic field line reconnection experiments: 5. current disruptions and double layers. *Journal of Geophysical Research: Space Physics*, 88(A6):4793–4804, 1983.

[94] M. Yamada, H. Ji, S. Hsu, T. Carter, R. M. Kulsrud, N. Bretz, F. Jobes, Y. Ono, and F. Perkins. Study of driven magnetic reconnection in a laboratory plasma. *Physics of Plasmas (1994-present)*, 4(5):1936–1944, 1997.

[95] H. Ji, M. Yamada, S. Hsu, and R. M. Kulsrud. Experimental test of the sweet-parker model of magnetic reconnection. *Physical Review Letters*, 80:3256–3259, Apr 1998.

[96] H. Ji, M. Yamada, S. Hsu, R. M. Kulsrud, T. Carter, and S. Zaharia. Magnetic reconnection with sweet-parker characteristics in two-dimensional laboratory plasmas. *Physics of Plasmas (1994-present)*, 6(5):1743–1750, 1999.

[97] Y. Ren, M. Yamada, S. Gerhardt, H. Ji, R. M. Kulsrud, and A. Kuritsyn. Experimental verification of the hall effect during magnetic reconnection in a laboratory plasma. *Physical Review Letters*, 95:055003, Jul 2005.

[98] J. Egedal, A. Fasoli, M. Porkolab, and D. Tarkowski. Plasma generation and confinement in a toroidal magnetic cusp. *Review of Scientific Instruments*, 71(9):3351–3361, 2000.

[99] J. Egedal, A. Fasoli, D. Tarkowski, and A. Scarabosio. Collisionless magnetic reconnection in a toroidal cusp. *Physics of Plasmas (1994-present)*, 8(5):1935–1943, 2001.

[100] J. Egedal, W. Fox, N. Katz, M. Porkolab, K. Reim, and E. Zhang. Laboratory observations of spontaneous magnetic reconnection. *Physical Review Letters*, 98(1):015003, 2007.

[101] N. Katz, J. Egedal, W. Fox, A. Lê, J. Bonde, and A. Vrublevskis. Laboratory observation of localized onset of magnetic reconnection. *Physical Review Letters*, 104(25):255004, 2010.

[102] J. Egedal, N. Katz, J. Bonde, W. Fox, A. Lê, M. Porkolab, and A. Vrublevskis. Spontaneous onset of magnetic reconnection in toroidal plasma caused by breaking of 2d symmetry. *Physics of Plasmas (1994-present)*, 18(11):–, 2011.

[103] J. Egedal, W. Fox, M. Porkolab, and A. Fasoli. Experimental evidence of fast reconnection via trapped electron motion. *Physics of Plasmas (1994-present)*, 11(5):2844–2851, 2004.

[104] W. Fox, M. Porkolab, J. Egedal, N. Katz, and A. Lê. Laboratory observation of electron phase-space holes during magnetic reconnection. *Physical Review Letters*, 101(25):255003, 2008.

[105] M. R. Brown. Experimental studies of magnetic reconnection. *Physics of Plasmas (1994-present)*, 6(5):1717–1724, 1999.

[106] M. R. Brown, C. D. Cothran, and J. Fung. Two fluid effects on three-dimensional reconnection in the swarthmore spheromak experiment with comparisons to space data. *Physics of Plasmas (1994-present)*, 13(5):056503, 2006.

[107] I. Furno, T. Intrator, E. Torbert, C. Carey, M. D. Cash, J. K. Campbell, W. J. Fienup, C. A. Werley, G. A. Wurden, and G. Fiksel. Reconnection scaling experiment: A new device for three-dimensional magnetic reconnection studies. *Review of scientific instruments*, 74(4):2324–2331, 2003.

[108] T. P. Intrator, X. Sun, G. Lapenta, L. Dorf, and I. Furno. Experimental onset threshold and magnetic pressure pile-up for 3d reconnection. *Nature Physics*, 5(7):521–526, 2009.

[109] P. M. Nilson, L. Willingale, M. C. Kaluza, C. Kamperidis, S. Minardi, M. S. Wei, P. Fernandes, M. Notley, S. Bandyopadhyay, M. Sherlock, R. J. Kingham, M. Tatarakis, Z. Najmudin, W. Rozmus, R. G. Evans, M. G. Haines, A. E. Dangor, and K. Krushelnick. Magnetic reconnection and plasma dynamics in two-beam laser-solid interactions. *Physical Review Letters*, 97:255001, Dec 2006.

[110] C. K. Li, F. H. Séguin, J. A. Frenje, J. R. Rygg, R. D. Petrasso, R. P. J. Town, O. L. Landen, J. P. Knauer, and V. A. Smalyuk. Observation of megagauss-field topology changes due to magnetic reconnection in laser-produced plasmas. *Physical Review Letters*, 99:055001, Aug 2007.

[111] W. Fox, A. Bhattacharjee, and K. Germaschewski. Fast magnetic reconnection in laser-produced plasma bubbles. *Physical Review Letters*, 106(21):215003, 2011.

[112] S. Jardin. *Computational methods in plasma physics.* CRC Press, 2010.

[113] I. Silin and J. Büchner. Nonlinear instability of thin current sheets in antiparallel and guided magnetic fields. *Physics of Plasmas (1994-present)*, 10(9):3561–3570, 2003.

[114] H. Schmitz and R. Grauer. Kinetic vlasov simulations of collisionless magnetic reconnection. *Physics of Plasmas (1994-present)*, 13(9):092309, 2006.

[115] T. Umeda, K. Togano, and T. Ogino. Structures of diffusion regions in collisionless magnetic reconnection. *Physics of Plasmas (1994-present)*, 17(5):052103, 2010.

[116] C. K. Birdsall and A. B. Langdon. *Plasma physics via computer simulation.* CRC Press, 2004.

[117] D. Winske, L. Yin, N. Omidi, H. Karimabadi, and K. Quest. Hybrid simulation codes: past, present and futurea tutorial. In *Space Plasma Simulation*, pages 136–165. Springer, 2003.

[118] T. Sugiyama and K. Kusano. Multi-scale plasma simulation by the interlocking of magnetohydrodynamic model and particle-in-cell kinetic model. *Journal of Computational Physics*, 227(2):1340–1352, 2007.

[119] S. Usami, H. Ohtani, R. Horiuchi, et al. First demonstration of collisionless driven reconnection in a multi-hierarchy simulation. *Plasma and Fusion Research*, 4:49, 2009.

[120] M. Ugai and T. Tsuda. Magnetic field-line reconnexion by localized enhancement of resistivity: Part 1. evolution in a compressible MHD fluid. *Journal of Plasma Physics*, 17(03):337–356, 1977.

[121] T. Sato and T. Hayashi. Externally driven magnetic reconnection and a powerful magnetic energy converter. *Physics of Fluids (1958-1988)*, 22(6):1189–1202, 1979.

[122] E. R. Priest and T. G. Forbes. New models for fast steady state magnetic reconnection. *Journal of Geophysical Research: Space Physics (1978–2012)*, 91(A5):5579–5588, 1986.

[123] D. Biskamp. Magnetic reconnection via current sheets. *Physics of Fluids (1958-1988)*, 29(5):1520–1531, 1986.

[124] J. N. Leboeuf, F. Brunel, T. Tajima, J. Sakai, C. C. Wu, and J. M. Dawson. Computer modeling of fast collisionless reconnection. *Geophysical Monograph Series*, 30:282–291, 1984.

[125] B. U. Ö. Sonnerup. Magnetic field reconnection. *Solar system plasma physics*, 1:45–108, 1979.

[126] T. Terasawa. Hall current effect on tearing mode instability. *Geophysical Research Letters*, 10(6):475–478, 1983.

[127] M. E. Mandt, R. E. Denton, and J. F. Drake. Transition to whistler mediated magnetic reconnection. *Geophysical Research Letters*, 21(1):73–76, 1994.

[128] Z. W. Ma and A. Bhattacharjee. Fast impulsive reconnection and current sheet intensification due to electron pressure gradients in semi-collisional plasmas. *Geophysical Research Letters*, 23(13):1673–1676, 1996.

[129] D. Biskamp, E. Schwarz, and J. F. Drake. Two-fluid theory of collisionless magnetic reconnection. *Physics of Plasmas*, 4(4):1002, 1997.

[130] M. A. Shay, J. F. Drake, R. E. Denton, and D. Biskamp. Structure of the dissipation region during collisionless magnetic reconnection. *Journal of Geophysical Research: Space Physics (1978–2012)*, 103(A5):9165–9176, 1998.

[131] M. A. Shay and J. F. Drake. The role of electron dissipation on the rate of collisionless magnetic reconnection. *Geophysical Research Letters*, 25(20):3759–3762, 1998.

[132] X. Wang, A. Bhattacharjee, and Z. W. Ma. Collisionless reconnection: Effects of hall current and electron pressure gradient. *Journal of Geophysical Research: Space Physics (1978–2012)*, 105(A12):27633–27648, 2000.

[133] J. Birn, J. F. Drake, M. A. Shay, B. N. Rogers, R. E. Denton, M. Hesse, M. M. Kuznetsova, Z. W. Ma, A. Bhattacharjee, A. Otto, and P. L. Pritchett. Geospace environmental modeling (gem) magnetic reconnection challenge. *Journal of Geophysical Research: Space Physics*, 106(A3):3715–3719, 2001.

[134] P. L. Pritchett. Geospace environment modeling magnetic reconnection challenge: Simulations with a full particle electromagnetic code. *Journal of Geophysical Research: Space Physics (1978–2012)*, 106(A3):3783–3798, 2001.

[135] M. Hesse and D. Winske. Electron dissipation in collisionless magnetic reconnection. *Journal of Geophysical Research: Space Physics (1978–2012)*, 103(A11):26479–26486, 1998.

[136] M. M. Kuznetsova, M. Hesse, and D. Winske. Kinetic quasi-viscous and bulk flow inertia effects in collisionless magnetotail reconnection. *Journal of Geophysical Research: Space Physics (1978–2012)*, 103(A1):199–213, 1998.

[137] M. Hesse, K. Schindler, J. Birn, and M. M. Kuznetsova. The diffusion region in collisionless magnetic reconnection. *Physics of Plasmas (1994-present)*, 6(5), 1999.

[138] M. Hesse, J. Birn, and M. M. Kuznetsova. Collisionless magnetic reconnection: Electron processes and transport modeling. *Journal of Geophysical Research: Space Physics (1978–2012)*, 106(A3):3721–3735, 2001.

[139] M. Hesse, M. M. Kuznetsova, and M. Hoshino. The structure of the dissipation region for component reconnection: Particle simulations. *Geophysical Research Letters*, 29(12):4–1, 2002.

[140] M. Hesse. Dissipation in magnetic reconnection with a guide magnetic field. *Physics of Plasmas (1994-present)*, 13(12):122107, 2006.

[141] J. Scudder and W. Daughton. illuminating electron diffusion regions of collisionless magnetic reconnection using electron agyrotropy. *Journal of Geophysical Research: Space Physics*, 113(A6), 2008.

[142] K. Fujimoto and R. D. Sydora. Particle description of the electron diffusion region in collisionless magnetic reconnection. *Physics of Plasmas (1994-present)*, 16(11):112309, 2009.

[143] T. D. Phan, J. F. Drake, M. A. Shay, F. S. Mozer, and J. P. Eastwood. Evidence for an elongated (>60 ion skin depths) electron diffusion region during fast magnetic reconnection. *Physical Review Letters*, 99(25):255002, 2007.

[144] J. F. Drake, M. Swisdak, K. M. Schoeffler, B. N. Rogers, and S. Kobayashi. Formation of secondary islands during magnetic reconnection. *Geophysical Research Letters*, 33(13), 2006.

[145] K. Fujimoto. Time evolution of the electron diffusion region and the reconnection rate in fully kinetic and large system. *Physics of Plasmas (1994-present)*, 13(7):–, 2006.

[146] W. Daughton, J. Scudder, and H. Karimabadi. Fully kinetic simulations of undriven magnetic reconnection with open boundary conditions. *Physics of Plasmas (1994-present)*, 13(7):–, 2006.

[147] H. Karimabadi, W. Daughton, and J. Scudder. Multi-scale structure of the electron diffusion region. *Geophysical Research Letters*, 34(13), 2007.

[148] M. A. Shay, J. F. Drake, and M. Swisdak. Two-scale structure of the electron dissipation region during collisionless magnetic reconnection. *Physical Review Letters*, 99:155002, Oct 2007.

[149] A. Klimas, M. Hesse, and S. Zenitani. Particle-in-cell simulation of collisionless reconnection with open outflow boundaries. *Physics of Plasmas (1994-present)*, 15(8), 2008.

[150] M. Hesse, S. Zenitani, and A. Klimas. The structure of the electron outflow jet in collisionless magnetic reconnection. *Physics of Plasmas (1994-present)*, 15(11), 2008.

[151] W. Daughton, V. Roytershteyn, H. Karimabadi, L. Yin, B. J. Albright, S. P. Gary, and K. J. Bowers. Secondary island formation in collisional and collisionless kinetic simulations of magnetic reconnection. In *MODERN CHALLENGES IN NONLINEAR PLASMA PHYSICS: A Festschrift Honoring the Career of Dennis Papadopoulos*, volume 1320, pages 144–159. AIP Publishing, 2011.

[152] R. L. Fermo, J. F. Drake, and M. Swisdak. Secondary magnetic islands generated by the kelvin-helmholtz instability in a reconnecting current sheet. *Physical Review Letters*, 108(25):255005, 2012.

[153] A. Lê, J. Egedal, O. Ohia, W. Daughton, H. Karimabadi, and V. S. Lukin. Regimes of the electron diffusion region in magnetic reconnection. *Physical Review Letters*, 110(13):135004, 2013.

[154] A. Lê. *Electron equations of state during magnetic reconnection.* PhD thesis, Massachusetts Institute of Technology, 2012.

[155] R. Horiuchi and T. Sato. Three-dimensional particle simulation of plasma instabilities and collisionless reconnection in a current sheet. *Physics of Plasmas (1994-present)*, 6(12):4565–4574, 1999.

[156] R. Horiuchi, W. Pei, and T. Sato. Collisionless driven reconnection in an open system. *EARTH PLANETS AND SPACE*, 53(6):439–446, 2001.

[157] P. L. Pritchett. Collisionless magnetic reconnection in a three-dimensional open system. *Journal of Geophysical Research: Space Physics (1978–2012)*, 106(A11):25961–25977, 2001.

[158] A. Zeiler, D. Biskamp, J. F. Drake, B. N. Rogers, M. A. Shay, and M. Scholer. Three-dimensional particle simulations of collisionless magnetic reconnection. *Journal of Geophysical Research: Space Physics (1978–2012)*, 107(A9):SMP–6, 2002.

[159] J. F. Drake, M. Swisdak, C. Cattell, M. A. Shay, B. N. Rogers, and A. Zeiler. Formation of electron holes and particle energization during magnetic reconnection. *Science*, 299(5608):873–877, 2003.

[160] P. L. Pritchett and F. V. Coroniti. Three-dimensional collisionless magnetic reconnection in the presence of a guide field. *Journal of Geophysical Research: Space Physics*, 109(A1):n/a–n/a, 2004.

[161] W. Daughton, V. Roytershteyn, H. Karimabadi, L. Yin, B. J. Albright, B. Bergen, and K. J. Bowers. Role of electron physics in the development of turbulent magnetic reconnection in collisionless plasmas. *Nature Physics*, 7(7):539–542, 2011.

[162] C. Cattell, J. Dombeck, J. Wygant, J. F. Drake, M. Swisdak, M. L. Goldstein, W. Keith, A. Fazakerley, M. André, E. Lucek, et al. Cluster observations of electron holes in association with magnetotail reconnection and comparison to simulations. *Journal of Geophysical Research: Space Physics (1978–2012)*, 110(A1), 2005.

[163] W. Daughton, G. Lapenta, and P. Ricci. Nonlinear evolution of the lower-hybrid drift instability in a current sheet. *Physical Review Letters*, 93(10):105004, 2004.

[164] M. V. Goldman, G. Lapenta, D. L. Newman, S. Markidis, and H. Che. Jet deflection by very weak guide fields during magnetic reconnection. *Physical Review Letters*, 107(13):135001, 2011.

[165] P. Ricci, G. Lapenta, and J. U. Brackbill. Gem reconnection challenge: Implicit kinetic simulations with the physical mass ratio. *Geophysical Research Letters*, 29(23):3–1–3–4, 2002.

[166] G. Lapenta, S. Markidis, A. Divin, M. Goldman, and D. Newman. Scales of guide field reconnection at the hydrogen mass ratio. *Physics of Plasmas (1994-present)*, 17(8):082106, 2010.

[167] M. M. Kuznetsova, M. Hesse, and D. Winske. Toward a transport model of collisionless magnetic reconnection. *Journal of Geophysical Research: Space Physics*, 105(A4):7601–7616, 2000.

[168] M. M. Kuznetsova, M. Hesse, and D. Winske. Collisionless reconnection supported by nongyrotropic pressure effects in hybrid and particle simulations. *Journal of Geophysical Research: Space Physics*, 106(A3):3799–3810, 2001.

[169] M. Hesse, M. M. Kuznetsova, and J. Birn. The role of electron heat flux in guide-field magnetic reconnection. *Physics of Plasmas (1994-present)*, 11(12):5387–5397, 2004.

[170] A. Divin, S. Markidis, G. Lapenta, V. S. Semenov, N. V. Erkaev, and H. K. Biernat. Model of electron pressure anisotropy in the electron diffusion region of collisionless magnetic reconnection. *Physics of Plasmas (1994-present)*, 17(12):–, 2010.

[171] M. M. Kuznetsova, M. Hesse, L. Rasttter, A. Taktakishvili, G. Toth, D. L. De Zeeuw, A. Ridley, and T. I. Gombosi. Multiscale modeling of magnetospheric reconnection. *Journal of Geophysical Research: Space Physics*, 112(A10):n/a–n/a, 2007.

[172] J. U. Brackbill. A comparison of fluid and kinetic models of steady magnetic reconnection. *Physics of Plasmas (1994-present)*, 18(3):032309, 2011.

[173] E. R. Birn and J. Priest. *Reconnection of Magnetic Fields.* Cambridge University Press, 2007.

[174] A. A. Vlasov. The vibrational properties of an electron gas. *Physics-Uspekhi*, 10(6):721–733, 1968.

[175] M. Hesse and J. Birn. Three-dimensional MHD modeling of magnetotail dynamics for different polytropic indices. *Journal of Geophysical Research: Space Physics (1978–2012)*, 97(A4):3965–3976, 1992.

[176] M. Hesse, D. Winske, and M. M. Kuznetsova. Hybrid modeling of collisionless reconnection in two-dimensional current sheets: Simulations. *Journal of Geophysical Research: Space Physics (1978–2012)*, 100(A11):21815–21825, 1995.

[177] G. F. Chew, M. L. Goldberger, and F. E. Low. The boltzmann equation and the one-fluid hydromagnetic equations in the absence of particle collisions. *Proc. Royal Soc. A*, 112:236, 1956.

[178] S. Chapman and T. G. Cowling. *The Mathematical Theory of Nonuniform Gases.* Cambridge University Press, 1970.

[179] J. P. Freidberg. *Plasma Physics and Fusion Energy.* Cambridge University Press, 2008.

[180] D. Biskamp. *Magnetic reconnection in plasmas.* Number 3. Cambridge University Press, 2005.

[181] É. J. M. Delhez and E. Deleersnijder. Overshootings and spurious oscillations caused by biharmonic mixing. *Ocean Modelling*, 17(3):183–198, 2007.

[182] K. Schindler and G. Hornig. Magnetic Reconnection. In P. Murdin, editor, *Encyclopedia of Astronomy and Astrophysics.* November 2000.

[183] P. M. Bellan. *Fundamentals of Plasma Physics.* Cambridge University Press, 2006.

[184] A. S. Kingsep, K. V. Chukbar, and V. V. Yan'kov. Reviews of plasma physics. 1990.

[185] A. V. Gordeev, A. S. Kingsep, and L. I. Rudakov. Electron magnetohydrodynamics. *Physics Reports*, 243(5):215–315, 1994.

[186] S. V. Bulanov, F. Pegoraro, and A. S. Sakharov. Magnetic reconnection in electron magnetohydrodynamics. *Physics of Fluids B: Plasma Physics (1989-1993)*, 4(8):2499–2508, 1992.

[187] L. Chacón, A. N. Simakov, and A. Zocco. Steady-state properties of driven magnetic reconnection in 2d electron magnetohydrodynamics. *Physical Review Letters*, 99:235001, Dec 2007.

[188] M. Ottaviani and F. Porcelli. Nonlinear collisionless magnetic reconnection. *Physical Review Letters*, 71:3802–3805, Dec 1993.

[189] A. N. Simakov and L. Chacón. Quantitative, comprehensive, analytical model for magnetic reconnection in hall magnetohydrodynamics. *Physical Review Letters*, 101(10):105003, 2008.

[190] A. N. Simakov and L. Chacón. Quantitative analytical model for magnetic reconnection in hall magnetohydrodynamicsa). *Physics of Plasmas (1994-present)*, 16(5):055701, 2009.

[191] L. M. Malyshkin. Model of two-fluid reconnection. *Physical Review Letters*, 103(23):235004, 2009.

[192] L. M. Malyshkin. Fast and slow two-fluid magnetic reconnection. *Physica Scripta*, 2010(T142):014033, 2010.

[193] V. S. Lukin. *Computational study of the internal kink mode evolution and associated magnetic reconnection phenomena.* PhD thesis, Princeton University, 2008.

[194] M. A. Shay, J. F. Drake, B. N. Rogers, and R. E. Denton. The scaling of collisionless, magnetic reconnection for large systems. *Geophysical Research Letters*, 26(14):2163–2166, 1999.

[195] M. A. Shay, J. F. Drake, M. Swisdak, and B. N. Rogers. The scaling of embedded collisionless reconnection. *Physics of Plasmas (1994-present)*, 11(5):2199–2213, 2004.

[196] J. D. Huba and L. I. Rudakov. Hall magnetic reconnection rate. *Physical Review Letters*, 93(17):175003, 2004.

[197] H. Isobe, H. Takasaki, and K. Shibata. Measurement of the energy release rate and the reconnection rate in solar flares. *The Astrophysical Journal*, 632(2):1184, 2005.

[198] M. Fujimoto, M. S. Nakamura, I. Shinohara, T. Nagai, T. Mukai, Y. Saito, T. Yamamoto, and S. Kokubun. Observations of earthward streaming electrons at the trailing boundary of a plasmoid. *Geophysical Research Letters*, 24(22):2893–2896, 1997.

[199] W-L. Teh, R. Nakamura, B. U. Ö. Sonnerup, J. P. Eastwood, M. Volwerk, A. N. Fazakerley, and W. Baumjohann. Evidence of the origin of the hall magnetic field for reconnection: Hall MHD reconstruction results from cluster observations. *Journal of Geophysical Research: Space Physics (1978–2012)*, 116(A11), 2011.

[200] A. L. Borg, M. Øieroset, T. D. Phan, F. S. Mozer, A. Pedersen, C. Mouikis, J. P. McFadden, C. Twitty, A. Balogh, and H. Rme. Cluster encounter of a magnetic reconnection diffusion region in the near-earth magnetotail on september 19, 2003. *Geophysical Research Letters*, 32(19):n/a–n/a, 2005.

[201] J. R. Wygant, C. A. Cattell, R. Lysak, Y. Song, J. Dombeck, J. McFadden, F. S. Mozer, C. W. Carlson, G. Parks, E. A. Lucek, A. Balogh, M. André, H. Reme, M. Hesse, and C. Mouikis. Cluster observations of an intense normal component of the electric field at a thin reconnecting current sheet in the tail and its role in the shock-like acceleration of the ion fluid into the separatrix region. *Journal of Geophysical Research: Space Physics*, 110(A9):n/a–n/a, 2005.

[202] R. G. Kleva, J. F. Drake, and F. L. Waelbroeck. Fast reconnection in high temperature plasmas. *Physics of Plasmas (1994-present)*, 2(1):23–34, 1995.

[203] J. Egedal, M. Øieroset, W. Fox, and R. P. Lin. In situ discovery of an electrostatic potential, trapping electrons and mediating fast reconnection in the earth's magnetotail. *Physical Review Letters*, 94(2):025006, 2005.

[204] L-J. Chen, N. Bessho, B. Lefebvre, H. Vaith, A. Fazakerley, A. Bhattacharjee, P. A. Puhl-Quinn, A. Runov, Y. Khotyaintsev, A. Vaivads, et al. Evidence of an extended electron current sheet and its neighboring magnetic island during magnetotail reconnection. *Journal of Geophysical Research: Space Physics (1978–2012)*, 113(A12), 2008.

[205] J. Egedal, W. Daughton, J. F. Drake, N. Katz, and A. Lê. Formation of a localized acceleration potential during magnetic reconnection with a guide field. *Physics of Plasmas (1994-present)*, 16(5):050701, 2009.

[206] J. Egedal, W. Daughton, and A. Lê. Large-scale electron acceleration by parallel electric fields during magnetic reconnection. *Nature Physics*, 8(4):321–324, 2012.

[207] J. Egedal. A drift kinetic approach to stationary collisionless magnetic reconnection in an open cusp plasma. *Physics of Plasmas (1994-present)*, 9(4):1095–1103, 2002.

[208] J. Egedal, W. Fox, E. Belonohy, and M. Porkolab. Kinetic simulation of the vtf magnetic reconnection experiment. *Computer physics communications*, 164(1):29–33, 2004.

[209] J. Egedal, A. Lê, and W. Daughton. A review of pressure anisotropy caused by electron trapping in collisionless plasma, and its implications for magnetic reconnection. *Physics of Plasmas (1994-present)*, 20(6):061201, 2013.

[210] R. D. Hazeltine. Recursive derivation of drift-kinetic equation. *Plasma Physics*, 15:77, 1973.

[211] R. M. Kulsrud. MHD description of plasma. In A. Galeev and R. Sudan, editors, *Basic Plasma Physics*, pages 115–145. North-Holland Publishing Company, 1983.

[212] V. S. Lukin and M. G. Linton. Three-dimensional magnetic reconnection through a moving magnetic null. *Nonlinear Processes in Geophysics*, 18(6):871–882, 2011.

[213] S. Balay, J. Brown, K. Buschelman, W. D. Gropp, D. Kaushik, M. G. Knepley, L. C. McInnes, B. F. Smith, and H. Zhang. PETSc Web page, 2013. http://www.mcs.anl.gov/petsc.

[214] J. Büchner and L. M. Zelenyi. Regular and chaotic charged particle motion in magnetotaillike field reversals: 1. basic theory of trapped motion. *Journal of Geophysical Research: Space Physics (1978–2012)*, 94(A9):11821–11842, 1989.

[215] A. Lê, J. Egedal, W. Daughton, J. F. Drake, W. Fox, and N. Katz. Magnitude of the hall fields during magnetic reconnection. *Geophysical Research Letters*, 37(3), 2010.

[216] G. H. A. Cole and K. Schindler. On the equilibrium configuration of the geomagnetic tail. *Cosmic Electrodynamics*, 3:275–284, 1972.

[217] F. J. Rich, V. M. Vasyliunas, and R. A. Wolf. On the balance of stresses in the plasma sheet. *Journal of Geophysical Research*, 77(25):4670–4676, 1972.

[218] S. W. H. Cowley. Plasma populations in a simple open model magnetosphere. *Space Science Reviews*, 26(3):217–275, 1980.